



UNIVERSITY
OF TASMANIA

The use of hot-films to characterise flow regimes on a sailing yacht hull - guidance for scaling

Christopher D. Hutchison, BEng.(Hons)

Submitted in fulfilment of the requirements for the degree of
Doctor of Philosophy

National Centre for Maritime Engineering & Hydrodynamics
Australian Maritime College
University of Tasmania

Academic Supervisors:

Dr. Jonathan Binns

Prof. Neil Bose

Assoc. Prof. Paul Brandner

July 2014

Declarations

Statement of Originality

I declare that this thesis contains no material which has been accepted for a degree or diploma by the University or any other institution, except by way of background information and duly acknowledged in the thesis, and to the best of my knowledge and belief no material previously published or written by another person except where due acknowledgement is made in the text of the thesis, nor does the thesis contain any material that infringes copyright.

Authority of Access

This thesis may be made available for loan and limited copying and communication in accordance with the Copyright Act 1968.

Copyright

I warrant that I have obtained, where necessary, permission from the copyright owners to use any third-party copyright material reproduced in the thesis, or to use any of my own published works in which the copyright is held by another party (e.g. publisher, co-author).



.....

Christopher D. Hutchison

July 2014

Abstract

Within the yacht testing community there has been a continuing interest in and concern with, the effectiveness of techniques used to extrapolate model scale resistance tests to full scale values. While there are many aspects which influence the effectiveness of scaling results from model yacht experiments; this thesis has investigated the use of hot-films to characterise boundary layer state so as to provide guidance in selection of model scale. A primary focus of this thesis was to ensure the method selected to characterise the boundary layer was suitable for commercial testing programs. The methodology included a robust technique for the installation and application of glue-on hot-film sensors and a modified data analysis method. The hull form used for this research was based on an International America's Cup Class yacht. The hull type has several features desirable in researching yacht hydrodynamics including; non-immersed transom, minimal distortion to the hull lines and high aspect ratio foils.

From data obtained from the hot-film sensors a series of conclusions were made. With turbulence stimulation, the on body flow was found to be fully turbulent for all Froude numbers tested (0.05 to 0.46). This implies that with appropriate boundary layer stimulation, the state of the boundary layer is not a limiting factor in the testing of a $1/8^{th}$ scale IACC yacht model. The hot-film data also showed that the change in C_f due to waves generated by the hull were half that of the change due to natural transition. The lower limits of applicability of the Grigson flat plate friction line were also examined using this experimental data. For the $1/8^{th}$ scale model tested these limits lie at a model $Re_L = 2.6 \times 10^6$ (Froude number of 0.27) as opposed to that reported in his paper as $Re_L = 1.5 \times 10^6$ (Froude number of 0.15).

In general it was concluded that if a yacht hull-form is slender with fair lines and no immersed transom and testing is at model speeds above 1.28 m/s (Froude number of 0.27) then it is possible to use a simple analytical approach to decide the correct model scale. If there is concern that there might be an issue with transition behaviour it has been shown that it is possible and relatively simple to use hot-films to verify the boundary layer state.

Acknowledgements

From the beginning of this PhD I expressed a desire, against better advice, to pursue a project involving sailing yachts. It can be hard to obtain funding for such work as it is often perceived to have little to offer the commercial sector. For this reason I am grateful for the in-kind and research grant support which was provided. To the design team behind BMW Oracle Racing; Ian Burns, Farr Yacht Design and Juan Kouyoumdjian, thank you for agreeing to allow me to use data from a former America's Cup campaign. Also Rob Pallard as part of the team at IOT, thank you for hunting down the data and answering my many questions regarding the subtleties of model testing at your facility. To Dr Jonathan Duffy and Dr Jonathan Binns many thanks in helping obtain funding through the UTAS early career research grants scheme; without which there would have been no model or hot-film equipment.

To my co-supervisors, Professor Neil Bose and Associate Professor Paul Brandner, thank you for feedback and direction along the way. To my primary supervisor Dr Jonathan Binns, while I will say thank you it does not cover the extent of my gratitude for the time, effort and encouragement that you have given to me during this project.

For my friends and family, especially my parents, thank you for your interest and willingness to listen. I know at times I must have seemed crazy to head back into study again. Finally to my wife, Suzanne, I have not the words to describe my gratitude for the love, support and understanding that you have given; both this work and my life would be poorer were it not for your involvement.

Contents

Declaration	ii
Abstract	iii
Acknowledgements	iv
Table of Contents	viii
List of Figures	xi
List of Tables	xii
Nomenclature	xiii
Coordinate Systems	xv
1 Introduction	1
1.1 Research Objectives	2
1.2 Testing Techniques and Measurements	4
1.3 Scaling Procedures	5
1.4 Model and Facility Testing Limitations	6

2	Background	11
2.1	Laminar to Turbulent Transition in Model Testing	11
2.2	Model Scale and Velocity	12
2.3	Flow Stimulators	12
2.4	Towing Tank	12
2.5	Yacht Models	13
2.6	Test Program	15
3	Forces and Moments	17
3.1	Introduction	17
3.2	Test Equipment	18
3.3	Data Reduction	22
3.4	Results and Discussion	25
3.5	Chapter Summary	38
4	Flow Dynamics	40
4.1	Introduction	40
4.2	Test Equipment and Set-up	41
4.3	Results and Discussion	52
4.4	Chapter Summary	70

5	Correlation of Forces and Moments with Flow Dynamics	72
5.1	Introduction	72
5.2	Direct Determination of the Model Scale Friction Coefficient	73
5.3	Influence of Friction Coefficient on the Residuary Resistance Coefficient	80
5.4	Chapter Summary	82
6	Conclusions	84
6.1	Experimental Outcomes	84
6.2	Guidance for Scaling	88
7	Further Work	89
	References	96
A	Test Program	A-1
B	Lines Plan	B-1
C	Uncertainty Analysis	C-1
C.1	1/8 th ACC Yacht Model Forces and Moments	C-1
C.2	1/3 rd IACC Yacht Model Forces and Moments	C-8
C.3	1/8 th IACC Yacht Model Hot-Films	C-8

D Model Measurement Datums	D-1
E Overheat Calculations	E-1
F Supplementary Force Data	F-1
G Supplementary Moment Data	G-1
H Supplementary Hot-Film Data for 4 Hz High-Pass Filter	H-1

List of Figures

1	Body fixed coordinate system.	xv
1.1	A demonstration of the effect of upper and lower towing tank carriage speed on model scale selection.	8
1.2	The theoretical lower limit of transition $Re_\theta = 320$ at various locations on a model for a range of speeds and model scales.	9
2.1	Schematic of Australian Maritime College towing tank, carriage and the IACC model used for the tests.	13
2.2	$1/8^{th}$ geosim of a v5 IACC yacht being towed at the Australian Maritime College towing tank.	14
3.2	General view of $1/8^{th}$ model showing the relative location of fore and aft post attachment points.	20
3.3	Variation of form factor with respect to model heel angle along. . .	24
4.1	Schematic showing layout of hot-film sensors and turbulence stimulators. All dimensions shown are model scale millimetres.	43
4.2	Close-up view of installed hot-film sensor number 4.	45
4.3	General view of internal connector.	45

4.4	Detailed view of internal connector.	46
4.5	BNC connector array. Each of the five connectors is hard wired to one of the five hot-films.	46
4.6	R^2 values for curves fit through no-stud speed sweep calculated at a range of frequencies.	49
4.7	Condition 13 intermittency for hot-film four plotted with respect to variation in Froude number	50
4.8	Time domain plot of zero meaned data of all hot-films for Run 107	54
4.9	Time domain plot of zero meaned data of all hot-films for Run 239	55
4.10	LogLog plot of amplitude with respect to frequency of zero meaned data of all hot-films with and without a 4 Hz high pass filter applied for Run 239	58
4.11	LogLog plot of amplitude with respect to frequency of zero meaned data of all hot-films with and without a 4 Hz high pass filter applied for Run 244	59
4.12	The theoretical lower limit of transition $Re_\theta = 320$ at various locations on a model for a range of speeds and model scales.	61
4.13	Intermittency plotted with respect to variation in Froude number of all hot-films.	65
4.14	Intermittency plotted with respect to variation in heel angle of all hot-films.	66
4.15	Intermittency plotted with respect to variation in yaw angle of all hot-films.	67

4.16	Intermittency plotted with respect to variation in trim tab angle of all hot-films	68
4.17	Intermittency plotted with respect to variation in rudder angle of all hot-films	69
5.2	1/8 th geosim of a v5 IACC yacht being towed at the Australian Maritime College towing tank showing bow and stern waves and a trough amidships.	77
5.3	Plot showing the relative changes due to a large wave and transi- tioning flow.	79
5.4	Plot of C_R with respect to variation in Froude number (Yaw 1 de- grees, Heel 10 degrees, Tab 4 degrees, Rudder 2 degrees).	81

List of Tables

2.1	1/8 th scale model principal particulars.	15
2.2	Abbreviated test program.	16
3.1	1/8 th and 1/3 rd towing tank cross-section information with respect to model size.	23

Nomenclature

A_{PP}	Submerged profile area of the prototype including foils
B_{MAX}	Maximum beam
B_{WL}	Waterline beam
C_D	Drag coefficient
C_f	Skin friction coefficient
C_F	ITTC friction coefficient
C_L	Lift coefficient
C_M	Moment coefficient
C_p	Pressure coefficient
C_P	Prismatic coefficient
C_R	Residuary resistance coefficient
C_T	Total drag coefficient
c	Chord
\bar{c}	Mean chord
D	Drag
$d_{CANOE BODY}$	Canoe body draft
Fr	Froude number
Fr_P	Froude number of prototype
f	Frequency
f_n	Natural frequency
g	Acceleration due to gravity
ITTC	International Towing Tank Conference
L	Heel Moment
L'	Non-Dimensional Heel Moment

L_{OA}	Length overall
L_P	Length waterline of prototype
L_{TP}	Total lift of the prototype
L_{WL}	Length waterline
M	Pitch Moment
N	Yaw Moment
N'	Non-Dimensional Yaw Moment
p	Pressure
Re_L	Reynolds number using L_{WL}
R_{TP}	Total drag or resistance of the prototype
Re_X	Reynolds number using longitudinal position on the surface
Re_θ	Momentum Reynolds number
T	Period
t	Model tickness
U	Velocity
V_P	Prototype velocity
$WSA_{CANOE\ BODY}$	Wetted surface area of canoe body
WSA_P	Wetted surface area of the canoe body of the prototype

Greek letters

α	Angle of attack
$\Delta_{SAILING}$	Model scale sailing displacement
θ	Momentum thickness
λ	Scale factor
μ	Viscosity
ν	Kinematic viscosity, μ/ρ
ρ	Density of water

Coordinate Systems

Two coordinate systems were used, body fixed and flow fixed. All primary force data was captured in body fixed coordinates and then transferred to flow fixed coordinates to give lift and drag values. A pictorial representation of the body fixed coordinate systems is provided in Figure 1. The flow fixed coordinates use the same axes except that the 'X' axis and 'Y' axis are rotated about the 'Z' axis such that positive 'X' points in the direction of travel of the towing carriage.

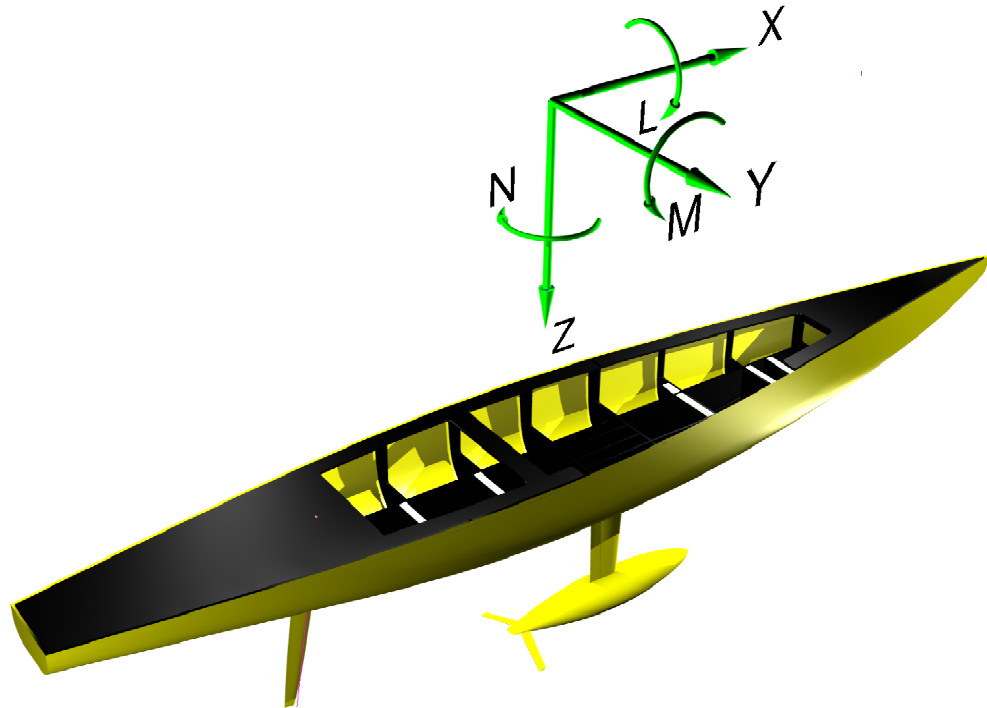


Figure 1: Body fixed coordinate system.

Chapter 1

Introduction

From the earliest work of William Froude, for example (19), (20), (21) and (22), there has been a continuing interest in and concern with, the effectiveness of the techniques used to extrapolate model scale resistance tests to full scale values. This concern has not been limited to the commercial world; with significant research into the various aspects of the model to full scale correlation of sailing vessels. A review of yacht model testing through history is provided in Debord et al.(12) and Kirkman(28).

One of the key components of a test program is the determination of the model's scale. From a purely theoretical standpoint the bigger the model the better but "...budget, time, program objectives and towing tank dimensions need to be evaluated jointly to achieve a practical compromise" Fassardi(18). Van Oossanen(42) suggests a more prescriptive approach is to establish the model scale based on achieving a minimum Reynolds number of 1×10^5 for the average chord length of the smallest foil (i.e. establish the required chord of the smallest foil to achieve the Reynolds number and then determine the rest of the model parameters from this value).

The supposed requirement to test with large models has been perpetuated by stories of unsuccessful vessel performance purportedly associated with incorrect

extrapolation of towing tank data conducted with small models. The most high profile of these, at least in the sailing community, is the case of *Mariner* an International 12 Metre racing yacht. She was designed with an unusual aft hull form. The model tests showed that the hull shape was effective. However, on launching and subsequent full scale testing against other 12 Metre class yachts it was found that *Mariner* exhibited poor performance. This apparent lack of correlation between tank and full-scale performance has been used as the reason to test large models; but it was shown by Brown(7) that the relatively poor performance of *Mariner* was to be expected based on the experimental results. In their paper they show a comparison of the results for both *Mariner* and *Courageous* which were both tested by the same facility. The comparison of the test results reveal that *Mariner* was in fact a poor candidate hull when compared to *Courageous*, a result which was also displayed at full-scale. Unfortunately this comparison was not able to be revealed at the time of the test due to confidentiality clauses between the test facility and the two separate America's Cup teams.

It should be noted that some of the figures and text that appears within this chapter have previously been published in Hutchison et al.(24).

1.1 Research Objectives

From the beginning of this project several core aims, both theoretical and physical, were identified:

1. Establish changes in forces and moments due to model scale for an IACC yacht hull.
2. Identify both the qualitative and quantitative flow regime around an IACC yacht hull.
3. Relate the identified flow regime to the forces and moments.

4. Incorporate methodologies developed to achieve item 1, 2 and 3 into standard experimental test procedures.

Determination of the forces and moments was undertaken using two geosims of an IACC yacht. Each of the geosim hulls was fully appended with rudder, keel strut with trim tab and a ballast bulb with wings. A matrix of test configurations were investigated with variation of heel angle, yaw angle, trim tab angle, rudder angle and model velocity. The test matrix was conducted on both models.

During the tests for force and moments, flow regime data was collected for the smaller model via sensors attached to the exterior of the hull. The sensors provided the necessary information to describe the flow in both qualitative, time and frequency domain voltage values, as well as quantitative values described in terms of intermittency.

The correlation of the force, moment and intermittency results made it possible to describe the nature of the flow with respect to the forces and moments. The correlated data was then used to demonstrate how the on-body flow regime influences the extrapolated data.

The quantitative measurement of forces and moments and especially fluid flow behaviour required care be taken at each stage of the installation, measurement and analysis process. For the measurements to become part of standard experimental procedures the techniques need to be robust and repeatable. In terms of the acquisition of forces and moments, the focus was placed on improving model alignment techniques to reduce the model set-up time as well as long-term repeatability. For the measurement of the fluid flow, the priority was both the application technique of the sensitive measuring instruments and establishing a relatively simple means to quantify the on-body flow state from the collected data.

1.2 Testing Techniques and Measurements

There are a number of reasons to make the decision to test yacht models in a towing tank. Three key reasons listed in Debord et al.(13) are:

1. Direct determination of hydrodynamic force data for use in performance predictions.
2. Collection of force data, flow visualization and special data for verification of analytic techniques.
3. Confirmation of results from other design studies, in the presence of a real free surface, and without simplifying assumptions.

The two main techniques for testing of model yachts are the semi-captive and “equilibrium” methods Debord et al.(12), Murdey(35) and Van Oossanen(42). The first technique involves ballasting the model to its scale displacement and correct trim and then restraining it so that it has only two degrees of freedom; heave and pitch. A range of heel, and yaw angles are tested over a range of speeds. The second technique is to tow the model from the theoretical centre of effort of the sails, with the model allowed three degrees of freedom; heave, pitch and yaw. The model is ballasted to the correct scale displacement and its trim and vertical centre of gravity are also adjusted to correspond to full-scale vessel. The model is towed by the carriage which is connected to a sliding frame on the model. The connection point on the frame is located at the centre of effort of the sails. The longitudinal position of the frame is adjusted by servos to ensure that the model achieves a steady yaw angle. The requirement to dynamically adjust the tow point is one of the key disadvantages of the ‘equilibrium’ method. This adds considerable cost to the model set-up as well as requiring sophisticated electronics. This complexity does mean that less runs are required to establish performance as the model is achieving the correct heel angle and thus only requiring a series of runs at different speeds and yaw angles. In comparison the semi-captive technique is quite simple from an

equipment perspective; but with the disadvantage that a large number of runs are required to adequately establish performance values. These runs are required to fill out a test matrix made up of a range of speeds, heel angles, yaw angles, rudder angles and even trim tab angles for every displacement and expected longitudinal trim angle. For this thesis all experiments, at both scales, were conducted using the semi-captive method.

1.3 Scaling Procedures

Commonly scaling is undertaken using the Froude assumption that resistance is made up of frictional and residuary resistance. The calculation of the frictional component typically involves the use of the ITTC 1957 line. Armstrong(2) states that it is important to note that the ITTC 1957 line, Equation (1.1), is not a flat plate friction line but a model ship correlation line. The ITTC 1957 line is in fact a version of the empirical Schoenherr formula, modified below $Re_L = 1 \times 10^7$, such that there is an improved correlation in the estimation of the friction coefficients from both large and small models, Date & Turnock(11) and Grigson(23).

$$C_{F-ITTC'57} = \frac{0.075}{(\log_{10} Re_L - 2)^2} \quad (1.1)$$

As part of this thesis investigates the viscous components of scaling model yacht test results, any scaling of data will be performed using a ‘true’ flat plate friction line. The work of Grigson(23) established two equations, reproduced here as Equation (1.3) and Equation (1.4) which are based on his formulation for a turbulent flat plate friction line Bose(6). The equations are applied as simple multipliers of the ITTC 1957 line as shown in Equation (1.2). The application of the equations improves the estimation of the friction coefficient and are now in common use within the yacht testing community. It is of note that each of Grigson’s equations is used for a different range of length Reynolds numbers and that there is a lower limit of applicability of $Re_L = 1.5 \times 10^6$. A brief discussion of the development

of Grigson's equations including an interpretation of how to directly calculate the friction line is also provided in Bose(6).

$$C_{F-Grigson} = C_{F-ITTC'57} \times G \quad (1.2)$$

Where for $1.5 \times 10^6 < Re < 20 \times 10^6$;

$$\begin{aligned} G = & 0.9335 + 0.147 [\log Re_L - 6.3]^2 \\ & - 0.071 [\log Re_L - 6.3]^3 \end{aligned} \quad (1.3)$$

and for $20 \times 10^6 < Re < 6 \times 10^9$;

$$\begin{aligned} G = & 1.0096 + 0.0456 [\log Re_L - 7.3] \\ & - 0.013944 [\log Re_L - 7.3]^2 \\ & + 0.001944 [\log Re_L - 7.3]^3 \end{aligned} \quad (1.4)$$

It has been suggested that to reliably scale the results of drag, there is a need to separate the viscous components due to the hull and appendages described as the stripping technique (13), (14) and (18). For the foils, data from numerical calculations or results obtained from specific tests in a wind tunnel can be used. For the hull a flat plate friction formula and a form factor is used. The form factor aims to add the 3D hull effects. The form factor is commonly obtained using the method described by Prohaska(39). A problem with this form factor approach is that if the form factor is used with the ITTC 1957 friction line, the form factor is effectively added to a 'friction' line that already has a form factor inbuilt. Hence, an approximation is added on top of another approximation. The methodology chosen and its implementation for this study are discussed in Chapter 3.

1.4 Model and Facility Testing Limitations

To better understand potential limitations of testing and how they relate to scale, an analysis was performed for a vessel with a nominal full-scale waterline length of

18.4 metres using Equation (1.5). The equation relates the two principal dimensionless parameters, Reynolds and Froude number, to the scale factor and was used to show how the scale and Froude number limit the model scale Reynolds number.

$$\text{Re}_L = \frac{\lambda^{-1.5} L_P^{1.5} \sqrt{g} \text{Fr}_P}{\nu} \quad (1.5)$$

Where:

Re_L is length Reynolds number of the model

λ is model scale factor

L_P is waterline length of prototype

g is acceleration due to gravity

Fr_P is length Froude number of prototype

ν is kinematic viscosity

The data from the analysis was then plotted as model scale with variation in model scale Reynolds number for a range of Froude numbers, Figure 1.1. Three additional lines have also been added which represent the upper and lower limits, 4.0 m/s and 0.5 m/s respectively, of the testing range for the Australian Maritime College towing tank carriage. Higher and lower speeds are possible but at higher speeds the length of data acquisition time is reduced and at lower speeds any errors in carriage velocity are magnified. A third line representing a carriage speed of 2.5 m/s has been included which represents the previous upper speed used for testing 1/8th IACC scale models. A carriage speed of 2.5 m/s was based on the vessel's operational profile and the structural limitations of the model. From this simple analysis we can see that a scale factor of eight is the only viable option, assuming the range of Froude numbers illustrated is required, for testing in the towing tank at the Australian Maritime College.

On examination of Figure 1.1 the one third scaling option appears to lie exactly

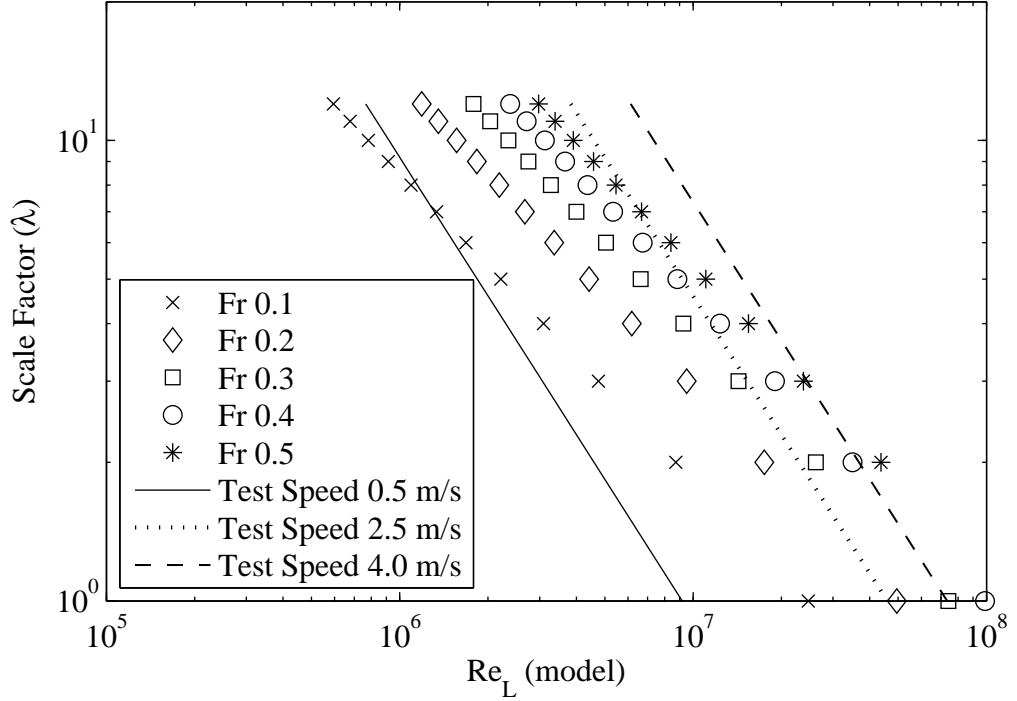


Figure 1.1: A demonstration of the effect of upper and lower towing tank carriage speed on model scale selection. Note ‘X’ and ‘Y’ axes are on a log scale.

within the speed limits set. The reasoning for such a scale working so well can be readily seen. However, it can also be seen that it is possible to reduce the scale factor to eight and still maintain reasonable testing speeds and Reynolds numbers. The added benefits of reduced costs and increased runs, make the smaller scales even more appealing when conducting test programs.

Now, the assumption that is generally used for towing tank tests is that the flow is fully turbulent over the length of the vessel at any speed. The importance of this assumption is revealed if we now replot the data from the previous figure as shown Figure 1.2.

In this figure velocity is plotted with variation with respect to scale factor for a range of Froude numbers; but there are four additional lines which represent the value of $Re_0 = 320$ at four positions along each of the scale models. Re_0 is the momentum Reynolds number, which is simply a Reynolds number where the length scale is defined by the momentum thickness of the boundary layer. Also as the

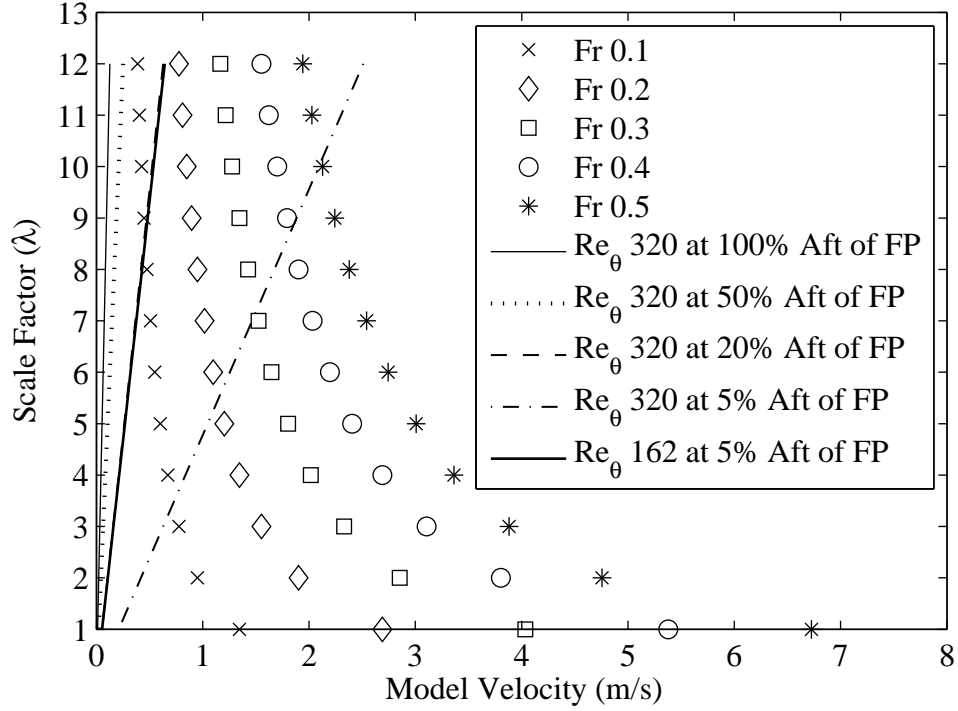


Figure 1.2: The theoretical lower limit of transition $Re_{\theta} = 320$ at various locations on a model for a range of speeds and model scales.

boundary layer grows along the model the value of Re_{θ} increases. It was reported in Preston(38) and Dyer(15) that $Re_{\theta} = 320$ is the theoretical lower limit below which there is insufficient energy in the boundary layer to enable the flow to remain fully turbulent; that is, there is not enough energy transfer through the boundary layer to be able to naturally transition from laminar to turbulent flow.

Examining the two model scales in question, $1/8^{th}$ and $1/3^{rd}$, the importance of scale and flow stimulation is apparent. For the $1/3^{rd}$ scale even at 5% (approximately 300mm) aft of the forward end of the waterline the flow has an Re_{θ} value of at least 320 even at a Froude number of 0.1. This indicates that the flow may naturally transition but will definitely transition at any line of stimulators 5% aft of the forward end of the waterline. For the $1/8^{th}$ case the situation appears more complex. It is not until a Froude number of 0.35 that the flow achieves a Re_{θ} value of at least 320 at this forward location. This illustrates that the stimulation device will not only have to produce disturbances to trip the flow but also provide additional momentum to the flow. This implies that stimulators will definitely be required

as there is no chance of the flow transitioning naturally. At speeds above Froude number of 0.35 the transition behaviour is shown to be as for the $1/3^{rd}$ scale model.

To further understand what might occur at the lower Froude numbers at $1/8^{th}$ scale an additional line for $Re_\theta = 162$ at 5% aft has been added. This line is difficult to see on the plot as it lies close to and is almost obscured by the $Re_\theta = 320$ at 20% aft line. It is stated in Preston(38) that above a value of $Re_\theta = 162$ and with stimulation of the flow there should be sufficient disturbance to start the transition close behind the stimulators. For the $1/8^{th}$ case, even at the lowest Froude number, the $Re_\theta = 162$ line lies to the left of the data point suggesting that with stimulation that there should be sufficient disturbance to start the transition to fully turbulent flow. This implies that with stimulation a $1/8^{th}$ scale model will experience fully transitioned turbulent flow at the desired range of test speeds.

All of the above discussion and calculations are based on flat plate values and as such three dimensional effects will alter the transition behaviour. However, the plot does give a solid first pass understanding of the limitations of particular model scales based on flow physics.

Chapter 2

Background

2.1 Laminar to Turbulent Transition in Model Testing

The level of background turbulence is a key element with regard to transition of the on-body flow from laminar to turbulent. Parson & Pallard(36) highlighted the importance of a “rough-up” run prior to undertaking tests and then keeping to a regular run schedule. For small models (i.e. less than approximately 2 m length waterline) there is both insufficient model speed and generation of background turbulence to ensure transition. Above this size, the combination of adequate background turbulence combined with a sufficiently large model (i.e. travelling fast enough) is enough to ensure transition. This was discussed by Debord et al.(13) and they found that:

Circulation and large-scale turbulence after repeated angle-of-attack tests has been found to be present in certain tanks but not others, and the characteristics of these problems can vary.

2.2 Model Scale and Velocity

The influence of model scale in defining the final test speeds has been discussed in Section 1.4; particularly within the framework of a test facility's capabilities. It is important to recognise there is also a significant effect on the fluid behaviour due to a change in model scale. As the scale is reduced or model becomes larger, the velocity at which it must be tested increases to maintain a given Froude number. As the test speed increases the Reynolds number of the model also increases, reducing the potential for differences in the small and large scale fluid phenomena between model and full-scale. Small scale items include on-body flow regime, boundary layer thickness and spray size; while large scale would include the wave making behaviour. This thesis will investigate some of the small scale items, in particular the state of the boundary layer through the use of glue-on film probes.

2.3 Flow Stimulators

The experiments contained in this work were conducted both with and without flow stimulators applied to the hull. For the tests with stimulators a number of alternatives were considered including: Hama triangles, wires, sand strips and cylindrical studs. For the $1/8^{th}$ tests using stimulators, a series of cylindrical stud type stimulators were applied to the model. They were approximately 3.2 mm in both diameter and height, placed at 20 mm centres and in two rows 200 mm apart around the model. The forward most row was placed 200 mm aft of the forward perpendicular which is located 28 mm forward of station zero. This arrangement represents a typical approach to yacht turbulence stimulation at the test facility.

2.4 Towing Tank

The towing tank at the Australian Maritime College has a length, breadth and depth of; 100 m, 3.5 m and 1.5 m respectively. For the tests conducted for this

thesis the water depth was reduced to 1.3 m to provide sufficient air draught for the model under the carriage structure. An electrically powered carriage running on rails attached to either side of the tank provided both the motive force and attachment point for the model. A schematic of the towing tank with carriage and model is shown in Figure 2.1.

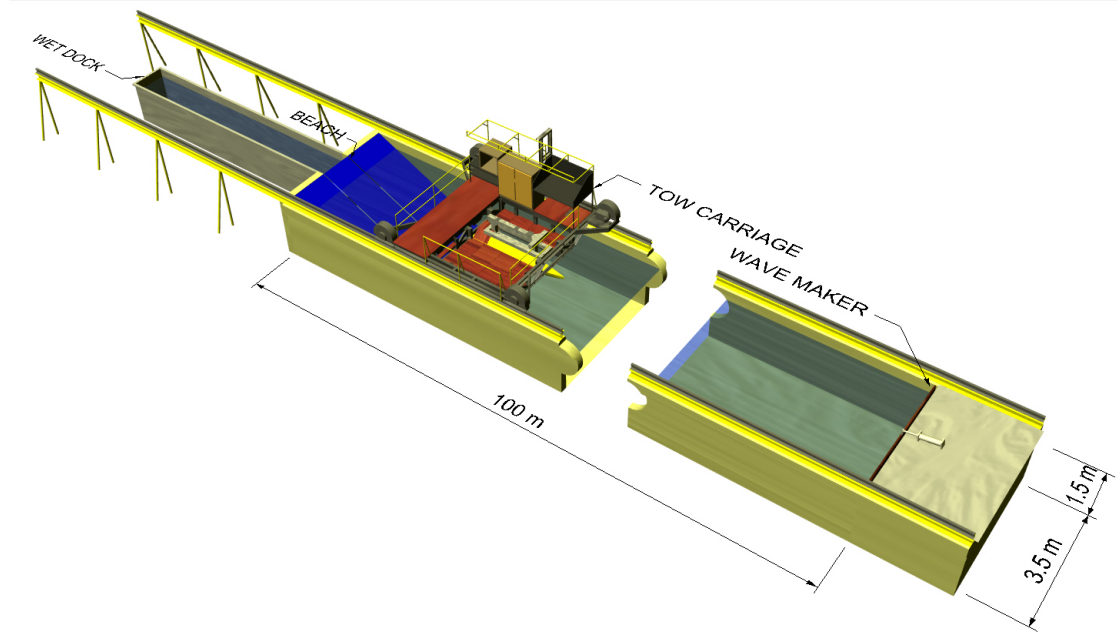


Figure 2.1: Schematic of Australian Maritime College towing tank, carriage and the IACC model used for the tests.

2.5 Yacht Models

The hull and appendages are a geosim of $1/3^{rd}$ scale model which had been used in a previous series of tests conducted on behalf of BMW Oracle Racing by the Canadian National Research Council Institute of Ocean Technology (NRC-IOT). Hull and appendage files were supplied along with ballast and trim information from the earlier tests. The hull form is that of a generic v5 IACC hull used for baseline testing. A photograph of the model during testing at the Australian Maritime College is shown in Figure 2.2.

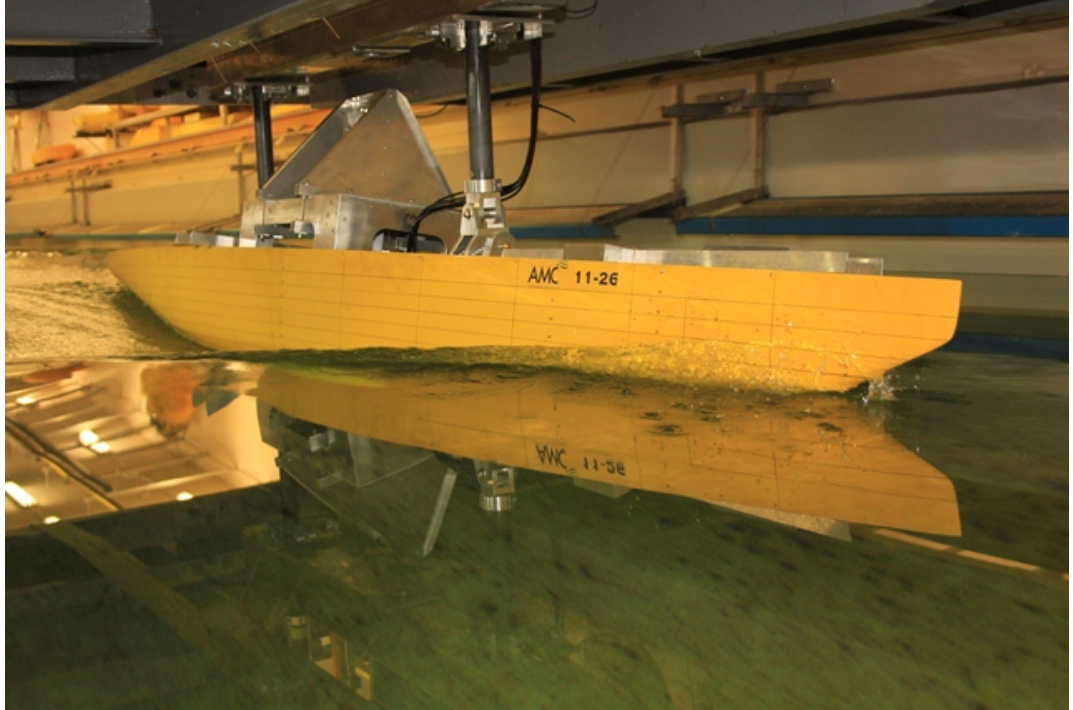


Figure 2.2: $1/8^{th}$ geosim of a v5 IACC yacht being towed at the Australian Maritime College towing tank.

This hullform was chosen as it was regularly used for bench marking tests at $1/3^{rd}$ scale and as such there was sufficient force and moment data that could be used for comparison with the tests on the $1/8^{th}$ scale model conducted as part of this research. The model's principal particulars are provide in Table 2.1 and a linesplan of the model is included in Appendix B. Unfortunately, it was not possible to include additional hull definition data within this document beyond the included linesplan and the principal particulars. This was due to restrictions agreed to at the outset of the project between the author and the organisations which supplied the hull-form.

Limited information about the manufacture and materials used for the $1/3^{rd}$ scale model was available other than that it was produced using CAD/CAM and that it is a geosim of the $1/8^{th}$ scale model.

The $1/8^{th}$ scale model was constructed using carbon foam sandwich inside female

Table 2.1: $1/8^{th}$ scale model principal particulars.

Item	Value	Units
L _{OA}	3.14	m
L _{WL}	2.31	m
B _{MAX}	0.46	m
B _{WL}	0.42	m
d _{CANOE BODY}	0.09	m
WSA _{CANOE BODY}	0.83	m ²
$\Delta_{SAILING}$	49.96	kg
C _P	0.58	

hull moulds. The hull moulds were constructed on male plugs that had been CNC cut. The foils were CNC machined from solid aluminium stock. Significant care was taken during the manufacture to achieve dimensional tolerances as low as possible and certainly within that described by the ITTC procedure. It was not possible to undertake a complete three-dimensional mapping of the surfaces of the model's hull and appendages. Instead the hull was measured at both the sheer line and the keel line and the appendages at a range of sections along each body. The measurements at the model's sheer were taken at each station and measured the beam at each station. The measurements along the keel line were canoe body drafts at the centreline for each station. The recorded measurements were compared to the as designed measurements which showed that both the hull centreline profile and sheer line were within ± 0.5 mm of the designed values. The foils were CNC machined to a tolerance of ± 0.1 mm which was confirmed via measurement using digital callipers with two decimal place precision.

2.6 Test Program

Testing of the $1/8^{th}$ model was undertaken for 18 conditions which made a total of 358 individual runs. An overview of the test conditions is provided in Table 2.2 with further details contained in Appendix A. So as to enable comparison between the geosims, the test conditions were based around those for which the $1/3^{rd}$ scale model had been tested. For the tests at $1/8^{th}$ scale, each test was conducted with and without turbulence stimulation.

Table 2.2: Abbreviated test program.

Condition	Details	Set Speed m/s	Yaw Angle degrees	Heel Angle degrees	Tab Angle degrees	Rudder Angle degrees
1	Sample Frequency Tests	1.90	0.00	0.00	0.00	NA
2	Hull & Keel Yaw Sweep	1.90	-6 to 6	0	0	NA
3	Tab Sweep	1.90	0	0	-12 to 12	0
4	Rudder Yaw Sweep	1.90	0	0	0	-8 to 8
5	Speed Sweep	0.26 to 2.21	1	10	4	2
8		1.92	-2 to 1	0	-2 to 4	0
9		1.28 & 1.37	-2 to 1	5	4 to 8	2, 4
10		1.28 & 1.37	-2 to 1	10	4 to 8	2, 4
11		1.56 & 1.65	-2 to 1	20	6 to 10	1 to 6
12		1.28 & 1.65	-1 & 1	-10 & 20	-4 & 6	-2 to 6
13	As per Condition 5 but no studs					
14	As per Condition 8 but no studs					
15	As per Condition 9 but no studs					
16	As per Condition 10 but no studs					
17	As per Condition 11 but no studs					
18	As per Condition 12 but no studs					

Chapter 3

Forces and Moments

3.1 Introduction

Typically one of the key items of a model test program is the determination of full-scale force data. Often the scaled results are used as inputs into velocity prediction programs or as a method of validating numerical studies, Larsson(30). In the planning stage of a model test program it is critical to understand the end use of the results along with items such as lead times and budget. Understanding the importance of each of these will help enable designers and engineers to make informed decisions. One of the key outcomes of these discussions is to ascertain which scale should be used for the model test. The typical thought is that a smaller model will be able to predict which candidate from a range of hull forms will provide the best performance; where best performance has been defined by the designer and/or client. The issue that arises is that the results from a smaller model are expected to be less representative of the full scale values than that possible when a larger model is used. The known compromise is that the smaller models give relative results at a significantly lower cost, not only the cost of model production but due to being able to test in a smaller more efficient test facility. If cost and time taken to change configurations is deemed less important then it is typical for designers to choose the largest scale model that is allowed, in the case of specific class rules, or

that which fits into a given facility. The thinking behind this is that as model size increases the flow physics become closer to that of the full scale vessel. While it is widely accepted that these compromises exist what is not so well understood is the magnitude of the change and how this would influence the outcome of the test program. As could be imagined if the final extrapolated values from either scale model are the same within uncertainty levels then it would be appropriate for a greater number of tests to be conducted at small scale. These limitations have also been discussed previously in Chapter 1.

The data contained within this chapter was obtained in two separate facilities; the first located in St. John's, Newfoundland and Labrador, Canada was used for testing the $1/3^{rd}$ scale model and the second was the towing tank located at the Australian Maritime College, in Launceston, Australia which was used for the $1/8^{th}$ scale model tests. For details of the two facilities and the models see Section 2.4 and Section 2.5 respectively.

Results from testing of the $1/3^{rd}$ scale model along with hull and appendage surfaces were generously supplied by the Canadian National Research Council Institute of Ocean Technology (NRC-IOT) on behalf of BMW Oracle Racing. The model was tested using the yacht dynamometer designed by the facility; the design of the dynamometer is discussed in Parsons & Pallard(36). Details of the force balance and data acquisition system used for the $1/8^{th}$ scale model tests are detailed in the following section.

3.2 Test Equipment

3.2.1 $1/8^{th}$ Model Set-up

The model was attached to the towing tank carriage via two carbon fibre posts, one forward and one aft which were free to heave and located within the six-component

force balance. The force balance was rigidly attached to the towing carriage. The forward post connected to an indexed heel fitting allowing the heel angle to be set in a quick and repeatable manner for heel angles ranging from negative 35 degrees to positive 35 degrees in five degree increments. The connection to the heel fitting was made via a spigot which was inserted inside the post and series of four bearings with their axis orientated athwartships. The aft post was attached via universal joint and slide, orientated fore and aft. The combination of the fore and aft posts and their attachments constrained the model in surge, sway, heel and yaw but allowed it to be free in heave and pitch. Figure 3.1 shows both the heel fitting and the aftslide arrangement.



(a) Heel fitting showing spigot and indexed holes for heel angle



(b) Aft slide and universal joint

Figure 3.1: Tow post attachment details for $1/8^{th}$ scale model.

Both the heel fitting and the aftslide were rigidly mounted to the model via an aluminium alignment plate. This plate, after alignment runs have been performed, was permanently bolted to the model's internal framing. The connection between the two fittings and the plate were made in such a way that they could be removed either for servicing or use on another model and then reinstalled in the same location with an accuracy of ± 0.1 mm. This method of attachment was undertaken so as to facilitate future research using this model as well as future comparisons to

the current test results. Figure 3.2 shows the relative location of the heel fitting and the aft slide and their overall location within the model and on the baseplate.

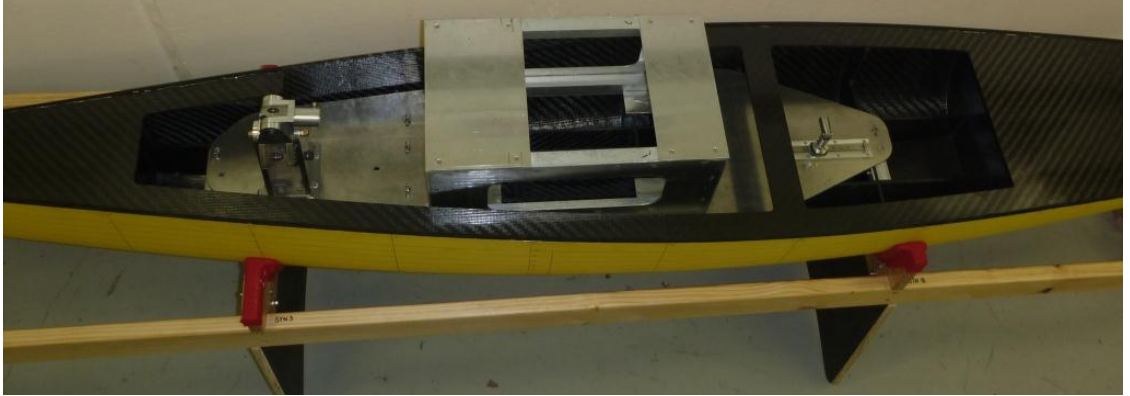


Figure 3.2: General view of $1/8^{th}$ model showing the relative location of fore and aft post attachment points.

3.2.2 Data Acquisition

The speed of the towing carriage was measured using a Red Lion Rotary Pulse Generator attached to a dedicated wheel. This instrument was not specifically calibrated for the tests but it is the same item used for commercial testing. As such it is expected that the speed of the model was measured to the tolerances recommended by the ITTC procedures(27) which states the speed of the model should be measured to within 0.1% of the maximum speed or to within 3 mm/s, whichever is the larger.

Sinkage fore and aft was measured using two Schaevitz 5000 DC-EC linear variable differential transformers (LVDTs). The running trim was calculated from the measured running sinkage forward and aft.

The water temperature was measured for the calculation of viscosity. It was measured at a depth of approximately half of the model draught using a mercury

thermometer. It was assumed that the water temperature was constant throughout the tank. Temperature measurements were recorded at least once per day, with daily variations expected to be less than ± 0.2 °C.

A six-component force balance was used to measure the hydrodynamic forces and moments. The force balance was designed as part of a previous research program at the Australian Maritime College; full details of the design, verification and accuracy of the balance are detailed in Appendix A of Binns(4). In summary the balance has a maximum load rating of 220 kg with an accuracy of alignment of at least 0.05 degrees. For loads up to 65 kg there will be a maximum crosstalk of 0.15% of which only 1% will be nonlinear.

Calibration of the six-component force balance occurred prior to the commencement of the tests to remove both the linear components of the cross talk and the influences of items within the data acquisition chain. The calibrations included all items of the measurement chain, including signal conditioner, amplifier, filter and analogue to digital converter. To ensure that the expected loads occurred within the linear region of the calibration the calibration was undertaken with a range of values greater than expected to be measured in the experiments. The linearity and repeatability of the calibration points were checked to quantify the accuracy of the calibration factor.

The signals from each instrument were recorded using a HP computer via a National Instruments PCI-6251M Multifunction Data Acquisition Card which was controlled by Labview. Post processing of the signals was performed using both MATLAB and Excel software. Data was sampled at 8192 Hz, with each run being recorded for 20 seconds and an analogue low-pass filter frequency set to 1000 Hz. This combination provided a sufficiently high sample rate to capture the predominant signal from all instruments whilst still having a low-pass filter to prevent aliasing of the signal.

3.3 Data Reduction

The conventional assumption made is that the full scale vessel will have a fully turbulent boundary layer. To attempt to recreate this at model scale, turbulence stimulating devices are required. Stud type simulators were used for the experiments undertaken; the size and location of which are detailed in Section 2.3. While the addition of the studs should provide the necessary energy to the flow to ensure transition, there is an associated increase in drag beyond that of the turbulent flow. To account for this increase it is necessary to undertake a correction for stud drag. The procedure used was as described in Molland et al.(34). This approach considers three aspects: increase to the model drag due to the studs; change in momentum thickness of the boundary layer due to the studs and the area forward of the studs which is expected to be laminar.

An assessment of the required correction to velocity to account for blockage was undertaken for the $1/8^{th}$ scale model using the method developed by Tamura and listed in the guidelines provided in ITTC procedures 7.5-02-02-01(27). The required velocity correction was found to be 0.003 m/s. As the required correction was an order of magnitude less than the increments of speed adjustment for setting the carriage speed, 0.01 m/s, the velocity correction was not included in the extrapolation procedure. For reference the cross-sectional information of the two towing tanks and the models, $1/8^{th}$ and $1/3^{rd}$, is included in Table 3.1. It should also be noted that the results presented are for the upright condition. This is significant as it represents the ‘worst case’; as the model is heeled, which is the case for the majority of the conditions, the ratios of model draught to water depth as well as model waterline beam to tank width will reduce. Also, no correction was undertaken for the $1/3^{rd}$ scale model tests as there was less blockage than for the $1/8^{th}$ scale model.

It is necessary as part of the extrapolation procedure to include the three-dimensional influences on the friction coefficient. The process undertaken was as described in Prohaska(39) whereby a series of low speed runs at Froude numbers ranging from

Table 3.1: $1/8^{th}$ and $1/3^{rd}$ towing tank cross-section information with respect to model size.

Item	$1/8^{th}$	$1/3^{rd}$
Tank Width (m)	3.55	12.00
Waterline Model Beam (m)	0.417	1.112
Ratio Model Beam to Towing Tank Width	0.12	0.09
Tank Depth (m)	1.30	7.00
Model Total Draught (m)	0.51	1.37
Ratio Model Total Draught to Water Depth	0.39	0.20
Tank Cross Sectional Area (m ²)	4.62	84.00
Model Immersed Cross Sectional Area (m ²)	0.04	0.28
Ratio Model CSA to Towing Tank CSA	0.009	0.003

0.13 to 0.25 at five heel angles were undertaken so as to calculate the form factor or value of $1 + k$. These runs were undertaken as part of the testing of the $1/3^{rd}$ scale model. As the vessel is a yacht with a large appendage area it was necessary to account for this area as part of the calculation of the form factor. The technique known as appendage stripping, was performed as described in Debord & Teeters(14). In this procedure the resistance due to the foils, including the keel bulb and wings, is removed. This is an essential process so as to ensure that the calculated form factor is only a function of the hull shape. The calculated form factors are presented in Figure 3.3 demonstrating a change in form factor occurs with a change in heel angle.

In the case of a flat plate the value of $1 + k$ would be one. Any value greater than one indicates that three-dimensional effects are influencing the frictional components of the hull drag. The relatively high value of $1 + k$ at zero degrees heel is indicative of the hull form being less like a flat plate in the upright condition as compared to that when heeled. As the vessel heels the hard turn of bilge towards the stern becomes immersed, while at the same time the rotation of the midsections of the hull lead to a reduction in waterline beam; there is also an increase in the length of the waterline. In order to simplify the data reduction procedure, an average value of form factor has been used for the extrapolation of both the $1/8^{th}$ and $1/3^{rd}$ results. Using an average value for the form factor will have an affect on the magnitude of the extrapolation but it is not of importance to this

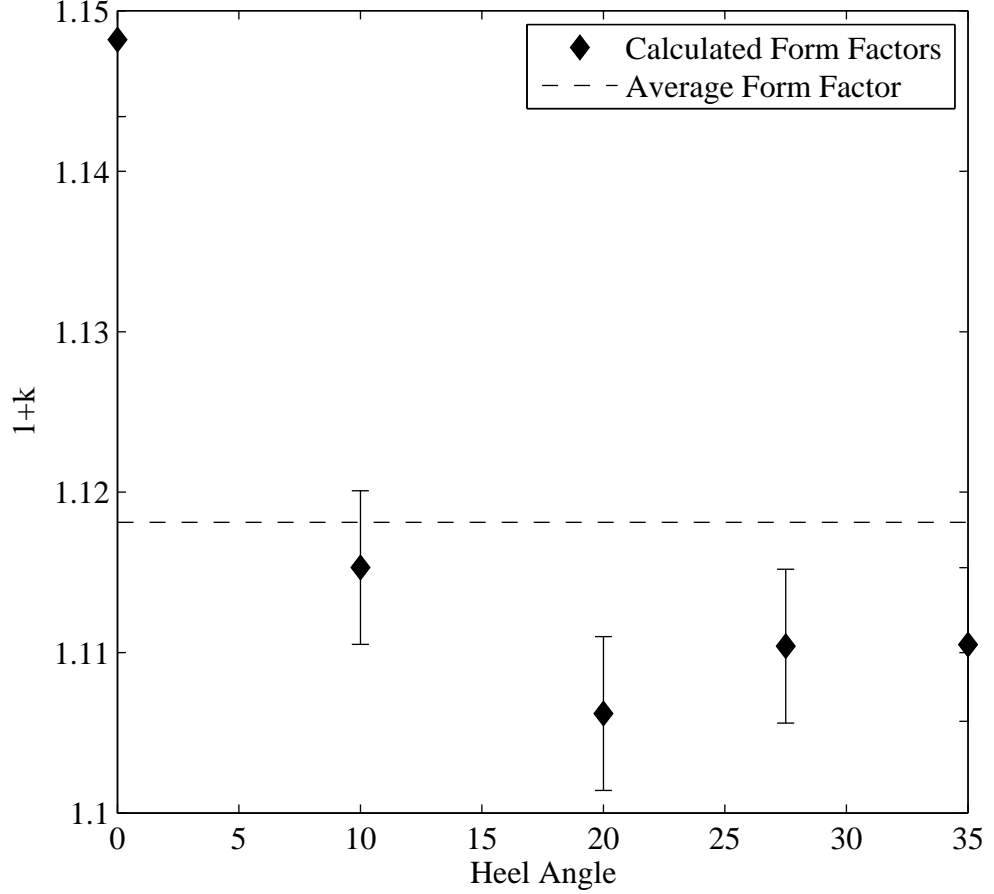


Figure 3.3: Variation of form factor with respect to model heel angle along. The average form factor applied in the data analyses is also included as a dashed horizontal line.

study which is focused on the relative behaviour due to model scale. The error bands in Figure 3.3 represent 95% confidence intervals, which were obtained using a bootstrapping technique as described in Efron & Tibshirani(17).

The moments measured at the force balance at the $1/8^{th}$ scale were transferred to the equivalent point as the $1/3^{rd}$ cases to allow comparison of the results. Yaw and heel moments were then extrapolated from the model test results using Equation (3.1).

$$\text{Moment}_S = \text{Moment}_M \times \frac{\rho_S R^4}{\rho_M} \quad (3.1)$$

3.3.1 Uncertainty Analysis

The background to the uncertainty calculations are contained in Appendix C. The uncertainty was calculated to be ± 0.0008 for C_T which when propagated through calculations gives a maximum $\pm 2\%$ for the forces. When these uncertainty bars are added to the standard scale plot they are smaller than the points representing the data. Due to this, no error bars are shown on any plots as the uncertainty does not affect the conclusions.

3.4 Results and Discussion

This section includes a sample of results with discussion of the forces, lift and drag, from both the $1/8^{th}$ scale experiments and $1/3^{rd}$ scale experiments. Comparisons are made between the $1/8^{th}$ scale experimental results, both with and without turbulence stimulators, to the $1/3^{rd}$ scale experimental results. For further insight cross plots of C_D variation with respect to C_L^2 are included in Section 3.4.5. An extended set of force and moment data is included in Appendix F and Appendix G respectively.

3.4.1 Drag Force

For this study, drag force was defined as the force acting parallel to the path along which the vessel travels; i.e. it is described in flow fixed coordinates. As such it is a vector sum of the vessel fixed ‘X’ and ‘Y’ forces acting parallel to the vessels direction of travel. Drag has been extrapolated from the model test using a combination of Grigson’s flat plate friction formulation, foil stripping and form factor corrections. For further explanation of the techniques used see Section 1.3 and Section 3.3. The drag data is presented as non-dimensional drag force (C_D) and was non-dimensionalised using Equation (3.2).

$$C_D = \frac{R_{TP}}{0.5 \rho V_P^2 WSA_P} \quad (3.2)$$

Where:

C_D is the coefficient of drag

R_{TP} is the total drag or resistance of the prototype

ρ is the density of sea water at 20°C as per ITTC 7.5-02-01-03

V_P is the velocity of the prototype

WSA_P is the wetted surface area of the canoe body of the prototype

Note that the designation prototype refers to the full scale values.

The first plot in Figure 3.4, Figure 3.4(a), shows a plot of C_D with respect to variation in Froude number. The data presented is for the $1/8^{th}$ tests with and without studs as well as $1/3^{rd}$ case. Unfortunately there was only one data point available from the $1/3^{rd}$ tests that could be used for comparison as no speed sweep data was available. The speed sweep covers velocities from a Froude number of 0.05 to 0.46 equating to a range in full-scale velocity of 1.4 to 12 knots. This speed range was selected to ensure that all typical upwind velocities would fall within this range. Drag increase was quadratic with speed for the $1/8^{th}$ tests. The agreement between the $1/8^{th}$ with and without studs cases is within uncertainty levels except at the lowest test speed; with the singular $1/3^{rd}$ case being approximately 15% less than either of the $1/8^{th}$ cases. The C_D results from the $1/8^{th}$ scale with studs reduces consistently with reduction in Froude number, until Froude number of 0.10 (~ 0.5 m/s at $1/8^{th}$ model scale) before increasing with decreasing Froude number. The increasing values of C_D could indicate that the studs are producing a higher drag relative to the velocity and surface area. As previously mentioned a calculation for stud correction was undertaken but may have underestimated the contribution of the studs at low speeds. The C_D results from the $1/8^{th}$ scale without studs observes a similar behaviour to the with studs case except at the lowest Froude number for which C_D decreases. The reduction in C_D at the lower speeds indicates that laminar flow may be present reducing the C_D value. This behaviour was also identified by McCarthy et al.(32) but discussed in terms of C_R .

The second and third plot in Figure 3.4, Figures 3.4(b) and 3.4(c), show a plot of C_D with respect to variation in trim tab angle. Two cases are provided as the first was a heeled case at moderate velocity while the second was upright at high velocity. Both plots contain data for the $1/8^{th}$ tests with and without studs as well as $1/3^{rd}$ case. In the first Figure 3.4(b) the C_D values for the $1/3^{rd}$ tests are an average of 15% less than those from the $1/8^{th}$ tests. For $1/3^{rd}$ results there is also a 4% relative increase in C_D with each two degrees of increased trim tab angle. For $1/8^{th}$ there is no change in C_D between four and six degrees of trim tab angle but there is then a 5% relative increase from six degrees to eight degrees of trim tab angle. In the second Figure 3.4(c) the C_D values for the $1/3^{rd}$ tests are an average of 21% less than those from the $1/8^{th}$ tests. For $1/3^{rd}$ results there no increase in C_D with increased trim tab angle. For $1/8^{th}$ results there is no change in C_D between zero and two degrees of trim tab angle but there is then a 3% relative increase from two degrees to four degrees of trim tab angle.

3.4.2 Lift Force

Lift force is defined as the force acting perpendicular to the path along which the vessel travels; i.e. it is described in flow fixed coordinates. As such it is a vector sum of the vessels fixed ‘X’ and ‘Y’ forces acting perpendicular to the vessels direction of travel. Lift was extrapolated from the model test results to full scale using the assumption that non-dimensional lift force (C_L) was independent of scale. The lift data is presented as non-dimensional lift force and was non-dimensionalised using Equation (3.3).

$$C_L = \frac{L_{TP}}{0.5 \rho V_P^2 A_{PP}} \quad (3.3)$$

Where:

C_L is the coefficient of lift

L_{TP} is the total lift of the prototype

ρ is the density of sea water at 20°C as per ITTC 7.5-02-01-03

V_P is the velocity of the prototype

A_{PP} is the profile area including foils of the prototype

Note that the designation prototype refers to the full scale values.

The first plot in Figure 3.5, Figure 3.5(a), shows a plot of C_L with respect to variation in Froude number. The data shown is for the $1/8^{th}$ tests with and without studs as well as the $1/3^{rd}$ case. Unfortunately there was only one data point available from the $1/3^{rd}$ tests that could be used for comparison as no speed sweep data was available. The speed sweep covers velocities from Froude number of 0.05 to 0.46 equating to a range in full-scale velocity of 1.4 to 12 knots. This speed range was selected to ensure that all typical upwind velocities would fall within this range. For Froude numbers greater than 0.10 the test cases with and without studs as well as with the $1/3^{rd}$ result agreed within uncertainty levels. For Froude numbers of 0.05 and 0.10 there was a difference of 10% and 15% respectively between the with and without stud cases.

The second and third plot in Figure 3.5, Figures 3.5(b) and 3.5(c), show a plot of C_L with respect to variation in trim tab angle. The two conditions are provided as the first is a heeled case at moderate velocity while the second is upright at high velocity. Both plots contain data for the $1/8^{th}$ tests with and without studs as well as $1/3^{rd}$ case. C_L was shown to be linear with increasing trim tab angle for both test conditions with agreement between results being within uncertainty levels. The linear change in C_L with respect to variation in trim tab angle was expected due to low angles of attack.

3.4.3 Heel Moment

Heel moment is defined as the moment about the 'X' axis. Where available results from the 1/3rd scale experiments are plotted along with those of the 1/8th test data. The heel moment data is presented as non-dimensional heel moment (L') and was non-dimensionalised using Equation (3.4).

$$L' = \frac{L}{0.5 \rho V_P^2 WSA_P d_{CANOE BODY}} \quad (3.4)$$

Where:

L' is non-dimensional heel moment

L is heel moment of the prototype

ρ is the density of sea water at 20°C as per ITTC 7.5-02-01-03

V_P is the velocity of the prototype

WSA_P is the wetted surface area of the canoe body of the prototype

$d_{CANOE BODY}$ is draft of the canoe body of the prototype

Note that the designation prototype refers to the full scale values.

The first plot in Figure 3.6, Figure 3.6(a), shows a plot of L' with respect to change in Froude number. The data shown is for the 1/8th tests with and without studs as well as 1/3rd case. The speed sweep covers velocities from Froude number of 0.05 to 0.46 equating to a range in full-scale velocity of 1.4 to 12 knots. This speed range was selected to ensure that all typical upwind velocities would fall within this range. Except for a Froude number of 0.05 the L' was found to be, within uncertainty levels, the same for the cases with and without studs as well as the 1/3rd case. The general trend of the L' is very similar to the that shown in Figure 3.5(a) and discussed in the Section 3.4.2. The similarity was likely due to an increase in lift, which is generated below the centre of heel, creating an increased heel moment.

The second and third plot in Figure 3.6, Figures 3.6(b) and 3.6(c), show a plot of L' with respect to variation in trim tab angle. The two cases are provided as the first was a heeled case at moderate velocity while the second was upright at high velocity. Both plots contain data for the $1/8^{th}$ tests with and without studs as well as the $1/3^{rd}$ case. L' was linear with respect to change in trim tab angle for all cases. For both Figure 3.6(b) and Figure 3.6(c) the magnitude of the differences in L' between $1/8^{th}$ and $1/3^{rd}$ cases was within experimental uncertainty.

3.4.4 Yaw Moment

Yaw moment is defined as the moment about the 'Z' axis. Where available results from the $1/3^{rd}$ scale experiments are plotted along with those of the $1/8^{th}$ test data. The yaw moment data is presented as non-dimensional yaw moment (N') and was non-dimensionalised using Equation (3.5).

$$N' = \frac{N}{0.5 \rho V_P^2 A_{PP} L_{WL}} \quad (3.5)$$

Where:

N' is non-dimensional yaw moment

N is yaw moment of the prototype

ρ is the density of sea water at 20°C as per ITTC 7.5-02-01-03

V_P is the velocity of the prototype

A_{PP} is the profile area including foils of the prototype

L_{WL} is the waterline length of the prototype

Note that the designation prototype refers to the full scale values.

The first plot in Figure 3.7, Figure 3.7(a), shows a plot of N' with respect to

change in Froude number. The data shown is for the $1/8^{th}$ tests with and without studs as well as $1/3^{rd}$ case. Unfortunately there was only one data point available from the $1/3^{rd}$ tests that could be used for comparison as no speed sweep data was available. The speed sweep covers velocities from Froude number of 0.05 to 0.46 equating to a range in full-scale velocity of 1.4 to 12 knots. This speed range was selected to ensure that all typical upwind velocities would fall within this range. The agreement between the $1/8^{th}$ with and without studs cases was within uncertainty levels except for a Froude number of 0.1; but it was not clear why this discrepancy exists. The singular $1/3^{rd}$ case was approximately 80% less than either of the $1/8^{th}$ cases. This large difference was surprising as the results for the same Froude number for C_L , C_D and L' were within uncertainty. This suggests that the difference is due to a different drag centre being used. In light of the difference the set-up of the model and extrapolation procedure for the $1/8^{th}$ results was verified; but it was not possible to verify the $1/3^{rd}$ test set-up.

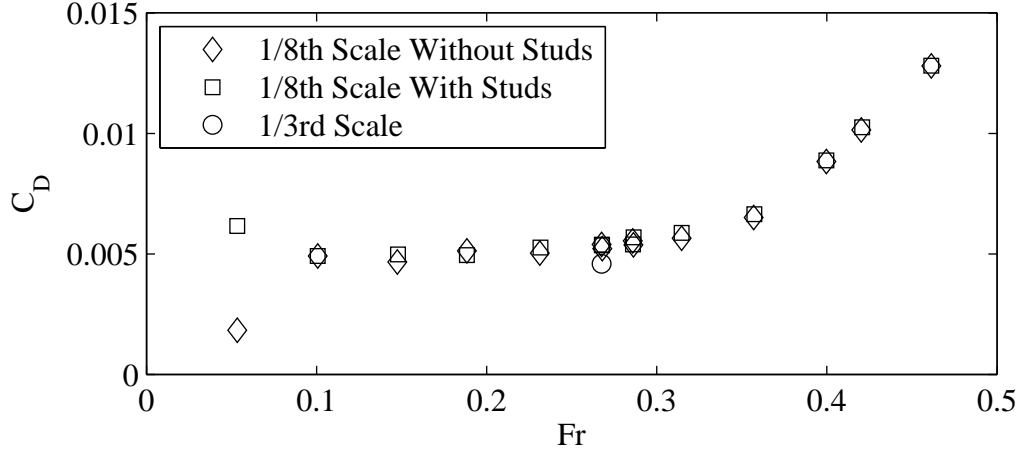
The second and third plots in Figure 3.7, Figures 3.7(b) and 3.7(c), show a plot of N' with respect to variation in trim tab angle. The two cases are provided as the first was a heeled case at moderate velocity while the second was upright at high velocity. Both plots contain data for the $1/8^{th}$ tests with and without studs as well as the $1/3^{rd}$ case. N' for all cases was linear with variation in trim tab angle and the $1/8^{th}$ data with and without studs was within uncertainty values for all trim tab angles. For the Froude number of 0.27, Figure 3.7(b), the lower slope of N' of the $1/3^{rd}$ case is due to the previously discussed incorrect centre of yaw; with the vertical offset due to an incorrect drag centre. For the Froude number of 0.40, Figure 3.7(c), the lower slope of N' of the $1/3^{rd}$ data was again due to the incorrect centre of yaw; but as this was a test condition with no heel or yaw angle it did not exhibit the same offset due the incorrect drag centre seen in Figure 3.7(b).

3.4.5 Cross Plots of Non-Dimensional Components

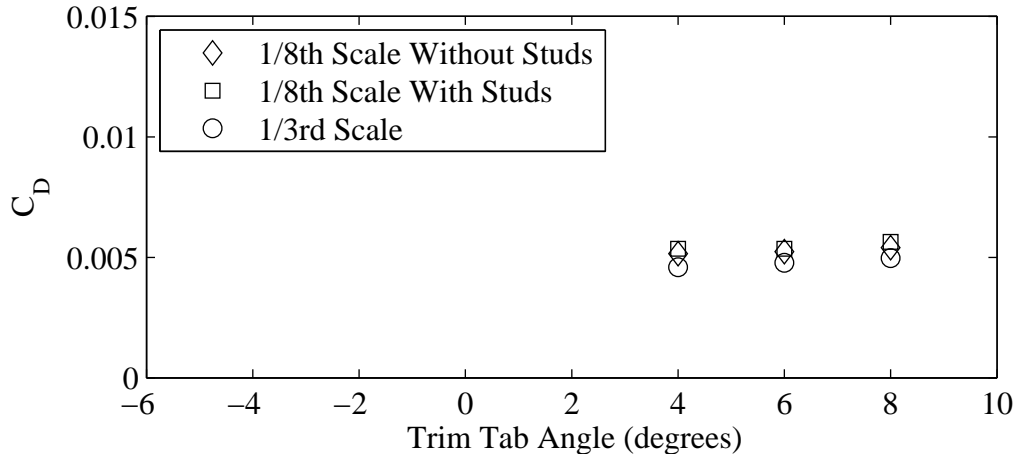
This section contains cross plots comparing non-dimensional properties. The first plot in Figure 3.8, Figure 3.8(a), shows a plot of C_D with respect to variation in

C_L^2 at three tab angles. The data presented is for the $1/8^{th}$ tests with and without studs as well as $1/3^{rd}$ case. For the $1/3^{rd}$ results there is a 4% relative increase in C_D with each two degrees of increased trim tab angle. For $1/8^{th}$ there is no change in C_D between four and six degrees of trim tab angle but there is then a 5% relative increase from six degrees to eight degrees of trim tab angle. There is also an average of 15% reduction in C_D values for the $1/3^{rd}$ tests as compared to the $1/8^{th}$ tests. There is an approximately 45% increase in C_L^2 for each two degree increase in trim tab angle. The greater increase in C_L^2 as compared to increase in C_D for increasing trim tab angle shows the efficiency of the trim tab in generating lift.

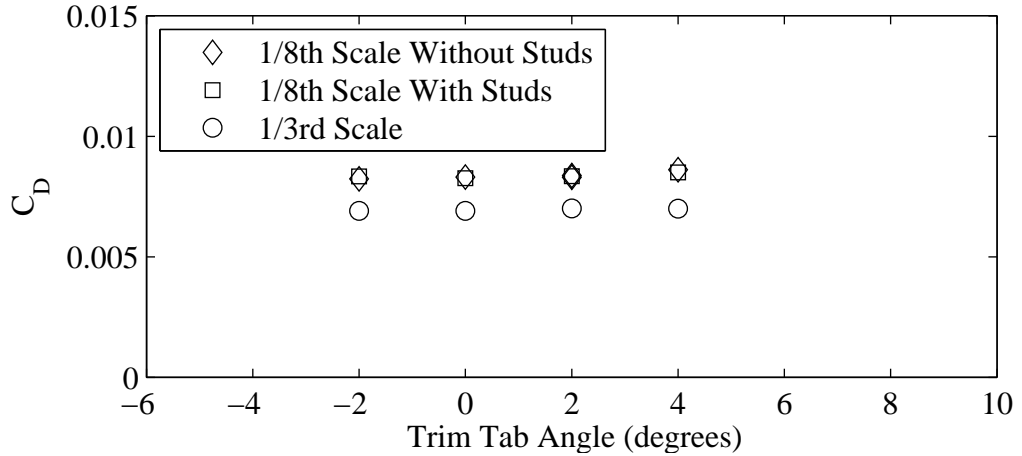
The second plot in Figure 3.8, Figure 3.8(b), shows a plot of C_D with respect to variation in C_L^2 at four tab angles. The data presented is for the $1/8^{th}$ tests with and without studs as well as $1/3^{rd}$ case. C_D values for the $1/3^{rd}$ tests are an average of 21% less than those from the $1/8^{th}$ tests. For $1/3^{rd}$ results there no increase in C_D with increased trim tab angle. For $1/8^{th}$ results there is no change in C_D between zero and two degrees of trim tab angle but there is then a 3% relative increase from two degrees to four degrees of trim tab angle. The 80% reduction in C_L^2 at four degrees trim tab angle as compared to the above case is due to a reduction of the yaw and rudder angle from one to zero degrees. The increase in C_D of approximately 35% as compared to Figure 3.8(a) is due to the increased Froude number.



(a) Yaw 1 degrees, Heel 10 degrees, Tab 4 degrees, Rudder 2 degrees.

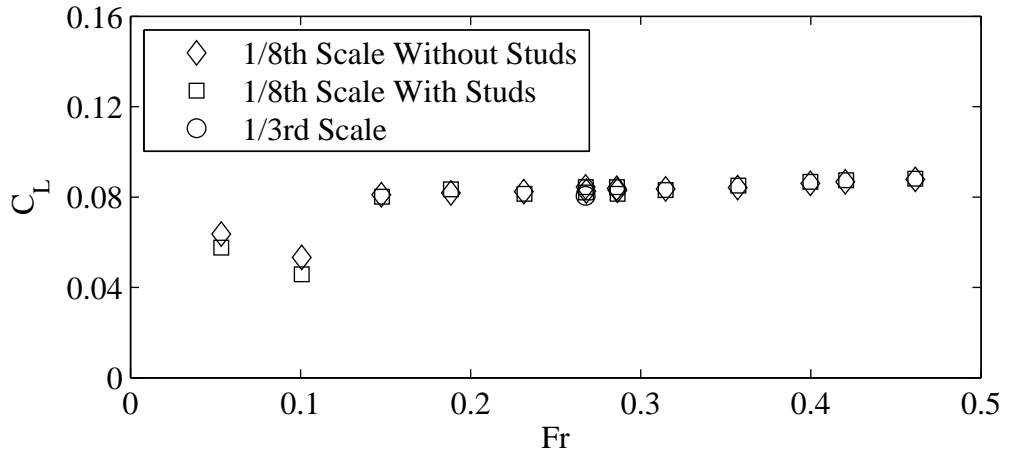


(b) Yaw 1 degrees, Heel 10 degrees, Rudder 2 degrees, Froude Number 0.27.

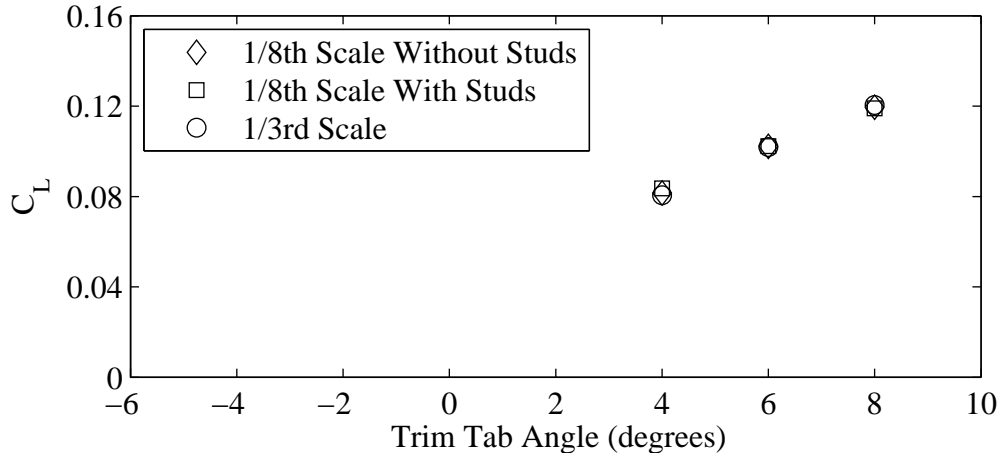


(c) Yaw 0 degrees, Heel 0 degrees, Rudder 0 degrees, Froude Number 0.40.

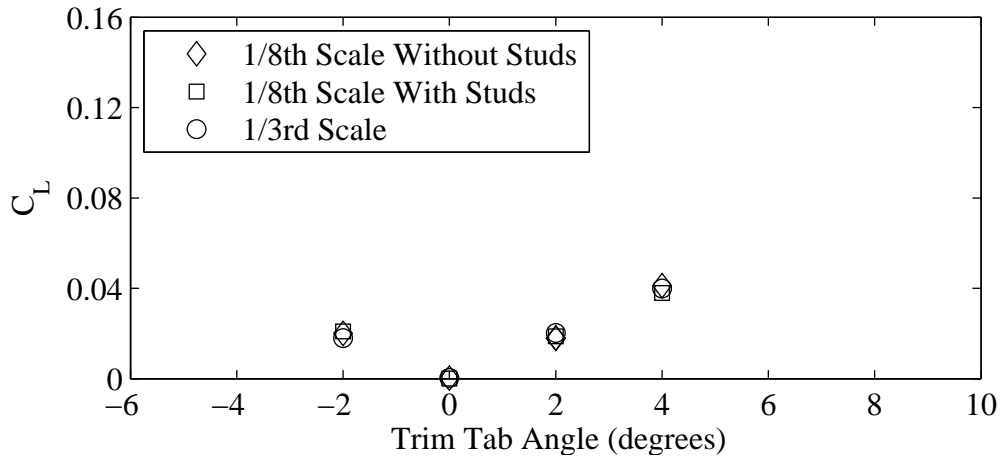
Figure 3.4: Plots of drag coefficient with respect to variation in Froude number and trim tab angle. Drag increase was quadratic with speed with the $1/3^{rd}$ result being $\approx 15\%$ less than the $1/8^{th}$. For Froude numbers of 0.05 and 0.1 the influence of the stud correction and laminar flow are evident. C_D did not change, within uncertainty limits, with increasing tab angle; but the $1/3^{rd}$ results reduced by 15% and 20%.



(a) Yaw 1 degrees, Heel 10 degrees, Tab 4 degrees, Rudder 2 degrees.

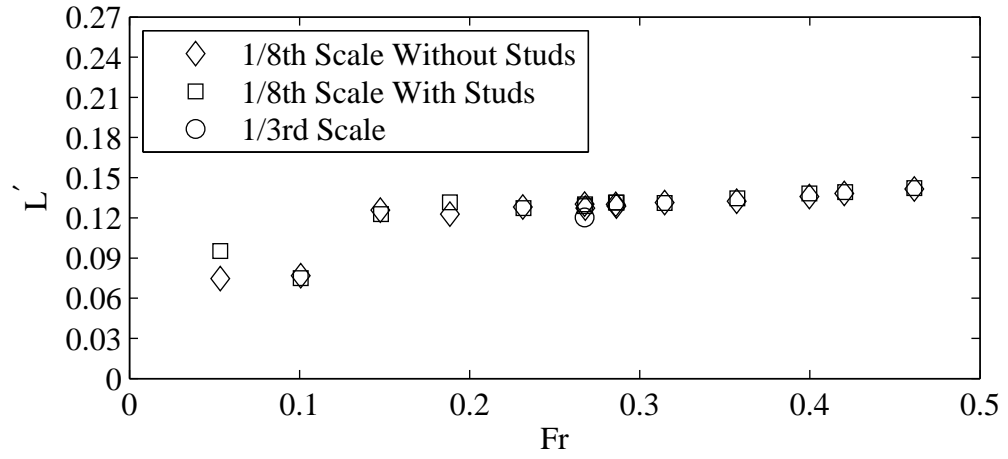


(b) Yaw 1 degrees, Heel 10 degrees, Rudder 2 degrees, Froude Number 0.27.

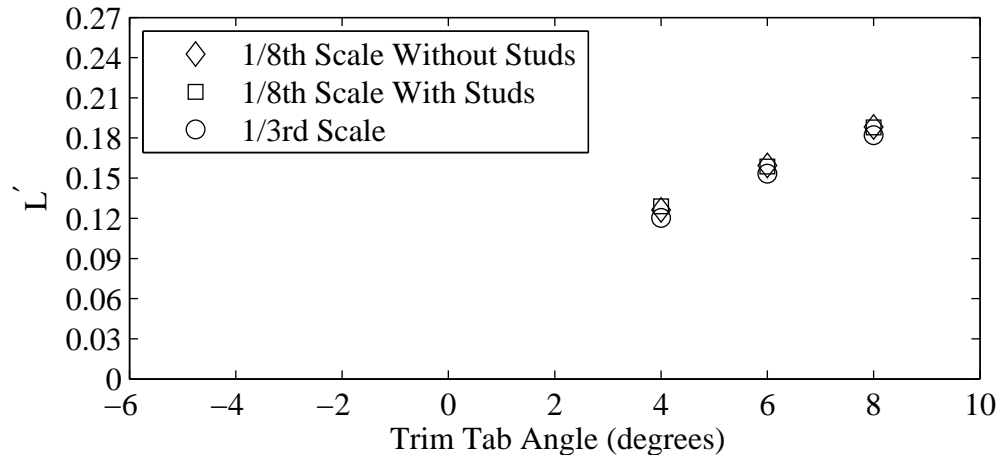


(c) Yaw 0 degrees, Heel 0 degrees, Rudder 0 degrees, Froude Number 0.40.

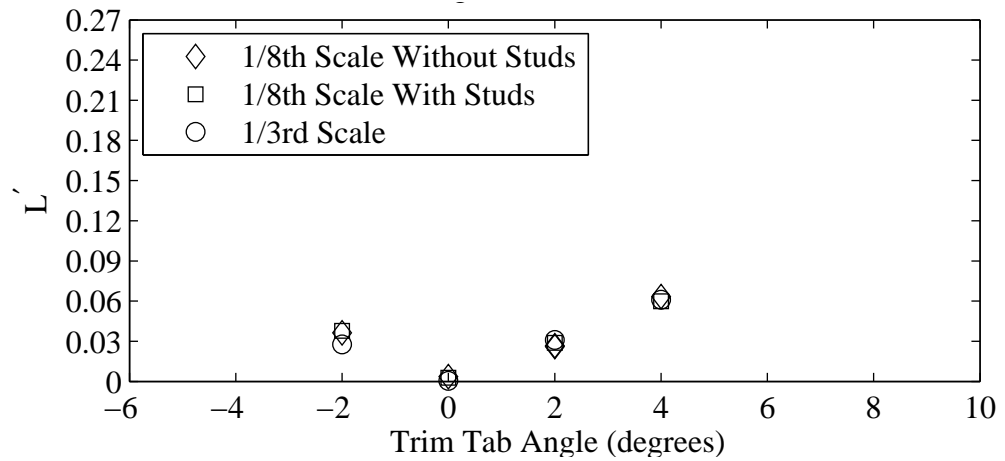
Figure 3.5: Plots of lift coefficient (C_L) with respect to variation in Froude number and trim tab angle. For Froude numbers greater than 0.10 results agreed within uncertainty levels. For Froude numbers of 0.05 and 0.10 there was a difference of 10% and 15%. For increasing trim tab angle the change in C_L was linear.



(a) Yaw 1 degrees, Heel 10 degrees, Tab 4 degrees, Rudder 2 degrees.

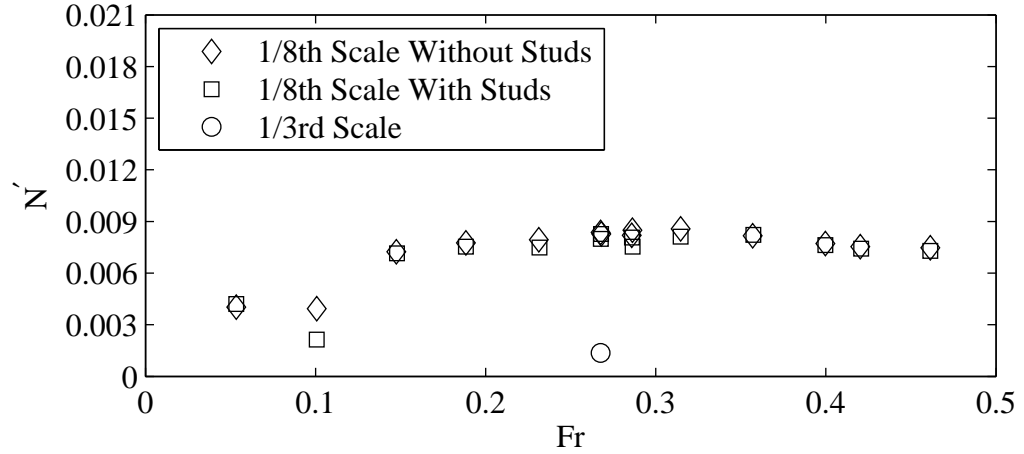


(b) Yaw 1 degrees, Heel 10 degrees, Rudder 2 degrees, Froude Number 0.27.

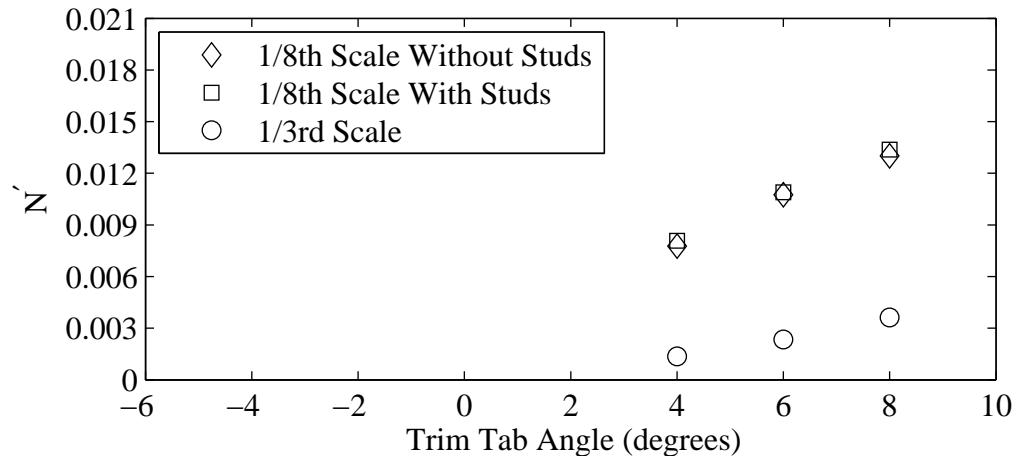


(c) Yaw 0 degrees, Heel 0 degrees, Rudder 0 degrees, Froude Number 0.40.

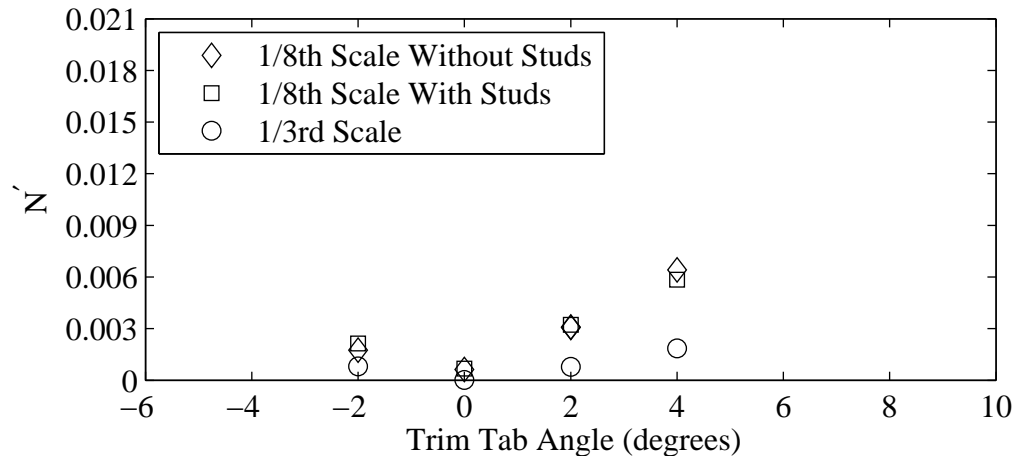
Figure 3.6: Plots of non-dimensional heel moment (L') with respect to variation in Froude number and trim tab angle. The general trend of the L' is very similar to the that shown in Figure 3.5(a) with the similarity due to changing lift causing an changed heel moment. L' was linear with respect to change in tab angle for all cases.



(a) Yaw 1 degrees, Heel 10 degrees, Tab 4 degrees, Rudder 2 degrees.

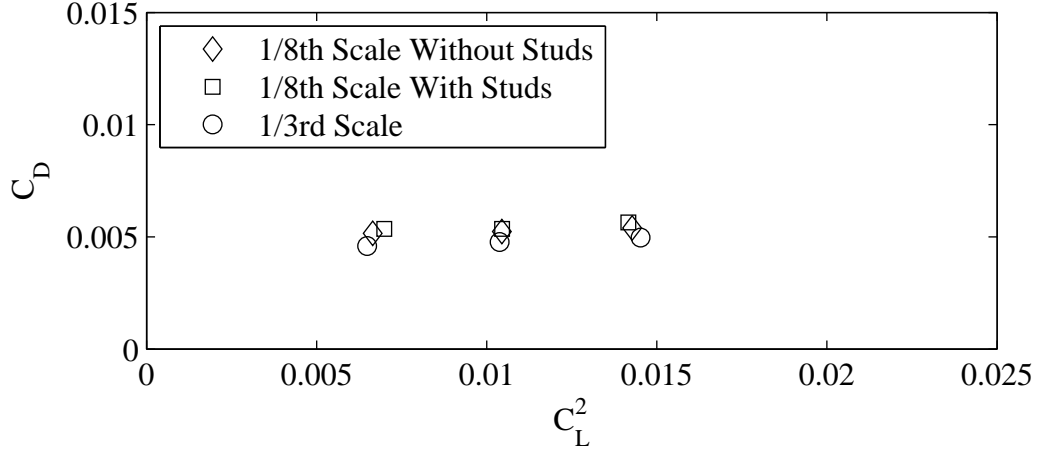


(b) Yaw 1 degrees, Heel 10 degrees, Rudder 2 degrees, Froude Number 0.27.

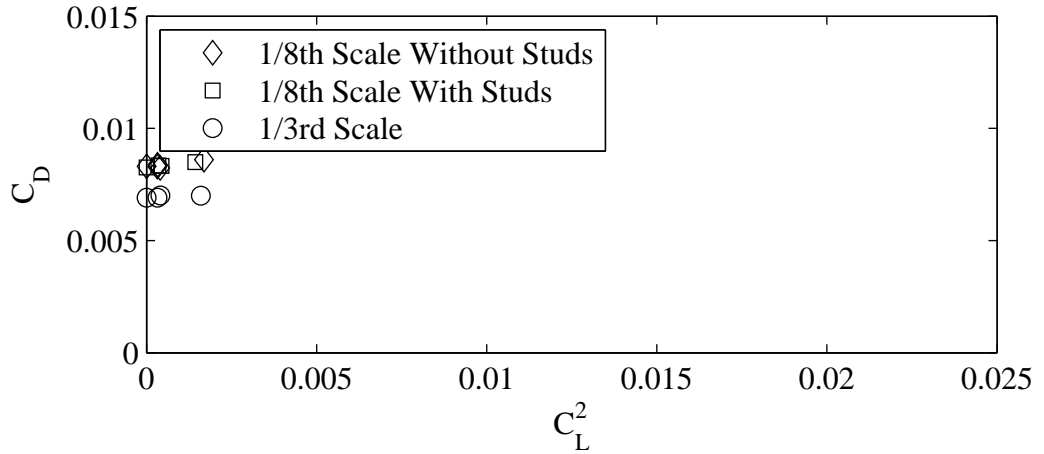


(c) Yaw 0 degrees, Heel 0 degrees, Rudder 0 degrees, Froude Number 0.40.

Figure 3.7: Plots of non-dimensional yaw moment (N') with respect to variation in Froude number and trim tab angle. The 1/8th data was within uncertainty levels except Froude number of 0.1 and the 1/3rd data was $\approx 80\%$ lower than either of the 1/8th cases. N' was linear with variation in trim tab angle. With the vertical offset due to an incorrect drag centre and a lower slope of due to an incorrect centre of yaw



(a) Yaw 1 degrees, Heel 10 degrees, Tab 4, 6 & 8 degrees, Rudder 2 degrees, Froude Number 0.27.



(b) Yaw 0 degrees, Heel 0 degrees, Tab 0, 2, -2 & 4 degrees, Rudder 0 degrees, Froude Number 0.40.

Figure 3.8: Plots of C_D with respect to variation in C_L^2 . In the first plot C_D remains the same within uncertainty levels; with an approximately 45% increase in C_L^2 for each two degree increase in trim tab angle. In the second plot C_D remains the same for changing trim tab angle. The 80% reduction in C_L^2 at 4 degrees trim tab angle relative to the above case is due reduction of the yaw and rudder angle from one to zero degrees. The increase in C_D as compared to first plot is due to the increased Froude number.

3.5 Chapter Summary

As a foundation to the investigation of the influence of scale on force and moment prediction from yacht tests in this thesis, a series of experiments were conducted on both $1/3^{rd}$ and $1/8^{th}$ geosims of a fully appended IACC yacht. The experimental data was recorded for a matrix of test cases including variation of: velocity, yaw angle, heel angle, trim tab angle and rudder angle. In addition the $1/8^{th}$ experiments were also conducted both with and without turbulence stimulation.

The change in non-dimensional drag (C_D) with respect to speed was seen to be quadratic for the $1/8^{th}$ tests from a Froude number of 0.10 to 0.46 with result of the $1/3^{rd}$ value at a Froude number of 0.27 being approximately 15% less. For a Froude number of 0.05 C_D increased for the $1/8^{th}$ case with studs as compared with the $1/8^{th}$ case without studs. These changes are possibly due to underestimation of the contribution of the studs to drag and laminar flow respectively. It was also shown that C_D increased between 0-4% for each two degrees of additional trim tab angle for both the $1/8^{th}$ and $1/3^{rd}$ geosims with the $1/3^{rd}$ values being between 15% and 21% less than the $1/8^{th}$ values.

For Froude numbers greater than 0.10 non-dimensional lift (C_L) changed approximately linearly for the $1/8^{th}$ data, with the $1/3^{rd}$ value at a Froude number of 0.27 being the same as the $1/8^{th}$ value at the same speed. For Froude numbers of 0.05 and 0.10 there was a difference of 10% and 15% respectively between the $1/8^{th}$ with and without stud cases. C_L was also shown to be linear with increasing trim tab angle for the $1/8^{th}$ case with studs and without studs.

Except for a Froude number of 0.05 the non-dimensional heel moment (L') was found to be, within uncertainty levels, the same for the cases with and without studs as well as the $1/3^{rd}$ case. The general trend of L' was very similar to that for C_L due to a change in lift being reflected in a change in heel moment. L' was linear with respect to change in trim tab angle for all cases.

For the $1/8^{th}$ with and without studs cases non-dimensional yaw moment (N') was within uncertainty levels except for a Froude number of 0.1; but it was not clear why this discrepancy exists. The $1/3^{rd}$ case at a Froude number of 0.27 was approximately 80% less than either of the $1/8^{th}$ cases. It was expected that the difference is due to a different drag centre being used. N' for all $1/8^{th}$ and $1/3^{rd}$ data was linear with variation in trim tab angle. For the Froude number of 0.27, the lower slope of N' of the $1/3^{rd}$ case is suspected to be due a different centre of yaw; with the vertical offset due to a different drag centre. For the Froude number of 0.40 the lower slope of N' of the $1/3^{rd}$ data was again due to a different centre of yaw; but as this was a test condition with no heel or yaw angle it did not exhibit the same offset due to a different drag centre.

From cross plots of C_D with variation of C_L^2 the following was established. With increasing trim tab angle there was a moderate increase in C_D of between 0-4% for each two degrees of additional trim tab angle. There was also approximately a 45% increase in C_L^2 for each two degree increase in trim tab angle. The greater increase in C_L^2 as compared to increase in C_D for increasing trim tab angle shows the efficiency of the trim tab in generating lift. Increasing Froude number from 0.27 to 0.40 and removing heel, yaw and rudder angle decreased C_L^2 by 80% and increased C_D by approximately 35%. There was also a 15% and 21% reduction in the value of C_D for the $1/3^{rd}$ tests as compared to the $1/8^{th}$ case for the two cases presented.

Chapter 4

Flow Dynamics

4.1 Introduction

The state of the boundary layer around the hull of a model, for a given velocity, has a profound affect on the resistance of the vessel. With quantitative knowledge of the boundary lay state it is possible to both assess the effectiveness of any turbulence stimulation and also calculate a C_F value to be used in model to full scale extrapolation.

Traditionally the boundary layer state has been assessed with visual techniques such as the use of dye films or dye injection. A review of dye films and dye injection techniques is provided in Merzkirch(33) and a general review of flow visualisation techniques is presented in Clayton & Massey(10). Visual techniques were found to provide relatively coarse boundary layer information along with a significant increase in testing times, noted by Townsin(41). This increase in time was also reported by Campbell & Claughton(8) in that both ink-bleed and dyed oil were too time consuming to be of use in a typical yacht test program. These issues led to the search for an alternative and ultimately the use of constant temperature anemometry utilising glue-on hot-films was investigated.

The use of glue-on hot-films for marine based model testing, while not novel in itself, has previously been relegated to projects that have both vast budgets and relatively low restrictions on the test program. Campbell & Claughton(8) note that due to the time consuming nature of the use of hot-films that they were not routinely used for yacht testing. There are a number of challenges in the use of hot-films on hull surfaces under water including: the waterproofing of the film and it's electrical connections; the application of the film to the hull; the running of the leads that connect the hot-film to the data acquisition system; survivability and reliability of the hot-films during the test session and analysis of the collected data.

This chapter details how each of these potential obstacles have been overcome providing a robust, simple, relatively cost effective method of obtaining and analysing hot-film data. Along with the methodology a comparison is also made between results from tests of a $1/8^{th}$ scale model of an IACC yacht both with and without turbulence stimulation.

4.2 Test Equipment and Set-up

4.2.1 Hot-film Details

The probes were Dantec Dynamics 7100S47 glue-on fibre-film probes which visually resemble a glue-on strain gauge. The hot-films were based on the standard 55R47 glue-on probe with an additional film coating to ensure they were waterproof. The probes are 16 mm long 8 mm wide and 0.1 mm thick. The sensor is nickel and is 0.9 mm long and 0.1 mm wide on a 0.05 mm thick polyimide foil. There is a $2\text{ }\mu\text{m}$ quartz coating on the film sensor. Additional details of the probe can be found in the Dantec Dynamics online catalogue(16). A constant current is supplied to the sensor wire, the wire heats up and the resistance of the system increases until the wire reaches a prescribed constant temperature. Through convection to the surrounding environment the resistance of the sensor wire changes producing a change

in voltage which can be measured by a data acquisition system. Due to its chaotic nature, turbulent flow is better able to transfer heat away from the sensor than laminar flow which, due to change in voltage, enables definition of the flow regime, Perry(37).

To supply the power to and measure the changes of the hot-films it was necessary to connect them to a constant temperature anemometer (CTA). A Dantec Dynamics model 54N80 CTA was used which was designed with a series of internal dip switches to define the operating parameters of each hot-film. The settings of the switches was based on the resistance of the items in the analysis chain, including the hot-film sensor, along with the desired operating and environmental temperature. The low-pass filter within the CTA was set to open, effectively no low-pass filter, for the tests as there was an analogue low pass filter used further along the data collection chain. Details of the overheat ratios for each of the hot-films, including the resistance and temperature information, along with the calculation method are included in Appendix E.

4.2.2 Location and Installation of Hot-films

Ideally the sensor film, the wire that is in the flow, is located perpendicular to the fluid flow. For the probes used in this research all probes were orientated so as to be perpendicular to the model's centreline such that in the case of zero yaw they would be aligned perpendicular to the flow. This assumed that the flow would not be affected by the three dimensional shape of the hull. Due to this alignment datum, the sensors were not perpendicular to the flow for cases in which the model was yawed relative to the free stream.

Location of Hot-Films

The location of the hot-films, both on the model and with respect to each other was carefully considered. The final arrangement was designed to both give an overview of the flow on the body including the influence of heel, while at the same time

minimising any downstream disturbance. The thickness of the hot-film was approximately 0.1 millimetres which is less than the expected boundary layer thickness of 0.4 millimetres at the forward most film. This boundary layer thickness is based on the flat plate Blasius solution for laminar flow as described in White(43) and used a length Reynolds number of 3.5×10^6 . This Reynolds number corresponds to a Froude Number of 0.36 which is the expected speed at which the theoretical lower limit of transition $Re_\theta = 320$ is reached for this location on the model (see Figure 1.2 for comparisons of model scale, Froude number and transition points). At lower speeds and positions further aft the laminar boundary layer is thicker and at higher speeds the boundary layer becomes turbulent and at least an order of magnitude thicker. Note also that the thickness of the hot-film is approximately 3% of the height of the studs used for turbulence stimulation.

To help visualise the location of the hot-films a schematic showing the layout of hot-film sensors and turbulence stimulators is included in Figure 4.1.

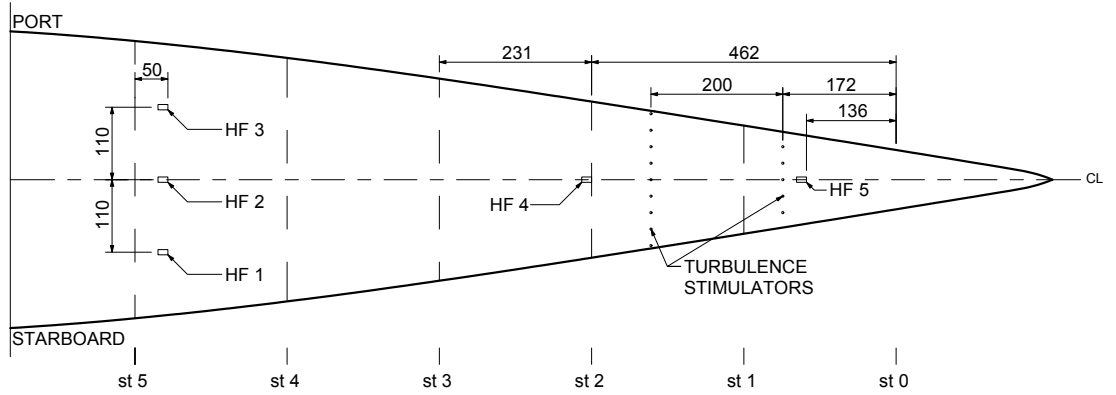


Figure 4.1: Schematic showing layout of hot-film sensors and turbulence stimulators. All dimensions shown are model scale millimetres.

Hot-film five was placed ahead of all turbulence stimulators to provide a common reference between the stimulated and unstimulated cases. Hot-film four was located directly aft of the turbulence stimulators so that a clear difference in intermittency would be observable between the with and with-out stud cases if the studs were in fact influencing the flow regime. Hot-films one, two and three were placed around the hull parallel and 50 millimetres forward of station five. The location of these hot-films was considered to be sufficiently aft to allow any turbulent energy due

to hot-film four in the no studs case to be mixed into the flow; but by being in an array around the hull could be used to help understand the flow on the hull in both the heeled and yawed condition.

Hot-Film Installation Methodology

There were two primary requirements in mounting the hot-films; the first was the attachment of the film to the hull surface and the second was how to lead the two connecting wires. Prior to attaching the hot-films to the model, arrangements needed to be made for the leading of the sensor wires in a manner to minimise influence of the boundary layer flow. The simplest method was to drill two small holes through the hull, pass the wires through and then ensure the holes were watertight. As the model used for the experiments was of foam cored construction extra precautions were required to ensure a water-tight seal around the wires. The quickest, simplest method was to drill a larger hole, in this case 8 mm in diameter, through only the outside skin, remove a small amount of core material ≈ 2 mm greater than the hole diameter. The hole was then back filled with a epoxy resin/fibre mix to a level 0.5 mm above the hull surface. This extra height allowed for minor shrinkage of the filler material and also allowed sufficient material for careful sanding of the filler so that it was flush with the model's surface. Two small holes of approximately one millimetre in diameter are then drilled through the solid resin 'plug' through which to pass the sensor wires. The hot-films were then glued to the hull using contact adhesive and the wires passed through the hull. The small holes were sealed with a small amount of liquid epoxy resin. Figure 4.2 shows the installed hot-film number four. The sensor wire is highlighted at 'A' and the connecting wires are highlighted at 'B'. In the same figure the whitish-blue material is epoxy resin/fibre filler.

Due to the fragile nature of the connecting wires built into the hot-films it was necessary to isolate them from any forces. This was especially important as it was a requirement that the model be removed from the tank and carriage after each

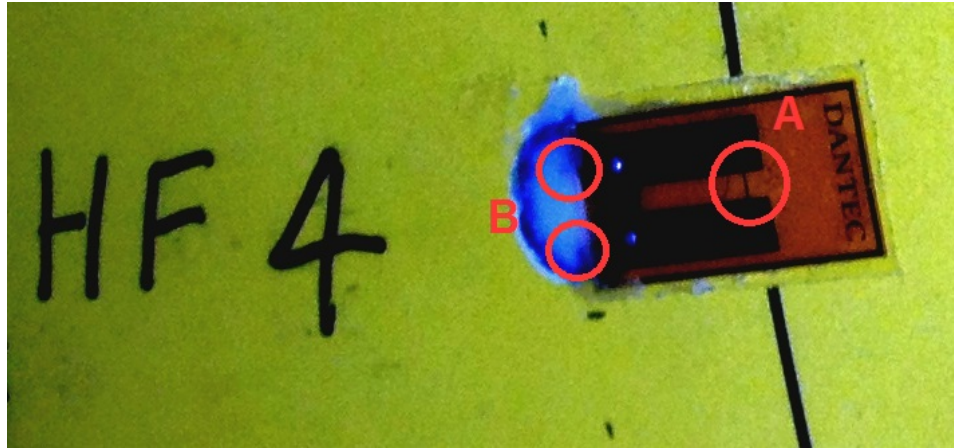


Figure 4.2: Close-up view of installed hot-film sensor number 4. Sensor wire highlighted at A and points where wire penetrates hull at B.

days testing. The isolation method consisted of two parts; a small connector pad and a rigidly mounted BNC connection. The small connector pad was attached to the inside of the hull, shown in Figure 4.3 and Figure 4.4, which provided a rigid connection point of the hot-film wire to the wire coming from the BNC connector. The addition of the rigidly mounted BNC connector, shown in Figure 4.5, ensured easy repeatable connection of the hot-films to the data acquisition system.



Figure 4.3: General view of internal connector.

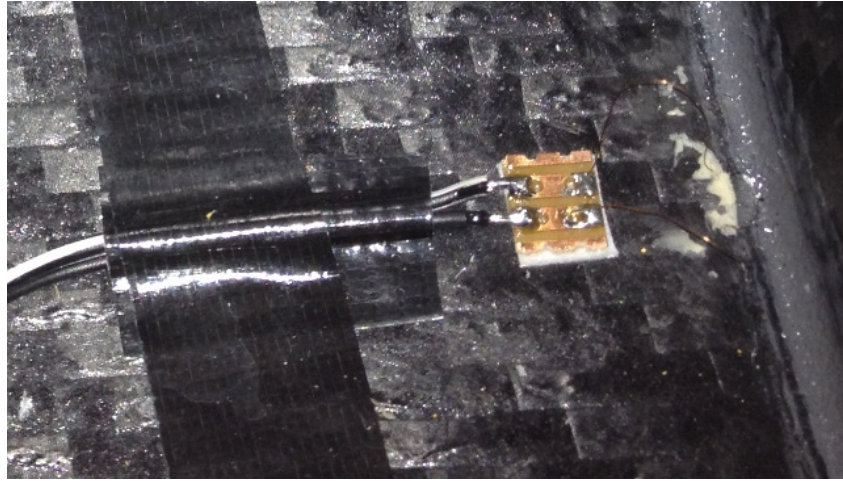


Figure 4.4: Detailed view of internal connector. The wires from the hot-film are connected to the right and the wires to left run to a BNC connector shown in Figure 4.5.

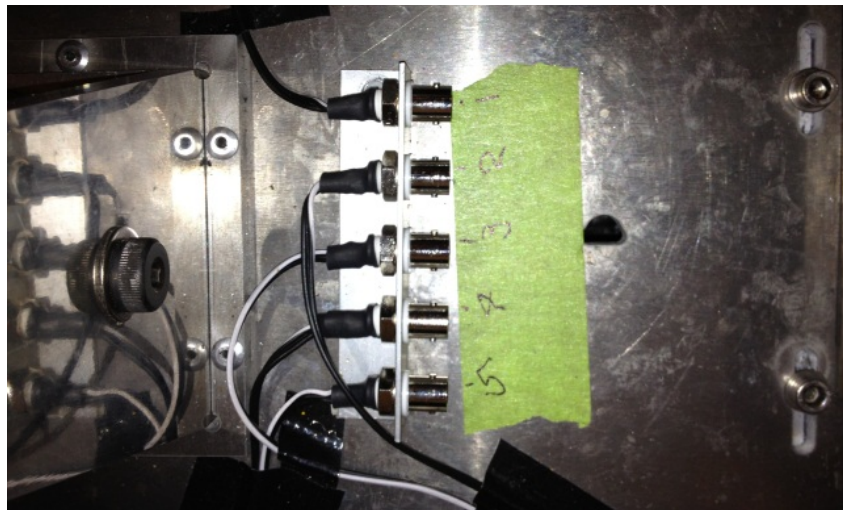


Figure 4.5: BNC connector array. Each of the five connectors is hard wired to one of the five hot-films.

4.2.3 Data Acquisition

The analysis chain included the hot-films, connecting leads, signal conditioner all of which was connected to a Hewlett-Packard PC. The PC recorded signals from each instrument via a National Instruments PCI-6251M Multifunction Data Acquisition Card controlled by Labview. No calibration of the glue-on hot-films was undertaken. Calibration of the hot-films would have required the hot-films to be attached (glued) to a fixture to enable calibration to take place. They would have then needed to be removed and then attached to the hull of the model. It was felt due to the fragile nature of the hot-films that the removal process had a high likelihood of causing them damage. Further, the purpose of the tests was to understand the flow regime which is possible without the explicit knowledge of the shear stress. Determination of the flow regime was possible and was measured in terms of intermittency.

During the set-up phase a series of runs were undertaken to assess the relative merits of different sampling frequencies and analogue low-pass filter settings. From the analysis of both time and frequency domain data of these runs, it was determined that the most suitable settings were a sample frequency of 8192 Hz with 1000 Hz analogue low-pass filter. This combination provided a sufficiently high sample rate to capture the predominant signal from all instruments whilst still having a low-pass filter to prevent aliasing.

4.2.4 Data Analysis

A quantitative method was required to describe the on-body flow regime. Solomon(40) describes a concept known as ‘transitional intermittency’ whereby the flow state on the body is described in terms of how turbulent it is on a scale of 0 to 1; with 1 being fully turbulent. Solomon(40) also notes that the calculation of the intermittency can be achieved using one of two broad analysis categories; either the kurtosis method or direct method. It has also been reported in Atencio(3) and

based on Abu-Ghannam & Shaw(1) that intermittency in the range of 0.25 to 0.75 is the region in which transition is occurring.

The kurtosis method relies on the statistical distribution of the data points, with a fully turbulent flow being represented by a Gaussian distribution and a kurtosis of three. The direct method in essence involves counting the individual values that are above a threshold, which is set either manually or as a non-dimensional parameter. An extended overview of the method including different application techniques is provided by Solomon(40).

Both the kurtosis and direct method require a level of subjective input whether it be high-pass filter values for use in the kurtosis method or detector function, windowing and threshold levels for the direct method. As such both the kurtosis and direct method have merit with the final choice of method being made with the desired outcomes in mind. For the work in this thesis it was hoped to not only obtain results of academic value but to also highlight a technique that would make intermittency analysis viable as part of more general research and commercial testing.

The intermittency calculations were undertaken following the procedure outlined in Binns et al.(5) with a change in the way in which the high-pass filter value was determined. This change was necessary due to an insufficient number of films arranged along the centreline of the model to accurately predict a value for the required high-pass filter as per their paper. This shortfall in sensors was a consequence of attempting to minimise any interference between the sensors; something that Binns et al.(5) was not faced. The revised method first required calculation of intermittency at hot-film four for all the Froude numbers in condition 13 using nine separate high-pass filter values. For reference, condition 13 was a speed sweep with no turbulence stimulation which ensured that the transition would occur ‘naturally’. The calculated intermittency data was then plotted with variation of Froude number, for each of the nine high-pass filter frequencies. Next, a cubic

spline was fit through each of the nine data series and the R^2 value of fit of each of the splines calculated. The values of R^2 were then plotted with respect to variation of high-pass frequency to give Figure 4.6.

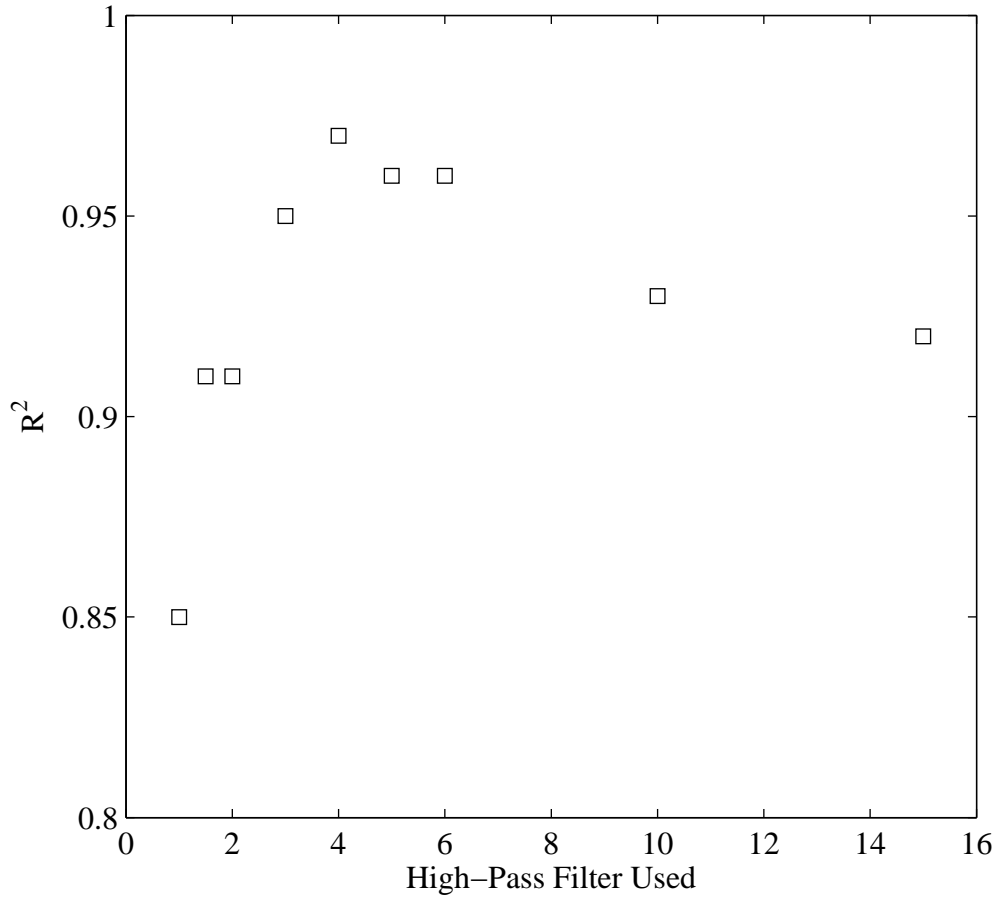


Figure 4.6: R^2 values for curves fit through no-stud speed sweep calculated at a range of frequencies.

The goal was to identify the high-pass filter frequency at which the R^2 value reached a maximum value as the highest value indicates the best fit. From the figure it can be seen that a high-pass filter value of 4 Hz gave the maximum value. This high-pass filter value was then used in the intermittency calculation process for the remainder of the test conditions.

A selected range of high-pass filter data plotted as intermittency against Froude number is included in Figure 4.7. A visual inspection of the data points generated using a 4 Hz high-pass filter show a steady change in intermittency with Froude

number from approximately zero at a Froude number of 0.10 to a value of one at a Froude number of 0.29. Several of the alternative high-pass filter values gave similar results however their lower quality of fit to the regression line discounted them. Note that the lowest Froude number of 0.05 was discounted when undertaking the spline fit. This was due to the high calculated level of intermittency of approximately 0.9; this value is highly unlikely as at this speed the flow should be laminar as evidenced by the low level of intermittency at a Froude number of 0.10. This erroneous level of intermittency at a Froude number of 0.05 was a result of a very low signal to noise ratio. This signal to noise ratio meant that the primary signal was random noise. As random noise tends to a Gaussian distribution the analysis method interprets the signal as mostly transitioned flow.

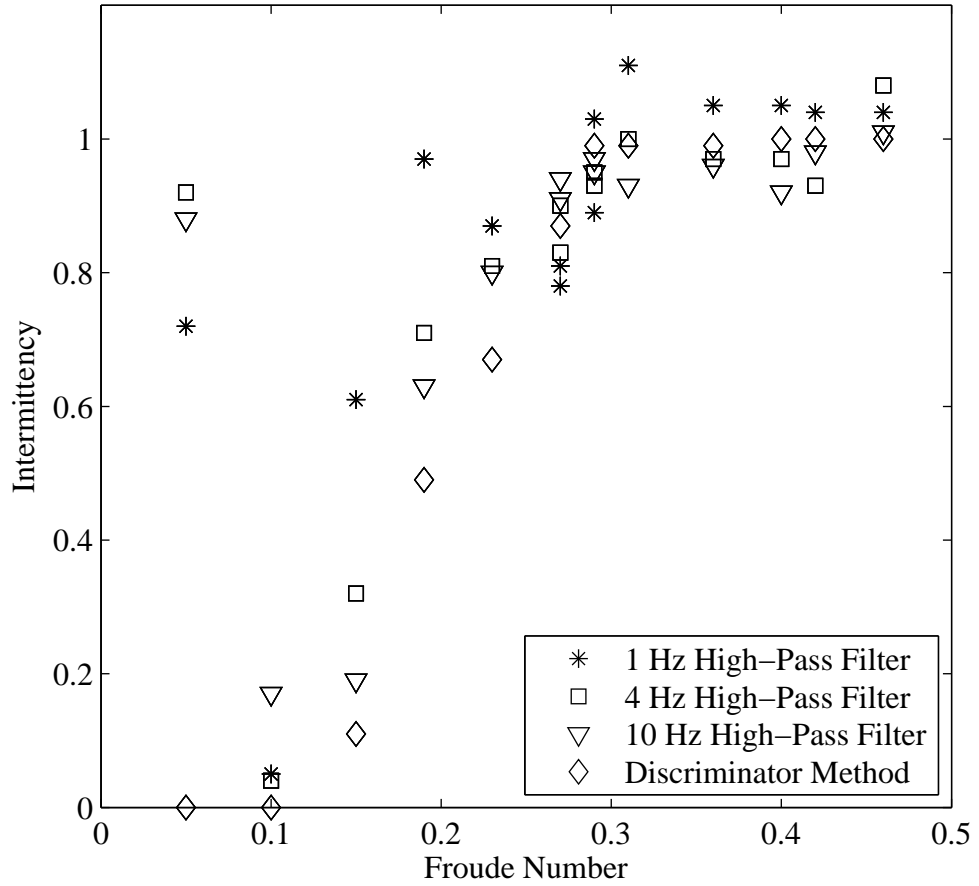


Figure 4.7: Condition 13 intermittency for hot-film four plotted with respect to variation in Froude number for a select range of high-pass filter values and a direct calculation method.

Calculations were also performed to assess the differences between the kurtosis and direct method and to provide a method of establishing the validity of the results of

the intermittency calculations. A modified version of the direct method outlined in Clarke et al.(9) was used to undertake the calculations with the related data points shown in Figure 4.7. The modification made to the method used by Clarke et al.(9) was to replace a peak-valley counting (PVC) algorithm with a simple smoothing function. The smoothing function averages bins or windows of data from the detector function. A simple sliding window was also implemented as it was reported by Solomon(40) to improve results. From the tests undertaken there appeared to be only 0.02 difference in the calculated intermittency when comparing the windowing approach to the sliding average results and it is unclear from the analysis which provided the better answer. The results of the direct method were within the expected range; but were sensitive to both the window period and the threshold values; this sensitivity was also noted by Koyabu and Tsukiji(29). The method was also found to be time consuming during the data analysis process and made reporting of the values used throughout the calculation difficult (threshold values changed for each velocity). Considering the assessed difficulties of implementation along with the desire to have a simple robust intermittency calculation method, it was determined that a kurtosis method would provide the best solution for this project.

4.2.5 Uncertainty Analysis

The background to the uncertainty calculations are contained in Appendix C.3 with the results in Table C.2. The magnitude of the results were sufficiently small, that if included on the hot-film plots the uncertainty bars would be approximately the same size of the data points, as such uncertainty bars have not been included.

4.3 Results and Discussion

The discussion of the results has been broken into six parts. The first section uses qualitative analysis of the time and frequency domain results. The remaining five sections discuss the quantitative intermittency results looking at each of the following areas of influence: velocity, heel angle, yaw angle, trim-tab angle and finally rudder angle. The plots included in the five sections were chosen as they either showed the clearest trends or were representative of the general behaviour; an extended set of results are included in Appendix H.

4.3.1 General Trends

As part of the initial analysis procedure checks were made of the time and frequency domain results. The time domain results, were also examined during the test program as a way to quickly establish whether the hot-films were functioning or otherwise.

Time Domain

Figure 4.8 and Figure 4.9 show time domain plots of the same model set-up except that in Figure 4.8 (Run 107) shows results with studs attached whilst Figure 4.9 (Run 239) was without. There is good correlation at hot-film five (located 6% aft of forward perpendicular) between both runs which suggests that there was consistency between the two tests and there was no clear change in background turbulence level; this allows the results from the other hot-films to be compared with confidence. At hot-film four, located immediately aft of the studs and 20% aft of the forward perpendicular, there is a clear difference between the with and without studs case. With studs attached there is a continuous high frequency signal indicating turbulent flow where as for case without studs there are voltage spikes in the signal representing the existence of turbulent bursts. It is important not to

compare the magnitude of the signals from each plot rather just the general shape of the time trace due to differences in resistance of each sensor channel. There is very good similarity in the behaviour of the time domain data between hot-film three, two and one (50% aft of the forward perpendicular). This shows that at the further aft position and for this speed that flow has transitioned. This is interesting as it correlates well with Figure 1.2 which shows at the 50% aft position that the flow should undertake natural transition. This correlation between the theoretical limits based on flat plates and the actual test provides support as to validity of theoretical methods as at least a first pass solution to determine model scale.

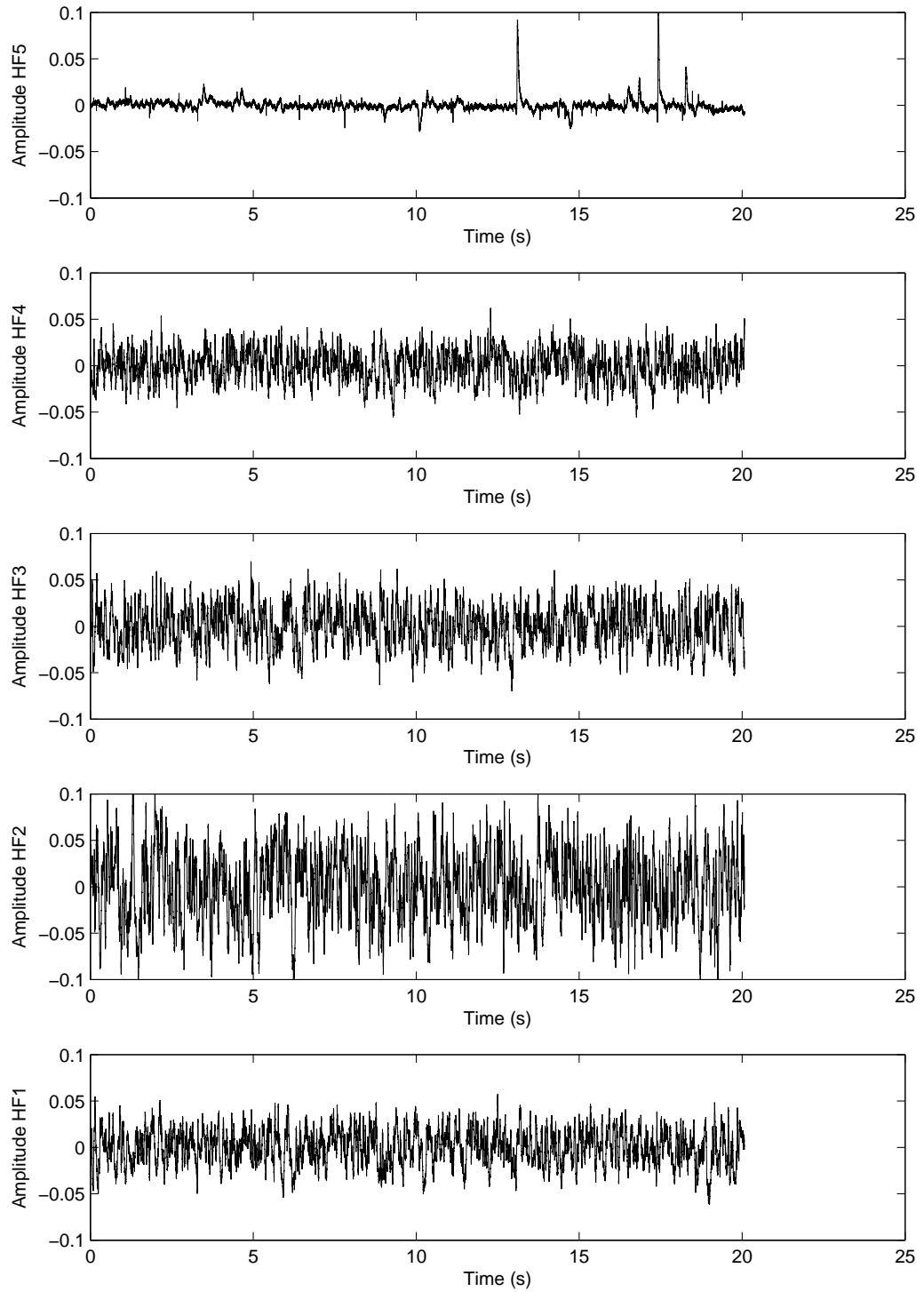


Figure 4.8: Time domain plot of zero meaned data of all hot-films for Run 107 (Yaw 1 degrees, Heel 10 degrees, Tab 4 degrees, Rudder 2 degrees and Froude number 0.15 with turbulence stimulation). The data shows laminar flow at hot-film five and turbulent flow at all other hot-film locations.

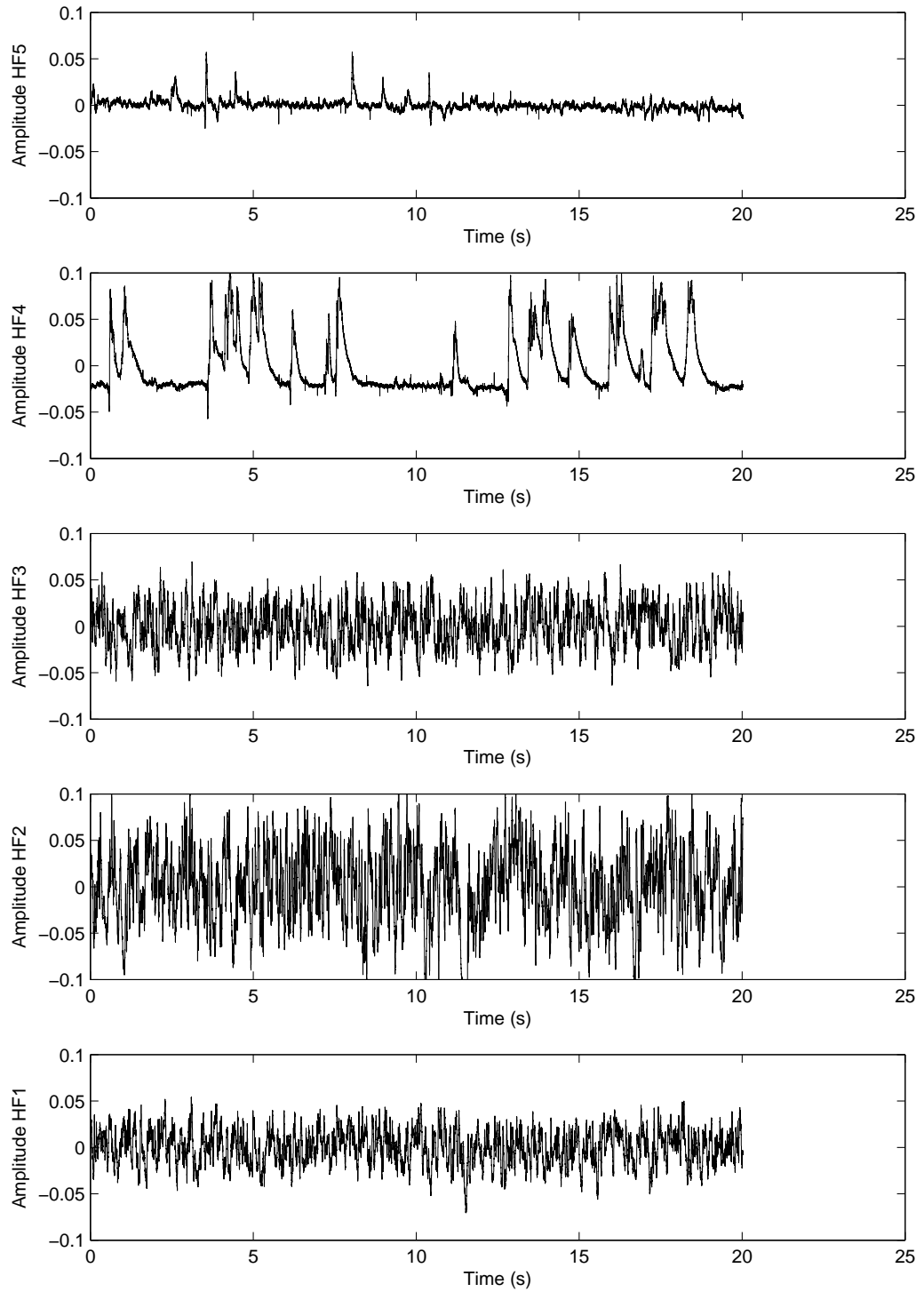


Figure 4.9: Time domain plot of zero meaned data of all hot-films for Run 239 (Yaw 1 degrees, Heel 10 degrees, Tab 4 degrees, Rudder 2 degrees and Froude number 0.15 without turbulence stimulation). The data shows laminar flow at hot-film five, transitioning flow at hot-film four and turbulent flow at all other hot-film locations.

Frequency Domain

Frequency domain results were assessed as they provide a qualitative method of understanding the change in the flow state with respect to speed. The results are qualitative in that they provide a way in which to show that the flow is indeed changing with speed; but cannot provide the absolute level of intermittency.

Condition 13 was of particular interest in the identification of the nature of the boundary layer with changing velocity as it was a speed sweep with no studs attached. From observation of the plots for the range of velocities tested, there was a clearly observable difference between Run 239 (Froude number of 0.15) and Run 244 (Froude number of 0.31); Figures 4.10 and 4.11 respectively. Each plot presents the signal response with variation of frequency for each of the five hot-films for the respective run and includes data traces with and without the digital high-pass filter.

The frequency results for hot-film five (6% aft) have both an earlier roll-off and reduced energy relative to the hot-films located further aft on the model. The earlier roll-off and reduced energy indicate either laminar or ‘bursty’ transitioning flow which is confirmed with inspection of the actual intermittency as shown in Figure 4.13.

We will now compare the relative behaviour of the signals at hot-film four (20% aft). For Run 239 (Froude number of 0.15), Figure 4.10, the magnitude of the signal rolls off quickly from approximately 4 Hz reducing by two orders of magnitude by approx 30 Hz; with 4 Hz being in the range of the natural frequency of the carriage structure. The roll off indicates that there is little energy transfer at this lower speed which is in turn indicative of laminar flow. The ‘bump’ at approximately 500 Hz may be due to the natural frequency of the sensor and hull; but will not influence the results as it is two orders of magnitude less than the primary signal. For the same hot-film but during Run 244 (Froude number of 0.31), Figure 4.11, the roll off is delayed to approximately 40 Hz. This indicates additional energy has been added to the system at the higher speed from the transitioned turbulent flow

on the hull.

The remaining hot-films, three, two and one will be discussed as a group as they are all located at 50% aft of the forward perpendicular. All three hot-films show similar results for a given velocity. For Run 239 (Froude number of 0.15), the roll-off frequency is delayed relative to hot-film four indicating an increase in intermittency due to increased energy in the signal. For Run 244 (Froude number of 0.31) there is no quantifiable difference to the roll-off frequency at hot-film four. This shows that the flow state has stabilised indicating transition has already occurred at or forward of hot-film four.

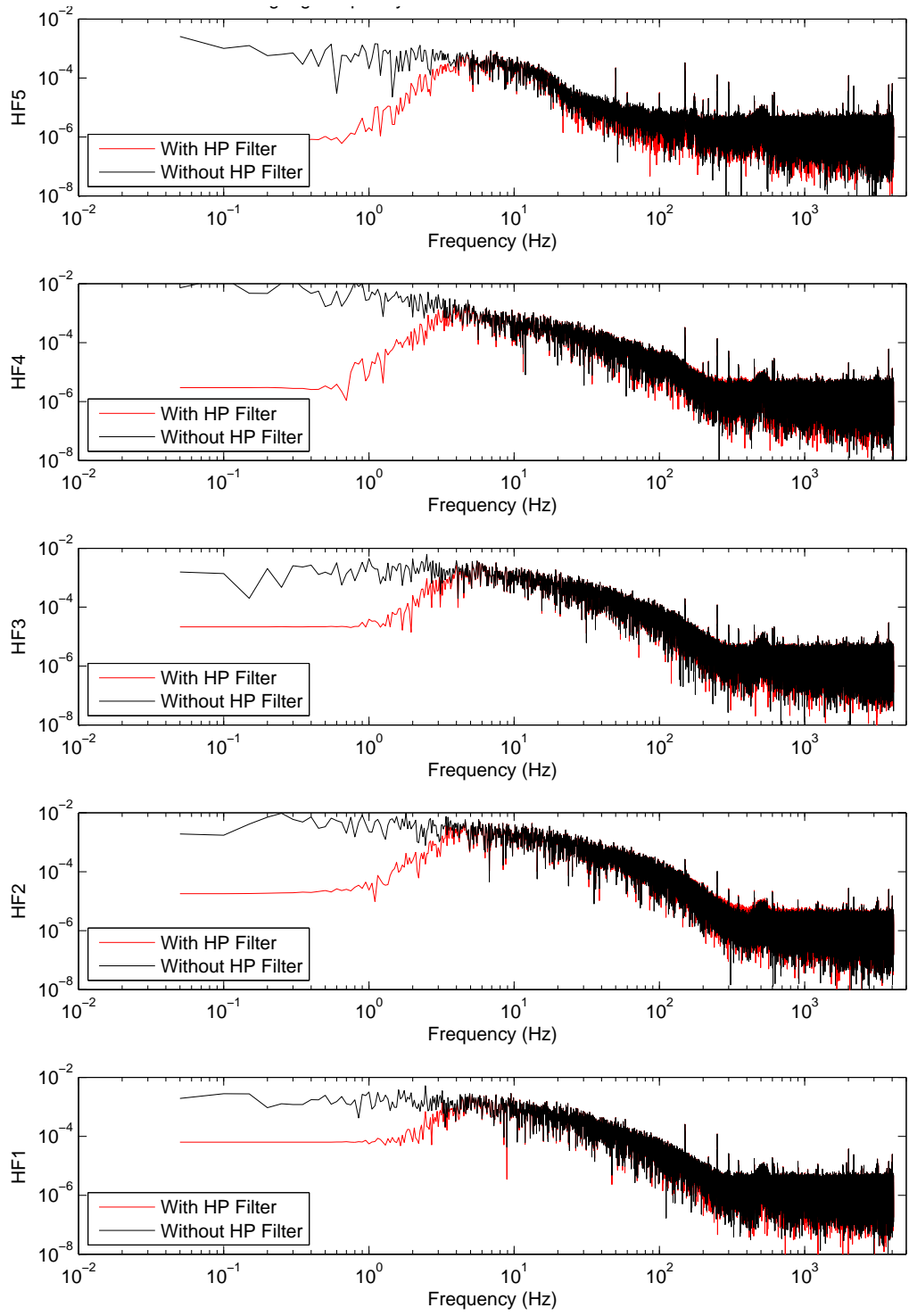


Figure 4.10: LogLog plot of amplitude with respect to frequency of zero meaned data of all hot-films with and without a 4 Hz high pass filter applied for Run 239 (Yaw 1 degrees, Heel 10 degrees, Tab 4 degrees, Rudder 2 degrees and Froude number 0.15 without turbulence stimulation). A quicker roll-off of the signal indicates lower turbulence levels. So, hot-film five has the lowest turbulence followed by hot-film four and then three, two and one show the highest turbulence.

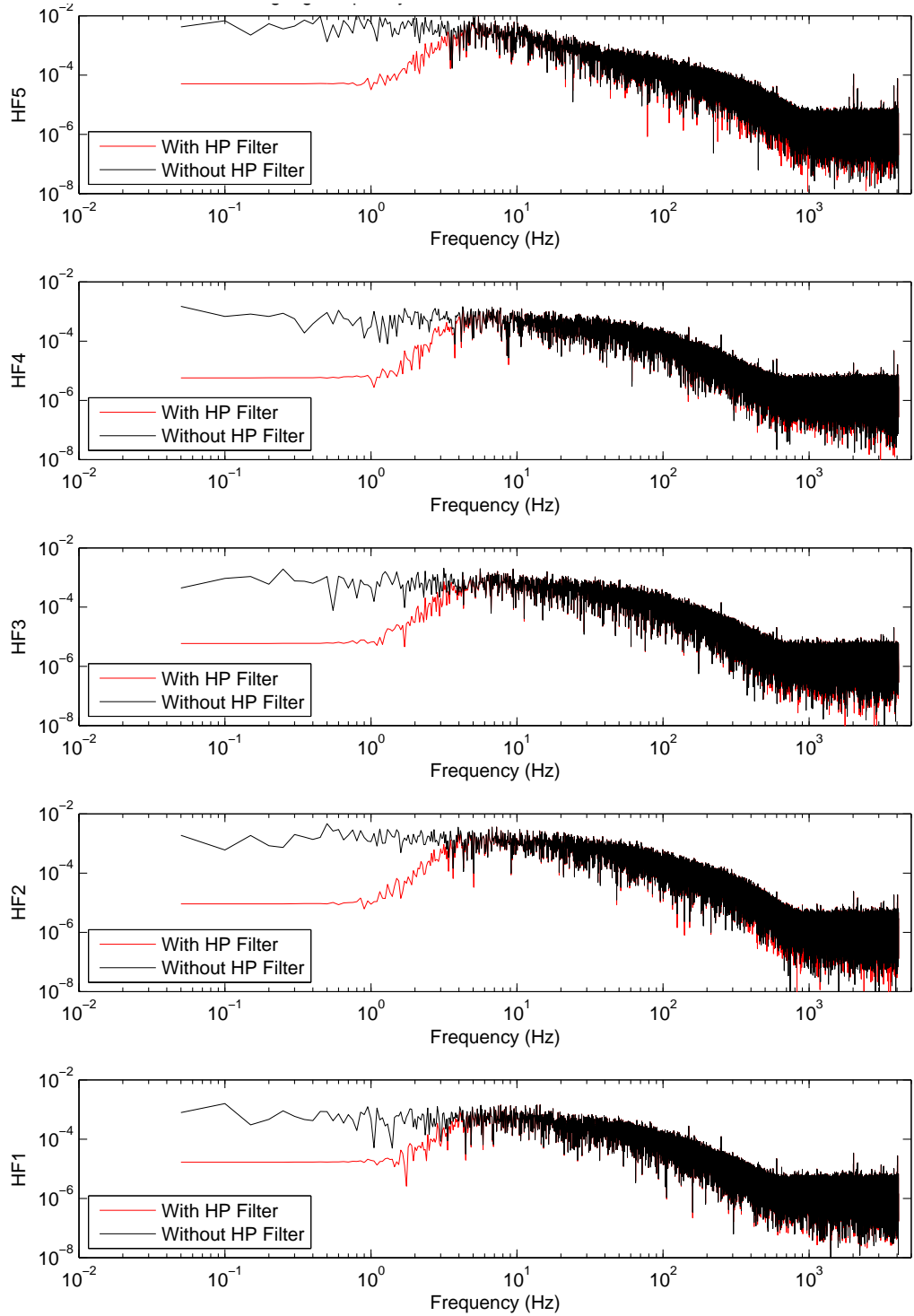


Figure 4.11: LogLog plot of amplitude with respect to frequency of zero meaned data of all hot-films with and without a 4 Hz high pass filter applied for Run 244 (Yaw 1 degrees, Heel 10 degrees, Tab 4 degrees, Rudder 2 degrees and Froude number 0.32 without turbulence stimulation). The quicker roll off of hot-film five indicates lower levels of turbulence compared to the remaining hot-films.

4.3.2 Effect of Model Velocity

The effects of model velocity on intermittency are presented using Figure 4.13. In this figure intermittency is plotted with respect to variation of Froude number at each hot-film with data from both with and without stud cases.

At hot-film 5 (6% aft), there is good general agreement in levels of intermittency for Froude numbers at or above 0.15. The location of this hot-film forward of the line of studs when fitted, made it particularly susceptible to background turbulence levels which could explain the differences, especially at the lower velocities. The forward location did however provide a method to establish whether there was consistency between two runs with and without studs.

The effectiveness of the studs in tripping the flow to turbulent is highlighted in Figure 4.13. This is most obvious at hot-film four and becomes less so at the measurement points further aft. In the case with studs fitted, full transition has occurred at a Froude number of 0.10 whereas without studs the flow is fully turbulent until a Froude number of 0.29.

In Section 1 a means of establishing, a priori, the expected transition behaviour on the model was introduced. The conclusions were made based on the data contained in Figure 1.1 and Figure 1.2; with Figure 1.2 repeated below as Figure 4.12 for reference.

With the results presented in Figure 4.13, the concepts and conclusions made earlier can be re-assessed. First, the test data reinforces the initial hypothesis that a scale factor of eight is a viable option, assuming the range of Froude numbers considered, for testing in the towing tank at the Australian Maritime College.

Previously the value of $Re_\theta = 320$ was introduced as the level below which there is insufficient energy transfer through the boundary layer for the flow to naturally transition from laminar to turbulent flow. Another threshold was also introduced

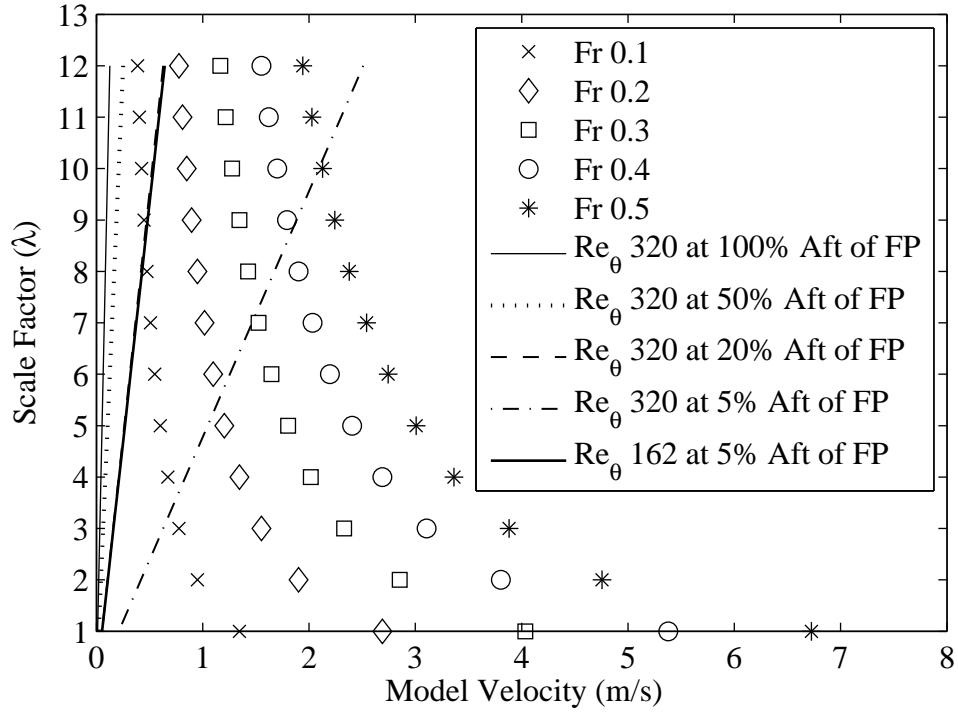


Figure 4.12: The theoretical lower limit of transition $Re_\theta = 320$ at various locations on a model for a range of speeds and model scales.

located at $Re_\theta = 162$. Preston(38) notes that above this level, with stimulation, there should be sufficient disturbance to start the transition close behind the stimulators. In Figure 4.12 $Re_\theta = 162$ is shown for the position 5% aft of the forward perpendicular. The slope of this line shows a noticeable steepening as compared to the $Re_\theta = 320$ at the same longitudinal position. Hence, as Re_θ is reduced the slope of the Re_θ line increases. So, in the same way, the line representing a position 20% aft of the forward perpendicular would also move to the left for $Re_\theta = 162$. This shows that it was expected that there would be sufficient disturbance from the studs to initiate the transition to fully turbulent flow for a $1/8^{th}$ scale model. It is shown in Figure 4.13 that the studs have a major influence on transition. For the case without studs transition does not occur at hot-film 4 (20% aft) until a Froude number of approximately 0.29 while with studs the model will experience fully transitioned turbulent flow at the desired range of test speeds except the lowest Froude number of 0.05. Note that this lowest Froude number is a speed outside the normal range of interest. The correlation between transition behaviour and the anticipated Re_θ values implies that if the value of intermittency is less than one,

then Re_θ can also be expected to be less than 320. This is reflected in a value of at least $Re_\theta = 320$ being required for fully transitioned flow.

Due to the three-dimensional hull shape it was expected that the laminar flow would exist at higher speeds than on a flat plate due to the negative pressure gradient. However, the results of the experiments have not detected the difference between tripping on a flat plate and tripping on the 3D body. This flow behaviour is likely a function of the fair and low curvature hull lines creating gradual changes in pressure along the body as well as the studs being particular effective at generating the required levels of flow stimulation.

The high level of intermittency observed in Figure 4.13, at the two lowest speeds for hot-film 5 (6% aft) and the lowest speed for hot-film 4 (20% aft), are unrealistic. From an inspection of the time domain results for these speeds a very low signal was observed. It is believed this low signal resulted in a very low signal to noise ratio at these speeds. This had the effect that the primary signal was random noise which tends to a Gaussian distribution. As the intermittency calculation method interprets a Gaussian distribution as fully turbulent flow an incorrect estimate of the level of intermittency was made. This highlights one of the limitations of the method employed for the intermittency analysis.

4.3.3 Effect of Heel angle

Figure 4.14 shows intermittency plotted with respect to variation in heel angle for yaw angle of 0 degrees, trim-tab angle of 8 degrees, rudder angle of 2 degrees and Froude Number of 0.29. At hot-film four the results show that studs are required. With studs there is no difference in intermittency with heel but without studs there is a decrease in intermittency of approximately 17% with heel angle increased from five to ten degrees. At the other measurement locations there is no significant variation between heel angles for the with and without studs test cases.

4.3.4 Effect of Yaw Angle

Figure 4.15 shows intermittency plotted with respect to variation in yaw angle for Heel 0 degrees, Tab 0 degrees, Rudder 0 degrees and Froude Number 0.40 for both the with and with out stud cases. For hot-film five there was an increase in intermittency of approximately 30% for both one degree positive and negative yaw angle. The increased intermittency may have been caused by accelerated flow around the hull body plan. With increasing yaw angle the flow becomes increasingly perpendicular to the hull sections. This change in angle combined with decrease in radius, relative to the curvature of the model's centreline profile, will cause the flow to be increasingly accelerated at each successive station forward. The accelerated fluid velocity would increase energy in the flow which in turn increases the momentum thickness and turbulence. This behaviour would be increased at each section closer to the forward perpendicular due to decreasing section radius. At hot-films three, two and one, all at the same most aft position, the difference in intermittency levels between the three transverse locations are within uncertainty. This is due to the flow being fully developed at this location.

4.3.5 Effect of Trim-Tab Angle

Figure 4.16 shows intermittency plotted with respect to variation in trim-tab angle for yaw angle of 0 degrees, heel angle of 0 degrees, rudder angle of 0 degrees and Froude Number 0.40. There is no significant relationship shown between the trim-tab angle and intermittency level. The trim-tab was located aft of all measurement points and as such would not be expected to influence the flow behaviour in the forward portion of the hull.

4.3.6 Effect of Rudder Angle

Intermittency is plotted with respect to variation in rudder angle for yaw angle of -2 degrees, heel angle of 20 degrees, trim-tab angle of 10 degrees and Froude

Number 0.33 in Figure 4.17. There is no significant relationship shown between the rudder angle and intermittency level, however there were differences in level of intermittency between stimulated and non-stimulated cases at hot-film four. The difference in intermittency level between the stimulated and non-stimulated cases is contrary to what was shown in speed sweep in Figure 4.13; where flow was turbulent for cases with and without studs. While the data in that plot was for the same Froude number range as Figure 4.17 it is important to note that the tests in Figure 4.17 were conducted at a greater heel angle, 20 degrees, and different yaw angle, -2 degrees. The different transition behaviour is likely due to the increased heel angle which was shown in Figure 4.14 to delay transition.

Although the results in Figure 4.17 do not show the influence of rudder angle the data for hot-film four shows that turbulence stimulation is required. It is unclear why there is one point for the non-stimulated case at hot-film four that does not follow the trend. As the rudder is located towards the aft end of the submerged portion of the hull it would not be expected to influence the flow behaviour in the forward portion of the hull where the hot-films were located.

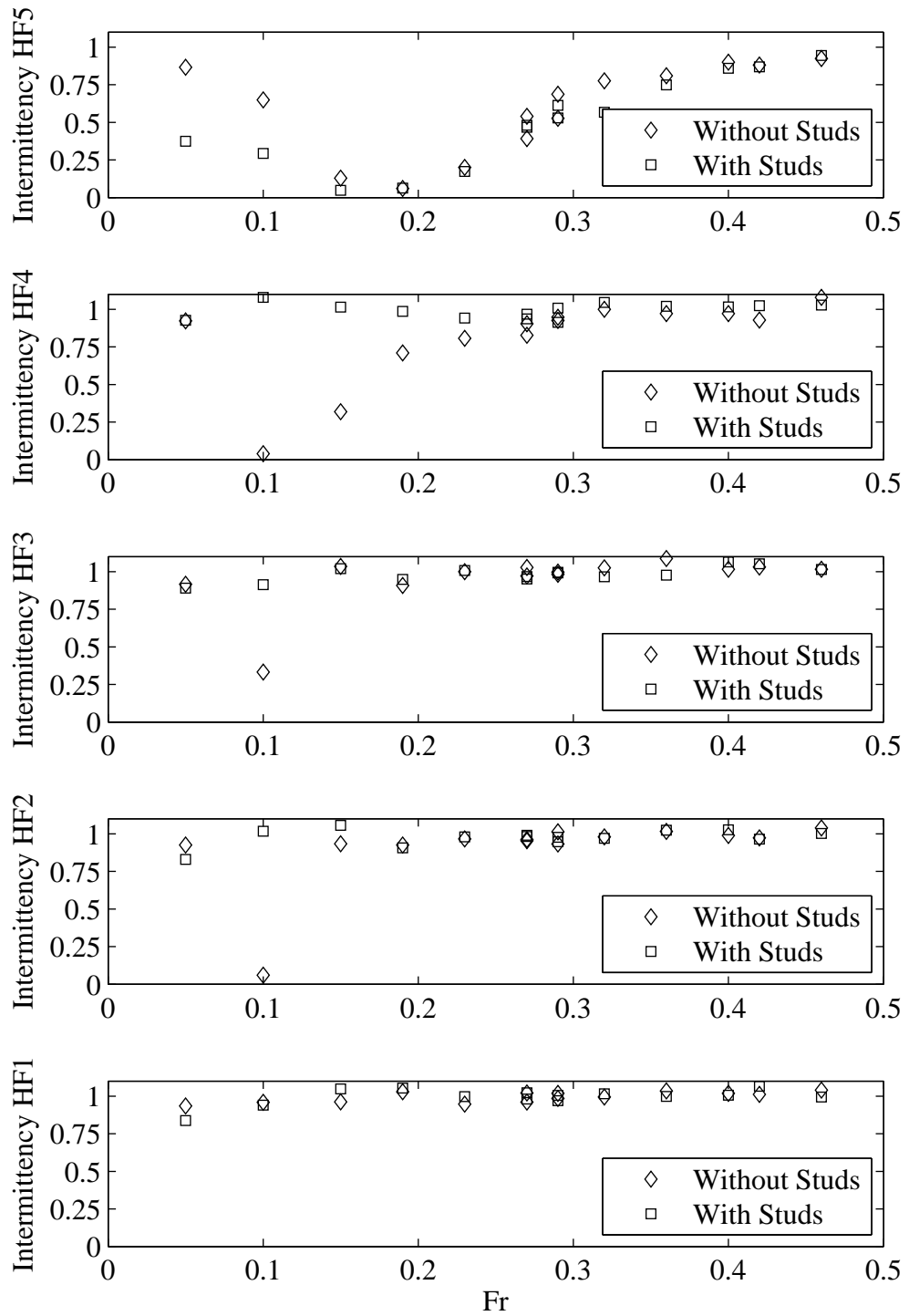


Figure 4.13: Intermittency plotted with respect to variation in Froude number of all hot-films (Yaw 1 degrees, Heel 10 degrees, Tab 4 degrees, Rudder 2 degrees). Hot-film five which was forward of the studs shows both increasing intermittency with increased Froude number and consistency between runs with and without studs. Hot-film four shows the effectiveness of the studs in tripping the flow.

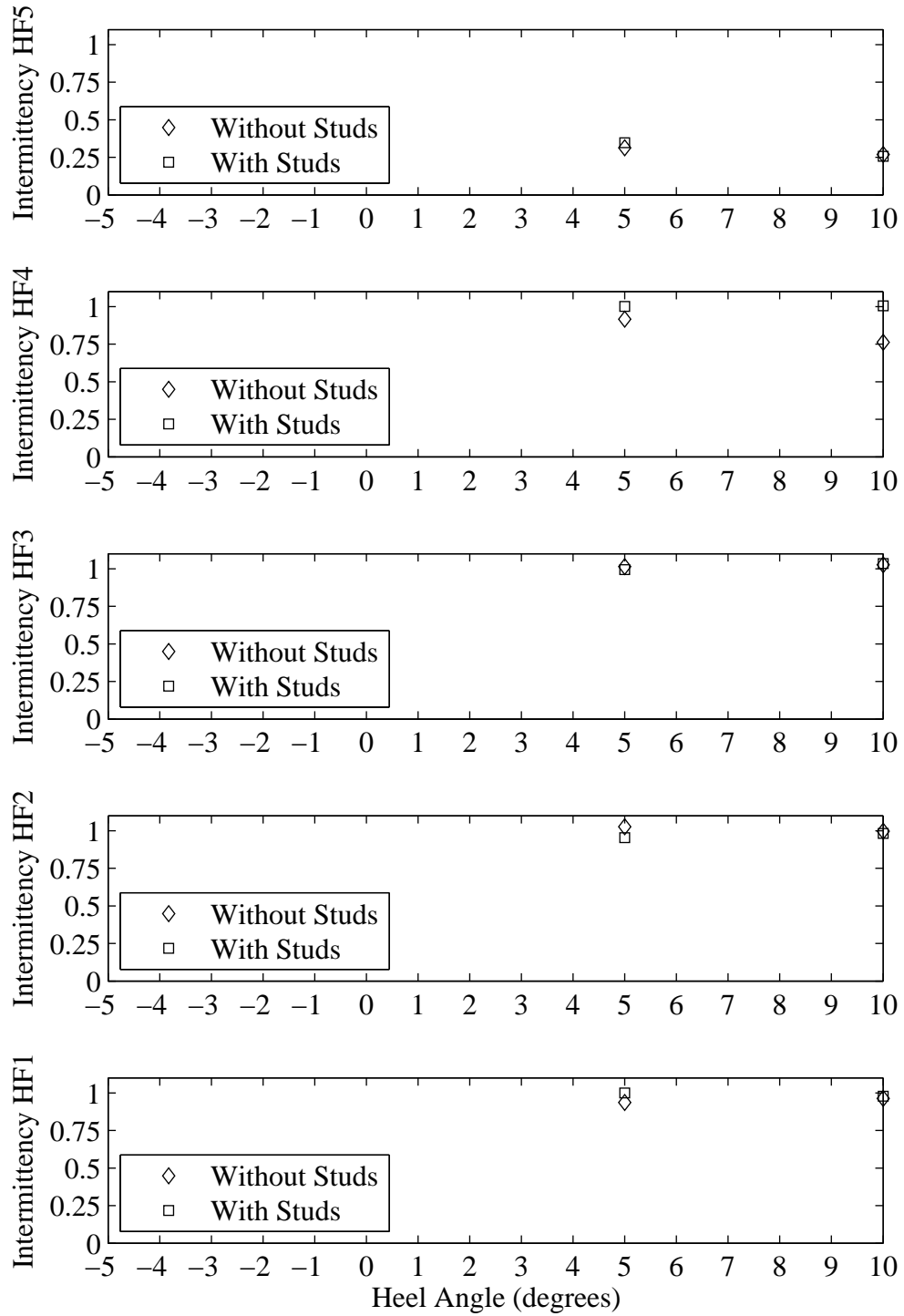


Figure 4.14: Intermittency plotted with respect to variation in heel angle of all hot-films (Yaw 0 degrees, Tab 8 degrees, Rudder 2 degrees, Froude Number 0.29). The reduced intermittency without studs four hot-film four, especially at 10 degrees heel, indicates that studs are required.

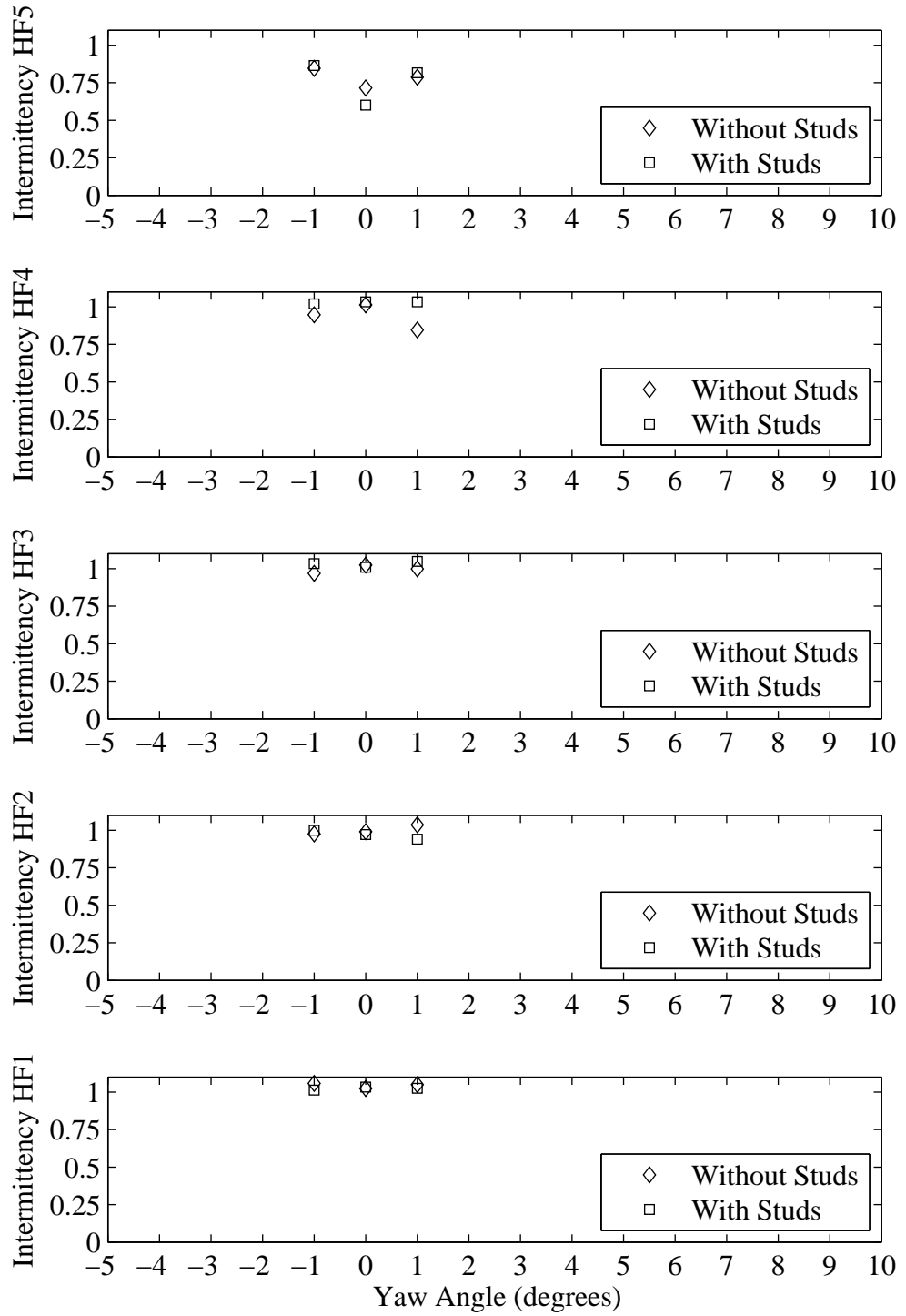


Figure 4.15: Intermittency plotted with respect to variation in yaw angle of all hot-films (Heel 0 degrees, Tab 0 degrees, Rudder 0 degrees, Froude Number 0.40). The increased intermittency for hot-film five is due to accelerated flow and the lower values for the unstimulated case at hot-film four are possibly due to flow separation.

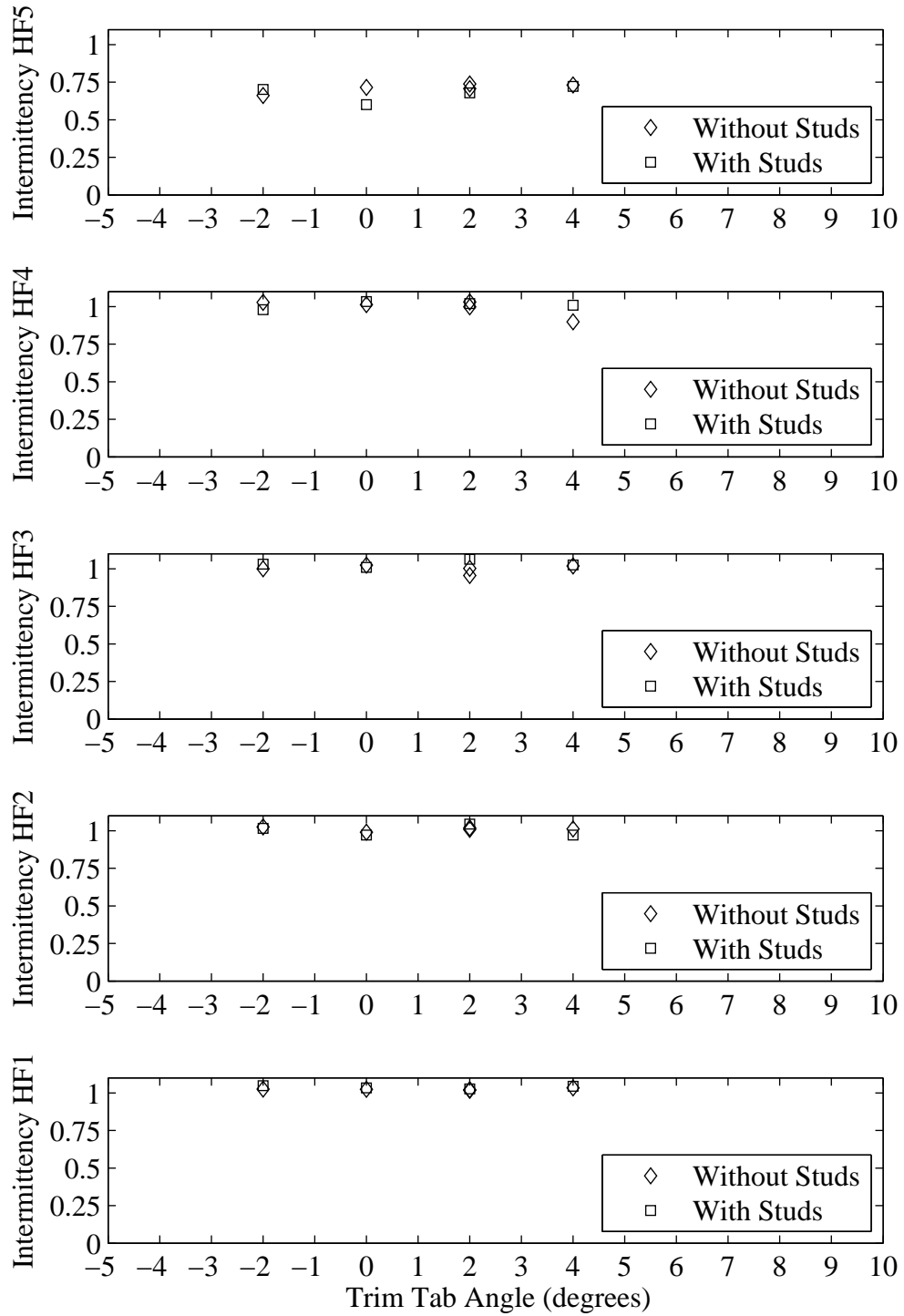


Figure 4.16: Intermittency plotted with respect to variation in trim tab angle of all hot-films (Yaw 0 degrees, Heel 0 degrees, Rudder 0 degrees, Froude Number 0.40). Due to the trim tab being located aft of the measurement points, it has not influenced the flow behaviour.

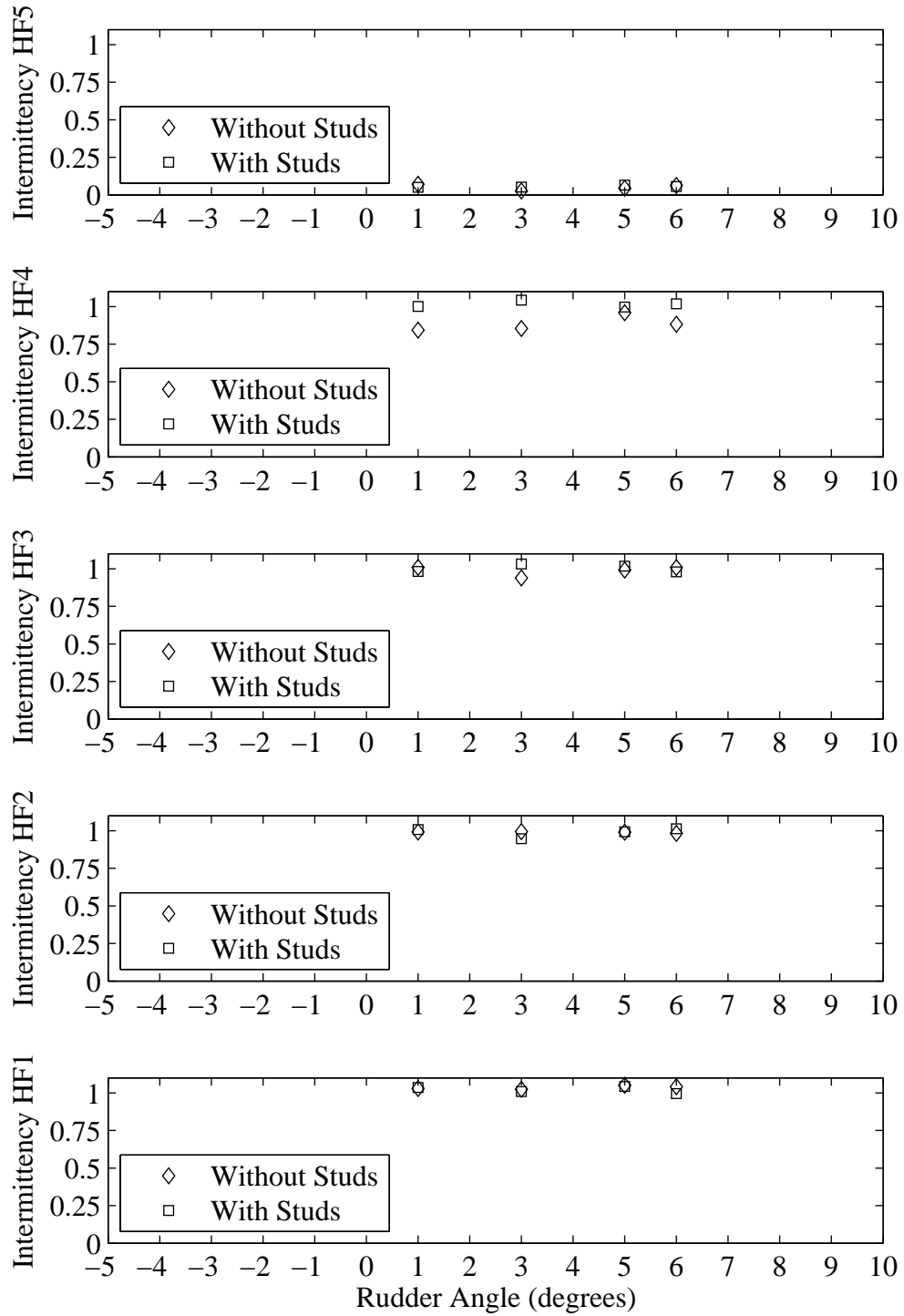


Figure 4.17: Intermittency plotted with respect to variation in rudder angle of all hot-films (Yaw -2 degrees, Heel 20 degrees, Tab 10 degrees, Froude Number 0.33). The reduced intermittency at hot-film four without studs demonstrates the need for flow simulation in this case.

4.4 Chapter Summary

This chapter has detailed the method and results of a series of experiments conducted using glue-on hot-films on a $1/8^{th}$ scale IACC model yacht hull. The method included the development of a robust hot-film installation technique as well as the adaptation of an existing intermittency analysis technique to suit the specifics of model testing. Intermittency calculations were undertaken using a method based on the kurtosis of the hot-film signal including the development of an alternative method to establish the high-pass filter value required by the method.

No calibration of the glue-on hot-films was undertaken due to the potential to cause damage during the removal and re-application of the films required as part of the calibration process. Throughout the testing all hot-films continued to work highlighting the robustness of both the installation and experimental procedure.

It was shown that the time and frequency domain plots of the hot-film data were effective as an initial method of understanding the flow behaviour. Further analysis using the level of intermittency, which quantifies the state of the on-body flow at each of the hot-films for each run, enabled comparisons of a range of independent variables.

Velocity, heel angle and yaw angle were all shown to effect the level of turbulence on the model's fore body region for the unstimulated cases; but only a change in yaw angle was able to influence the flow for both the stimulated and unstimulated cases. Trim-tab and rudder angle were shown to have no affect on the turbulence levels

With studs fitted there was transitioned flow for all Froude numbers tested (0.05-0.46) at each of the five measurement locations. For the two lowest Froude numbers tested, 0.05 and 0.10, the analysis method incorrectly described the flow state for the no stud case which was a function of a low signal to noise ratio. With increasing velocity and constant yaw angle, the flow state, i.e. completely turbulent,

along the body was as predicted by flat plate theory despite the model having a three-dimensional shape which could be expected to delay transition. This flow behaviour is likely a function of the fair and low curvature hull lines creating gradual changes in pressure along the body as well as the studs being particularly effective at generating the required levels of flow stimulation.

Without studs fitted several observations were made with respect to variation of Froude number. Laminar flow was observed at and below Froude numbers of 0.1 for all measurement locations. Partial laminar flow was observed to exist at hot-film five (6% aft of the forward perpendicular) and four (20% aft of the forward perpendicular), for Froude numbers between 0.10 and 0.29. For Froude numbers from 0.29 and above, the flow was fully turbulent except at hot-film five.

The influence of heel angle, for the unstimulated cases, on the flow state may have been a function of a changed pressure gradient due to accelerated flow. It is also possible that local wave behaviour contributed to the change in intermittency as the two measurement points where the effect was measured were the forward most points and were both in the region of the bow wave. The local wave behaviour is examined in detail in the following chapter with comparisons made between experimental flat plate data and the $1/8^{th}$ scale data.

Yaw angle was shown to increase the level of intermittency, for the unstimulated cases, at the forward most measurement point which was thought to be a function of the cross sectional shape, at this position along the vessel, increasing the transverse flow velocity and thereby increasing the energy in the flow.

The results show that with turbulence stimulation the on-body flow became fully turbulent for all Froude numbers tested, which highlights that with appropriate boundary layer stimulation, the state of the boundary layer is not a limiting factor in the testing of a $1/8^{th}$ scale IACC yacht model.

Chapter 5

Correlation of Forces and Moments with Flow Dynamics

5.1 Introduction

This chapter investigates the two primary dependent variables of the drag extrapolation procedure, friction coefficient (C_F) and residuary resistance coefficient (C_R). Conventionally C_F is calculated using one of a number of so called flat plate friction lines, sometimes modified to try and better represent flow on a three-dimensional body. An alternative method of calculating C_F is presented based on the recorded on-body flow state, with comparisons made to experimental flat plate data and Grigson's(23) flat plate friction line. The second part of this chapter will examine results of C_R including coupling to the results of C_F . The coupling of the two coefficients is a function of their relation through the fundamental extrapolation equation, $C_T = C_F + C_R$.

5.2 Direct Determination of the Model Scale Friction Coefficient

In Chapter 1 the concept of basing model scale on flat plate Re_θ values was introduced and demonstrated through Figures 1.1 and 1.2. This provided a means of establishing where the limits may lie, with respect to model scale, for the testing of the IACC yacht model. It was shown from the extrapolated drag and lift data in Chapter 3, in Figures 3.4 and 3.5 respectively, that stable trends existed for experimental data from the model scale ($\lambda = 8$) resulting from the established limits. This nicely supports the suggestion that the empirical method is a useful first pass tool in defining a suitable model scale for a known range of test speeds and facility limitations.

The hot-film data in Chapter 4 showed that for the $1/8^{th}$ model fitted with studs, transition can be expected to occur from behind the studs from the highest to lowest speeds tested. The transition behaviour is clearly shown in Figure 4.13 where at each of the hot-film measurement locations aft of the studs (4, 3, 2 and 1) there were levels of intermittency of one; with a value of one indicating fully turbulent flow.

Traditionally, indeed even within the forces and moments section of this thesis, estimation of C_F is undertaken using equations based on regression analysis of tank test results on flat plates. For this work estimation of C_F used Grigson's(23) flat plate friction line (see Section 1.3 for details of Grigson's method and its application). The addition of a form factor, based on Prohaska's(39) method, was included in the extrapolation process in an attempt to better account for three-dimensional effects. Generally these equations rely solely on the model's waterline length to give a length based Reynolds number, with the length scale being the static or dynamic waterline length. The assumptions tend to work best on slender hull-forms, which are the closest to flat plates. This effect was clearly shown in Section 3.3 where as the model heeled and became more slender the form factor

decreased; i.e. the three-dimensional effects on drag reduced as the model became more like a flat plate. This says that for yacht testing, if using slender hull forms, particularly when heeled, which is the upwind case, that it may be possible to use traditional methods to calculate C_F . However, when the vessel is upright, or of a fuller form a different approach is needed. This is also the case for a hull with a submerged transom, for which Prohaska's(39) method is not ideally suited.

So what can be done to improve the C_F estimation? The simplest answer is to directly calculate the value from the flow over the model. The first technique considered was to use stereo particle image velocimetry (SPIV) as undertaken by Marquardt(31). This methodology introduces a number of technical challenges including health and safety restrictions associated with the use of lasers, particle seeding in a model test facility as well as the transformation of the particle velocity data to values of C_F . While none of these challenges are insurmountable, they add significant complication to the test program and are not easy to integrate into a typical commercial test program. As an alternative experimental method, direct determination of C_F from the hot-films was considered and provided a number of advantages. It required no additional safety procedures to be implemented, had no affect on the operation of the test facility in terms of additional equipment beyond what would be used in routine testing and provided a relatively simple method through which to calculate the C_F values.

The method used to establish the C_f values from the hot-films resembles the process used in computational fluid dynamics; whereby a series of local C_f values are established. The individual values are then combined to give a total C_F value for the model for a given speed. It should be noted that the nomenclature of C_f and C_F is deliberate; with the former describing the local skin friction coefficient where as C_F is the friction coefficient for the entire model. Adapting the technique to use with the data from the glue-on hot-films required a number of discrete steps. First the hull static wetted surface was divided into four longitudinal zones, with associated wetted surface areas. Each zone was bounded at the forward and aft

end by transverse stations located at series of measurement points along the model. The zones and the associated stations are as follows: zone one was bounded by the forward perpendicular (FP) and hot-film 5; zone two by hot-film 5 and hot-film 4; zone three by hot-film 4 and hot-film 2 and zone four by hot-film 2 and the aft perpendicular. Next the proportion of the flow to be considered turbulent was determined using the intermittency information from the hot-films at each longitudinal location. The C_f value was then calculated using flat plate laminar and turbulent equations, Equation 5.1 and Equation 5.2 reproduced from White(43), with a proportional value of C_f being attributed for the amount laminar and turbulent flow found at each location.

$$C_f = 0.664 \times \text{Re}_X^{-\frac{1}{2}} \quad (5.1)$$

$$C_f = 0.027 \times \text{Re}_X^{\frac{1}{7}} \quad (5.2)$$

Where:

C_f is the skin friction coefficient

R_X is Reynolds number using the longitudinal position on the surface

A C_f value for each zone was then calculated as a simple mean of the values obtained at the forward and aft ends of the zone. In doing so this process assumed that the change in intermittency was linear between each successive longitudinal position. The area of each zone was then used to weight the C_f value for the zone to provide values that were then summed to give a total C_F for the model at the particular test condition. This method of calculating C_F was undertaken for both the stimulated and unstimulated cases. For all calculations it was assumed that intermittency and by definition C_F was zero at the forward perpendicular. The results of this analysis procedure have been plotted along with those obtained using Grigson's flat plate friction line, as C_F with variation in Froude number, Figure 5.1.

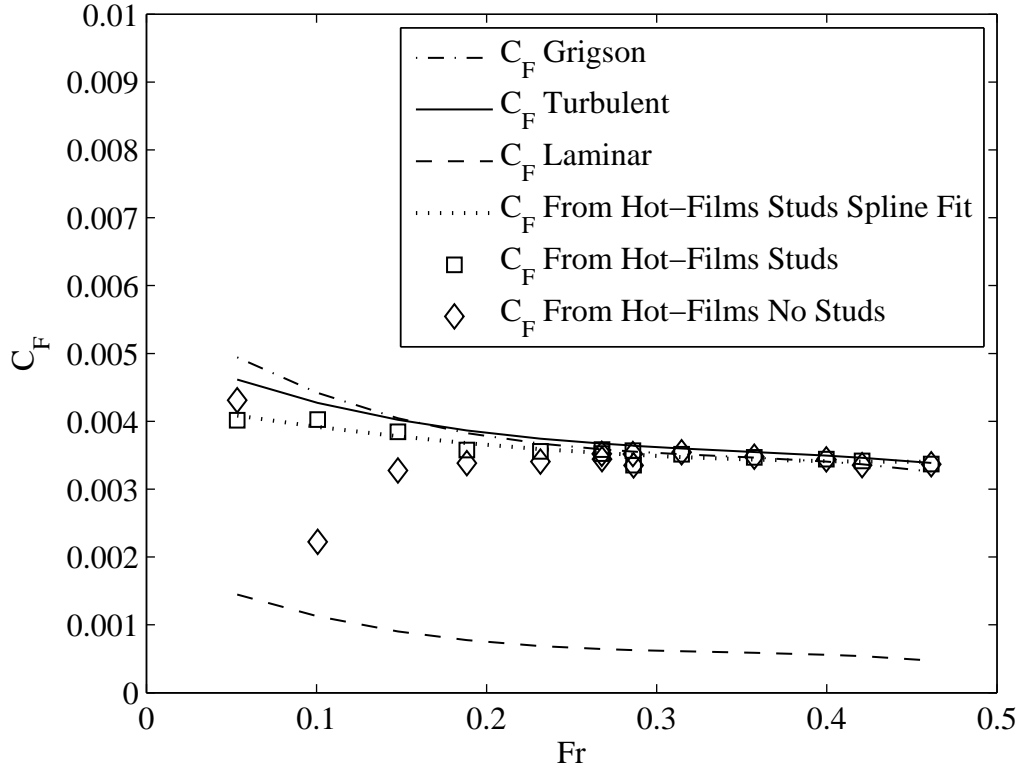


Figure 5.1: Plot of C_F with respect to variation in Froude number (Yaw 1 degrees, Heel 10 degrees, Tab 4 degrees, Rudder 2 degrees). Highlights influence of laminar flow on calculation of C_F .

In trend terms there was agreement, within uncertainty limits, between the C_F values obtained from the hot-film data, Grigson's flat plate friction line and the turbulent flow values for Froude numbers of 0.27 to 0.46. However both the hot-film data and Grigson's flat plate friction line show an offset of the trend lines of approximately 3% as compared to the fully turbulent calculation. The offset is a consequence of the inclusion of natural transition in the Grigson equation and the results from the hotfilms including a small measured amount of laminar flow from the forward end of the vessel. Below a Froude number of 0.27 (model $Re_L = 2.6 \times 10^6$) the divergence of the C_F values of the the hot-film data relative to those obtained from using Grigson's flat plate friction line provides experimental evidence of the limitations of the traditional methods used for estimating C_F . It is important to note that the value of C_F at a Froude number of 0.05 for the unstimulated case is erroneous. As was shown in Figure 4.13 and discussed in the previous chapter, the level of intermittency was incorrectly estimated at a Froude number of

0.05 due to the method assessing the random noise in the signal as turbulent flow. As the C_F value calculated from the experiments used the level of intermittency to determine the proportion of laminar and turbulent flow to be assigned at each location; then the incorrect, high levels of intermittency lead to the incorrect high level of C_F at this speed.

One of the effects of a vessel's hull is to increase the flow velocity around the hull creating a favourable pressure gradient. The variation in pressure distribution along the hull, higher at the bow and stern and lower amidships, causes a peak to form at the bow and stern and a trough to form at amidships. An image of the $1/8^{th}$ scale model under tow at the Australian Maritime College towing tank demonstrating this phenomena is included in Figure 5.2. Although the peaks and trough shown in Figure 5.2 were obvious visually, it was not possible to quantify the effect on C_f from these observations, particularly in comparison to changes in C_f due to transition behaviour.

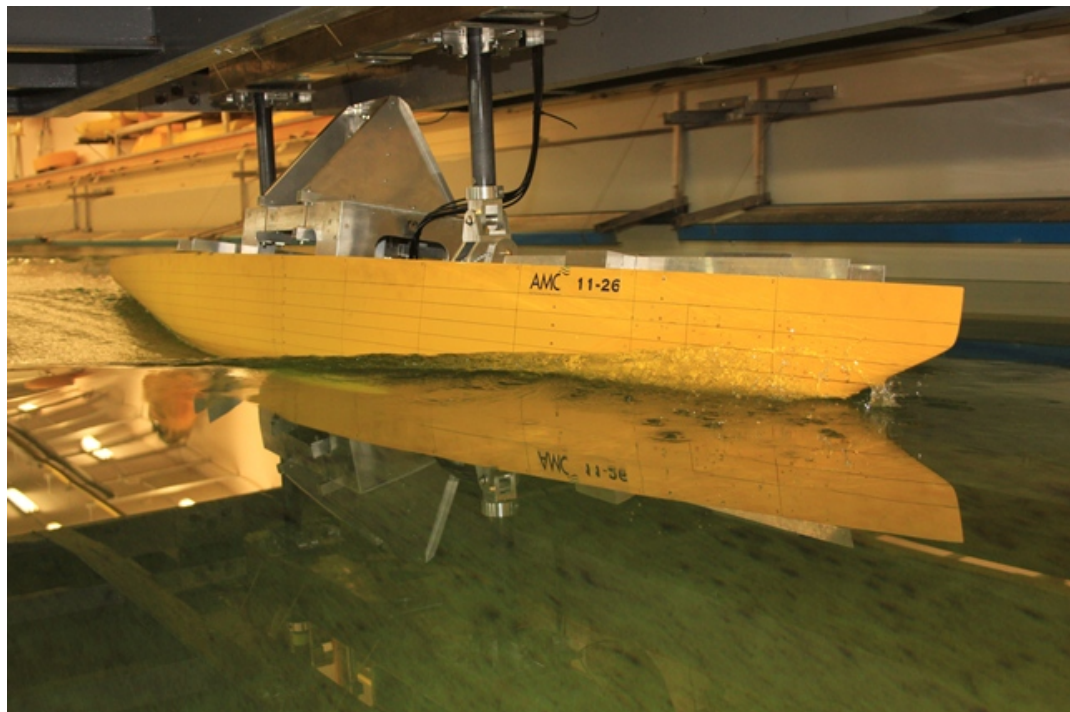


Figure 5.2: $1/8^{th}$ geosim of a v5 IACC yacht being towed at the Australian Maritime College towing tank showing bow and stern waves and a trough amidships.

The influence of the peak and trough wave pattern on C_f was investigated by Marquardt(31), who conducted an extensive survey of the submerged surface of a surface piercing flat plate. The work utilised stereo particle image velocimetry (SPIV) which enabled calculation of a range of flow velocity information including θ values. The tests were undertaken at a carriage velocity of 1.37 m/s which for the $1/8^{th}$ scale IACC model equates to a Froude number of 0.27. Marquardt(31) recorded measurements at a number of cross-sections vertically and longitudinally. There were two conditions tested, one in calm water and one with a generated Stokes wave. The Stokes wave was generated by a submerged foil and had a peak at the leading and trailing edge of the plate and trough aligned with the middle of the plate. For both cases θ values ranged from ≈ 0.001 at 25% aft of the leading edge of the plate to ≈ 0.002 at 75% aft. These θ values equate to $Re_\theta = 1234$ and $Re_\theta = 2501$ respectively. As these values are an order of magnitude larger than $Re_\theta = 320$, the theoretical lower limit below which there is insufficient energy in the boundary layer to enable the flow to remain fully turbulent Preston(38), then the flow was certainly fully turbulent.

Marquardt(31) also provides C_f values for both the calm water and the Stokes wave case. The C_f values for the no wave case ranged from approximately 4.4×10^{-3} at the 25% aft location, 4.1×10^{-3} at the 50% aft location and 3.6×10^{-3} at the 75% aft location. With the Stokes wave C_f ranged from 4.4×10^{-3} at the 25% aft location, 4.5×10^{-3} at the 50% aft location and 3.5×10^{-3} for the 75% aft location. The Marquardt data as well as the turbulent and hot-film generated values of C_f have been combined and plotted in Figure 5.3.

With respect to non-dimensional length, the C_f values calculated by Marquardt show two trends. The first is that the inclusion of a wave increases C_f and the second is that C_f reduces with longitudinal position. The increase in C_f with a wave trough ($\approx 5 \times 10^{-4}$), is a reflection of the increased flow velocity in the trough. At the forward and aft measurement points, located at 25% and 75% aft, the wave height of the Stokes wave was equal to the calm water level. As such the flow

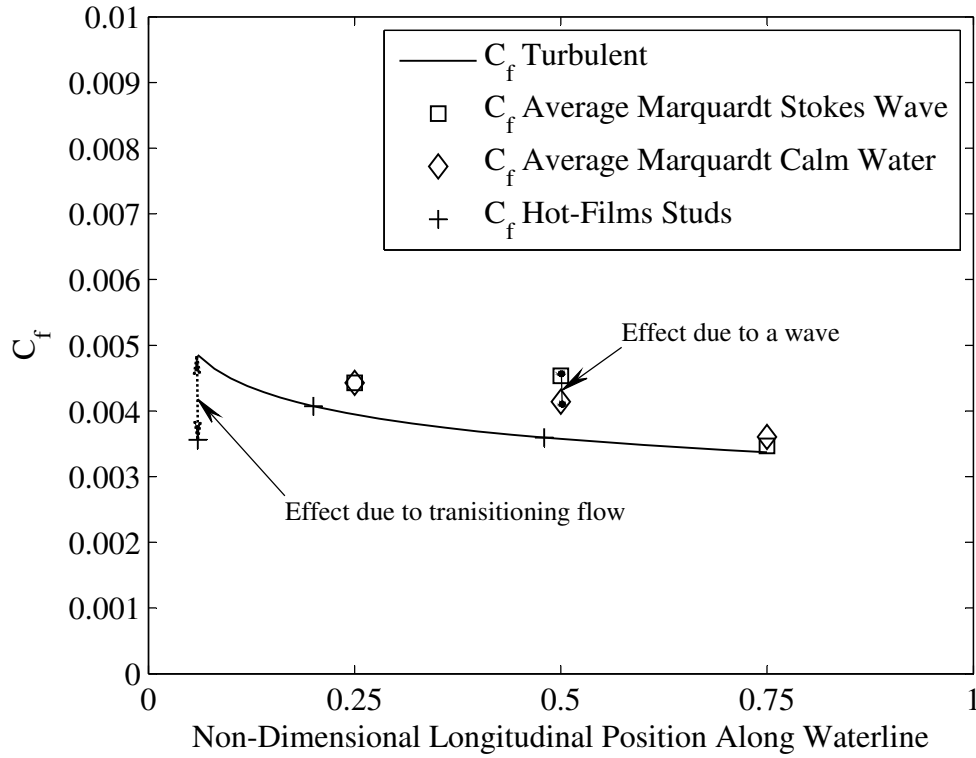


Figure 5.3: Plot of C_f with respect to variation in non-dimensional longitudinal position for a model test speed of 1.36 m/s (Froude number of 0.29) for both $1/8^{th}$ scale model and a flat plate. Shows the relative changes due to a large wave and changes due to transitioning flow. Note that a non-dimensional length of 0 indicates the forward perpendicular and 1 the aft perpendicular.

velocity and consequently the value of C_f were the same with and with out a wave at these two locations.

The variation of C_f due to a large wave (wave height was 18.5% of the draft of the plate) is clear from Marquardt's work; however the magnitude of the changes, 5×10^{-4} , were only half of the change due to natural transition 1×10^{-3} , Figure 5.3. This shows that transition behaviour has a greater impact on the value of C_f than hull generated waves; highlighting that quantifying the behaviour of the on body flow is critical to the selection of model scale.

5.3 Influence of Friction Coefficient on the Residuary Resistance Coefficient

The following discussion is separated into high and low speed comparisons. The delineating speed for the ‘high’ and ‘low’ speed ranges is a Froude number of 0.35; this is the point at which the wave making drag of vessel begins to increase dramatically as shown previously in Figure 3.4(a).

5.3.1 High-Speed Comparison

As part of the extrapolation procedure a stud correction factor was included which aimed to account for the increase in drag due to the studs. The expectation of the technique is that the results from two separate tests, one with and one without studs, the resulting value of C_R would be the same as long as the with out studs case had developed turbulent flow. It was shown previously from the intermittency levels, Figure 4.13, that at Froude numbers of at least 0.35 the on-body flow was fully turbulent for both the with and without stud cases. As such, the agreement within uncertainty at high-speeds between the C_R values for the with and without stud cases, Figure 5.4, indicates that the stud correction technique was successful.

The C_F values obtained using the hot-film data, Figure 5.1, were consistent between the with and with out studs cases for the high speeds. All values were an order of magnitude smaller than C_R , highlighting the relatively small influence of the friction component of resistance at these speeds.

5.3.2 Low-Speed Comparison

At low-speeds, C_R values for the with and without stud cases were found to be in agreement within uncertainty levels, Figure 5.4, except for the lowest Froude

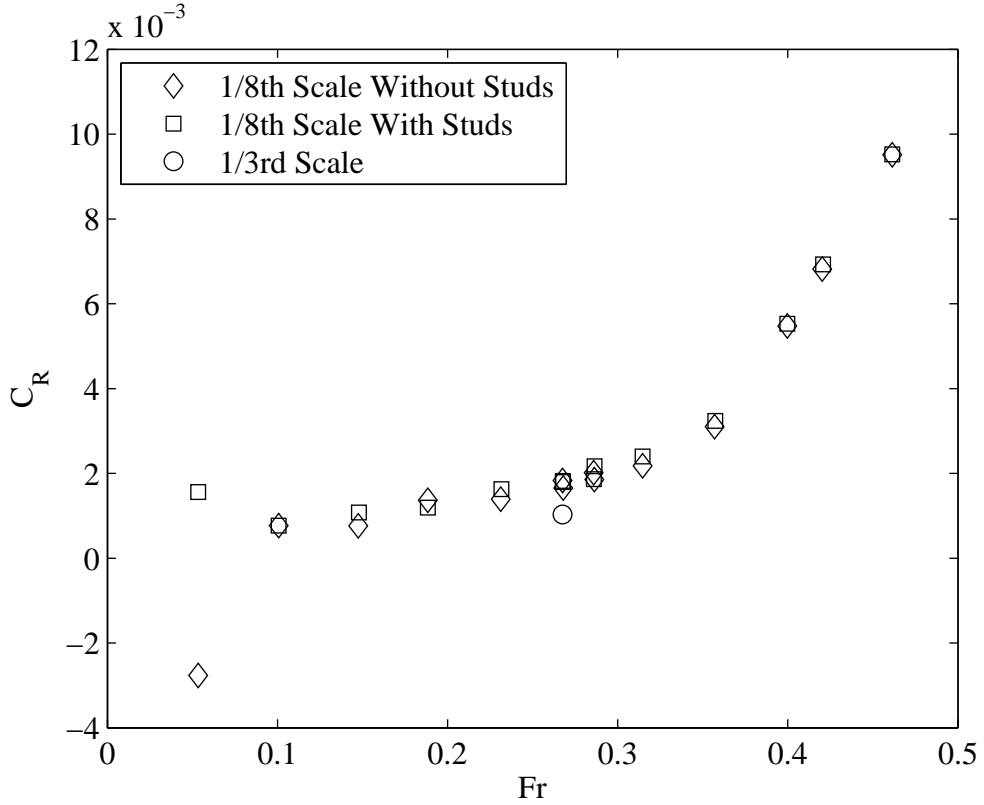


Figure 5.4: Plot of C_R with respect to variation in Froude number (Yaw 1 degrees, Heel 10 degrees, Tab 4 degrees, Rudder 2 degrees).

number. It was shown previously from the intermittency levels, Figure 4.13, that apart from the lowest Froude number the on-body flow was fully turbulent for the with studs case. As seen in the high speed cases, the existence of fully turbulent flow implies that if the stud correction factor was correct then C_R should be the same for both the with and without stud runs. This was indeed the case except for the lowest speed which was shown to have a large portion of laminar flow on the forward sections of the model. The difference in C_R values of 4.0×10^{-3} , between the with and without studs case at Froude number 0.05 is a consequence of using the Grigson flat plate friction line when laminar flow exists. Laminar flow reduces the measured drag value, or drag coefficient (C_T) in non-dimensional terms, relative to a run with turbulent flow. When the C_F value obtained using Grigson's flat plate friction line, which is the same value for both the stimulated and unstimulated cases, is subtracted from C_T the resultant lower C_R value reflects the lower C_T .

Poor correlation was found between the C_R values for the $1/3^{rd}$ and $1/8^{th}$ results; with the $1/3^{rd}$ values 44% less than the $1/8^{th}$ values. This difference is significant in terms of the extrapolation procedure as C_R is considered to be scale independent when undertaking the extrapolation procedure. Extensive checking of the data, both supplied and experimentally obtained, as well as the analysis did not show a reason for this difference.

There is a clear discrepancy in C_F obtained using the hot-film data, between the with and without stud cases below Froude number of 0.20, Figure 5.1. As such studs are necessary to ensure correct values of C_F are calculated from the hot-film data. The high C_F value at a Froude number of 0.05 for the no studs case is erroneous due to a low-signal to noise ratio. It has been shown previously that at this speed the flow is laminar and thus the calculated C_F value, based on the flat plate C_F calculation, should not exceed 1.5×10^{-3} .

5.4 Chapter Summary

The two primary dependant variables of the drag extrapolation procedure, friction coefficient C_F and residuary resistance coefficient C_R have been investigated. An alternative method of calculating C_F was presented based on the recorded on-body flow state, with comparisons made to experimental flat plate data and Grigson's flat plate friction line. Results of C_R including coupling to the values obtained for C_F have been made.

In trend terms there was excellent agreement between the C_F values obtained from the hot-film data, Grigson's flat plate friction line and the turbulent flow values from a Froude number of 0.27 to 0.46. However both the hot-film data and Grigson's flat plate friction line show an offset of the trend lines of approximately 3% as compared to the fully turbulent calculation.

The lower limits of applicability of the Grigson flat plate friction line have been examined experimentally. For the $1/8^{th}$ scale model tested these limits lie at a model $Re_L = 2.6 \times 10^6$ (Froude number of 0.27) as opposed to that reported in his paper as $Re_L = 1.5 \times 10^6$ (Froude number of 0.15). Below $Re_L = 2.6 \times 10^6$ the values of C_F increased relative to those obtained from using the hot-film data.

The influence of the primary wave system was examined with the C_f from the current tests being compared to experimental flat plate data using SPIV from literature. It was possible to see the influence of a wave on C_f , with a change of 5×10^{-4} ; but this was only half of the change due to natural transition, 1×10^{-3} .

For Froude numbers of 0.35 and above, C_R for both the with and without stud cases for the $1/8^{th}$ scale experiments were the same within uncertainty levels. At Froude numbers below 0.35 the C_R values for both the with and without stud cases were found to be in agreement within uncertainty levels, except for the lowest Froude number of 0.05. Poor correlation was found with the $1/3^{rd}$ results, with extensive checking of the data and analysis methodology providing no source of this difference.

Chapter 6

Conclusions

Within the yacht testing community there has been a continuing interest in and concern with, the effectiveness of the techniques used to extrapolate model scale resistance tests to full scale values. While there are many aspects which influence the effectiveness of scaling results from model yacht experiments; this thesis has investigated the use of hot-films to characterise boundary layer state so as to provide guidance in selection of model scale.

6.1 Experimental Outcomes

As a foundation to the research, a series of experiments were conducted on both $1/3^{rd}$ and $1/8^{th}$ geosims of a fully appended IACC yacht. The experimental data was recorded for a matrix of test cases including variation of: velocity, yaw angle, heel angle, trim tab angle and rudder angle. In addition, the $1/8^{th}$ experiments were also conducted both with and without turbulence stimulation.

6.1.1 Drag

The change in non-dimensional drag (C_D) with respect to speed was seen to be quadratic for the $1/8^{th}$ tests from a Froude number of 0.10 to 0.46 with the $1/3^{rd}$ value at a Froude number of 0.27 being approximately 15% less. For a Froude number of 0.05, C_D increased for the $1/8^{th}$ case with studs as compared with the $1/8^{th}$ case without studs. These changes are possibly due to underestimation of the

contribution of the studs to drag and laminar flow respectively. It was also shown that C_D increased between 0-4% for each two degrees of additional trim tab angle for both the $1/8^{th}$ and $1/3^{rd}$ geosims with the $1/3^{rd}$ values being between 15% and 21% less than the $1/8^{th}$ values.

6.1.2 Lift

Lift was shown to change linearly with change in angle of attack; whether due to change in yaw or trim tab angle. For Froude numbers greater than 0.10 non-dimensional lift (C_L) changed approximately linearly for the $1/8^{th}$ data, with the $1/3^{rd}$ values matching within uncertainty levels. For Froude numbers of 0.05 and 0.10 there was a difference of 10% and 15% respectively between the $1/8^{th}$ with and without stud cases. C_L was also shown to be linear with increasing trim tab angle for both $1/8^{th}$ and $1/3^{rd}$ data, with agreement between results being within uncertainty levels.

6.1.3 Hot-films

During the tests for force and moments, flow regime data was collected for the $1/8^{th}$ scale model via sensors attached to the exterior of the hull. The sensors provided the necessary information to describe the flow in qualitative, time and frequency domain voltage values, as well as quantitative values described in terms of intermittency.

As part of the process it was necessary to develop a robust hot-film installation technique as well as adapt an existing intermittency analysis technique to suit the specifics of model testing. Intermittency calculations were undertaken using a method based on the kurtosis of the hot-film signal including the development of an alternative method to establish the high-pass filter value required by the method. No calibration of the glue-on hot-films was undertaken due to the potential damage during the removal and re-application of the films required to undertake calibration. Throughout the testing all hot-films continued to work highlighting the robustness of both the installation and experimental procedure.

Velocity, heel angle and yaw angle were all shown to affect the level of turbulence on the model's fore body region for the unstimulated cases; but only a change in yaw angle was able to influence the flow for both the stimulated and unstimulated cases. Trim-tab and rudder angle were shown to have no affect on the turbulence levels.

For all Froude numbers tested (0.05-0.46) at each of the five measurement locations, there was transitioned flow when turbulence stimulation was used. For the two lowest Froude numbers tested, 0.05 and 0.10, the analysis method incorrectly described the flow state for the no stud case which was a function of a low signal to noise ratio. Without studs fitted several observations were made. Laminar flow was observed at and below Froude numbers of 0.1 for all measurement locations. Partial laminar flow was observed to exist at hot-film five (6% aft of the forward perpendicular) and four (20% aft of the forward perpendicular), for Froude numbers between 0.10 and 0.29. For Froude numbers from 0.29 and above, the flow was fully turbulent except at hot-film five.

The reduction in intermittency with increased heel angle for the unstimulated cases, approximately 17% at hot-film four, may have been a function of a changed pressure gradient due to accelerated flow. It is also possible that local wave behaviour contributed to the change in intermittency as the two measurement points where the effect was measured, were the forward most points and were both in the region of the bow wave.

A one degree increase in yaw angle was shown to increase the level of intermittency by approximately 30% at the forward most measurement point, hot-film five, for both the stimulated and unstimulated cases. This was a function of the cross sectional shape, at this position along the vessel, increasing the transverse flow velocity and thereby increasing the energy in the flow. At hot-films three, two and one, all located at 50% aft of the forward perpendicular, the difference in intermit-

tency levels between the three transverse locations are within uncertainty. This is due to the flow being fully developed at this location.

6.1.4 Correlation

The two primary dependent variables of the drag extrapolation procedure, friction coefficient (C_F) and residuary resistance coefficient (C_R) were investigated. An alternative method of calculating C_F was presented based on the recorded on-body flow state, with comparisons made to experimental flat plate data and Grigson's flat plate friction line. Results of C_R including connections to the values obtained for C_F were made.

In trend terms there was excellent agreement between the C_F values obtained from the hot-film data, Grigson's flat plate friction line and the turbulent flow values from a Froude number of 0.27 to 0.46. Both the hot-film data and Grigson's flat plate friction line showed a reduction in C_F of approximately 3% as compared to the fully turbulent calculation.

The lower limits of applicability of the Grigson flat plate friction line have been examined experimentally. For the $1/8^{th}$ scale model tested these limits lie at a model $Re_L = 2.6 \times 10^6$ (Froude number of 0.27) as opposed to that reported in his paper as $Re_L = 1.5 \times 10^6$ (Froude number of 0.15).

The influence of the primary wave system was examined with the C_f from the current tests being compared to experimental flat plate SPIV data from literature. It was possible to see the influence of a wave on C_f , with a change of 5×10^{-4} ; but this was only half of the change due to natural transition, 1×10^{-3} .

For Froude numbers of 0.35 and above, C_R for both the with and without stud cases for the $1/8^{th}$ scale experiments were the same within uncertainty levels. At Froude numbers below 0.35 C_R values for both the with and without stud cases were found to be in agreement within uncertainty levels, except for the lowest

Froude number of 0.05. The $1/3^{rd}$ results were 44% less than the $1/8^{th}$ scale data; extensive checking of the data and analysis methodology provided no clear source for this difference.

6.2 Guidance for Scaling

With turbulence stimulation the on-body flow became fully turbulent for all Froude numbers tested, which implies that with appropriate boundary layer stimulation, the state of the boundary layer is not a limiting factor in the testing of a $1/8^{th}$ scale IACC yacht model.

The lower limits of applicability of the Grigson flat plate friction line have been examined experimentally. For the $1/8^{th}$ scale model tested these limits lie at a model $Re_L = 2.6 \times 10^6$ (Froude number of 0.27) which is higher than reported in his paper, $Re_L = 1.5 \times 10^6$ (Froude number of 0.15). Also, the change in C_f due to waves generated by the hull was demonstrated to be half that due to natural transition.

It has been demonstrated that it is possible to use a simple analytical approach to determine the correct model scale for a yacht hull-form as long as it is slender, with fair lines and no immersed transom and testing is at model speeds above 1.28 m/s (Froude number of 0.27). If there is concern that there might be an issue with transition behaviour it has been shown that it is possible and relatively simple to use hot-films to verify the boundary layer state.

Chapter 7

Further Work

In a research program it is inevitable that there will be items which, with benefit of hindsight, may have been approached differently. Reflecting upon the work of this thesis a number of items of interest were revealed; which have been loosely separated into two groups; important or desirable.

The two key areas of further work to address would be to find a method to calibrate the hot-films in-situ and also to re-do the $1/3^{rd}$ tests with hot-films. The development of a means of calibrating the hot-films would enable direct calculation of the shear stress from the measured on-body flow; while the testing at $1/3^{rd}$ scale would be both interesting from an academic and operational perspective. While it may seem desirable to test with a smaller model to help establish the minimum scale, the author believes that the $1/8^{th}$ is the smallest size model to be feasible for the tests conducted. This limit is due to the physical limitations that smaller models impose. This is especially the case for the foils and their operation and the installation of the hot-film sensors where, even at $1/8^{th}$ scale, access into the model for installation of the hot-films was restricted. Through obtaining experimental data at $1/3^{rd}$ scale a much more detailed comparison of the flow behaviour due to scale would be possible. This is especially important in light of the findings with regard to the importance of turbulence stimulation on ensuring that the

flow has fully transitioned. From an operational stand point it would be interesting to see whether the techniques used with the hot-films that were successful at $1/8^{th}$ scale, installation and operational, are also relevant to the larger models or whether there are factors that might hamper their use on such models. This is of particular interest to the author as one of the tenets of the work was to ensure that any techniques developed should be suitable for use in a commercial testing environment. It would also be instructive while undertaking these measurements to record the levels of background turbulence within the towing tank. While normal test methods attempt to maintain consistency across a series of tests, for example maintaining a consistent interval between runs, it would be very useful to be able to gather information of one of the key external influences on transition.

There were a number of items that fall into what might be best described as desirable. Throughout the data analysis some of the limitations of the test matrix selected became obvious. The test matrix used was based on that of the supplied $1/3^{rd}$ data which had been originally planned to be used as an input into a velocity prediction program. As such the test matrix covers a large part of the design space; but in less detail than would be ideal for research purposes. With the hindsight provided from the $1/8^{th}$ scale test results the first priority for additional runs would be to undertake additional heel and yaw sweeps as these were the two variables that were shown to have an influence on transition. The addition of surface pressure sensors would also provide useful data to help quantify the pressure gradients around the hull, potentially providing experimental confirmation of some of the hypotheses of this thesis. These tests and the $1/3^{rd}$ tests could be further leveraged if PIV was utilised to examine the flow around the body, especially downstream of the keel. Care would be required in particle sizing so as to capture the near body flow behaviour and the far field data. If possible PIV measurements should be taken at the same time as the hot-film data to provide greater certainty in the comparisons between techniques.

Experiments utilising flat plates were evaluated at the early stages of the research

program. After consideration they were deemed to add too much time, complexity and cost to the test program while not providing any data for heel and yawed models. This is especially pertinent with the knowledge obtained from the $1/8^{th}$ model that heel and yaw had noticeable influence on transition behaviour. Notwithstanding this knowledge; a set of experiments using the PIV techniques outlined in the work of Marquardt(31), along with hot-film and drag measurements on a parametric set of flat plates, would add to the research community. This data would have significant value beyond scaling as it would provide an extremely detailed set of data for validation of CFD calculations.

As a longer term project it would be instructive to see whether computational fluid dynamics is able to replicate the measured results. With the ever increasing computer power it may be possible to undertake a detailed study of the flow. The computational resources required are likely to be vast as an investigation of this kind should include detailed modelling of the boundary layer.

References

- [1] Abu-Ghannam, B. J. & Shaw, R. Natural transition of boundary layers - the effects of turbulence, pressure gradient, and flow history. *Journal of Mechanical and Engineering Science*, volume 22:pages 213–228, October 1980
- [2] Armstrong, N. *On the Viscous Resistance and Form Factor of High-Speed Catamaran-Ferry Hull Forms*. Phd, The School of Mechanical and Manufacturing Engineering, 2000
- [3] Atencio, B. *Measurements and Prediction of Laminar-Turbulent Transition at High Free-Stream Turbulence in Boundary Layers with Pressure Gradients*. Masters, Chalmers University of Technology, 2011
- [4] Binns, J. *Extreme motions of modern sailing yachts - quantifying re-righting*. Phd, Australian Maritime College, Engineering, 2005
- [5] Binns, J., Albina, F., & Burns, I. Looking for ‘laminars’: Measuring intermittency on the america’s cup race course. *Experimental Thermal and Fluid Science*, volume 33(5):pages 865–874, 2009
- [6] Bose, N. *Marine Powering Prediction and Propulsors*. Society of Naval Architects and Marine Engineers, New Jersey, 2008
- [7] Brown, P. & Savitsky, D. Some correlations of 12 Metre model test results. In *18th International Towing Tank Conference*. SNAME, Kobe, Japan., 1987
- [8] Campbell, I. & Claughton, A. The interpretation of results from tank tests on 12m yachts. In *The 8th Chesapeake Sailing Yacht Symposium*. SNAME, Annapolis, Maryland., 1987

- [9] Clarke, D. B., Brandner, P., & G.J., W. Computational and experimental investigation of flow around a 3-1 prolate spheroid, December 2007
- [10] Clayton, B. R. & Massey, B. S. Flow visualization in water: A review of techniques. *Journal of Scientific Instruments*, volume 44(1), 1967
- [11] Date, J. C. & Turnock, S. R. Computational fluid dynamics estimation of skin friction experienced by a plane moving through water. *Transactions of the Royal Institute of Naval Architects*, volume 142:page 20, 2000
- [12] Debord Jr, F., Kirkman, K., & Savitsky, D. D. The evolving role of the towing tank for grand prix sailing yacht design. In *27th American Towing Tank Conference*, page 7. St. Johns, Newfoundland and Labrador, Canada, 2004
- [13] Debord Jr, F., Reichel, J., Rosen, B., & Fassardi, C. Design optimization for the international americas cup class. *SNAME Transactions*, volume 110:pages 31–53, 2002
- [14] Debord Jr, F. & Teeters, J. Accuracy, test planning and quality control in sailing yacht performance model testing. In *New England Sailing Yacht Symposium*. New London, Connecticut, 1990
- [15] Dyer, T. Turbulence stimulation on yacht models. In *15th American Towing Tank Conference*, volume 3. Ottawa, Canada, 1968
- [16] Dynamics, D. Probes for hot-wire anemometry, 2011
 URL http://www.dantecdynamics.com/Admin/Public/DWSDownload.aspx?File=%2fFiles%2ffiler%2fProducts+and+Services%2fGeneral+literature%2fHot-wire_catalog_238.pdf
- [17] Efron, B. & Tibshirani, R. J. *An introduction to the bootstrap*. Chapman and Hall, 1993
- [18] Fassardi, C. Tank testing and data analysis techniques for the assessment of sailboat hydrodynamics characteristics. In *High Performance Yacht Design Conference*, page 9. Auckland, New Zealand, 2002

- [19] Froude, W. Observations and suggestions on the subject of determining by experiment the resistance of ships, 1868
- [20] Froude, W. Experiments on the surface-friction experienced by a plane moving through water, August, 1872
- [21] Froude, W. The fundamental principles of the resistance of ships, May, 1876
- [22] Froude, W. Experiments upon the effect produced on the wave-making resistance of ships by length of parallel middle body, March, 1877
- [23] Grigson, C. A planar friction algorithm and its use in analysing hull resistance. *Transactions of the Royal Institute of Naval Architects*, volume 142, 2000
- [24] Hutchison, C., Binns, J., Duffy, J., & Brandner, P. Model testing - what is the point? a review of yacht testing and the implications for yacht designers. In *Proceedings of the 4th International High Performance Yacht Design Conference*, pages 119–125. RINA, 2012
- [25] ITTC. Testing and extrapolation methods, resistance, uncertainty analysis spreadsheet for resistance measurements. *Recommended Procedures and Guidelines*, volume 7.5-02-02-03, 2002
- [26] ITTC. Testing and extrapolation methods, general, density and viscosity of water. *Recommended Procedures and Guidelines*, volume 7.5-02-01-03, 2006
- [27] ITTC. Testing and data analysis resistance test. *Recommended Procedures and Guidelines*, volume 7.5-02-02-01, 2008
- [28] Kirkman, K. L. Scale experiments with the 5.5 metre yacht antiope. In *The Chesapeake Sailing Yacht Symposium*. SNAME, Annapolis, Maryland., 1974
- [29] Koyabu, E. & Tsukiji, T. Wake-induced bypass transition over a flat plate under favorable and adverse pressure gradients. *JSME International Journal*, volume 48(3), 2005
- [30] Larsson, L. Scientific methods in yacht design. *Annual Review of Fluid Mechanics*, volume 22(1):pages 349–385, 1990

- [31] Marquardt, M. *Effects of waves and the free surface on a surface piercing flat-plate turbulent boundary layer and wake*. Master's thesis, Graduate College, 2009
- [32] McCarthy, J., Power, J., & Huang, T. The roles of transition, laminar separation, and turbulence stimulation in the analysis of axisymmetric body drag. In *Eleventh ONR Symposium on Naval Hydrodynamics*, pages 69–95. Mechanical Engineering Publications Ltd, London, 1976
- [33] Merzkirch, W. *Flow Visualization*. Academic Press, Orlando, 2nd edition, 1987. ILL from RMIT University 620.1064 M577 2ND ED
- [34] Molland, A., Wellicome, J., & Couser, P. Resistance experiments on a systematic series of high speed displacement catamaran forms: variation of length-displacement ratio and breadth-draught ratio. Technical report, University of Southampton, 1994. Contains a method to account for stud drag
- [35] Murdey, D., Molyneux, W., & Killing, S. Techniques for testing sailing yachts. In *International Towing Tank Conference*. SNAME, Kobe, Japan., 1987
- [36] Parsons, B. & Pallard, R. The institute for marine dynamics model yacht dynamometer. In *The Thirteenth Chesapeake Sailing Yacht Symposium*. Annapolis, Maryland, 1997
- [37] Perry, A. E. Hot-wire anemometry - introduction. In *Hot-Wire Anemometry*. Clarendon Press, Oxford, 1982
- [38] Preston, J. The minimum reynolds number for a turbulent boundary layer and the selection of a transition device. *Journal of Fluid Mechanics*, volume 3(04):pages 373–384, 1958
- [39] Prohaska, C. A simple method for the evaluation of the form factor and the low speed wave resistance. In *11th International Towing Tank Conference*. SNAME, Tokyo, 1966
- [40] Solomon, W. *Unsteady Boundary Layer Transition on Axial Compressor Blades*. Phd, University of Tasmania, 1996

- [41] Townsin, R. Results from the use of an unobtrusive technique during ship model testing. *Transactions of the Royal Institute of Naval Architects*, volume 102:pages 192–201, 1960
- [42] van Oossanen, P. Predicting the speed of sailing yachts. In *Proceedings of the 1993 Annual Meeting of the Society of Naval Architects and Marine Engineers*, volume 101, page 61. 1993
- [43] White, F. *Fluid Mechanics*. McGraw-Hill Higher Education, Boston, 5th edition, 2003

Appendix A

Test Program

The table below provides the complete list of the test runs included in the force, moment and hot-film analyses of the $1/8^{th}$ scale model. The choice of the specific test conditions was based around the data supplied from the $1/3^{rd}$ tests such that wherever possible they matched those from the $1/3^{rd}$ tests. Unfortunately due to some of the specific rudder, heel and vertical force specified in the supplied data there was less overlap in the results than would have been desired.

Condition	Details	Run #	Date	Time	Water Temperature	Set Speed	Yaw Angle	Heel Angle	Tab Angle	Rudder Angle
					degrees C	m/s	degrees	degrees	degrees	degrees
5	Speed Sweep	105	11/07/2012	10:05	15.80	0.26	1	10	4	2
5	Speed Sweep	106	11/07/2012	10:14	15.80	0.48	1	10	4	2
5	Speed Sweep	107	11/07/2012	10:24	15.80	0.71	1	10	4	2
5	Speed Sweep	108	11/07/2012	10:35	15.80	0.90	1	10	4	2
5	Speed Sweep	109	11/07/2012	10:46	15.80	1.11	1	10	4	2
5	Speed Sweep	111	11/07/2012	11:00	15.80	1.28	1	10	4	2
5	Speed Sweep	114	11/07/2012	11:42	15.80	1.37	1	10	4	2
5	Speed Sweep	115	11/07/2012	11:53	15.80	1.51	1	10	4	2
5	Speed Sweep	116	11/07/2012	12:07	15.80	1.71	1	10	4	2
5	Speed Sweep	117	11/07/2012	12:19	15.8	1.92	1	10	4	2
5	Speed Sweep	118	11/07/2012	12:32	15.80	2.02	1	10	4	2
5	Speed Sweep	119	11/07/2012	12:44	15.80	2.21	1	10	4	2
5	Speed Sweep	123	11/07/2012	13:49	15.80	1.28	1	10	4	2
5	Speed Sweep	124	11/07/2012	14:04	15.80	1.37	1	10	4	2
6	Incorrect Model Set-up									
7	Incorrect Model Set-up									
8		125	11/07/2012	14:18	15.80	1.92	1	0	0	0
8		126	11/07/2012	14:28	15.80	1.92	1	0	-2	0
8		128	11/07/2012	14:50	15.80	1.92	0	0	0	0
8		129	11/07/2012	15:02	15.80	1.92	0	0	2	0
8		130	11/07/2012	15:12	15.80	1.92	0	0	4	0
8		131	11/07/2012	15:25	15.80	1.92	-1	0	4	0
8		132	11/07/2012	15:35	15.80	1.92	-1	0	2	0

continued on next page

continued from previous page

Condition	Details	Run #	Date	Time	Water Temperature	Set Speed	Yaw Angle	Heel Angle	Tab Angle	Rudder Angle
					degrees C	m/s	degrees	degrees	degrees	degrees
8		133	11/07/2012	15:45	15.80	1.92	-1	0	0	0
8		134	11/07/2012	15:55	15.80	1.92	-1	0	-2	0
8		135	11/07/2012	16:10	15.80	1.92	-2	0	4	0
8		209	13/07/2012	12:01	15.95	1.92	0	0	-2	0
9		136	11/07/2012	16:24	15.80	1.37	-2	5	4	4
9		137	11/07/2012	16:34	15.80	1.37	-2	5	6	2
9		138	11/07/2012	16:44	15.80	1.28	-2	5	6	2
9		139	11/07/2012	16:55	15.80	1.28	-2	5	8	2
9		140	11/07/2012	17:05	15.80	1.37	-2	5	8	2
9		141	11/07/2012	17:20	15.80	1.28	0	5	8	2
9		142	11/07/2012	17:30	15.80	1.37	0	5	8	2
9		143	11/07/2012	17:40	15.80	1.37	0	5	6	2
9		144	11/07/2012	17:50	15.80	1.28	0	5	6	2
9		145	11/07/2012	18:01	15.80	1.28	0	5	4	2
9		146	11/07/2012	18:10	15.80	1.37	0	5	4	2
9		147	12/07/2012	08:55	15.90	1.37	1	5	4	2
9		148	12/07/2012	09:05	15.90	1.28	1	5	4	2
9		149	12/07/2012	09:15	15.90	1.28	1	5	6	2
9		150	12/07/2012	09:25	15.90	1.37	1	5	6	2
9		151	12/07/2012	09:36	15.90	1.37	1	5	8	2
9		152	12/07/2012	09:46	15.90	1.28	1	5	8	2
10		153	12/07/2012	10:00	15.90	1.37	1	10	8	2
10		154	12/07/2012	10:10	15.90	1.28	1	10	8	2
10		155	12/07/2012	10:20	15.90	1.28	1	10	6	2
10		156	12/07/2012	10:30	15.90	1.37	1	10	6	2
10		157	12/07/2012	10:40	15.90	1.37	1	10	4	2

continued on next page

continued from previous page

Condition	Details	Run #	Date	Time	Water Temperature	Set Speed	Yaw Angle	Heel Angle	Tab Angle	Rudder Angle
					degrees C	m/s	degrees	degrees	degrees	degrees
10		158	12/07/2012	10:50	15.90	1.28	1	10	4	2
10		159	12/07/2012	11:02	15.90	1.28	0	10	4	2
10		160	12/07/2012	11:13	15.90	1.37	0	10	4	2
10		161	12/07/2012	11:23	15.90	1.37	0	10	6	2
10		162	12/07/2012	11:33	15.90	1.28	0	10	6	2
10		163	12/07/2012	11:43	15.90	1.28	0	10	8	2
10		164	12/07/2012	11:53	15.90	1.37	0	10	8	2
10		165	12/07/2012	12:04	15.90	1.37	-2	10	8	2
10		166	12/07/2012	12:14	15.90	1.28	-2	10	8	2
10		167	12/07/2012	12:24	15.90	1.28	-2	10	6	2
10		168	12/07/2012	12:33	15.90	1.37	-2	10	6	2
10		169	12/07/2012	12:44	15.90	1.37	-2	10	4	4
11		170	12/07/2012	13:34	15.90	1.65	-2	20	8	3
11		171	12/07/2012	13:44	15.90	1.65	-2	20	8	5
11		172	12/07/2012	13:54	15.90	1.65	-2	20	8	6
11		173	12/07/2012	14:04	15.90	1.65	-2	20	10	6
11		174	12/07/2012	14:15	15.90	1.56	-2	20	10	6
11		175	12/07/2012	14:24	15.90	1.65	-2	20	10	5
11		176	12/07/2012	14:35	15.90	1.56	-2	20	10	5
11		177	12/07/2012	14:45	15.90	1.56	-2	20	10	3
11		178	12/07/2012	14:55	15.90	1.65	-2	20	10	3
11		179	12/07/2012	15:05	15.90	1.65	-2	20	10	1
11		180	12/07/2012	15:15	15.90	1.56	-2	20	10	1
11		181	12/07/2012	15:29	15.90	1.65	0	20	10	1
11		182	12/07/2012	15:39	15.90	1.65	0	20	10	3
11		183	12/07/2012	15:49	15.90	1.65	0	20	10	5
11		184	12/07/2012	15:59	15.90	1.65	0	20	10	6

continued on next page

continued from previous page

Condition	Details	Run #	Date	Time	Water Temperature	Set Speed	Yaw Angle	Heel Angle	Tab Angle	Rudder Angle
					degrees C	m/s	degrees	degrees	degrees	degrees
11		185	12/07/2012	16:09	15.90	1.65	0	20	8	6
11		186	12/07/2012	16:20	15.90	1.65	0	20	8	5
11		187	12/07/2012	16:30	15.90	1.65	0	20	8	3
11		188	12/07/2012	16:46	15.90	1.65	0	20	8	1
11		189	12/07/2012	16:56	15.90	1.65	0	20	6	1
11		190	12/07/2012	17:06	15.90	1.65	0	20	6	3
11		191	12/07/2012	17:16	15.90	1.65	0	20	6	5
11		193	12/07/2012	17:40	15.90	1.65	1	20	6	6
11		194	12/07/2012	17:50	15.90	1.65	1	20	6	5
11		195	12/07/2012	17:59	15.90	1.65	1	20	6	3
11		197	12/07/2012	18:21	15.90	1.65	1	20	6	1
11		198	13/07/2012	08:47	15.95	1.65	1	20	6	1
11		199	13/07/2012	08:57	15.95	1.65	1	20	8	1
11		200	13/07/2012	09:07	15.95	1.65	1	20	8	3
11		201	13/07/2012	09:17	15.95	1.65	1	20	8	5
11		202	13/07/2012	09:27	15.95	1.65	1	20	8	6
11		203	13/07/2012	09:38	15.95	1.65	1	20	10	6
11		204	13/07/2012	09:47	15.95	1.65	1	20	10	5
11		205	13/07/2012	09:58	15.95	1.65	1	20	10	3
11		207	13/07/2012	10:19	15.95	1.65	1	20	10	1
11		208	13/07/2012	11:24	15.95	1.65	0	20	6	6
12		213	13/07/2012	14:12	15.95	1.28	-1	-10	-4	-2
12		214	13/07/2012	14:23	15.95	1.28	-1	-10	-4	-2
12		215	13/07/2012	14:35	15.95	1.28	-1	-10	-4	-2
12		216	13/07/2012	14:46	15.95	1.28	-1	-10	-4	-2
12		217	13/07/2012	14:56	15.95	1.28	-1	-10	-4	-2
12		218	13/07/2012	15:06	15.95	1.28	-1	-10	-4	-2

continued on next page

continued from previous page

Condition	Details	Run #	Date	Time	Water Temperature	Set Speed	Yaw Angle	Heel Angle	Tab Angle	Rudder Angle
					degrees C	m/s	degrees	degrees	degrees	degrees
12		219	13/07/2012	15:16	15.95	1.28	-1	-10	-4	-2
12		220	13/07/2012	15:26	15.95	1.28	-1	-10	-4	-2
12		221	13/07/2012	15:36	15.95	1.28	-1	-10	-4	-2
12		222	13/07/2012	15:46	15.95	1.28	-1	-10	-4	-2
12		224	13/07/2012	16:35	15.95	1.65	1	20	6	6
12		225	13/07/2012	16:45	15.95	1.65	1	20	6	6
12		226	13/07/2012	16:55	15.95	1.65	1	20	6	6
12		227	13/07/2012	17:05	15.95	1.65	1	20	6	6
12		228	13/07/2012	17:14	15.95	1.65	1	20	6	6
12		229	13/07/2012	17:24	15.95	1.65	1	20	6	6
12		230	13/07/2012	17:35	15.95	1.65	1	20	6	6
12		231	13/07/2012	17:47	15.95	1.65	1	20	6	6
12		232	13/07/2012	17:56	15.95	1.65	1	20	6	6
12		233	13/07/2012	18:06	15.95	1.65	1	20	6	6
12		234	14/07/2012	10:11	16.00	1.65	1	20	6	6
12		235	14/07/2012	10:21	16.00	1.65	1	20	6	6
12		236	14/07/2012	10:31	16.00	1.65	1	20	6	6
13		237	14/07/2012	15:01	16.00	0.26	1	10	4	2
13		238	14/07/2012	15:10	16.00	0.48	1	10	4	2
13		239	14/07/2012	15:20	16.00	0.71	1	10	4	2
13		240	14/07/2012	15:30	16.00	0.90	1	10	4	2
13		241	14/07/2012	15:40	16.00	1.11	1	10	4	2
13		242	14/07/2012	15:50	16.00	1.28	1	10	4	2
13		243	14/07/2012	16:00	16.00	1.37	1	10	4	2
13		244	14/07/2012	16:10	16.00	1.51	1	10	4	2
13		245	14/07/2012	16:20	16.00	1.71	1	10	4	2
13		246	14/07/2012	16:32	16.00	1.92	1	10	4	2

continued on next page

continued from previous page

Condition	Details	Run #	Date	Time	Water Temperature	Set Speed	Yaw Angle	Heel Angle	Tab Angle	Rudder Angle
					degrees C	m/s	degrees	degrees	degrees	degrees
13		247	14/07/2012	16:43	16.00	2.02	1	10	4	2
13		248	14/07/2012	16:54	16.00	2.21	1	10	4	2
13		249	14/07/2012	17:04	16.00	1.28	1	10	4	2
13		250	14/07/2012	17:14	16.00	1.37	1	10	4	2
14		251	14/07/2012	17:29	16.00	1.92	1	0	0	0
14		252	14/07/2012	17:39	16.00	1.92	1	0	-2	0
14		253	14/07/2012	17:49	16.00	1.92	0	0	-2	0
14		254	14/07/2012	17:59	16.00	1.92	0	0	0	0
14		255	14/07/2012	18:09	16.00	1.92	0	0	2	0
14		256	14/07/2012	18:18	16.00	1.92	0	0	2	0
14		257	14/07/2012	18:28	16.00	1.92	0	0	4	0
14		258	14/07/2012	18:40	16.00	1.92	-1	0	4	0
14		259	14/07/2012	18:50	16.00	1.92	-1	0	2	0
14		260	14/07/2012	19:00	16.00	1.92	-1	0	0	0
14		261	14/07/2012	19:10	16.00	1.92	-1	0	-2	0
14		262	14/07/2012	19:23	16.00	1.92	-2	0	4	0
15		263	14/07/2012	19:35	16.00	1.37	-2	5	4	4
15		264	14/07/2012	19:44	16.00	1.37	-2	5	6	2
15		265	14/07/2012	21:04	16.00	1.28	-2	5	6	2
15		266	14/07/2012	21:13	16.00	1.28	-2	5	8	2
15		267	14/07/2012	21:23	16.00	1.37	-2	5	8	2
15		268	14/07/2012	21:34	16.00	1.37	0	5	8	2
15		269	14/07/2012	21:43	16.00	1.28	0	5	8	2
15		270	14/07/2012	21:53	16.00	1.28	0	5	6	2
15		271	14/07/2012	22:03	16.00	1.37	0	5	6	2
15		272	14/07/2012	22:13	16.00	1.37	0	5	4	2

continued on next page

continued from previous page

Condition	Details	Run #	Date	Time	Water Temperature	Set Speed	Yaw Angle	Heel Angle	Tab Angle	Rudder Angle
					degrees C	m/s	degrees	degrees	degrees	degrees
15		273	14/07/2012	22:23	16.00	1.28	0	5	4	2
15		274	14/07/2012	22:34	16.00	1.28	1	5	4	2
15		275	14/07/2012	22:44	16.00	1.37	1	5	4	2
15		276	14/07/2012	22:54	16.00	1.37	1	5	6	2
15		277	14/07/2012	23:03	16.00	1.28	1	5	6	2
15		278	14/07/2012	23:13	16.00	1.28	1	5	8	2
15		279	14/07/2012	23:22	16.00	1.37	1	5	8	2
16		280	15/07/2012	11:15	16.00	1.28	1	10	8	2
16		281	15/07/2012	11:25	16.00	1.37	1	10	8	2
16		282	15/07/2012	11:34	16.00	1.37	1	10	6	2
16		283	15/07/2012	11:45	16.00	1.28	1	10	6	2
16		284	15/07/2012	11:55	16.00	1.28	1	10	4	2
16		285	15/07/2012	12:05	16.00	1.37	1	10	4	2
16		286	15/07/2012	12:16	16.00	1.37	0	10	4	2
16		287	15/07/2012	12:25	16.00	1.28	0	10	4	2
16		288	15/07/2012	12:35	16.00	1.28	0	10	6	2
16		289	15/07/2012	12:46	16.00	1.37	0	10	6	2
16		290	15/07/2012	12:55	16.00	1.37	0	10	8	2
16		291	15/07/2012	13:06	16.00	1.28	0	10	8	2
16		292	15/07/2012	14:35	16.00	1.28	-2	10	8	2
16		293	15/07/2012	14:45	16.00	1.37	-2	10	8	2
16		294	15/07/2012	14:55	16.00	1.37	-2	10	6	2
16		295	15/07/2012	15:05	16.00	1.28	-2	10	6	2
16		296	15/07/2012	15:15	16.00	1.37	-2	10	4	4
17		297	15/07/2012	15:31	16.00	1.65	-2	20	8	3
17		298	15/07/2012	15:39	16.00	1.65	-2	20	8	5

continued on next page

continued from previous page

Condition	Details	Run #	Date	Time	Water Temperature	Set Speed	Yaw Angle	Heel Angle	Tab Angle	Rudder Angle
					degrees C	m/s	degrees	degrees	degrees	degrees
17		299	15/07/2012	15:49	16.00	1.65	-2	20	8	6
17		300	15/07/2012	16:00	16.00	1.65	-2	20	10	6
17		301	15/07/2012	16:12	16.00	1.56	-2	20	10	6
17		302	15/07/2012	16:22	16.00	1.56	-2	20	10	5
17		303	15/07/2012	16:32	16.00	1.65	-2	20	10	5
17		304	15/07/2012	16:42	16.00	1.65	-2	20	10	3
17		305	15/07/2012	16:52	16.00	1.56	-2	20	10	3
17		306	15/07/2012	17:03	16.00	1.56	-2	20	10	1
17		307	15/07/2012	17:13	16.00	1.65	-2	20	10	1
17		308	15/07/2012	17:25	16.00	1.65	0	20	10	1
17		309	15/07/2012	17:35	16.00	1.65	0	20	10	3
17		310	15/07/2012	17:45	16.00	1.65	0	20	10	5
17		311	15/07/2012	17:55	16.00	1.65	0	20	10	6
17		312	15/07/2012	18:06	16.00	1.65	0	20	8	6
17		313	15/07/2012	19:20	16.00	1.65	0	20	8	5
17		314	15/07/2012	19:30	16.00	1.65	0	20	8	3
17		315	15/07/2012	19:40	16.00	1.65	0	20	8	1
17		316	15/07/2012	19:50	16.00	1.65	0	20	6	1
17		317	15/07/2012	20:00	16.00	1.65	0	20	6	3
17		318	15/07/2012	20:10	16.00	1.65	0	20	6	5
17		319	15/07/2012	20:21	16.00	1.65	0	20	6	6
17		320	15/07/2012	20:33	16.00	1.65	1	20	6	6
17		321	15/07/2012	20:43	16.00	1.65	1	20	6	5
17		322	15/07/2012	20:53	16.00	1.65	1	20	6	3
17		323	15/07/2012	21:03	16.00	1.65	1	20	6	1
17		324	15/07/2012	21:13	16.00	1.65	1	20	8	1
17		325	15/07/2012	21:23	16.00	1.65	1	20	8	3
17		326	15/07/2012	21:33	16.00	1.65	1	20	8	5

continued on next page

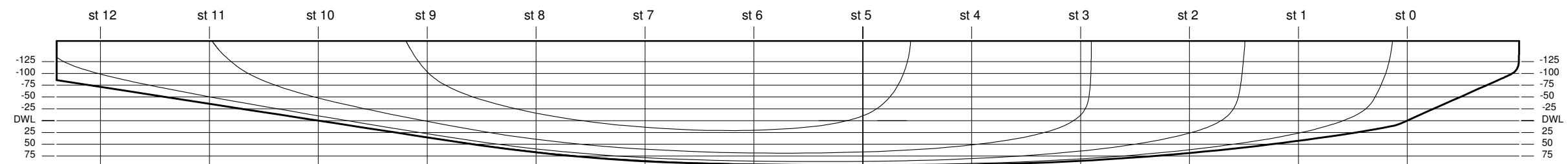
continued from previous page

Condition	Details	Run #	Date	Time	Water Temperature	Set Speed	Yaw Angle	Heel Angle	Tab Angle	Rudder Angle
					degrees C	m/s	degrees	degrees	degrees	degrees
17		327	15/07/2012	21:43	16.00	1.65	1	20	8	6
17		328	15/07/2012	21:54	16.00	1.65	1	20	10	6
17		329	15/07/2012	22:03	16.00	1.65	1	20	10	5
17		330	15/07/2012	22:13	16.00	1.65	1	20	10	3
17		331	15/07/2012	22:24	16.00	1.65	1	20	10	1
18		332	16/07/2012	08:55	16.05	1.28	-1	-10	-4	-2
18		333	16/07/2012	09:05	16.05	1.28	-1	-10	-4	-2
18		334	16/07/2012	09:15	16.05	1.28	-1	-10	-4	-2
18		335	16/07/2012	09:25	16.05	1.28	-1	-10	-4	-2
18		336	16/07/2012	09:35	16.05	1.28	-1	-10	-4	-2
18		337	16/07/2012	09:45	16.05	1.28	-1	-10	-4	-2
18		339	16/07/2012	09:55	16.05	1.28	-1	-10	-4	-2
18		340	16/07/2012	10:05	16.05	1.28	-1	-10	-4	-2
18		341	16/07/2012	10:15	16.05	1.28	-1	-10	-4	-2
18		342	16/07/2012	10:25	16.05	1.28	-1	-10	-4	-2
18		349	16/07/2012	11:39	16.05	1.65	1	20	6	6
18		350	16/07/2012	11:49	16.05	1.65	1	20	6	6
18		351	16/07/2012	11:58	16.05	1.65	1	20	6	6
18		352	16/07/2012	12:08	16.05	1.65	1	20	6	6
18		353	16/07/2012	12:17	16.05	1.65	1	20	6	6
18		354	16/07/2012	12:28	16.05	1.65	1	20	6	6
18		355	16/07/2012	12:38	16.05	1.65	1	20	6	6
18		356	16/07/2012	12:48	16.05	1.65	1	20	6	6
18		357	16/07/2012	12:58	16.05	1.65	1	20	6	6
18		358	16/07/2012	13:08	16.05	1.65	1	20	6	6

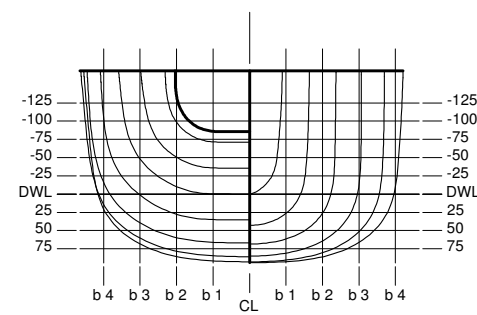
Appendix B

Lines Plan

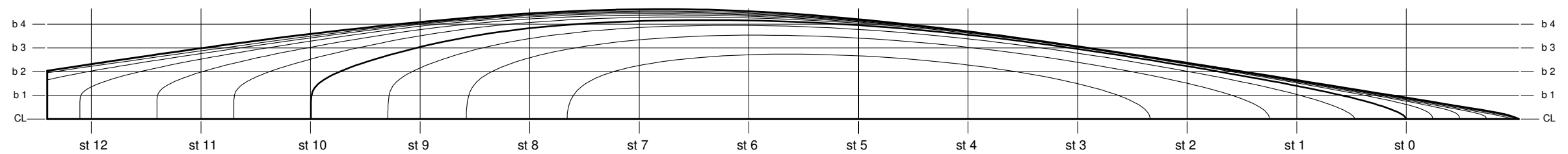
As noted in Section 2.5 it was not possible to include additional hull definition data within this document beyond the linesplan in this appendix and the principal particulars in Section 2.5. This was due to restrictions agreed to at the outset of the project between the author and the organisations which supplied the hull-form.



PROFILE



BODY PLAN



PLAN

Figure B.1: Lines plan of the model used for both 1/3rd and 1/8th tests.

Appendix C

Uncertainty Analysis

The purpose of this chapter is to provide the detail behind the uncertainty calculations, explain the uncertainty analysis process and also provide the ‘value’ of uncertainty that is applied to data from both sets of testing. Uncertainty calculations for the forces and moments as well as the hot-film calculations are included.

C.1 1/8thACC Yacht Model Forces and Moments

The uncertainty calculations for the 1/8th model were performed using the ITTC ‘Standard Form for Documenting Uncertainty Analysis, Resistance (C_T)’(25). The rationale behind the values selected for use in the calculations are included in the following sections as is a copy of the Excel sheets.

C.1.1 Total Drag Coefficient Values

Uncertainty was calculated based on repeat runs at two different velocities. The Total drag coefficient (C_T) values from each set was analysed independently and the largest error from the two test cases was applied to all runs. In this way the error presented is a ‘worst case’ with regard to expected uncertainty values.

C.1.2 Wetted Surface

It was not possible to undertake a complete three-dimensional mapping of the surfaces of the model's hull and appendages. Instead the hull was measured at both the sheer line and the keel line and the appendages at a range of sections along each body. The measurements at the model's sheer were taken at each station and measured the beam at each station. The measurements along the keel line were canoe body drafts at the centreline for each station. The recorded measurements were compared to the as designed measurements which showed that both the hull centreline profile and sheer line were within ± 0.5 mm of the designed values. The foils were CNC machined to a tolerance of ± 0.1 mm which was confirmed via a series of cross-sections measurement using digital callipers with two decimal place precision.

C.1.3 Speed

The uncertainty value used is the maximum that is allowed by the ITTC(27) for resistance tests. All commercial tests conducted at the Australian Maritime College are reported to be conducted to this level of uncertainty. As this work used the same carriage and speed sensors used in the commercial tests it was assumed that this same level uncertainty exists for the tests carried out for this thesis.

C.1.4 Resistance

The work of Binns(4) included the design and validation of the six-component force balance used for the tests conducted for the work in this thesis. Part of the design process included rigorous uncertainty assessments of the levels of linearity and cross talk inherent to the force balance. It was concluded from those tests that the force balance had a maximum load rating of 220 kg with an accuracy of alignment of at least 0.05 degrees. Also for loads up to 65 kg there will be a maximum

crosstalk of 0.15% of which only 1% will be nonlinear. During the testing for the current research the maximum force measured was 6.7 kg, two orders of magnitude less than maximum load limit and one order of magnitude less than the level of associated with the crosstalk and linearity. This confirms that the experiments were undertaken well within the limits of the force balance. To establish the errors to be used for the forces and moments an assessment was made from the calibration data taken prior to the experimental program. The calibration was undertaken with all components of the measurement chain connected with error values provided in Table C.1.

Table C.1: Force balance error estimate.

Force/Moment	Max Error	Min Error	Assumed Error	Units
X	0.014	-0.031	± 0.031	kg
Y	0.023	-0.027	± 0.027	kg
Z	0.022	-0.013	± 0.022	kg
L	0.005	-0.009	± 0.009	kgm
M	0.013	-0.019	± 0.019	kgm
N	0.015	-0.020	± 0.020	kgm

C.1.5 Model Basin Water Properties

The temperature of the towing tank water was recorded each day during the testing. Over the duration of the tests there was a maximum variation of 0.25°C . Based on the values provided in ITTC 7.5-02-01-03(26), this gives a variation in water density of 0.03 kg/m^3 .

**STANDARD FORM FOR DOCUMENTING UNCERTAINTY ANALYSIS
RESISTANCE (C_T) (4/11/02)**

Table of Contents

1. General information
2. Data reduction equations
3. Single or multiple test uncertainty
4. Input variables
5. Uncertainty analysis equations
6. Bias Limits
 - 6.1 Wetted surface
 - 6.2 Speed
 - 6.3 Resistance
 - 6.4 Model basin water properties
 - 6.5 Sensitivity coefficients
 - 6.6 Total bias of resistance coefficient C_T
7. Precision limit
8. Total uncertainty

1. General information

Statement of Purpose:

The purpose of this spreadsheet is to calculate the Uncertainty for the model Resistance C_T using single or multiple test method.

Facility:

Type of ship:

Period of tests performed:

References:

2. Data Reduction Equations

$$C_T^{15 \text{ deg}} = C_T^{tw} + (C_F^{15 \text{ deg}} - C_F^{tw})(1 + k)$$

where

$$C_T^{tw} = \frac{M_X^{tw} g}{\frac{1}{2} \rho V^2 S}$$

$$C_F = \frac{0.075}{(\log_{10} Re - 2)^2}$$

3. Single or Multiple Test Uncertainty

Enter # of tests (1 = single, >1 = mult.)

10

For single test, enter average measured C_T and best available standard deviation of C_T

	C _T	C _T (15 deg C)
Measured C _T (Single Test)		
Std Dev, σ _{C_T} (Single Test)		

For multiple test, enter C_T for each test

Test #	C_T	$C_T(15 \text{ deg C})$
1	0.077467178	0.077467178
2	0.078221698	0.078221698
3	0.077778151	0.077778151
4	0.077005646	0.077005646
5	0.078514378	0.078514378
6	0.076440042	0.076440042
7	0.076163217	0.076163217
8	0.077243753	0.077243753
9	0.077489339	0.077489339
10	0.076164012	0.076164012
11		
12		
13		
14		
15		

Average C_T (Multiple Test)	0.077248742	0.077248742
Std Dev, σ_{CT} (Multiple Test)	0.000816665	

4. Input Variables

Ship Particulars			
Definitions	Symbol	Ship model	Units
Length along waterline	L_{WL}	2.31	m
Beam	B	0.418	m
Draft, even keel	T	0.094	m
Wetted surface incl. rudder	S	0.841	m ²

Constants			
Definitions	Symbol	Value	Units
Gravity	g	9.81	m/s ²
Density, model basin water	ρ	1000	kg/m ³
Kinematic viscosity, model basin water	ν	1.1154E-06	m ² /s
Form Factor	k	0.11812	----
Frictional resistance coefficient at 15 deg C	$C_F(15 \text{ deg C})$	0.003836656	----
Coverage factor for standard deviation	K	2.262	----

Measured Values			
Definition	Symbol	Value	Units
Model Speed	V	1.274	m/s
Froude Number	Fr	0.267626389	----
Mass, total resistance in x-direction	Mx	5.374366283	kg
Resistance (average)	Rx	52.72253323	N
Total Resistance Coefficient (average @ 15 deg C)	C_T	0.077248742	----
Water Temperature	t_w	15.95	deg C
Frictional resistance coeff. at measured temp, t_w	$C_F^{t_w}$	0.003836656	----

5. Uncertainty Analysis Equations

$$(U_{C_T})^2 = (B_{C_T})^2 + (P_{C_T})^2$$

$$(B_{C_T}^{tw})^2 = (\theta_S B_S)^2 + (\theta_V B_V)^2 + (\theta_{M_x} B_{M_x})^2 + (\theta_\rho (B_\rho + \theta_{\rho tw \rho} B_{tw}))^2$$

$$P_{C_T} = \frac{K \sigma_{CT}}{\sqrt{M}}$$

6. Bias Limit

6.1 Wetted Surface

$$(B_S)^2 = (B_{S1}^2 + B_{S2}^2)$$

	units	% of (B _S) ²
B_{S1} (Assumed error in hull form):	0.00000025 m ²	0.015597577
B_{S2} (Error in displacement):	0.00002002 m ²	99.98440242

Wetted Surface Bias	units	% of S
B_S (Wetted Surface):	2.00176E-05 m ²	0.002380211

6.2 Speed

	units	% of V
B_V (Speed):	0.003 m/s	0.235478807

6.3 Resistance

$$(B_{M_x})^2 = (B_{M_x1}^2 + B_{M_x2}^2 + B_{M_x3}^2 + B_{M_x4}^2)$$

	units	% of (B _{Mx}) ²
B_{Mx1} (Calibration):	0.031 kg	100
B_{Mx2} (Curve fit bias):	0 kg	0
B_{Mx3} (Load cell misalignment):	0.000 kg	1.44987E-11
B_{Mx4} (Towing force inclination):	0 kg	0
B _{Mx} (Total Resistance Mass):	units	% of Mx
	0.031 kg	0.576812193

6.4 Model Basin Water Properties

	units	% of t _w
B_{tw} (Water Temperature):	0.25 deg C	1.567398119
	units	% of ρ
B_ρ (Water Density):	0.03 kg/m ³	0.003

6.5 Sensitivity Coefficients

$$\theta_S = \frac{\partial C_T}{\partial S} = \frac{M_X g}{\frac{1}{2} \rho V^2} \left(-\frac{1}{S^2} \right) \quad \theta_U = \frac{\partial C_T}{\partial V} = \frac{M_X g}{\frac{1}{2} \rho S} \left(-\frac{2}{V^3} \right)$$

$$\theta_{M_X} = \frac{\partial C_T}{\partial M_X} = \frac{g}{\frac{1}{2} \rho V^2 S} \quad \theta_\rho = \frac{\partial C_T}{\partial \rho} = \frac{M_X g}{\frac{1}{2} V^2 S} \left(-\frac{1}{\rho^2} \right)$$

$$\theta_{\rho_{tw\rho}} = \frac{\partial \rho}{\partial t_w} (t_w = 15 \text{ deg C}) = |0.0638 - 0.0173 t_w + 0.0001897 t_w^2|$$

		units
θ_S (Wetted Surface):	-0.091853438	1/m^2
θ_V (Speed):	-0.12126961	1/(m/s)
θ_{M_X} (Total Mass Resistance):	0.014373554	m/N*s^2
θ_ρ (Water Density):	-7.72487E-05	m^3/kg
$\theta_{\rho_{tw\rho}}$ (Water Temperature):	0.153175	1/deg C

$$B_{CT}^2 = (B_S \theta_S)^2 + (B_V \theta_V)^2 + (B_{M_X} \theta_{M_X})^2 + (\theta_\rho \times (B_\rho + B_{tw} \theta_{\rho_{tw\rho}}))^2$$

6.6 Total Bias of Resistance Coefficient C_T

		units	% of $C_T^{15 \text{ deg C}}$
B_{CT} (Resistance Coefficient C_T):	0.000575265	-----	0.744691671

7. Precision Limit

$$P_{C_T} = \frac{K \sigma_{C_T}}{\sqrt{M}}$$

		units	
σ_{C_T} (Standard Deviation of C_T):	0.000816665	-----	
M(1 for Single, else Multiple):	10	-----	
		units	% of $C_T^{15 \text{ deg C}}$
P_{CT} (Resistance Coefficient C_T):	0.000584166	-----	0.756214577

8. Total Uncertainty

		units	% of $U_{CT}^{15 \text{ deg C}}$
B_{CT} (Resistance Coefficient C_T):	0.000575265	-----	49.23231537
P_{CT} (Resistance Coefficient C_T):	0.000584166	-----	50.76768463

$$U_{CT}^2 = B_{CT}^2 + P_{CT}^2$$

Total Uncertainty		units	% of $C_T^{15 \text{ deg C}}$
$U_{CT}^{15 \text{ deg C}}$ (Resistance Coefficient C_T):	0.000819866	-----	1.061332263

C.2 1/3rdIACC Yacht Model Forces and Moments

Insufficient data was available to undertake an uncertainty analysis of the 1/3rd testing and results. It has therefore been assumed that uncertainty for the 1/3rd cases was the same as for the 1/8th tests.

C.3 1/8thIACC Yacht Model Hot-Films

The uncertainty levels as shown in Table C.2 were established using the results from Conditions 12 and 18. The two conditions were identical except that Condition 12 was conducted with studs whilst Condition 18 was without studs; this gave four groups that could be used for analysis. Each test group contained 10 runs which provided sufficient information to undertake a statical analysis of the standard deviation in measured intermittency about the mean of the repeated runs. The estimate of the 95% confidence level was undertaken using Equation C.1.

$$Uncertainty\ range = \pm t \frac{s}{\sqrt{n}} \quad (C.1)$$

where:

$t = T\ critical\ value = 2.262$

$s = standard\ deviation$

$n = number\ of\ samples$

The magnitude of the uncertainty levels were sufficiently small that if included on the hot-film plots the uncertainty bars would be approximately the same size of the data points. As such uncertainty bars have not been included on the hot-film plots.

Table C.2: Results of calculation of 95% confidence intervals from repeat runs in Conditions 12 and 18. The values shown are the maximum and minimum variation in intermittency for the 95% confidence interval.

Condition	HF 1	HF 2	HF 3	HF 4	HF 5
Condition 12, Runs 213-222	± 0.02	± 0.01	± 0.02	± 0.02	± 0.04
Condition 12, Runs 224-236	± 0.01	± 0.02	± 0.01	± 0.01	± 0.04
Condition 18, Runs 332-342	± 0.02	± 0.02	± 0.02	± 0.03	± 0.03
Condition 18, Runs 349-358	± 0.01	± 0.03	± 0.02	± 0.03	± 0.03
Maximum Values	± 0.02	± 0.03	± 0.02	± 0.03	± 0.04

Appendix D

Model Measurement Datums

The image on the following page shows the location of the zero point of the force balance coordinates relative to the model zero point and the tow point.

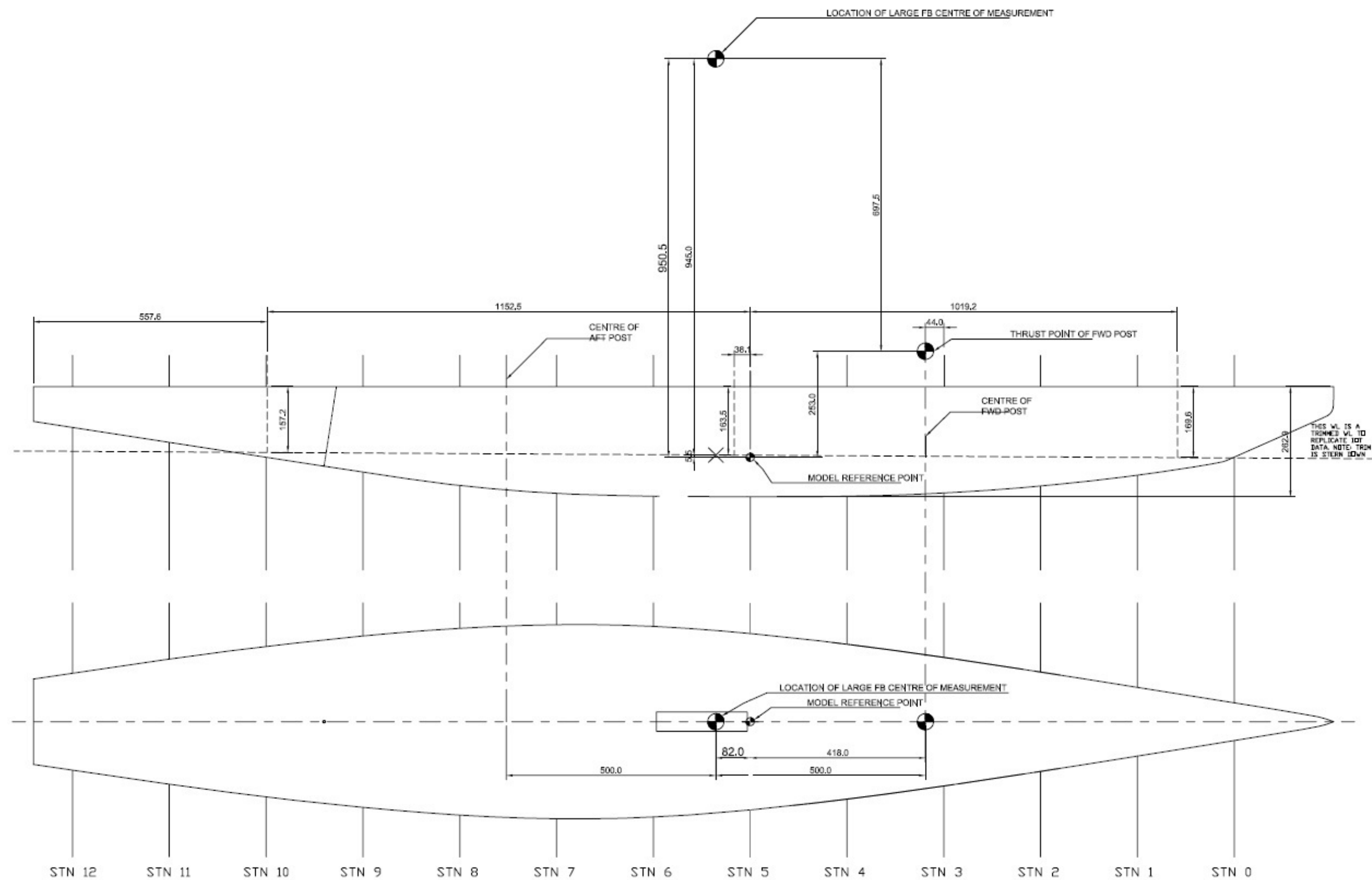


Figure D.1: Dimensions used for transfer of moments for force and moment calculations

Appendix E

Overheat Calculations

This section contains screen shots of the overheat calculation information and the associated dip switch settings. These calculations were undertaken using an Excel spreadsheet program supplied by Dantec Dynamics which is available at: [http://www.dantecdynamics.com/Admin/Public/DWSDownload.aspx?File= %2fFiles %2fFiler %2fProducts+and+Services %2fMiniCTA _Excel_spreadsheet_7a.XLS](http://www.dantecdynamics.com/Admin/Public/DWSDownload.aspx?File=%2fFiles%2fFiler%2fProducts+and+Services%2fMiniCTA_Excel_spreadsheet_7a.XLS)

Insert probe specific parameters etc.

Sensor resistance, R_{20}	10.49 Ω	See probe box
Sensor lead resist., R_L	0.20 Ω	On probe box
Support resistance, R_s	0.40 Ω	Non standard
Cable resistance, R_c	0.20 Ω	Cable 9006A1863
Sensor TCR, α_{20}	0.31% /K	
Desired sensor temp., T_w	55 $^{\circ}\text{C}$	Sensor temperature
Temperature of flow	16 $^{\circ}\text{C}$	Temperature during measurement

Click box below to select cable length.

(Standard: 4 (4-10) meters)

4 meters

Set decade controls as follows:
(grey dot indicates switch in down position)

Calculated sensor operating resistance etc.

Over temperature, ΔT	40 $^{\circ}\text{C}$
Operating resist., R_w	11.63 Ω
Total resistance, R_T	12.43 Ω
Overheat ratio, a	0.11
Bridge ratio, M	1:20
Decade resistance, R_D	248.6 Ω
Obtained wire temp., T_w	$^{\circ}\text{C}$

NOTE

Max. recommended sensor temperature $T_w = 60\text{ }^{\circ}\text{C}$ in water at atmospheric conditions (1 bar).

Figure E.1: Overheat data and dip switch setting information for hot-film one.

Insert probe specific parameters etc.

Sensor resistance, R_{20}	11.91 Ω	See probe box
Sensor lead resist., R_L	0.20 Ω	On probe box
Support resistance, R_s	0.40 Ω	Non standard
Cable resistance, R_c	0.20 Ω	Cable 9006A1863
Sensor TCR, α_{20}	0.36% /K	
Desired sensor temp., T_w	55 $^{\circ}\text{C}$	Sensor temperature
Temperature of flow	16 $^{\circ}\text{C}$	Temperature during measurement

Click box below to select cable length.

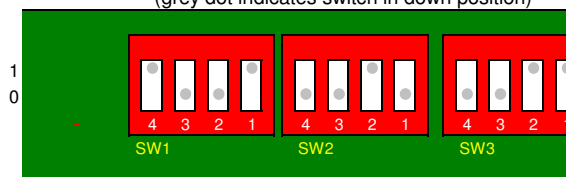
(Standard: 4 (4-10) meters)

4 meters

Calculated sensor operating resistance etc.

Over temperature, ΔT	40 $^{\circ}\text{C}$
Operating resist., R_w	13.41 Ω
Total resistance, R_T	14.21 Ω
Overheat ratio, a	0.13
Bridge ratio, M	1:20
Decade resistance, R_D	284.2 Ω
Obtained wire temp., T_w	$^{\circ}\text{C}$

Set decade controls as follows:
(grey dot indicates switch in down position)



NOTE

Max. recommended sensor temperature $T_w = 60$ $^{\circ}\text{C}$ in water at atmospheric conditions (1 bar)

Figure E.2: Overheat data and dip switch setting information for hot-film two.

Insert probe specific parameters etc.

Sensor resistance, R_{20}	9.82 Ω	See probe box
Sensor lead resist., R_L	0.20 Ω	On probe box
Support resistance, R_s	0.40 Ω	Non standard
Cable resistance, R_c	0.20 Ω	Cable 9006A1863
Sensor TCR, α_{20}	0.33% /K	
Desired sensor temp., T_w	55 $^{\circ}\text{C}$	Sensor temperature
Temperature of flow	16 $^{\circ}\text{C}$	Temperature during measurement

Click box below to select cable length.

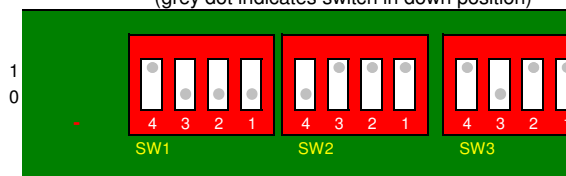
(Standard: 4 (4-10) meters)

4 meters

Calculated sensor operating resistance etc.

Over temperature, ΔT	40 $^{\circ}\text{C}$
Operating resist., R_w	10.95 Ω
Total resistance, R_T	11.75 Ω
Overheat ratio, a	0.12
Bridge ratio, M	1:20
Decade resistance, R_D	235.1 Ω
Obtained wire temp., T_w	$^{\circ}\text{C}$

Set decade controls as follows:
(grey dot indicates switch in down position)



NOTE

Max. recommended sensor temperature $T_w = 60$ $^{\circ}\text{C}$ in water at atmospheric conditions (1 bar)

Figure E.3: Overheat data and dip switch setting information for hot-film three.

Insert probe specific parameters etc.

Sensor resistance, R_{20}	10.84 Ω	See probe box
Sensor lead resist., R_L	0.20 Ω	On probe box
Support resistance, R_s	0.40 Ω	Non standard
Cable resistance, R_c	0.20 Ω	Cable 9006A1863
Sensor TCR, α_{20}	0.32% /K	
Desired sensor temp., T_w	55 $^{\circ}\text{C}$	Sensor temperature
Temperature of flow	16 $^{\circ}\text{C}$	Temperature during measurement

Click box below to select cable length.

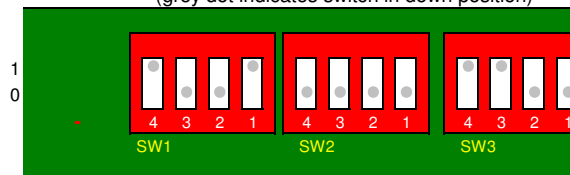
(Standard: 4 (4-10) meters)

4 meters

Calculated sensor operating resistance etc.

Over temperature, ΔT	40 $^{\circ}\text{C}$
Operating resist., R_w	12.05 Ω
Total resistance, R_T	12.85 Ω
Overheat ratio, a	0.11
Bridge ratio, M	1:20
Decade resistance, R_D	257.1 Ω
Obtained wire temp., T_w	$^{\circ}\text{C}$

Set decade controls as follows:
(grey dot indicates switch in down position)



NOTE

Max. recommended sensor temperature $T_w = 60$ $^{\circ}\text{C}$ in water at atmospheric conditions (1 bar)

Figure E.4: Overheat data and dip switch setting information for hot-film four.

Insert probe specific parameters etc.

Sensor resistance, R_{20}	11.18 Ω	See probe box
Sensor lead resist., R_L	0.20 Ω	On probe box
Support resistance, R_s	0.40 Ω	Non standard
Cable resistance, R_c	0.20 Ω	Cable 9006A1863
Sensor TCR, α_{20}	0.35% /K	
Desired sensor temp., T_w	55 $^{\circ}\text{C}$	Sensor temperature
Temperature of flow	16 $^{\circ}\text{C}$	Temperature during measurement

Click box below to select cable length.

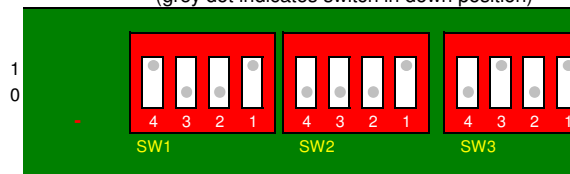
(Standard: 4 (4-10) meters)

4 meters

Calculated sensor operating resistance etc.

Over temperature, ΔT	40 $^{\circ}\text{C}$
Operating resist., R_w	12.55 Ω
Total resistance, R_T	13.35 Ω
Overheat ratio, a	0.12
Bridge ratio, M	1:20
Decade resistance, R_D	267.0 Ω
Obtained wire temp., T_w	$^{\circ}\text{C}$

Set decade controls as follows:
(grey dot indicates switch in down position)



NOTE

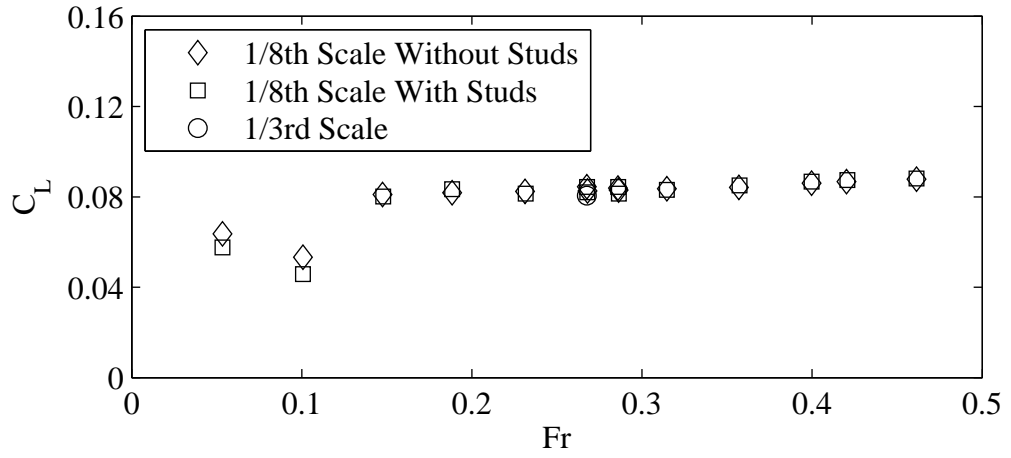
Max. recommended sensor temperature $T_w = 60$ $^{\circ}\text{C}$ in water at atmospheric conditions (1 bar)

Figure E.5: Overheat data and dip switch setting information for hot-film five.

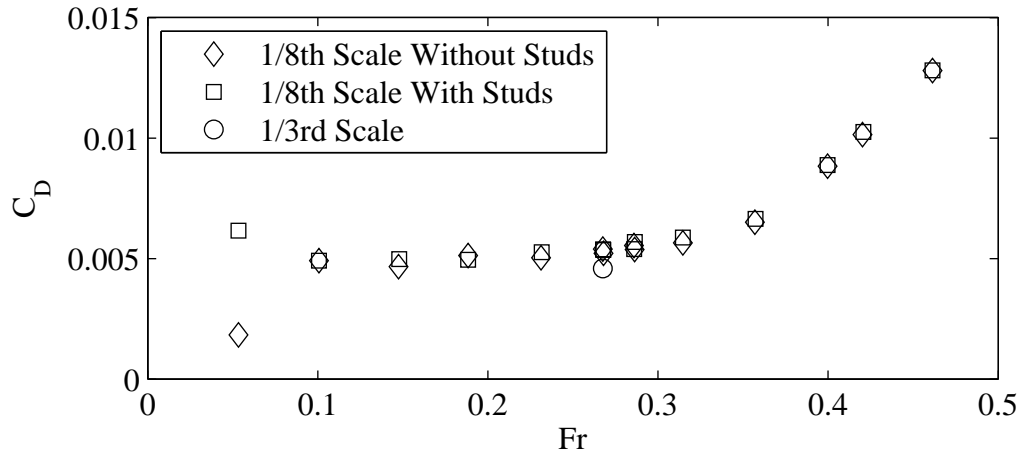
Appendix F

Supplementary Force Data

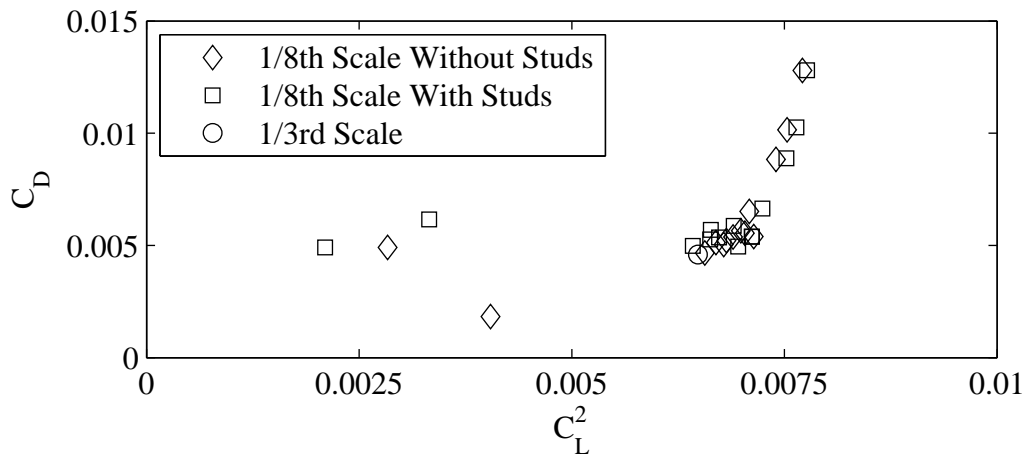
This section contains plots of the coefficient of lift (C_L) and drag (C_D) with variation in Froude number, rudder angle and trim tab angle. In addition plots of the coefficient of drag (C_D) with respect to variation in C_L^2 data have been included. Where available results from the $1/3^{rd}$ model tests are plotted along with those of the $1/8^{th}$ test data.



(a) Coefficient of lift plotted against variation in Froude number.

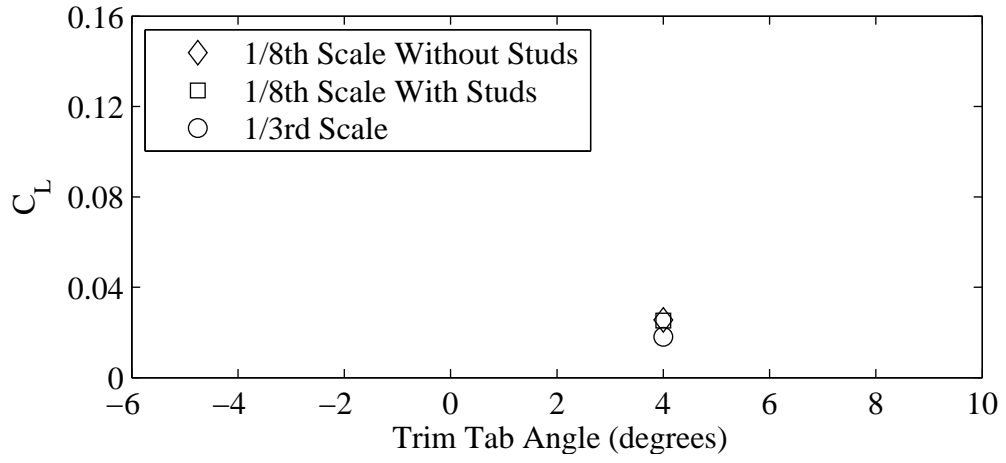


(b) Coefficient of drag plotted against variation in Froude number.

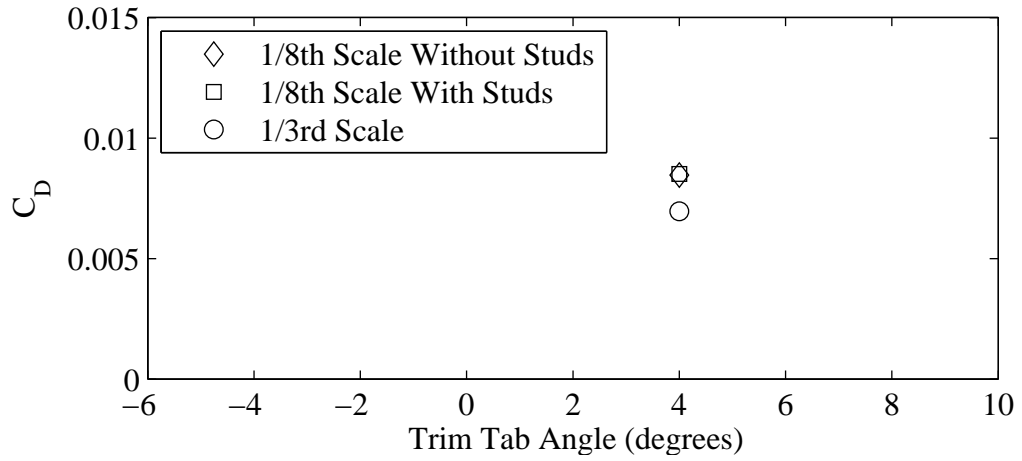


(c) Coefficient of drag plotted against variation in coefficient of lift squared.

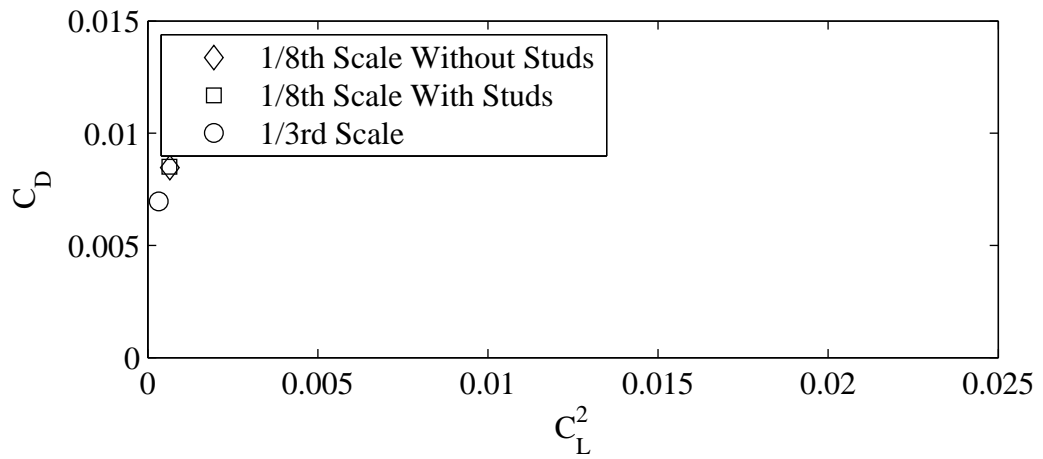
Figure F.1: Yaw 1 degrees, Heel 10 degrees, Tab 4 degrees, Rudder 2 degrees.



(a) Coefficient of lift plotted against variation in trim tab angle.

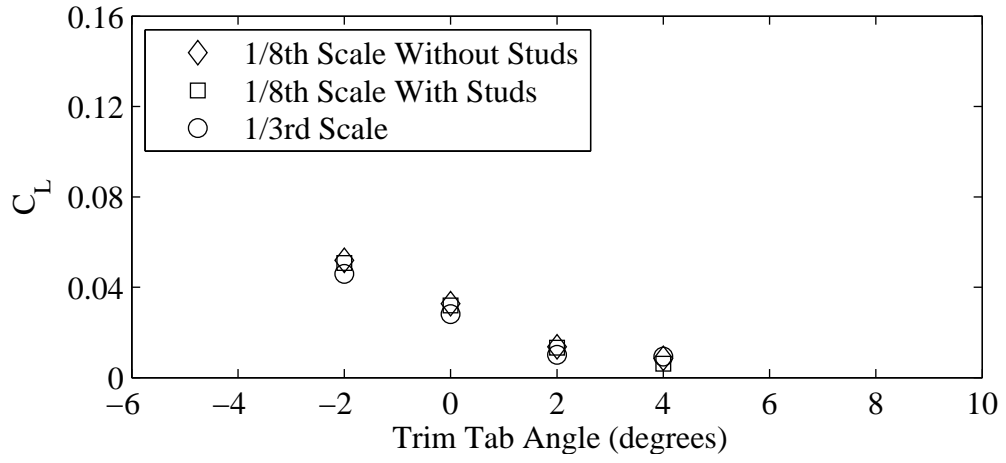


(b) Coefficient of drag plotted against variation in trim tab angle.

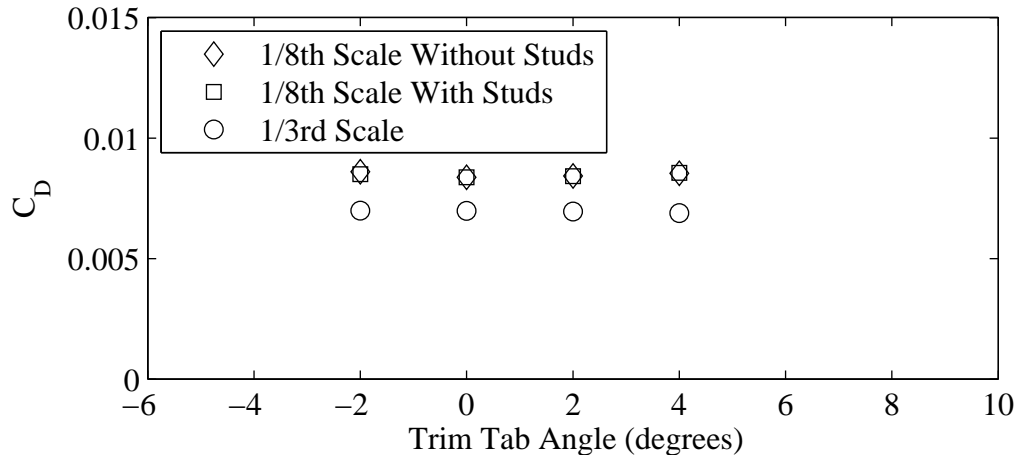


(c) Coefficient of drag plotted against variation in coefficient of lift squared.

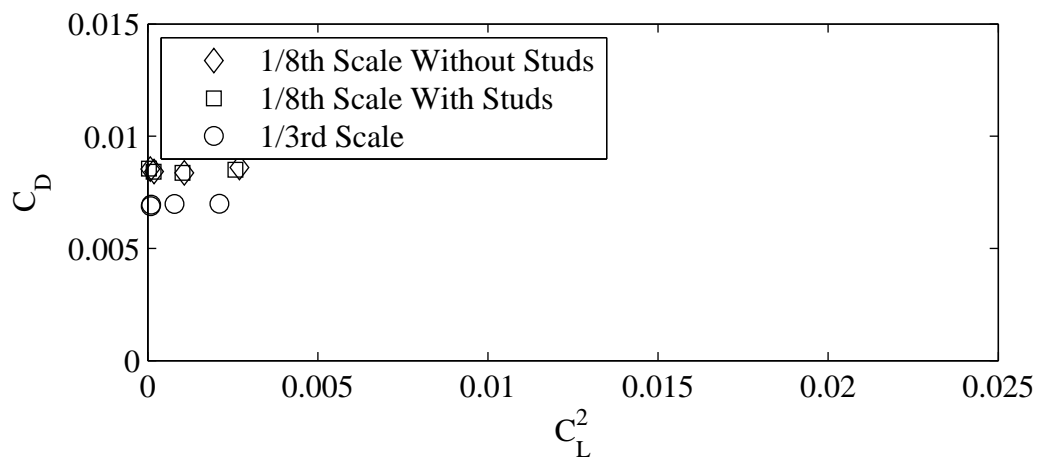
Figure F.2: Froude number 0.40, Yaw -2 degrees, Heel 0 degrees, Rudder 0 degrees.



(a) Coefficient of lift plotted against variation in trim tab angle.

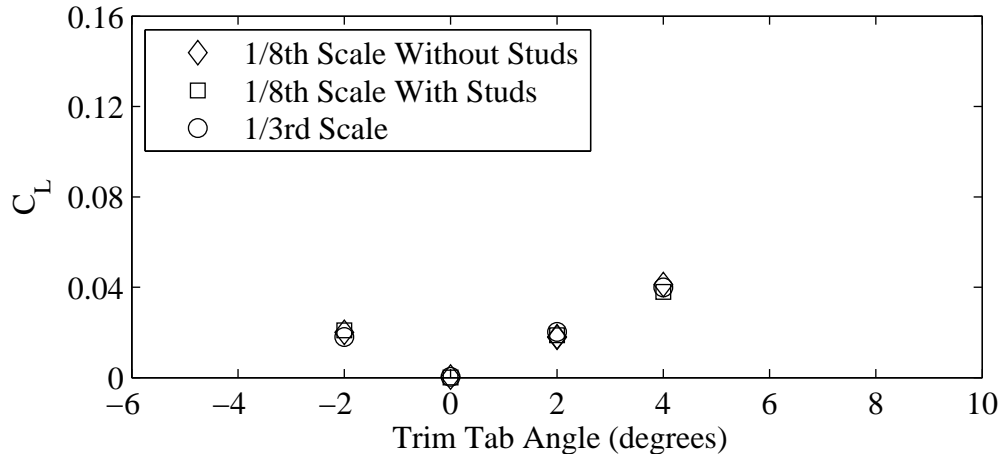


(b) Coefficient of drag plotted against variation in trim tab angle.

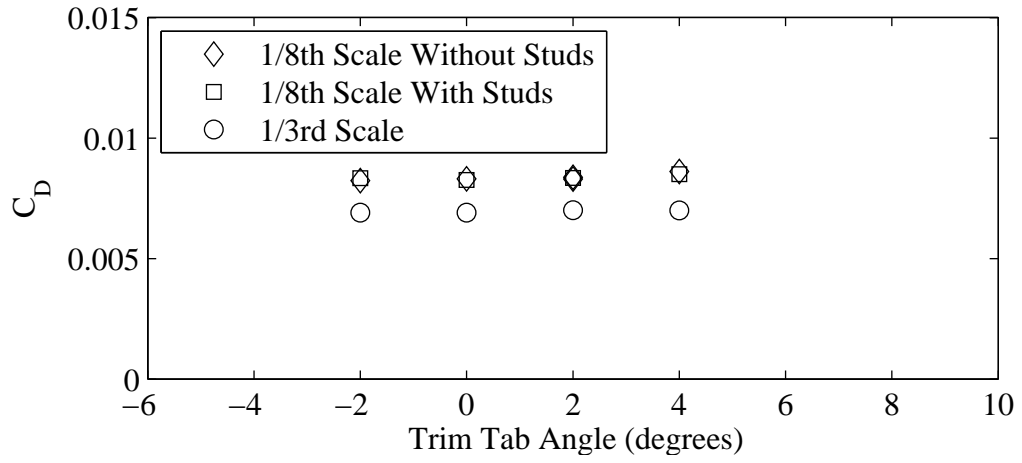


(c) Coefficient of drag plotted against variation in coefficient of lift squared.

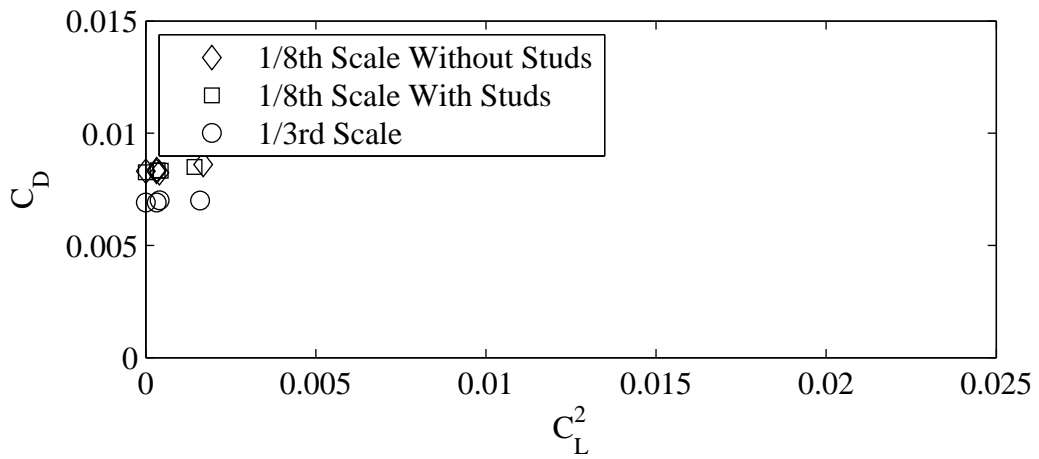
Figure F.3: Froude number 0.40, Yaw -1 degrees, Heel 0 degrees, Rudder 0 degrees.



(a) Coefficient of lift plotted against variation in trim tab angle.

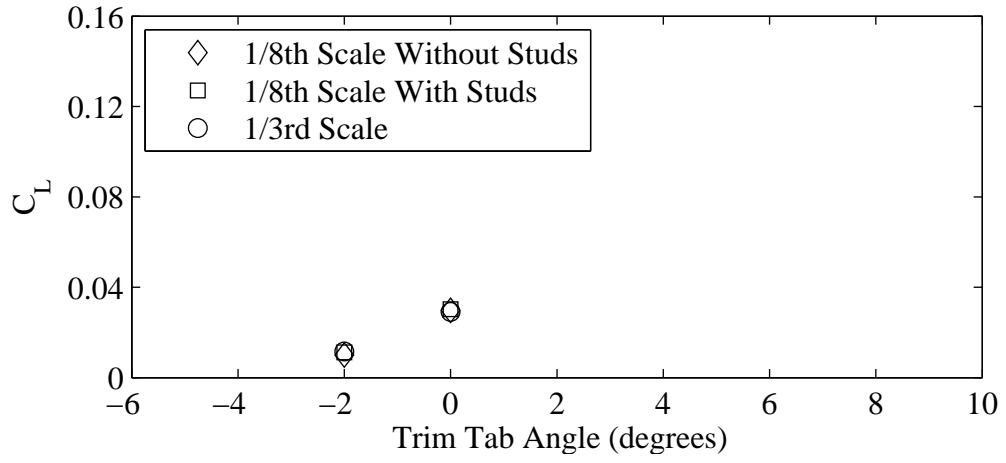


(b) Coefficient of drag plotted against variation in trim tab angle.

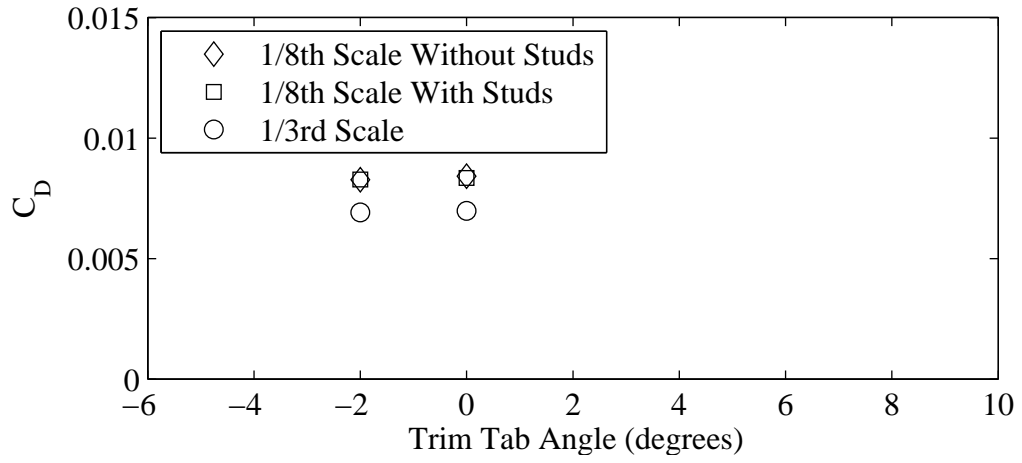


(c) Coefficient of drag plotted against variation in coefficient of lift squared.

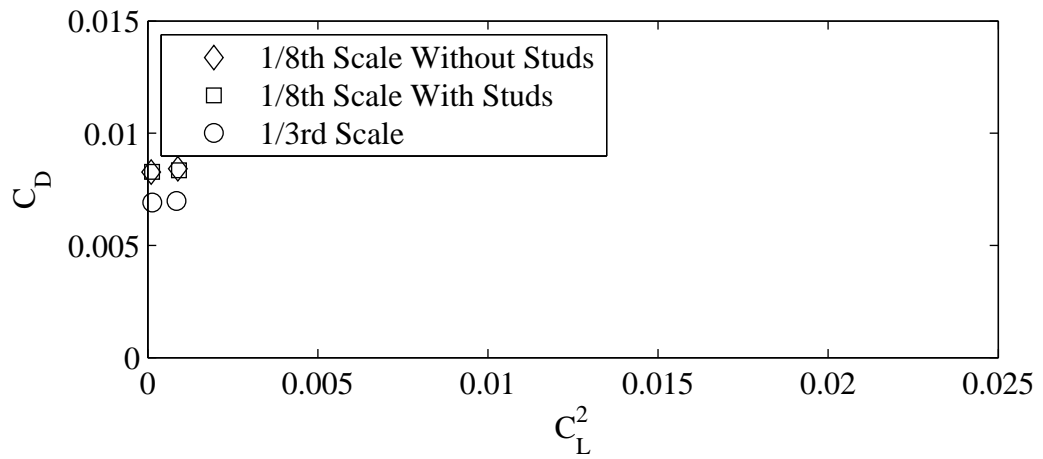
Figure F.4: Froude number 0.40, Yaw 0 degrees, Heel 0 degrees, Rudder 0 degrees.



(a) Coefficient of lift plotted against variation in trim tab angle.

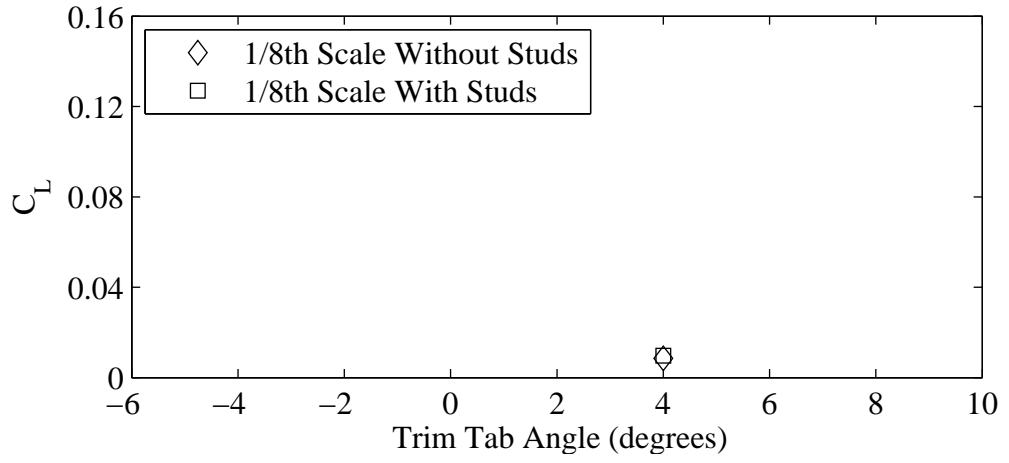


(b) Coefficient of drag plotted against variation in trim tab angle.

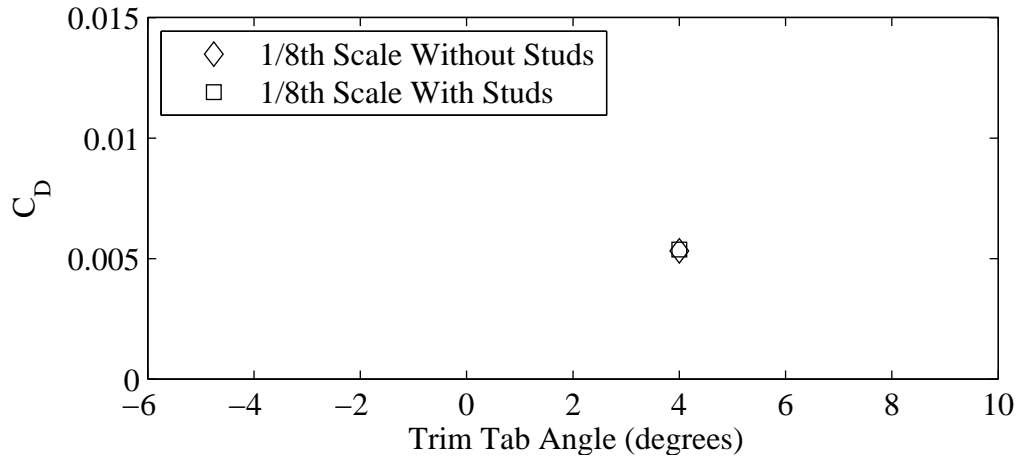


(c) Coefficient of drag plotted against variation in coefficient of lift squared.

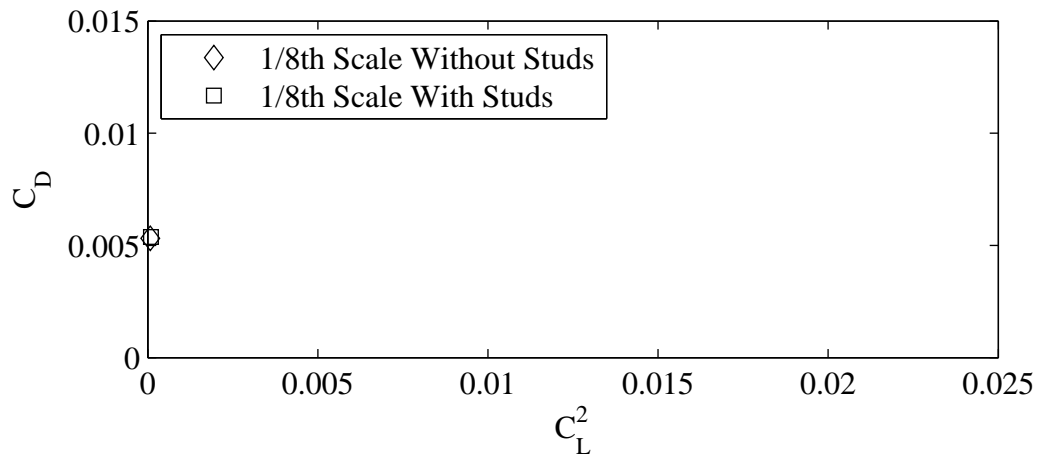
Figure F.5: Froude number 0.40, Yaw 1 degrees, Heel 0 degrees, Rudder 0 degrees.



(a) Coefficient of lift plotted against variation in trim tab angle.

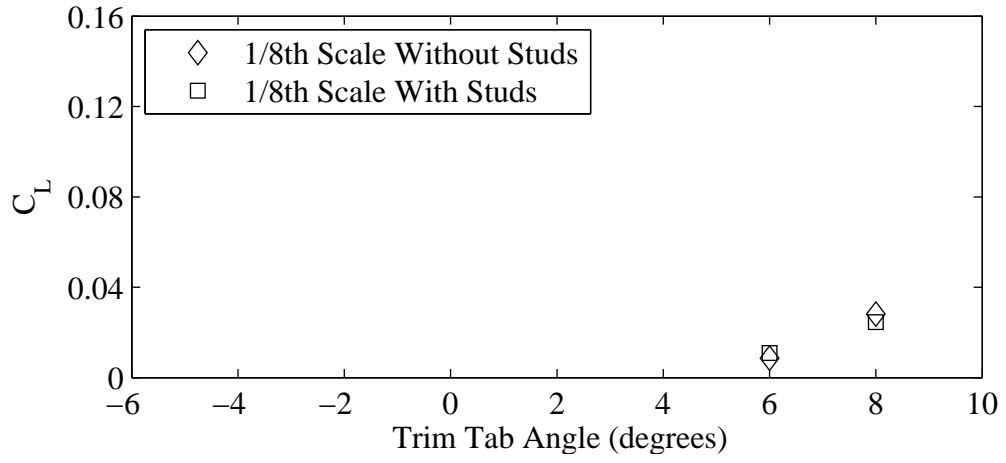


(b) Coefficient of drag plotted against variation in trim tab angle.

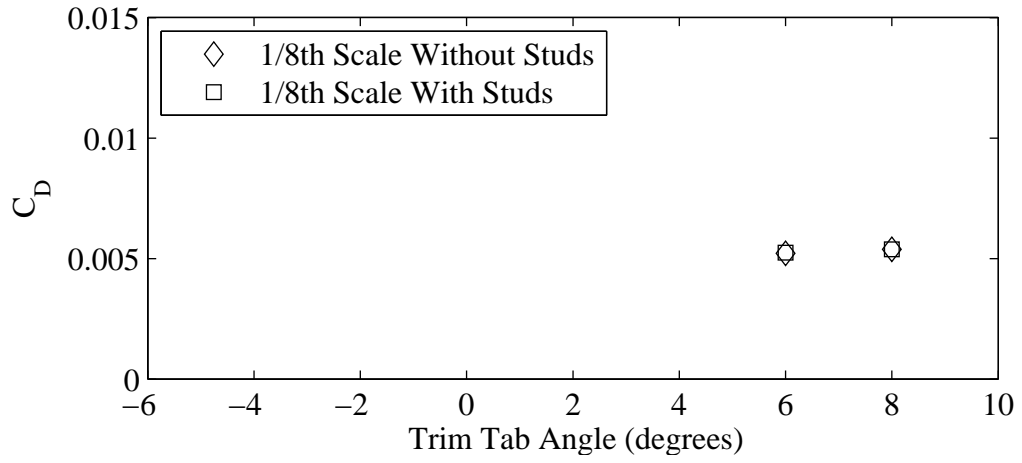


(c) Coefficient of drag plotted against variation in coefficient of lift squared.

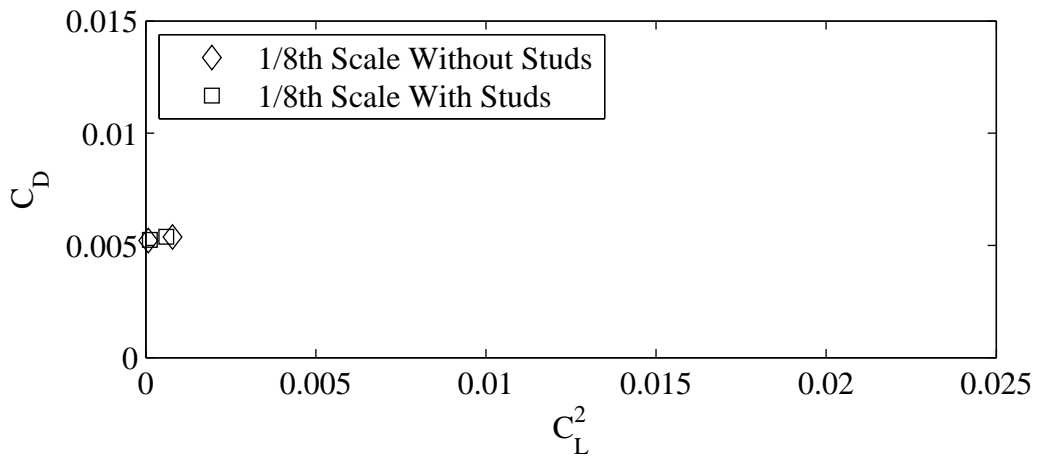
Figure F.6: Froude number 0.29, Yaw -2 degrees, Heel 5 degrees, Rudder 4 degrees.



(a) Coefficient of lift plotted against variation in trim tab angle.

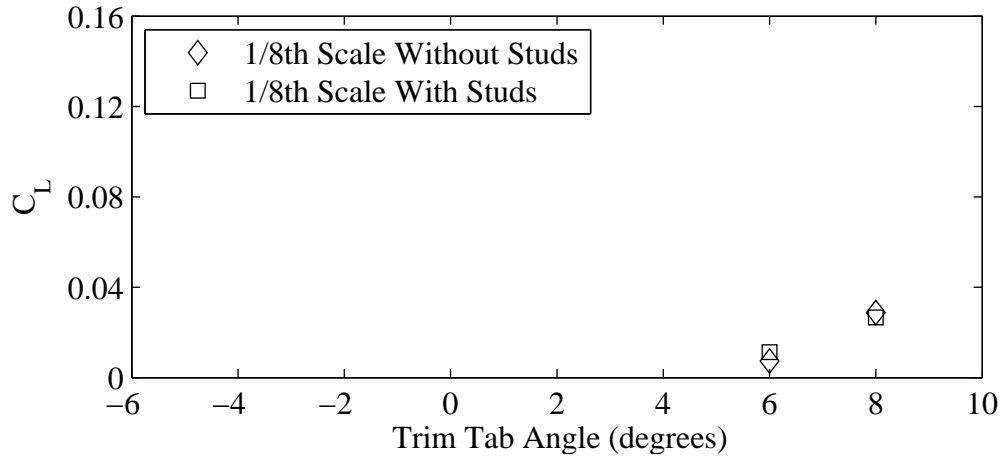


(b) Coefficient of drag plotted against variation in trim tab angle.

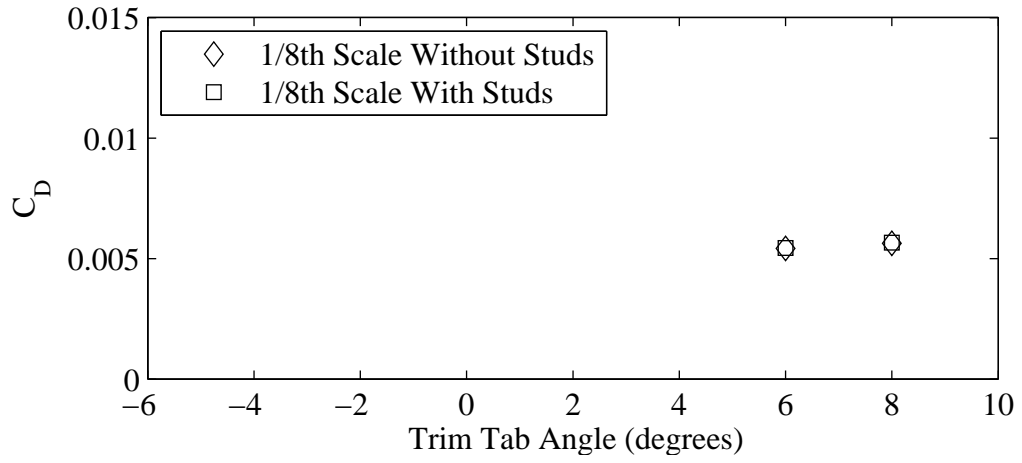


(c) Coefficient of drag plotted against variation in coefficient of lift squared.

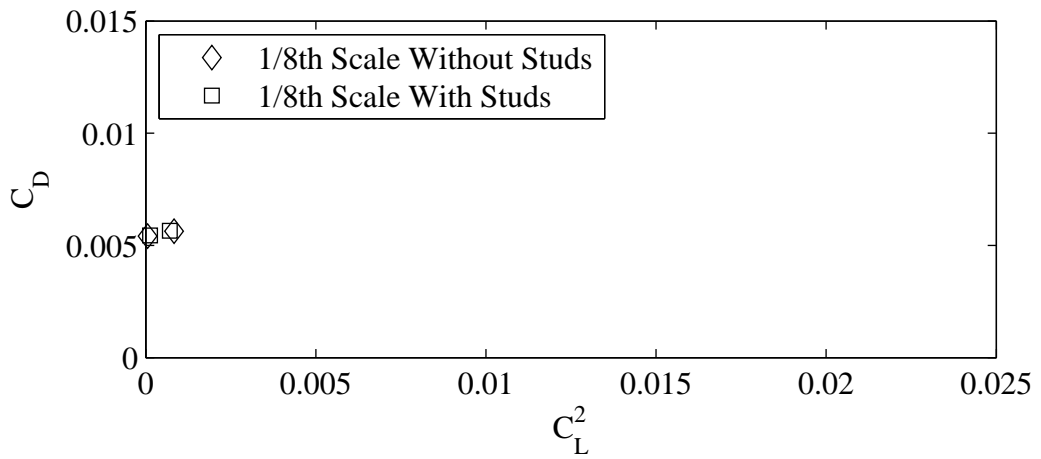
Figure F.7: Froude number 0.27, Yaw -2 degrees, Heel 5 degrees, Rudder 2 degrees.



(a) Coefficient of lift plotted against variation in trim tab angle.

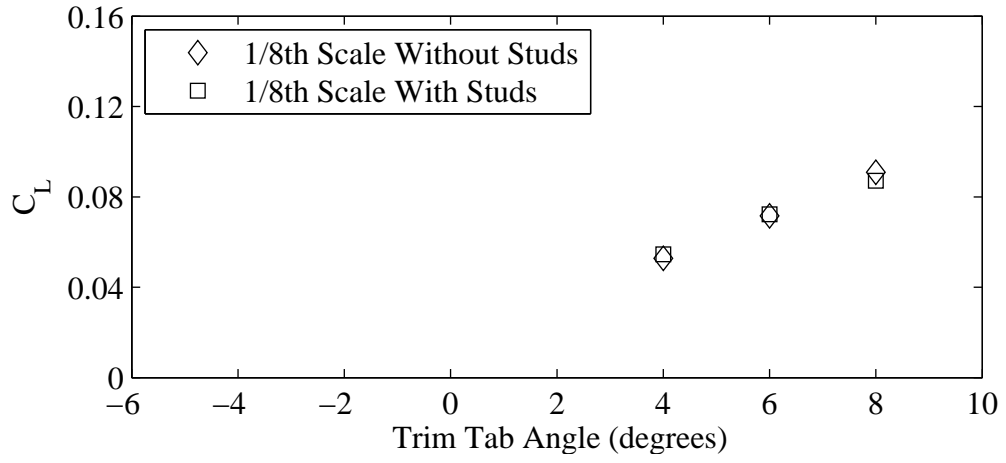


(b) Coefficient of drag plotted against variation in trim tab angle.

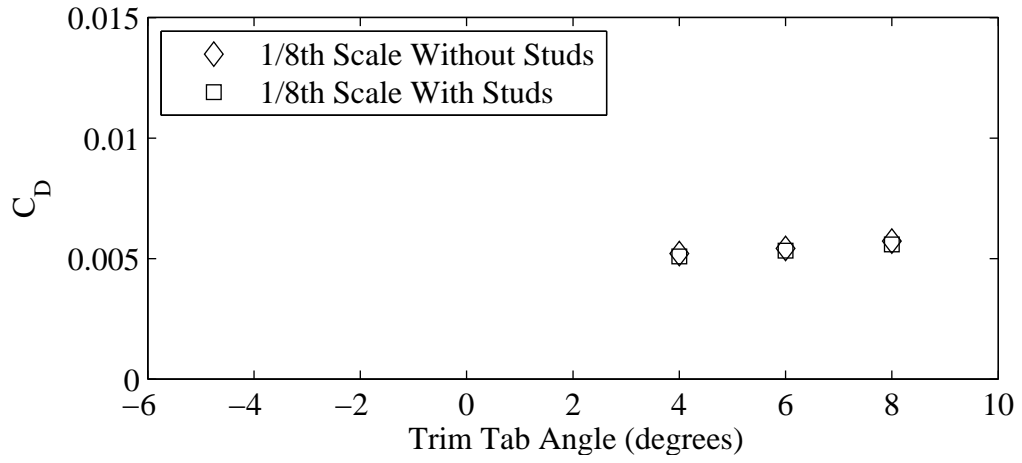


(c) Coefficient of drag plotted against variation in coefficient of lift squared.

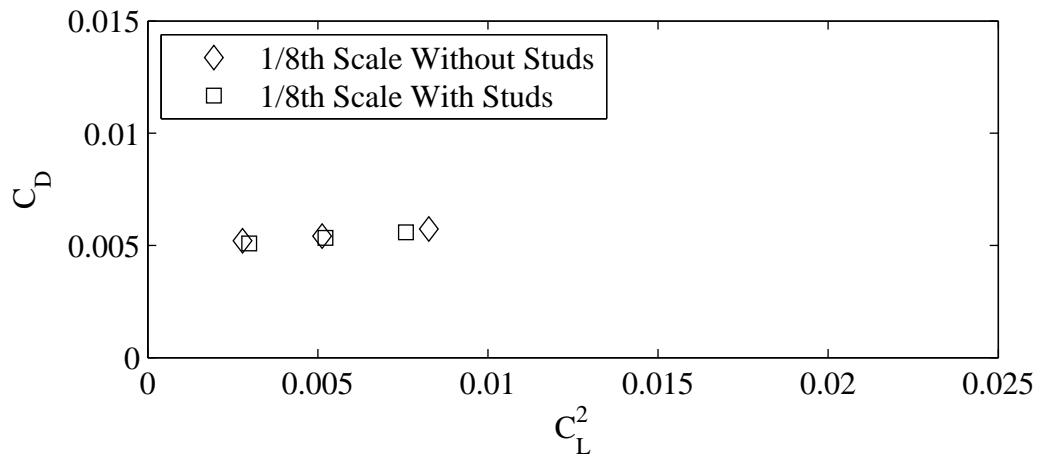
Figure F.8: Froude number 0.29, Yaw -2 degrees, Heel 5 degrees, Rudder 2 degrees.



(a) Coefficient of lift plotted against variation in trim tab angle.

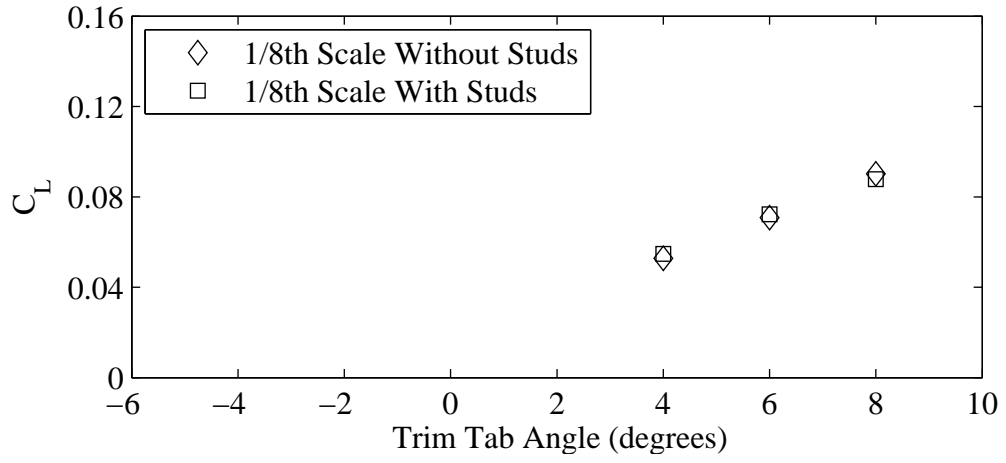


(b) Coefficient of drag plotted against variation in trim tab angle.

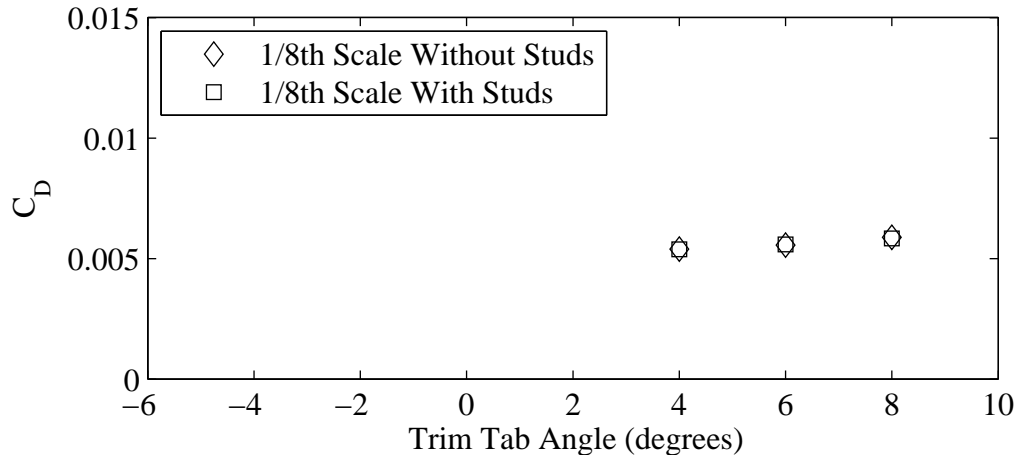


(c) Coefficient of drag plotted against variation in coefficient of lift squared.

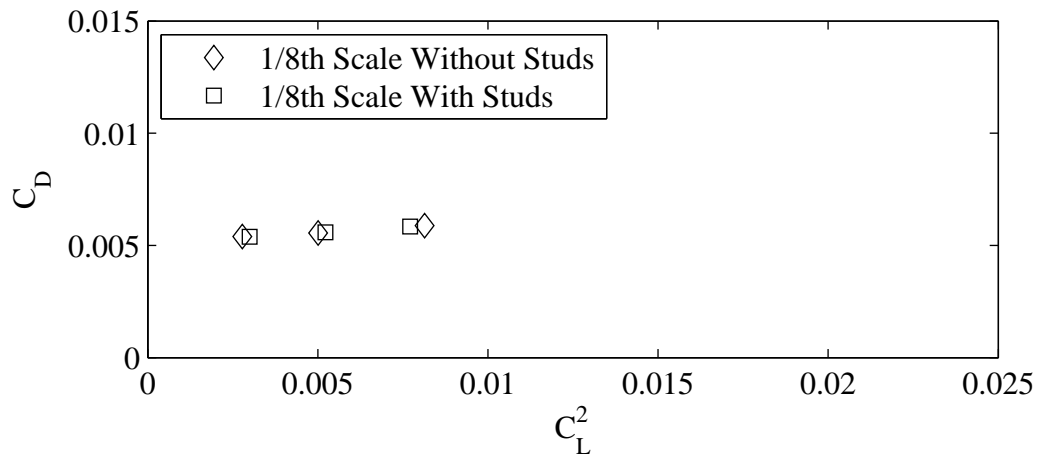
Figure F.9: Froude number 0.27, Yaw 0 degrees, Heel 5 degrees, Rudder 2 degrees.



(a) Coefficient of lift plotted against variation in trim tab angle.

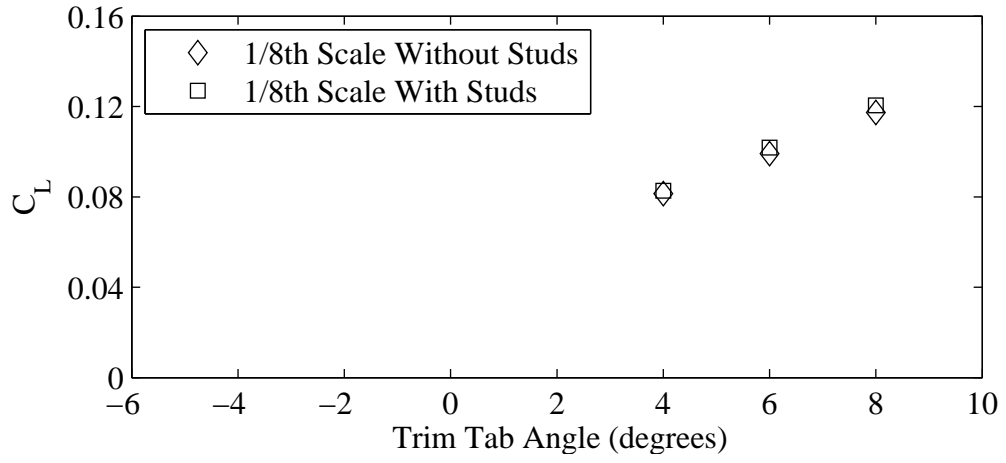


(b) Coefficient of drag plotted against variation in trim tab angle.

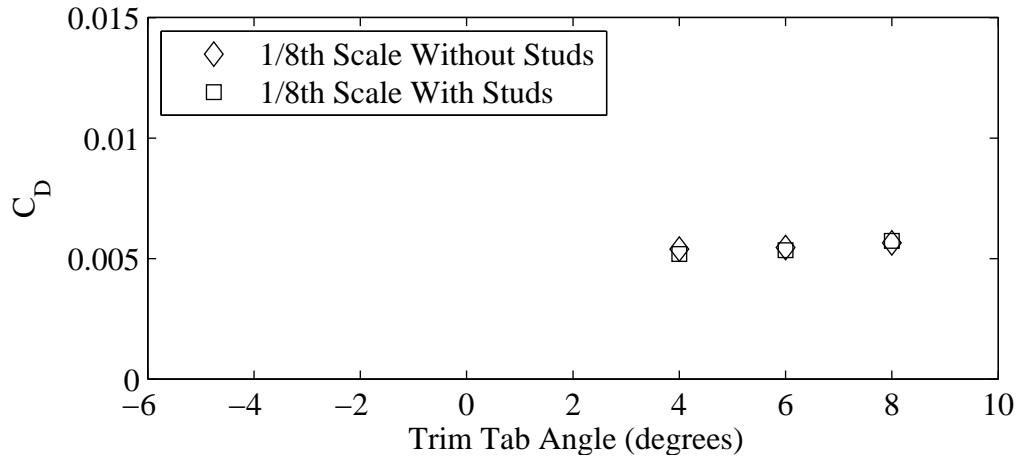


(c) Coefficient of drag plotted against variation in coefficient of lift squared.

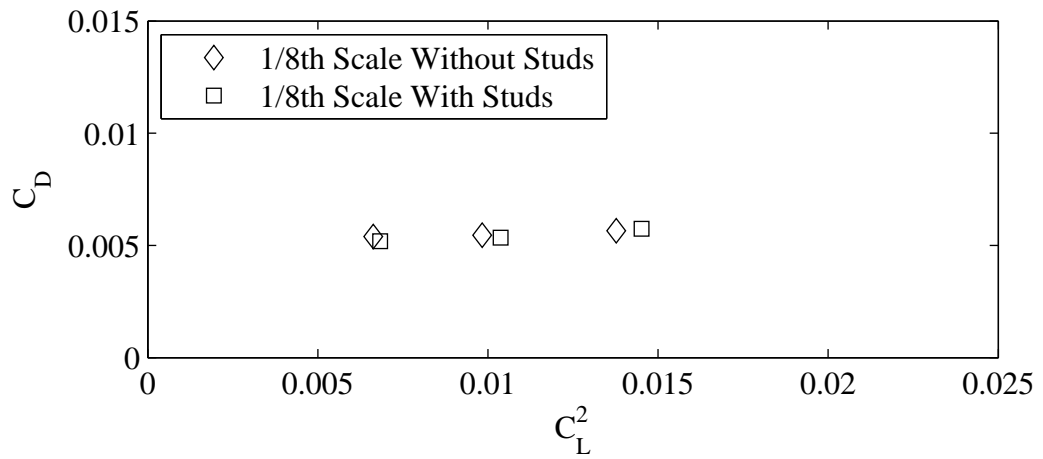
Figure F.10: Froude number 0.29, Yaw 0 degrees, Heel 5 degrees, Rudder 2 degrees.



(a) Coefficient of lift plotted against variation in trim tab angle.

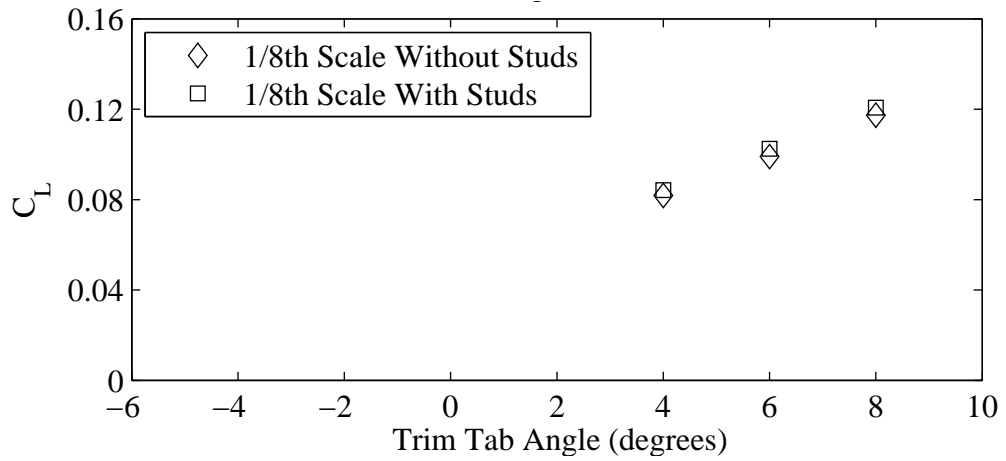


(b) Coefficient of drag plotted against variation in trim tab angle.

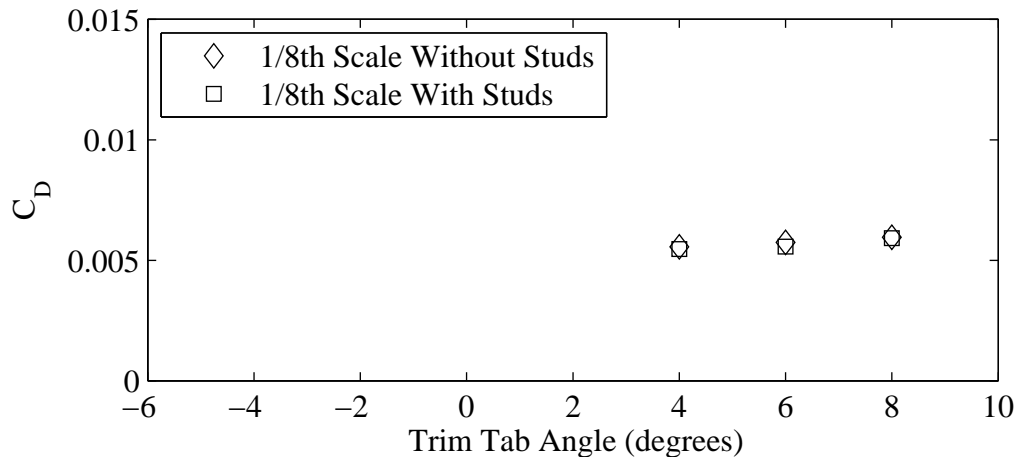


(c) Coefficient of drag plotted against variation in coefficient of lift squared.

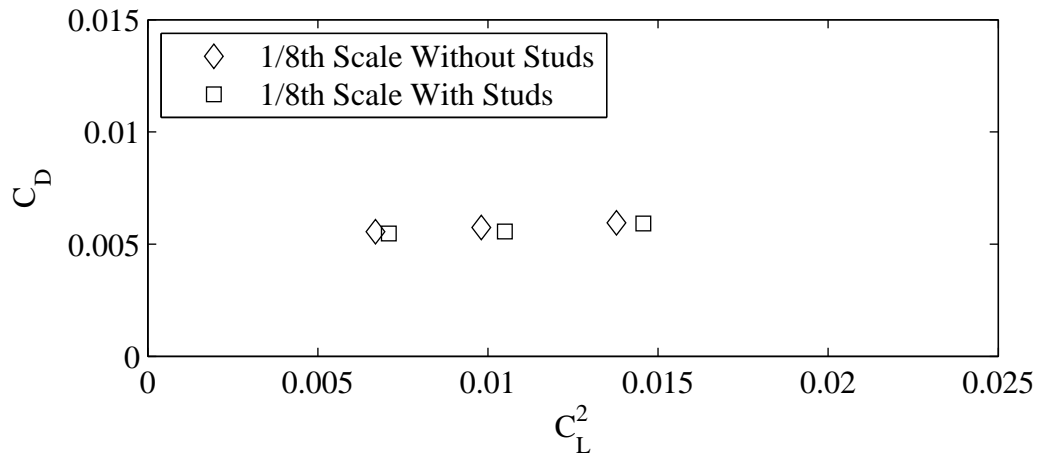
Figure F.11: Froude number 0.27, Yaw 1 degrees, Heel 5 degrees, Rudder 2 degrees.



(a) Coefficient of lift plotted against variation in trim tab angle.

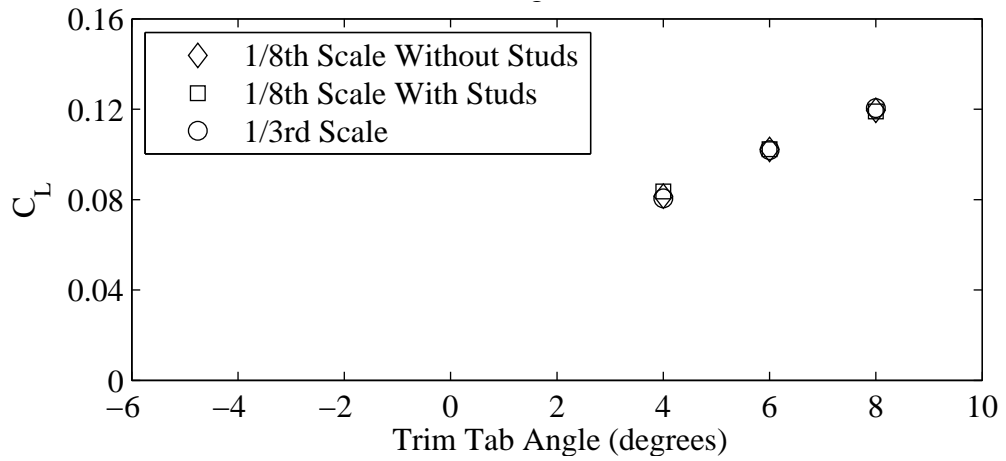


(b) Coefficient of drag plotted against variation in trim tab angle.

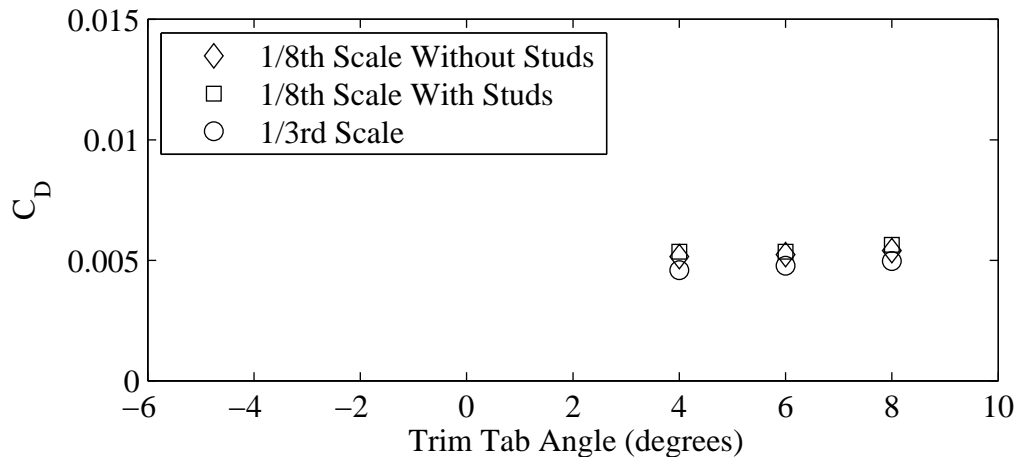


(c) Coefficient of drag plotted against variation in coefficient of lift squared.

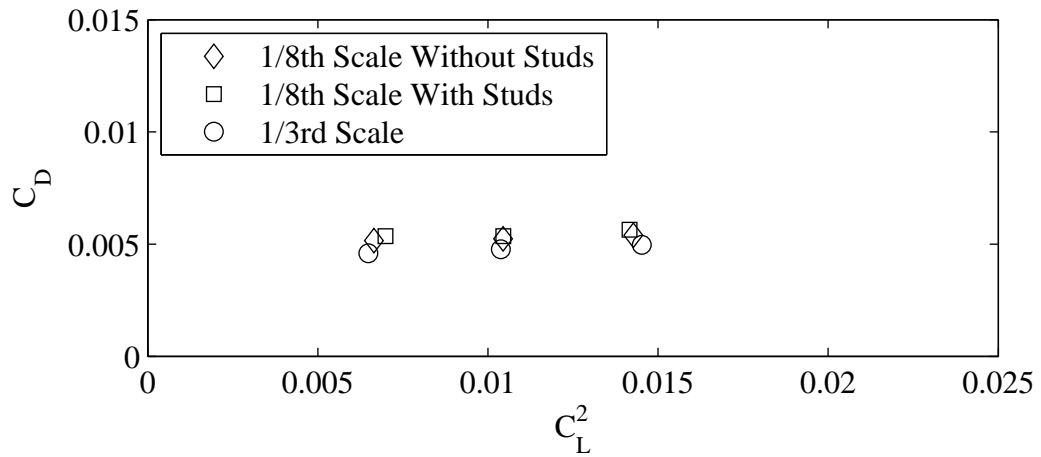
Figure F.12: Froude number 0.29, Yaw 1 degrees, Heel 10 degrees, Rudder 2 degrees.



(a) Coefficient of lift plotted against variation in trim tab angle.

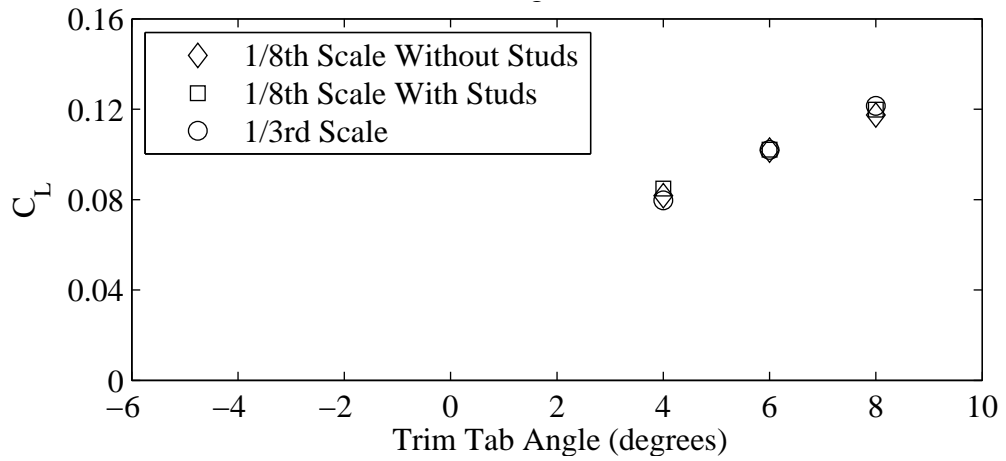


(b) Coefficient of drag plotted against variation in trim tab angle.

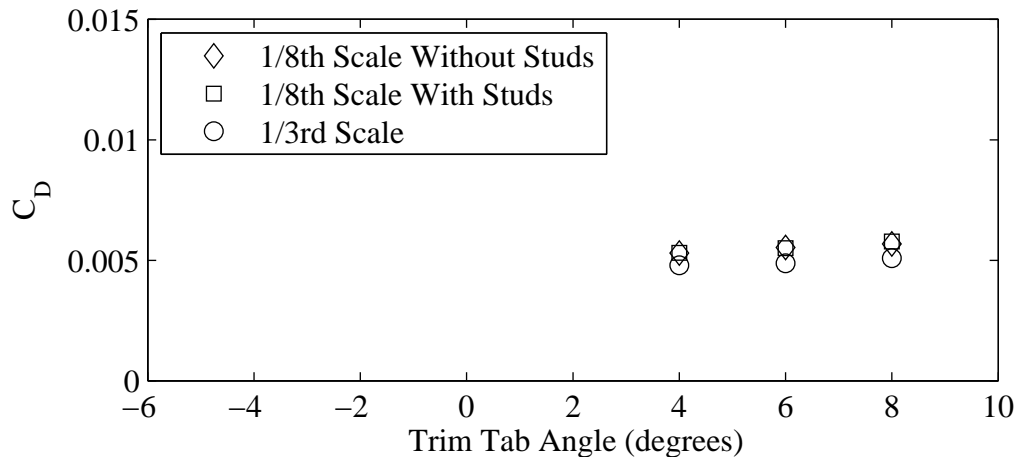


(c) Coefficient of drag plotted against variation in coefficient of lift squared.

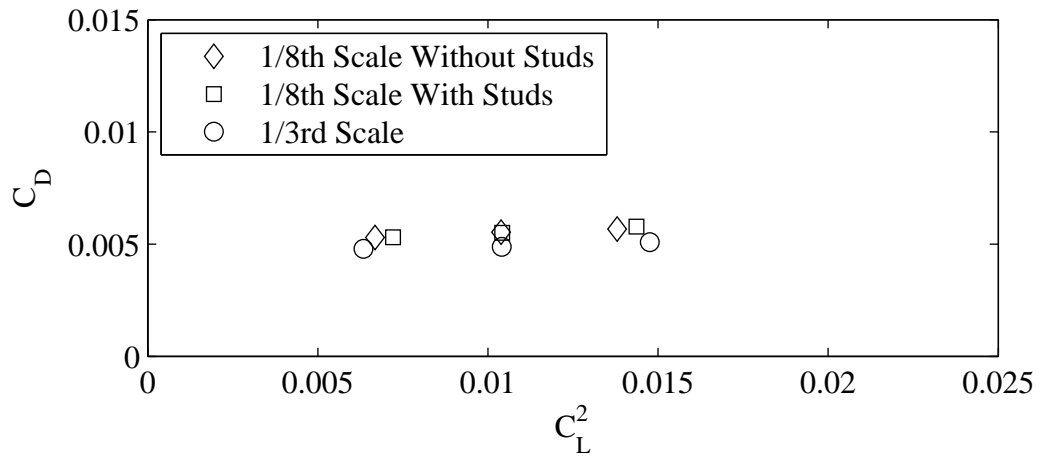
Figure F.13: Froude number 0.27, Yaw 1 degrees, Heel 10 degrees, Rudder 2 degrees.



(a) Coefficient of lift plotted against variation in trim tab angle.

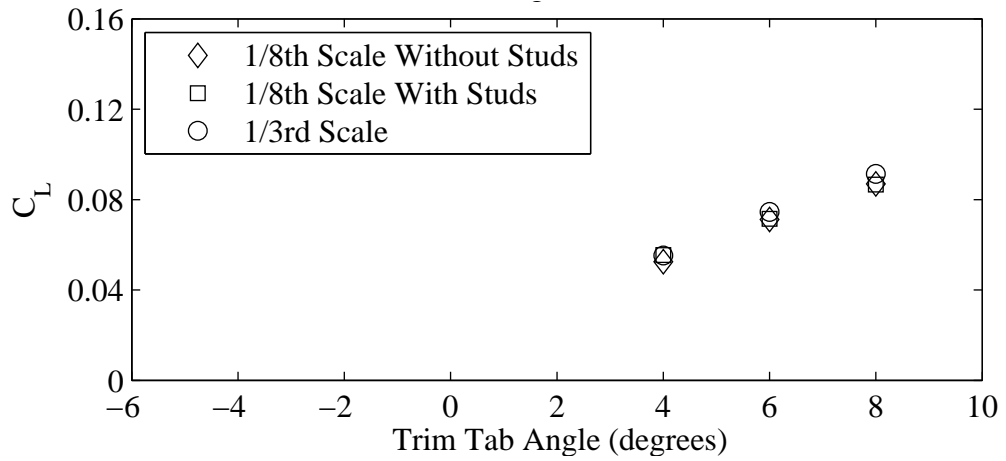


(b) Coefficient of drag plotted against variation in trim tab angle.

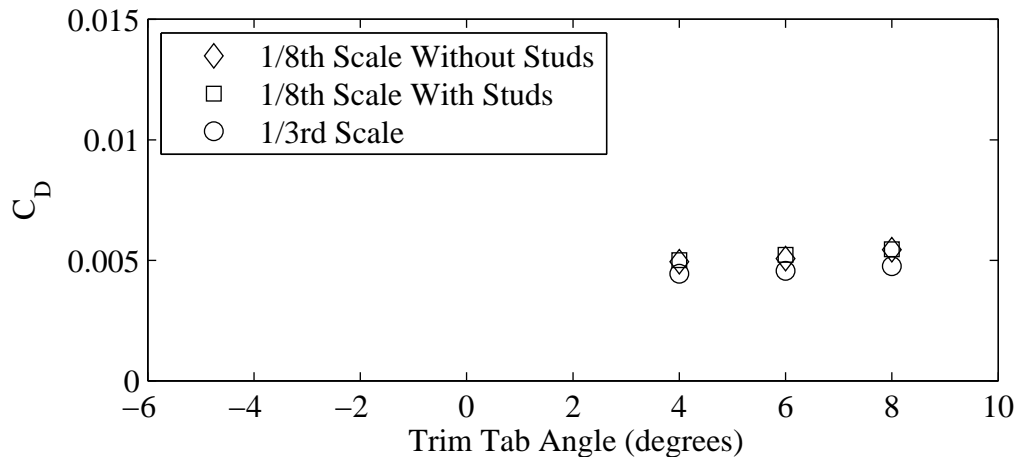


(c) Coefficient of drag plotted against variation in coefficient of lift squared.

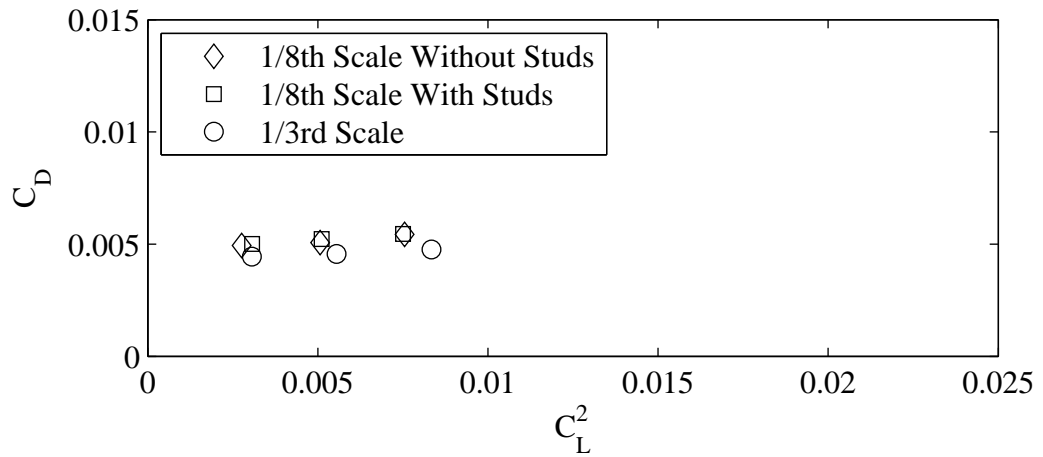
Figure F.14: Froude number 0.29, Yaw 1 degrees, Heel 10 degrees, Rudder 2 degrees.



(a) Coefficient of lift plotted against variation in trim tab angle.

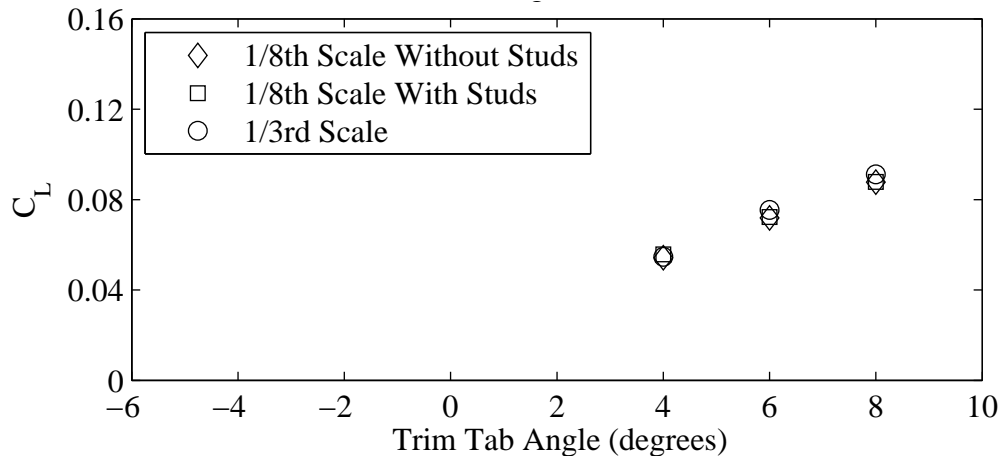


(b) Coefficient of drag plotted against variation in trim tab angle.

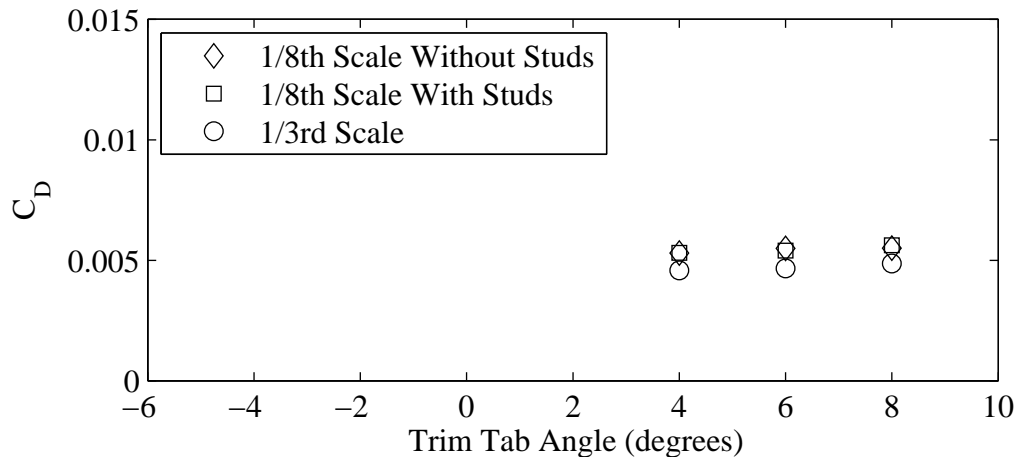


(c) Coefficient of drag plotted against variation in coefficient of lift squared.

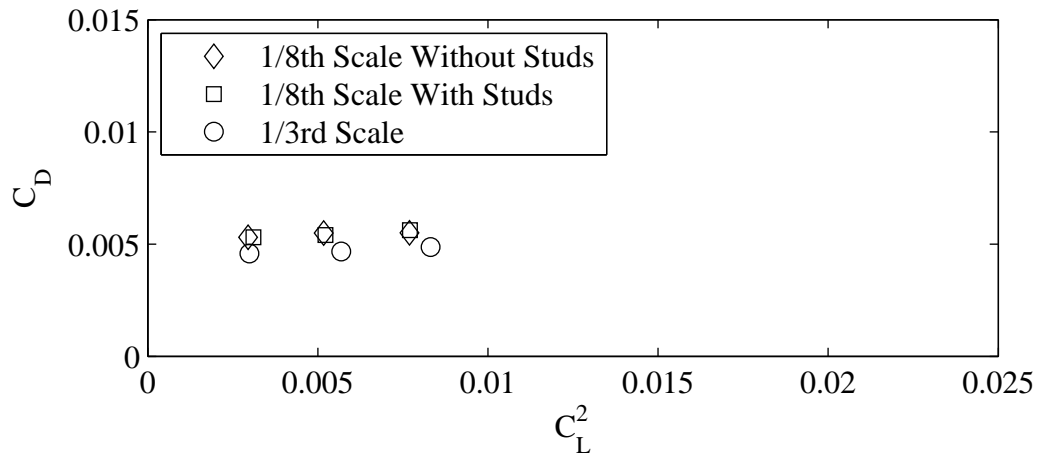
Figure F.15: Froude number 0.27, Yaw 0 degrees, Heel 10 degrees, Rudder 2 degrees.



(a) Coefficient of lift plotted against variation in trim tab angle.

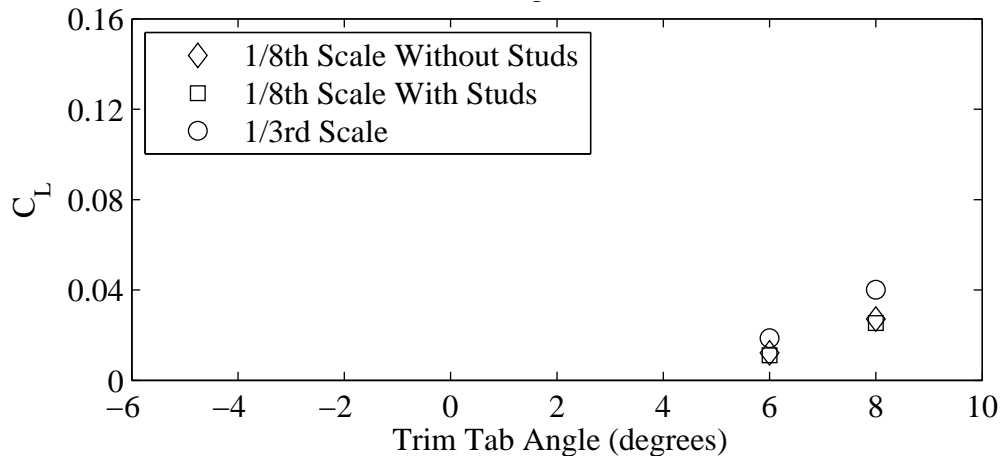


(b) Coefficient of drag plotted against variation in trim tab angle.

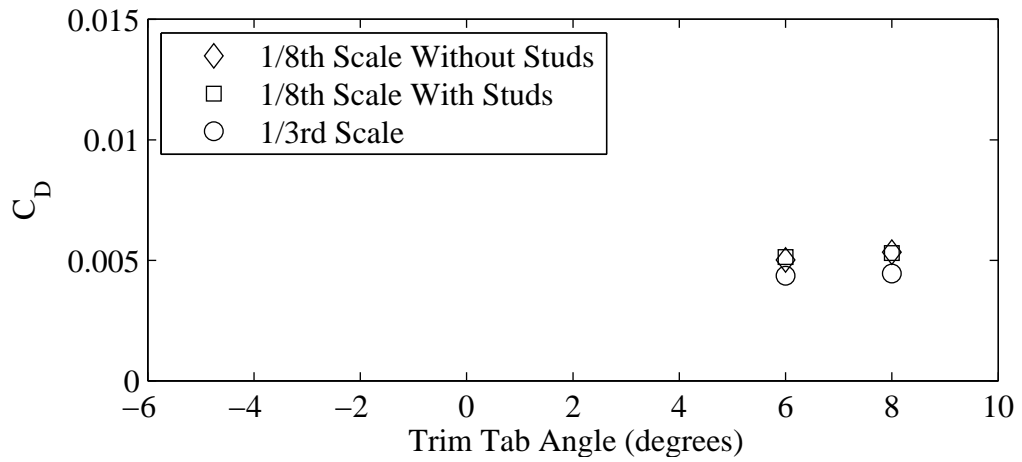


(c) Coefficient of drag plotted against variation in coefficient of lift squared.

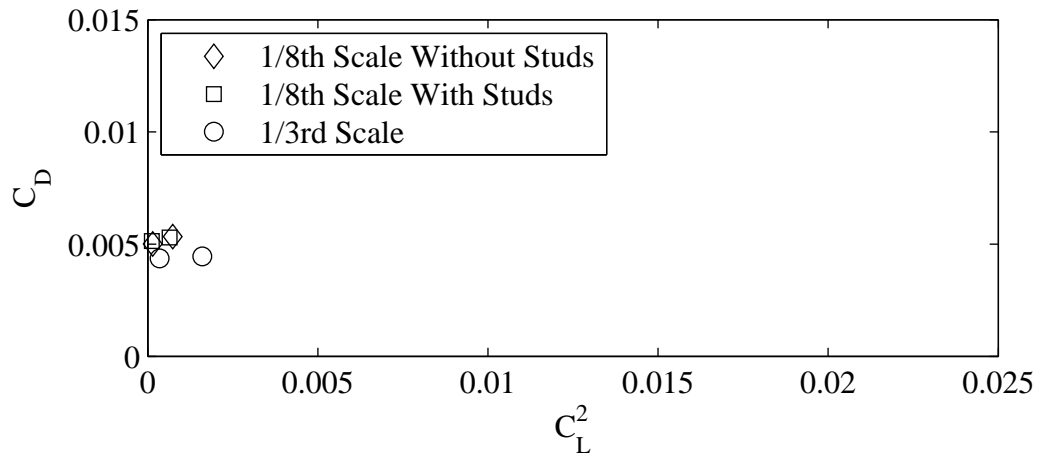
Figure F.16: Froude number 0.29, Yaw 0 degrees, Heel 10 degrees, Rudder 2 degrees.



(a) Coefficient of lift plotted against variation in trim tab angle.

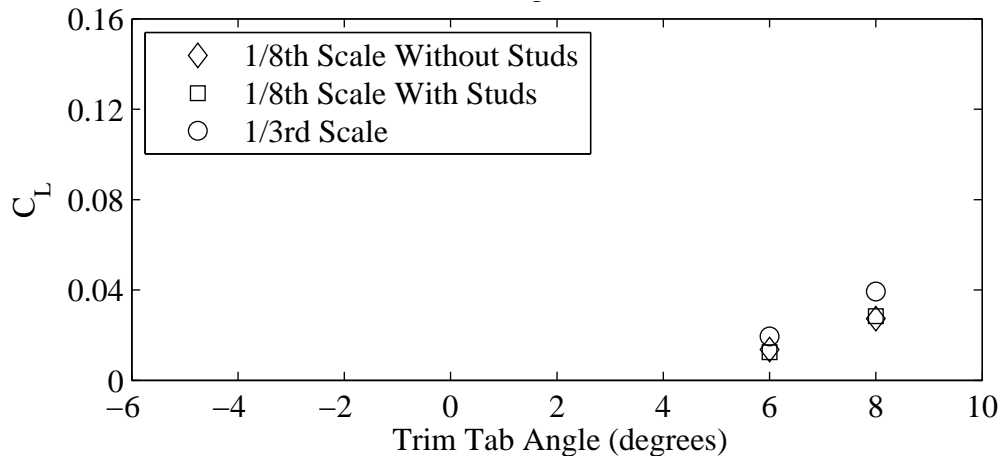


(b) Coefficient of drag plotted against variation in trim tab angle.

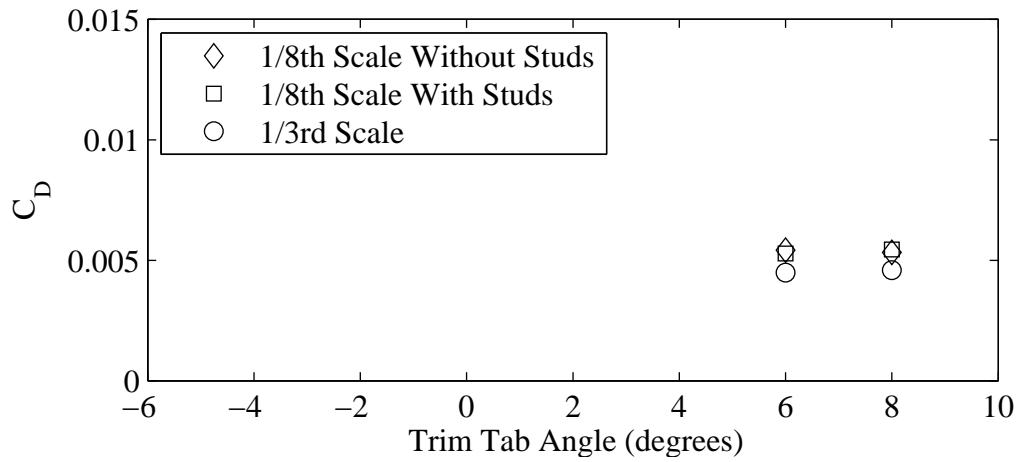


(c) Coefficient of drag plotted against variation in coefficient of lift squared.

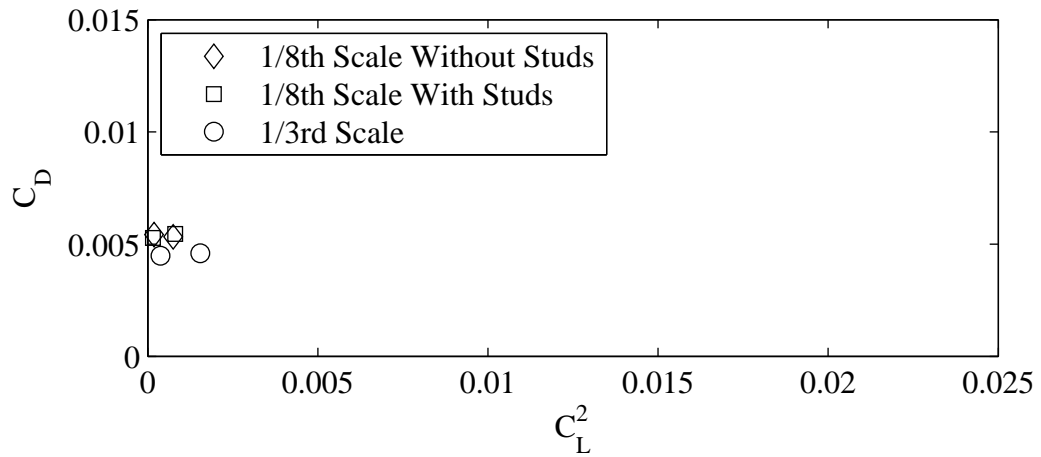
Figure F.17: Froude number 0.27, Yaw -2 degrees, Heel 10 degrees, Rudder 2 degrees.



(a) Coefficient of lift plotted against variation in trim tab angle.

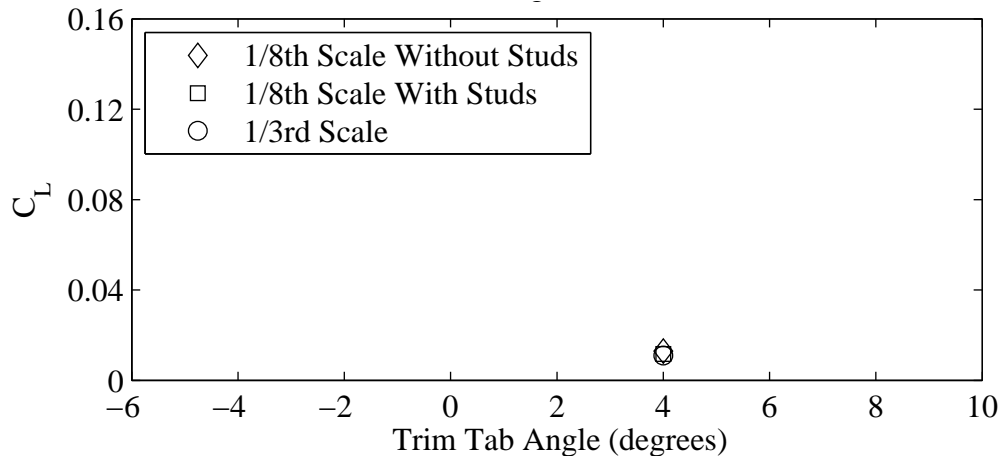


(b) Coefficient of drag plotted against variation in trim tab angle.

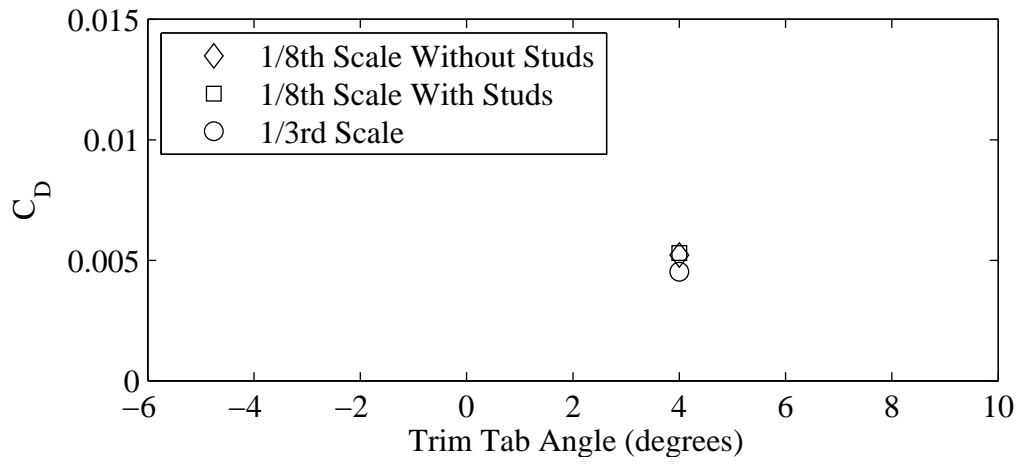


(c) Coefficient of drag plotted against variation in coefficient of lift squared.

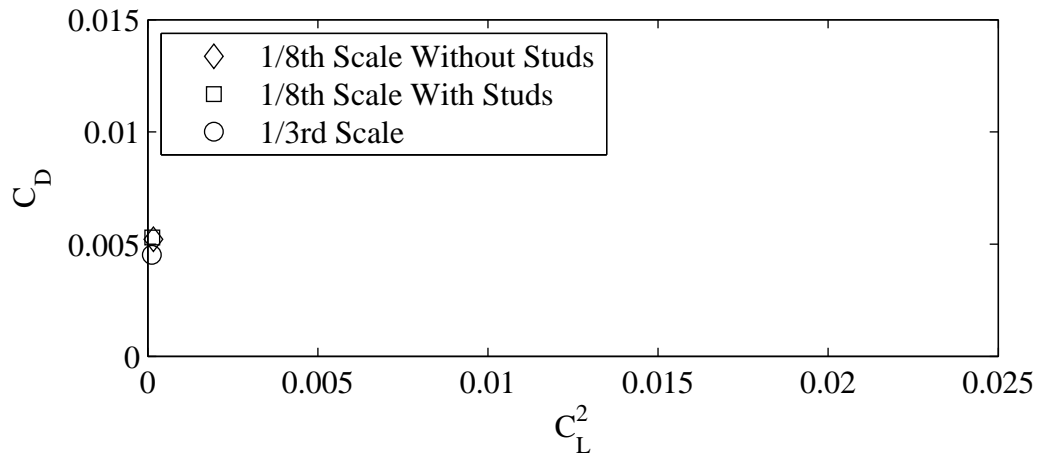
Figure F.18: Froude number 0.29, Yaw -2 degrees, Heel 10 degrees, Rudder 2 degrees.



(a) Coefficient of lift plotted against variation in trim tab angle.

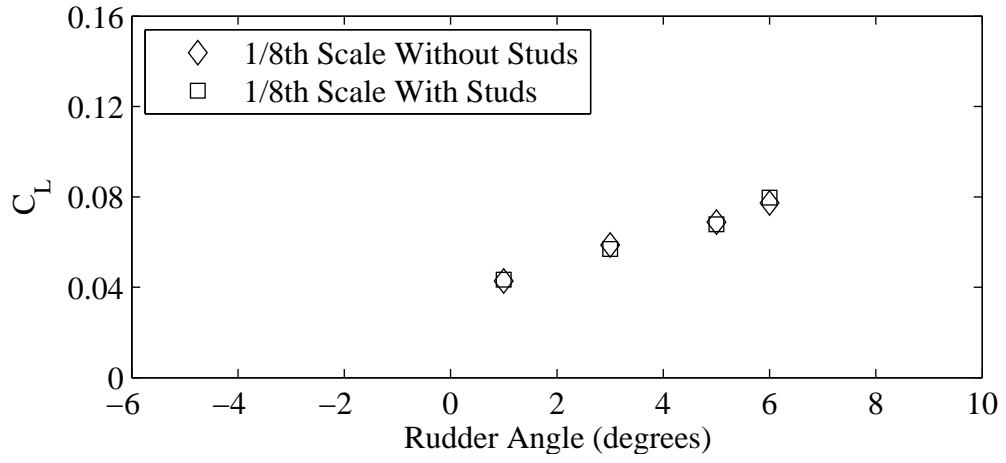


(b) Coefficient of drag plotted against variation in trim tab angle.

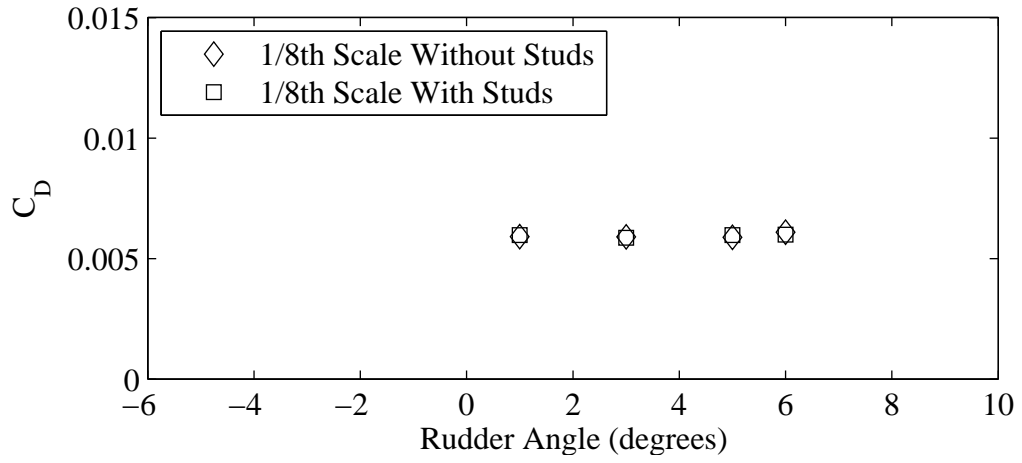


(c) Coefficient of drag plotted against variation in coefficient of lift squared.

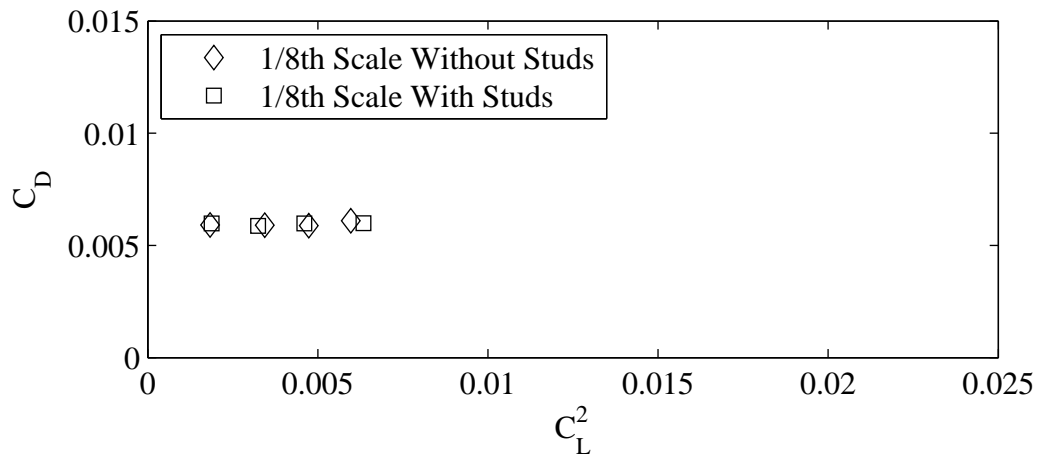
Figure F.19: Froude number 0.29, Yaw -2 degrees, Heel 10 degrees, Rudder 4 degrees.



(a) Coefficient of lift plotted against variation in rudder angle.

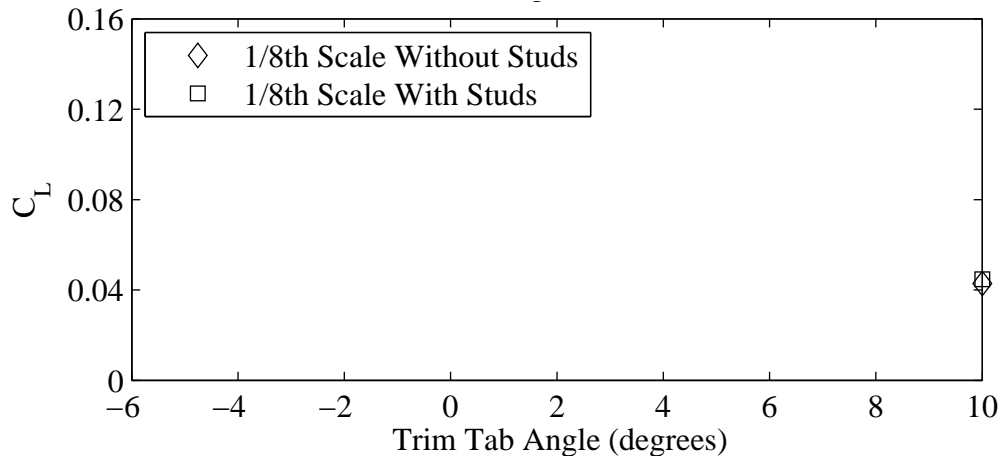


(b) Coefficient of drag plotted against variation in rudder angle.

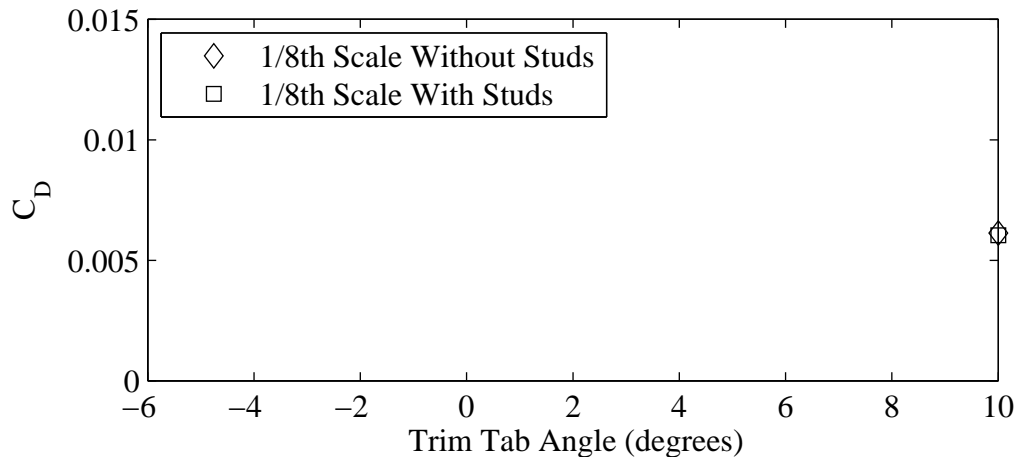


(c) Coefficient of drag plotted against variation in coefficient of lift squared.

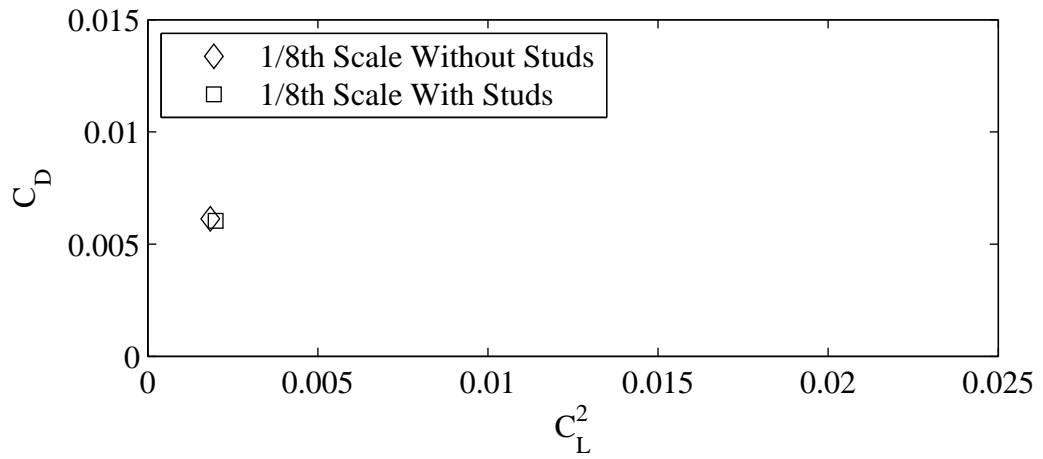
Figure F.20: Froude number 0.32, Yaw -2 degrees, Heel 20 degrees, Tab 10 degrees.



(a) Coefficient of lift plotted against variation in trim tab angle.

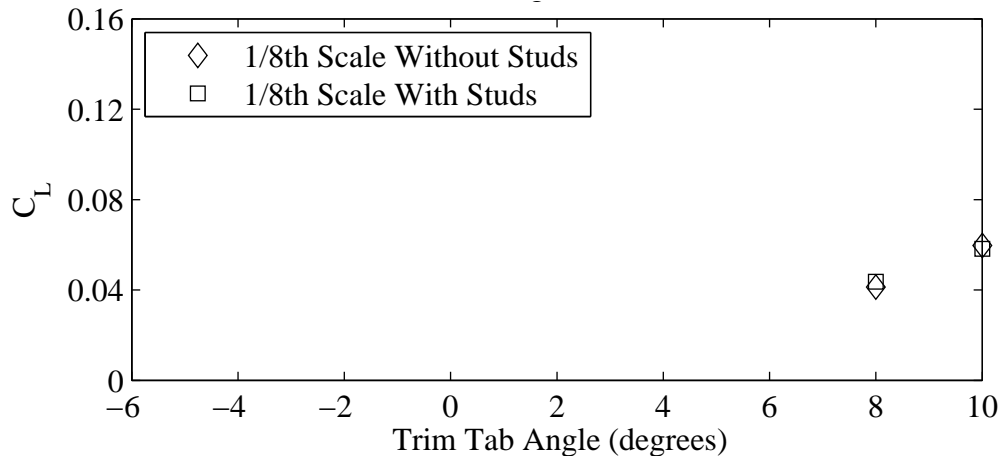


(b) Coefficient of drag plotted against variation in trim tab angle.

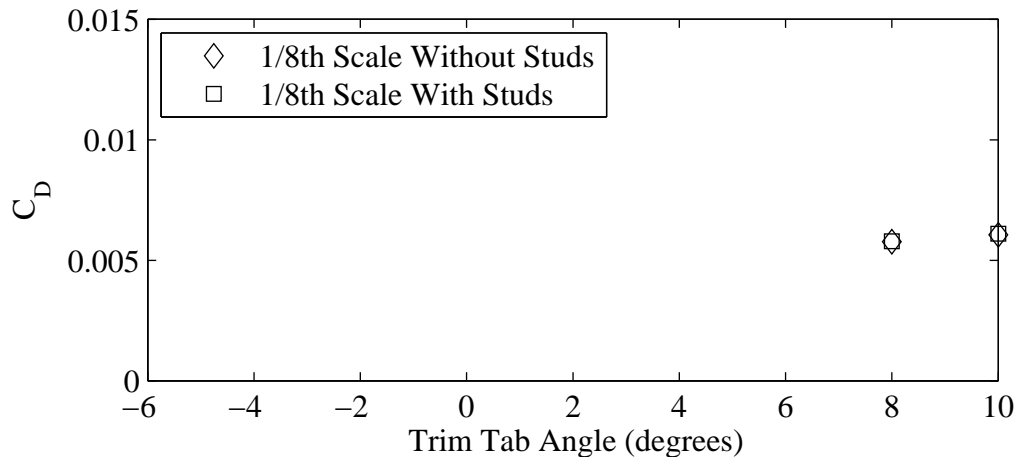


(c) Coefficient of drag plotted against variation in coefficient of lift squared.

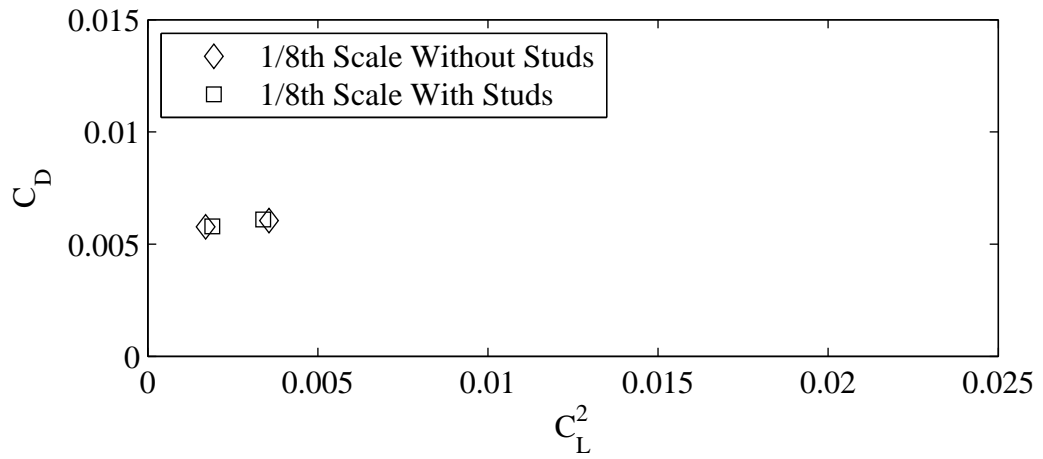
Figure F.21: Froude number 0.34, Yaw -2 degrees, Heel 20 degrees, Rudder 1 degrees.



(a) Coefficient of lift plotted against variation in trim tab angle.

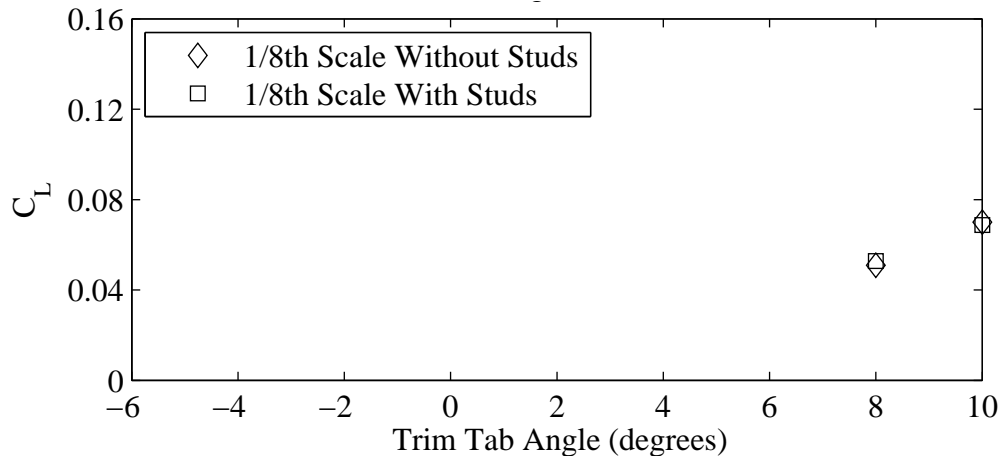


(b) Coefficient of drag plotted against variation in trim tab angle.

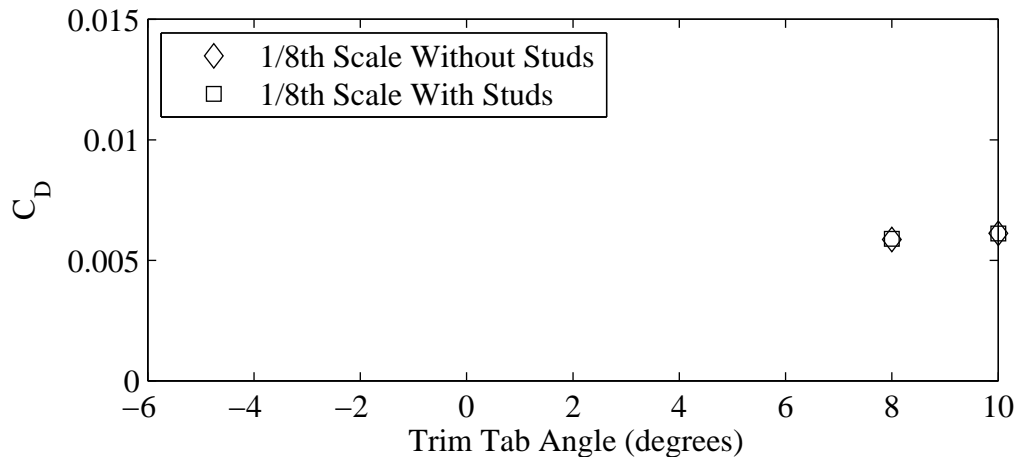


(c) Coefficient of drag plotted against variation in coefficient of lift squared.

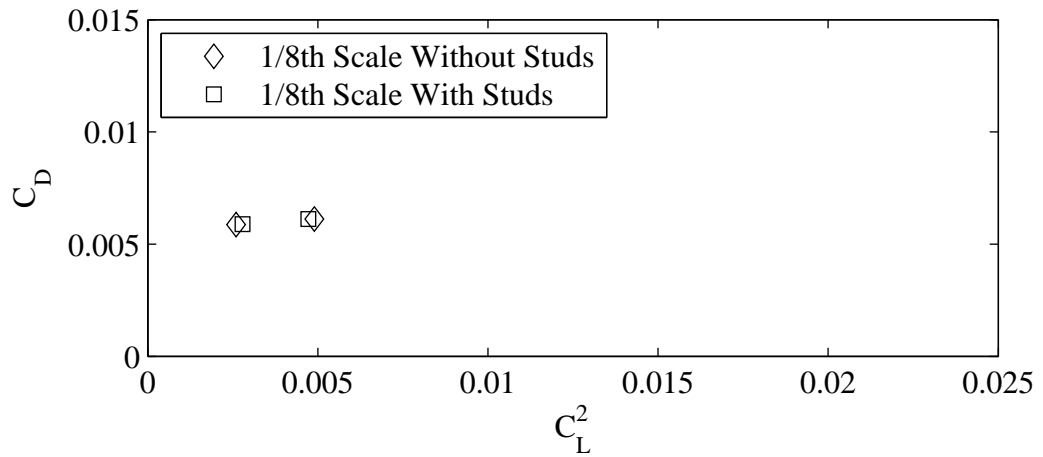
Figure F.22: Froude number 0.34, Yaw -2 degrees, Heel 20 degrees, Rudder 3 degrees.



(a) Coefficient of lift plotted against variation in trim tab angle.

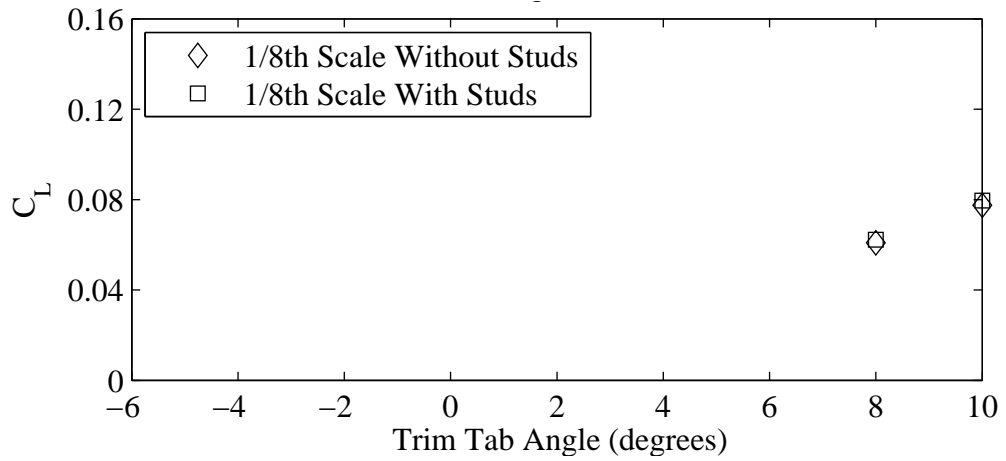


(b) Coefficient of drag plotted against variation in trim tab angle.

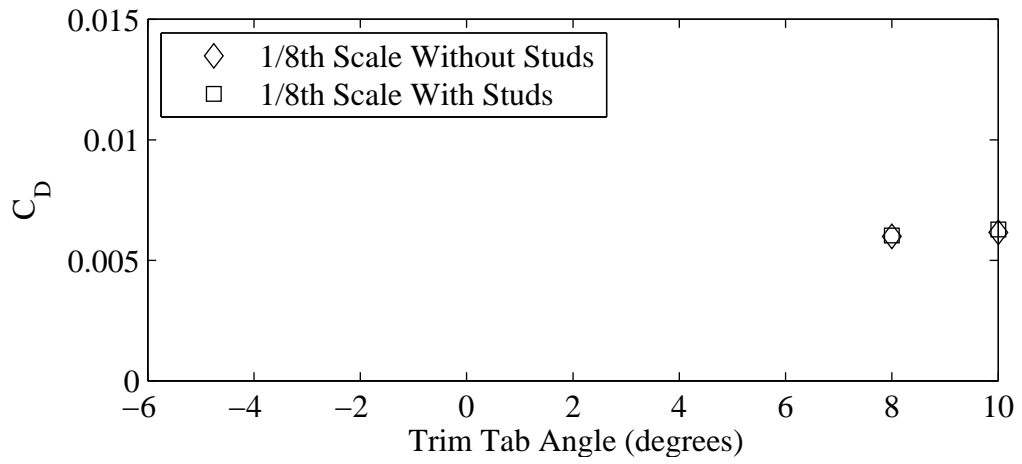


(c) Coefficient of drag plotted against variation in coefficient of lift squared.

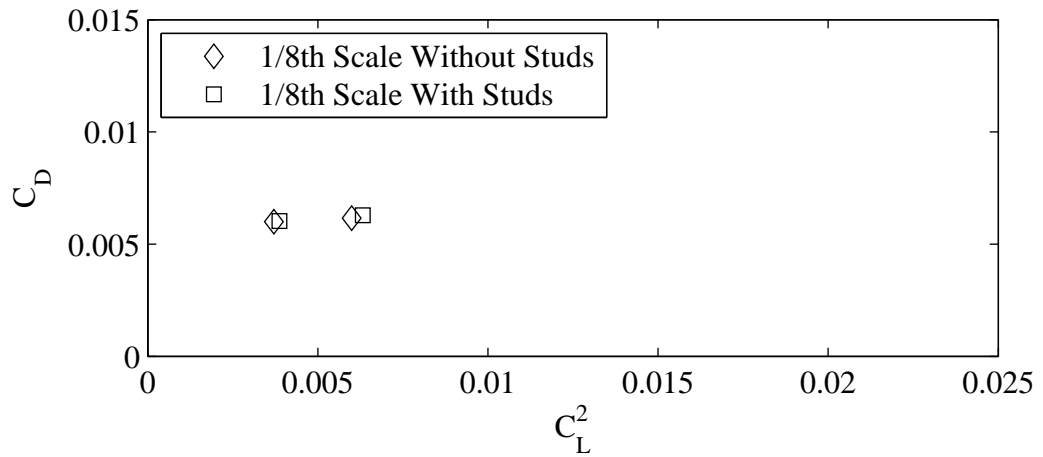
Figure F.23: Froude number 0.34, Yaw -2 degrees, Heel 20 degrees, Rudder 5 degrees.



(a) Coefficient of lift plotted against variation in trim tab angle.

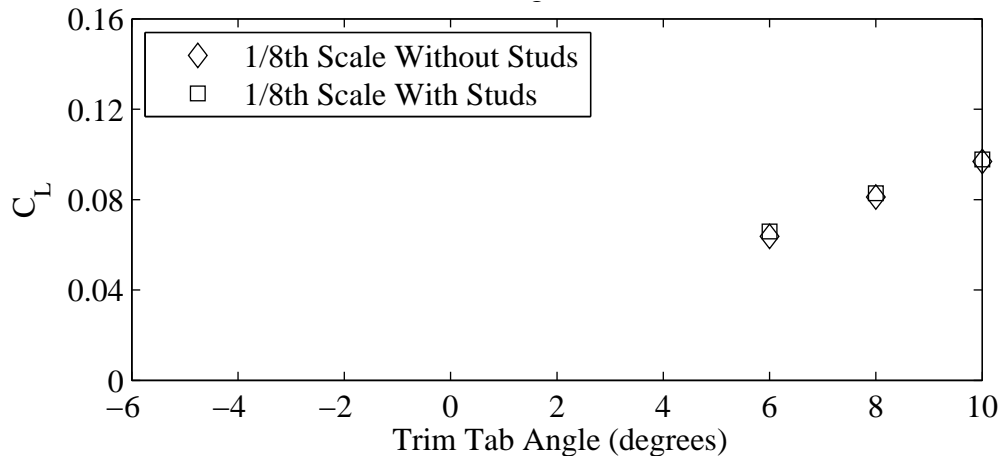


(b) Coefficient of drag plotted against variation in trim tab angle.

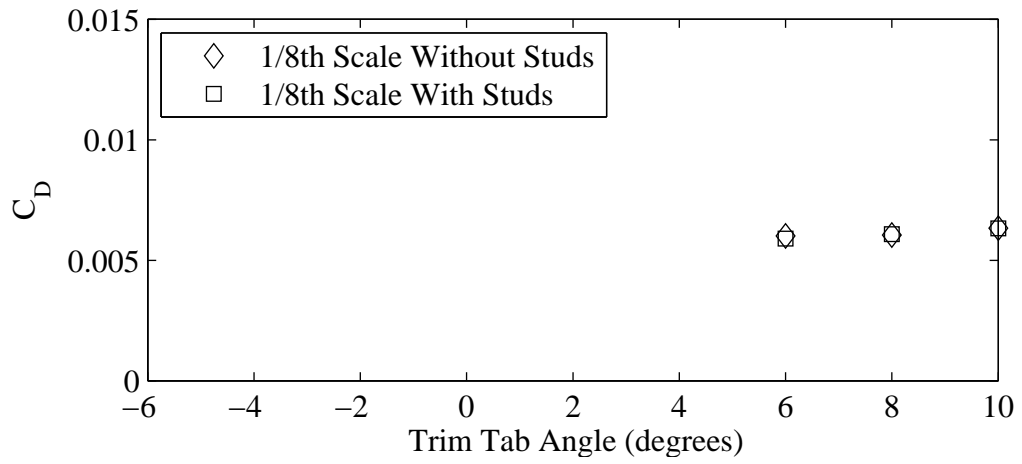


(c) Coefficient of drag plotted against variation in coefficient of lift squared.

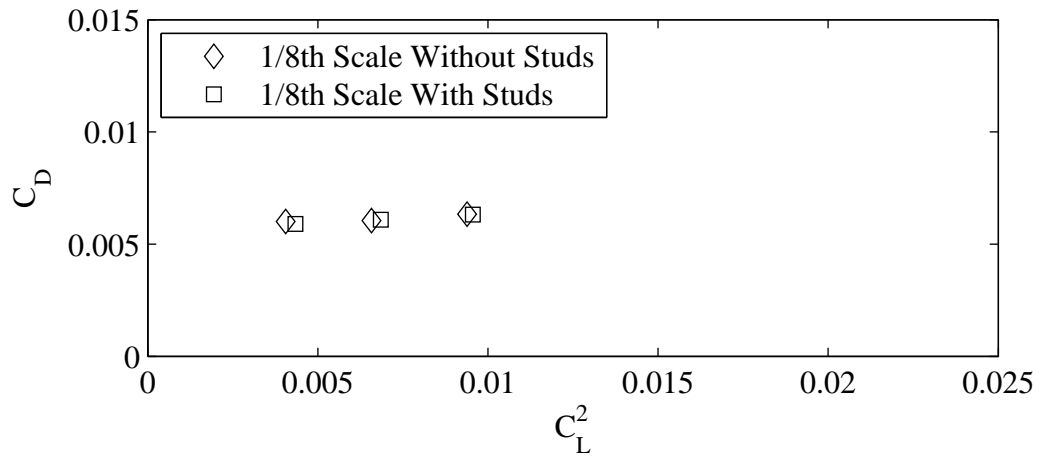
Figure F.24: Froude number 0.34, Yaw -2 degrees, Heel 20 degrees, Rudder 6 degrees.



(a) Coefficient of lift plotted against variation in trim tab angle.

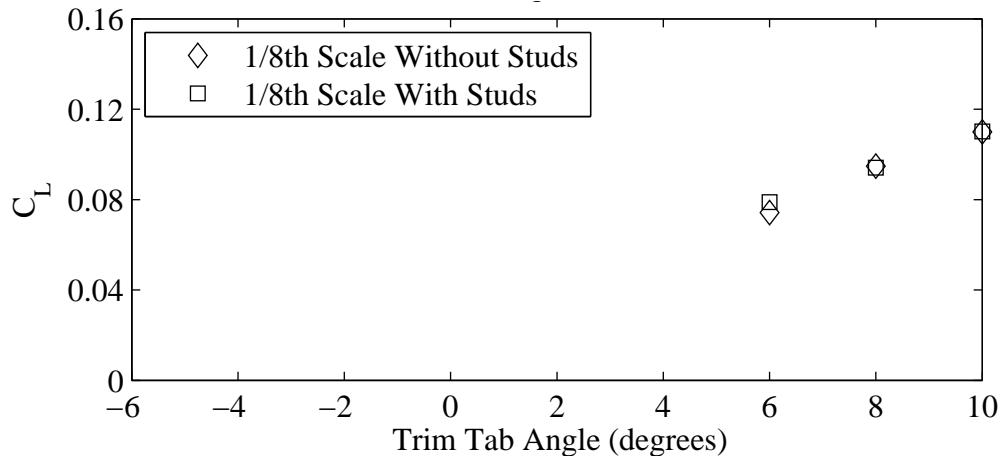


(b) Coefficient of drag plotted against variation in trim tab angle.

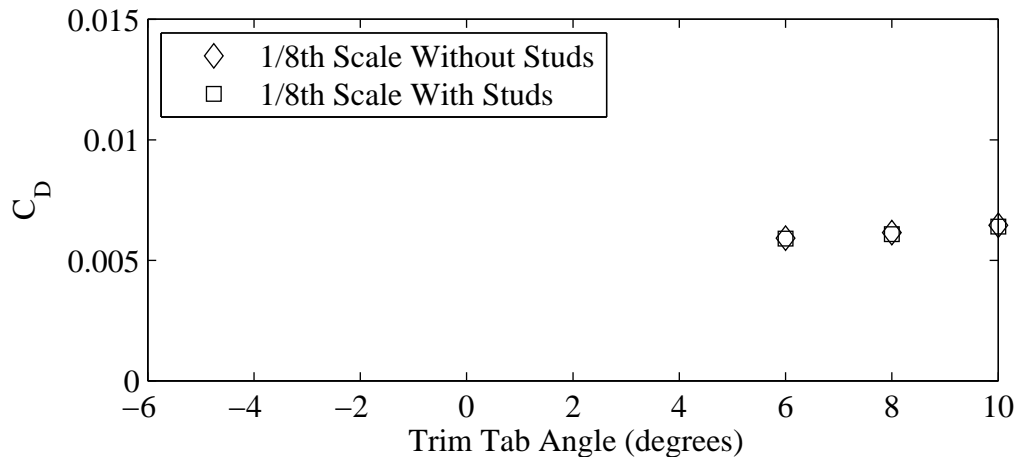


(c) Coefficient of drag plotted against variation in coefficient of lift squared.

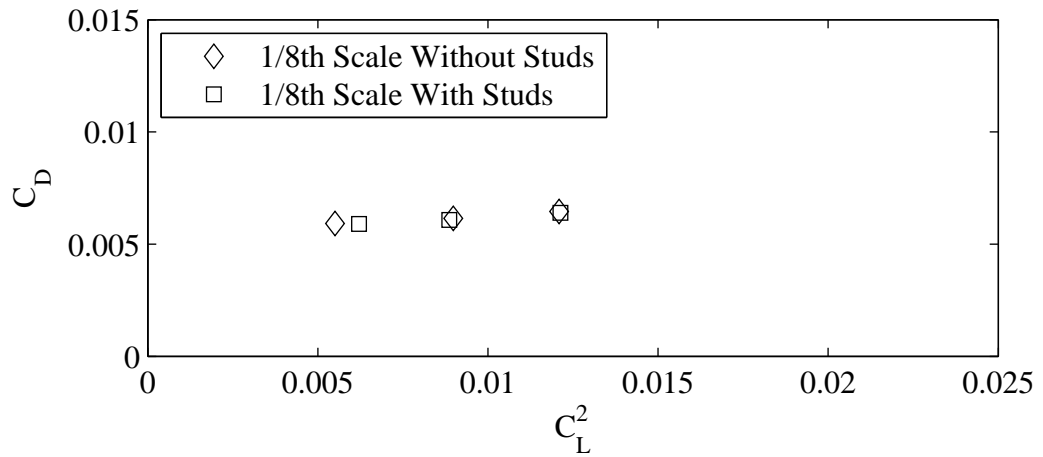
Figure F.25: Froude number 0.34, Yaw 0 degrees, Heel 20 degrees, Rudder 1 degrees.



(a) Coefficient of lift plotted against variation in trim tab angle.

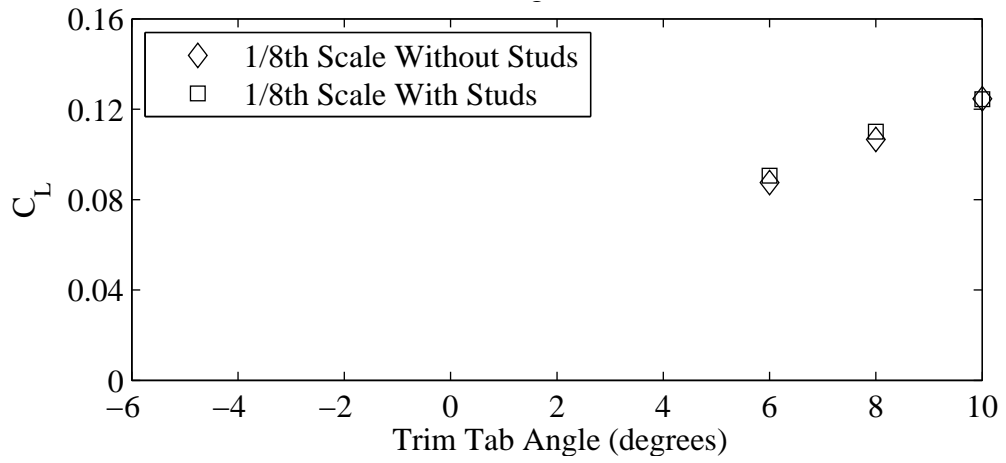


(b) Coefficient of drag plotted against variation in trim tab angle.

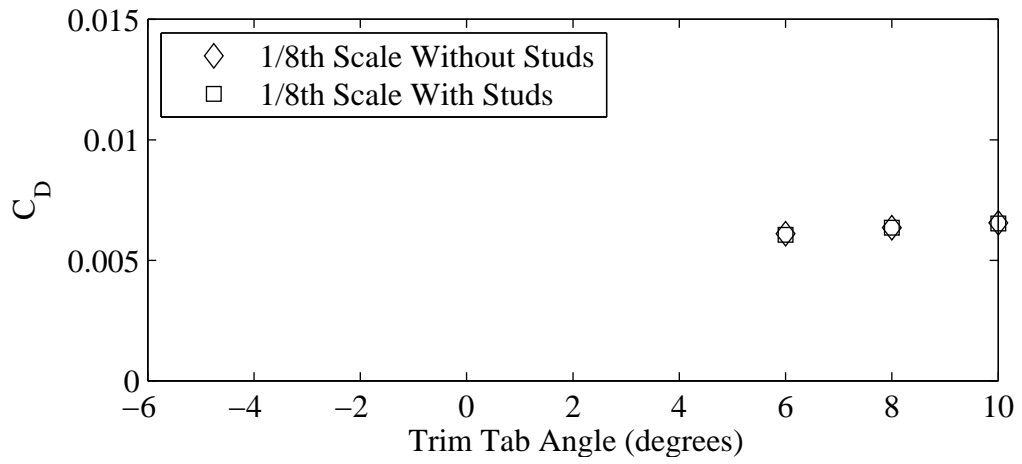


(c) Coefficient of drag plotted against variation in coefficient of lift squared.

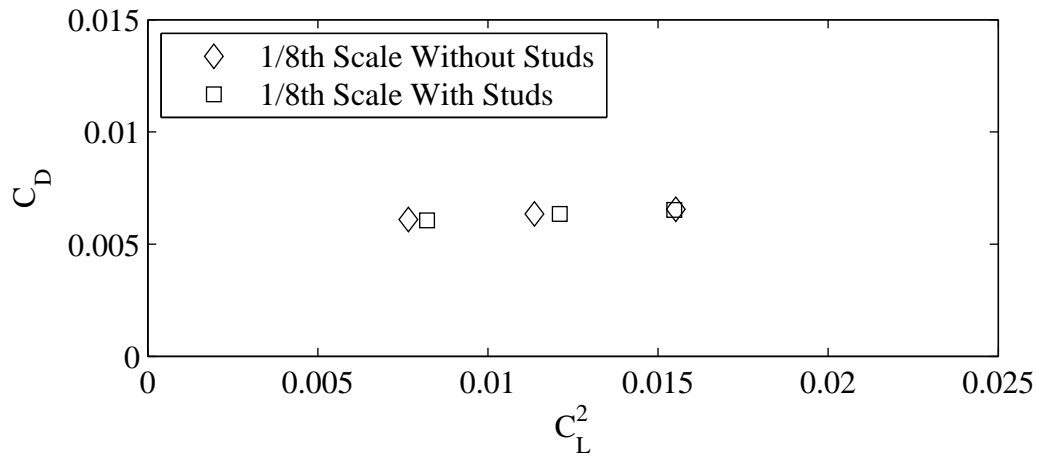
Figure F.26: Froude number 0.34, Yaw 0 degrees, Heel 20 degrees, Rudder 3 degrees.



(a) Coefficient of lift plotted against variation in trim tab angle.

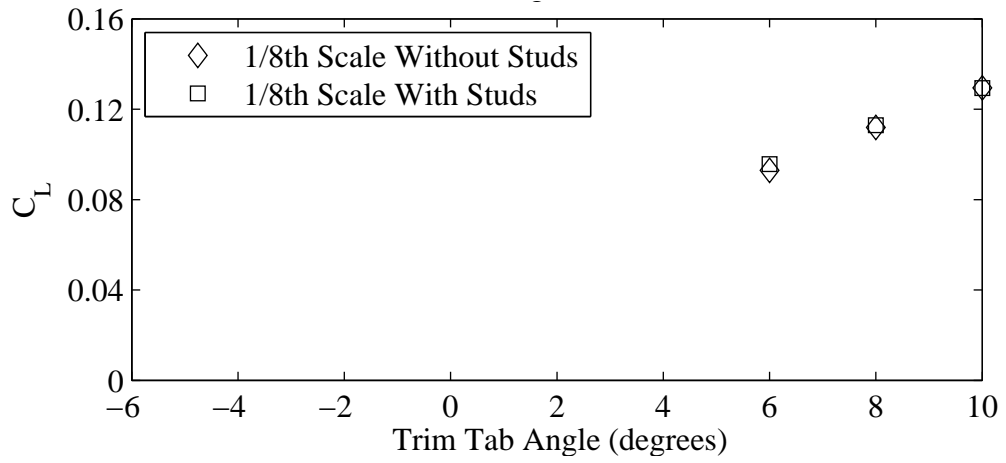


(b) Coefficient of drag plotted against variation in trim tab angle.

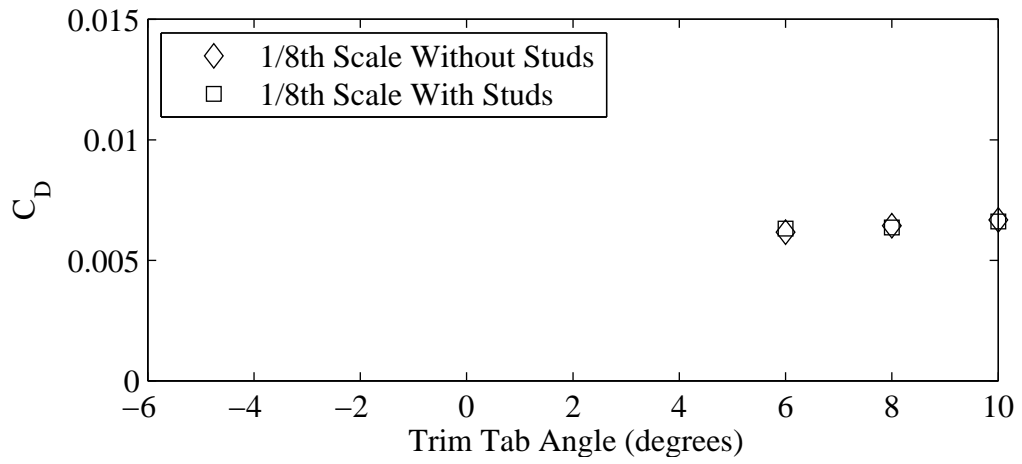


(c) Coefficient of drag plotted against variation in coefficient of lift squared.

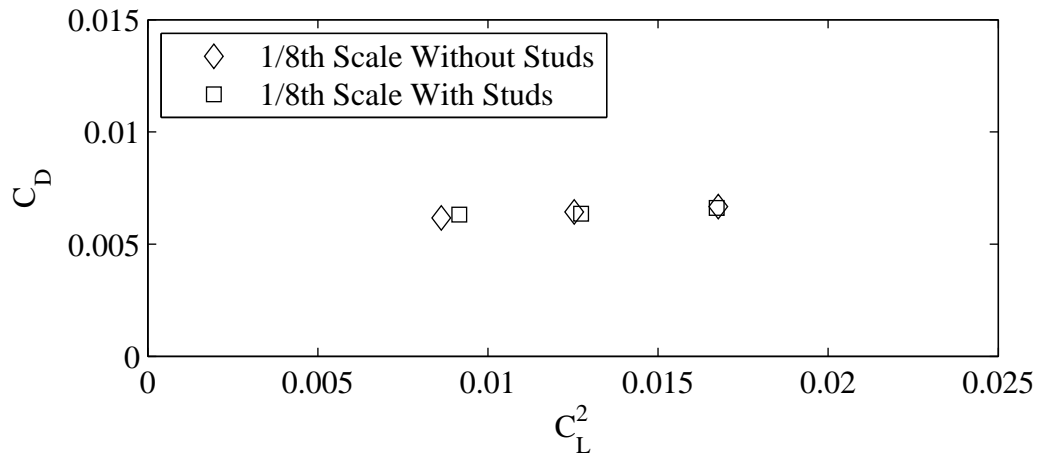
Figure F.27: Froude number 0.34, Yaw 0 degrees, Heel 20 degrees, Rudder 5 degrees.



(a) Coefficient of lift plotted against variation in trim tab angle.

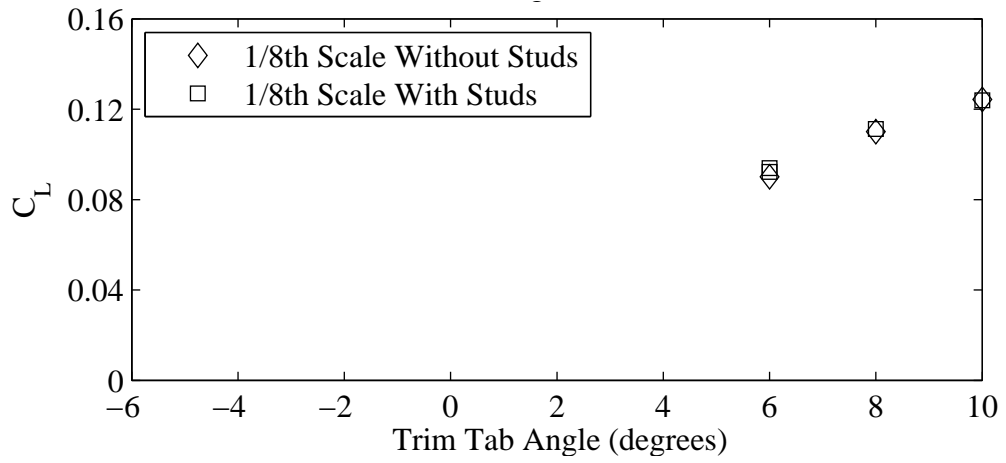


(b) Coefficient of drag plotted against variation in trim tab angle.

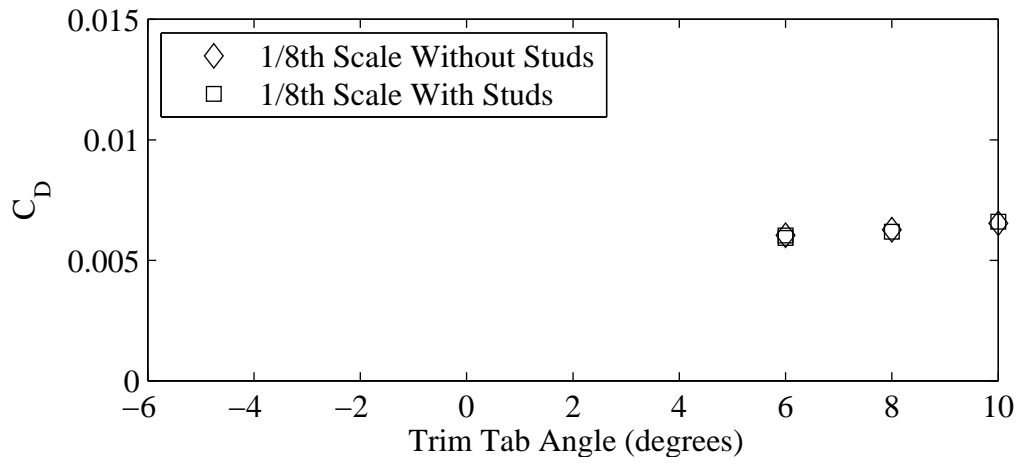


(c) Coefficient of drag plotted against variation in coefficient of lift squared.

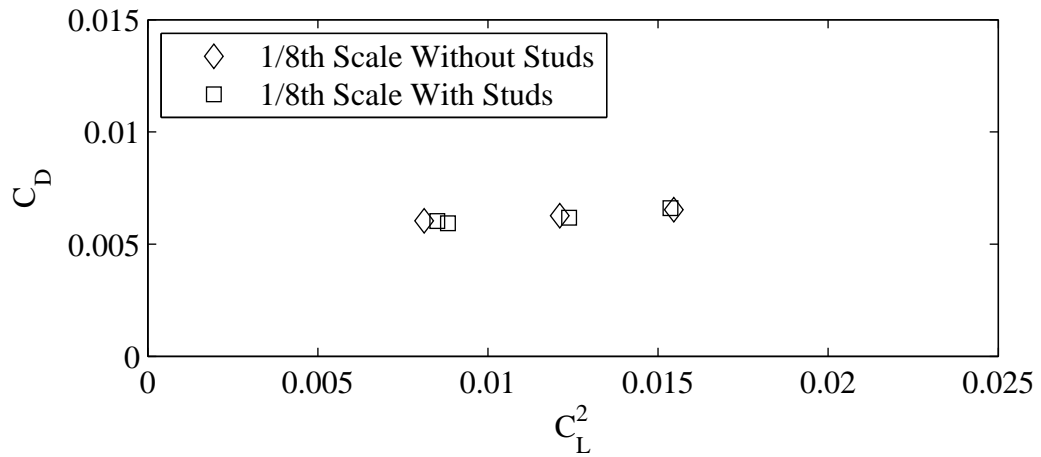
Figure F.28: Froude number 0.34, Yaw 0 degrees, Heel 20 degrees, Rudder 6 degrees.



(a) Coefficient of lift plotted against variation in trim tab angle.

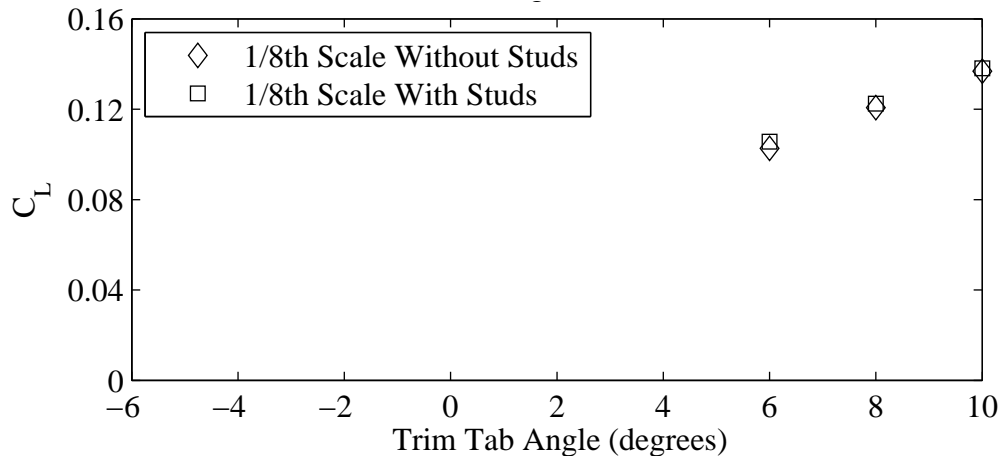


(b) Coefficient of drag plotted against variation in trim tab angle.

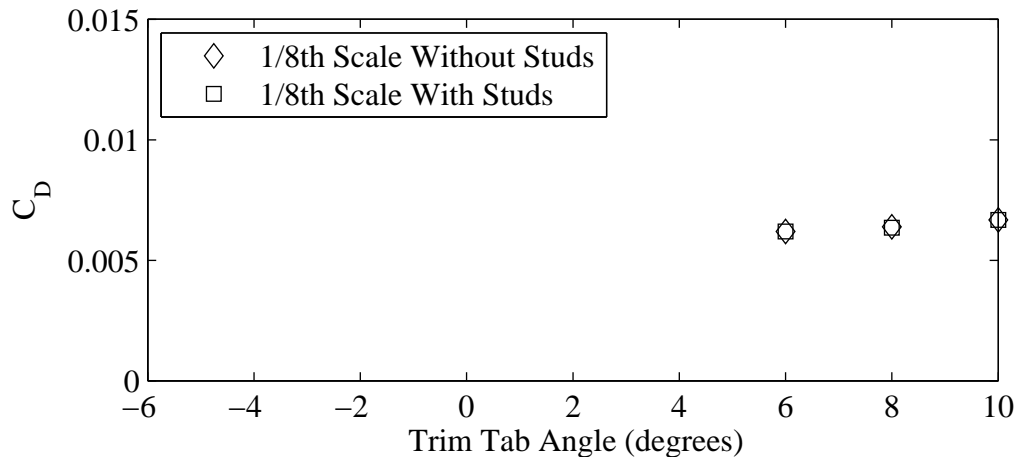


(c) Coefficient of drag plotted against variation in coefficient of lift squared.

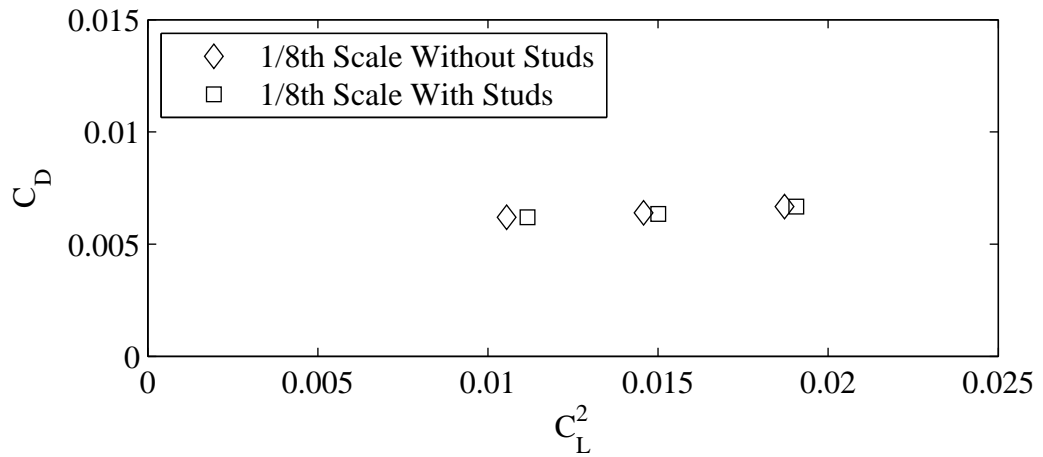
Figure F.29: Froude number 0.34, Yaw 1 degrees, Heel 20 degrees, Rudder 1 degrees.



(a) Coefficient of lift plotted against variation in trim tab angle.

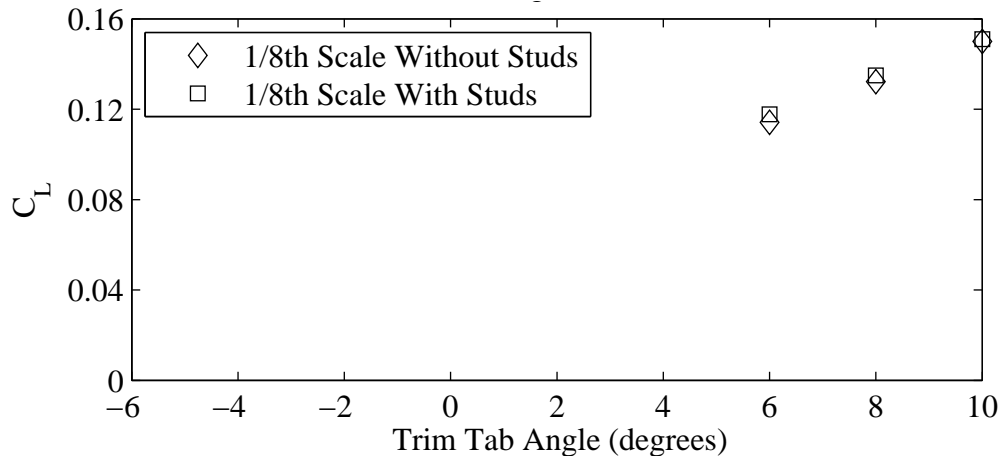


(b) Coefficient of drag plotted against variation in trim tab angle.

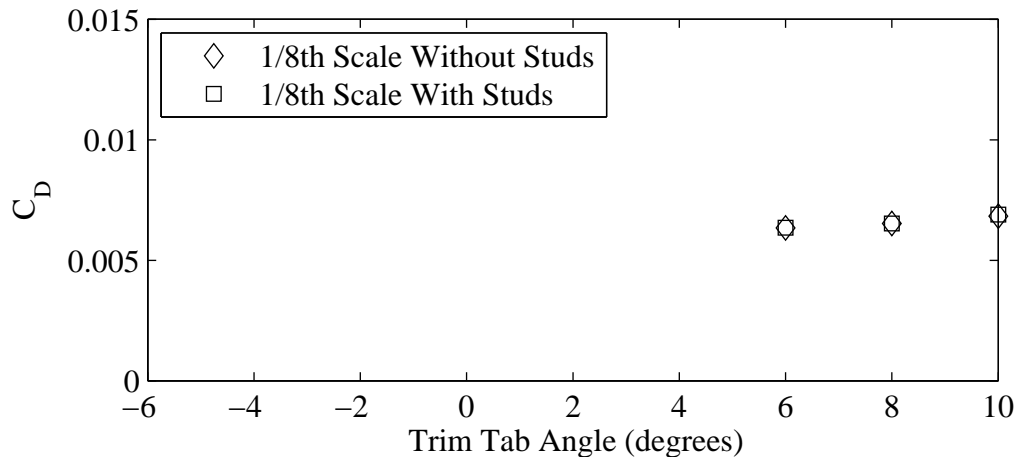


(c) Coefficient of drag plotted against variation in coefficient of lift squared.

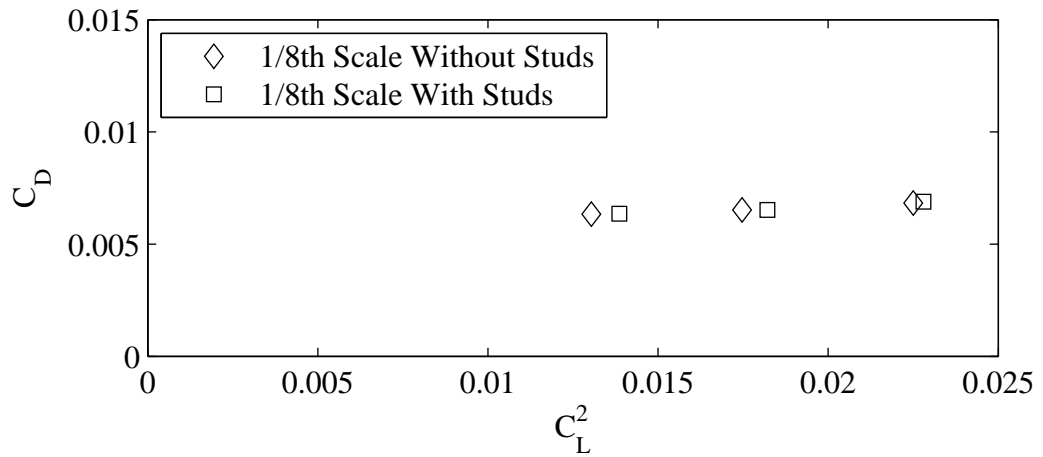
Figure F.30: Froude number 0.34, Yaw 1 degrees, Heel 20 degrees, Rudder 3 degrees.



(a) Coefficient of lift plotted against variation in trim tab angle.

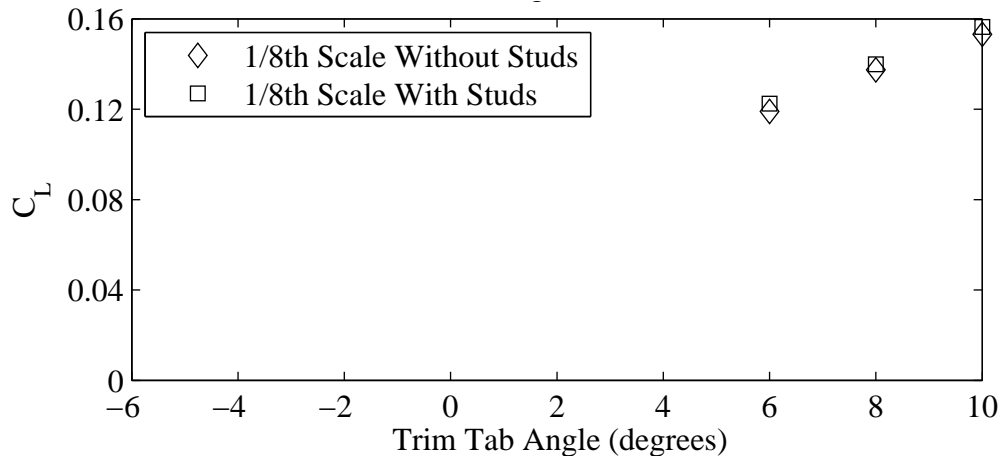


(b) Coefficient of drag plotted against variation in trim tab angle.

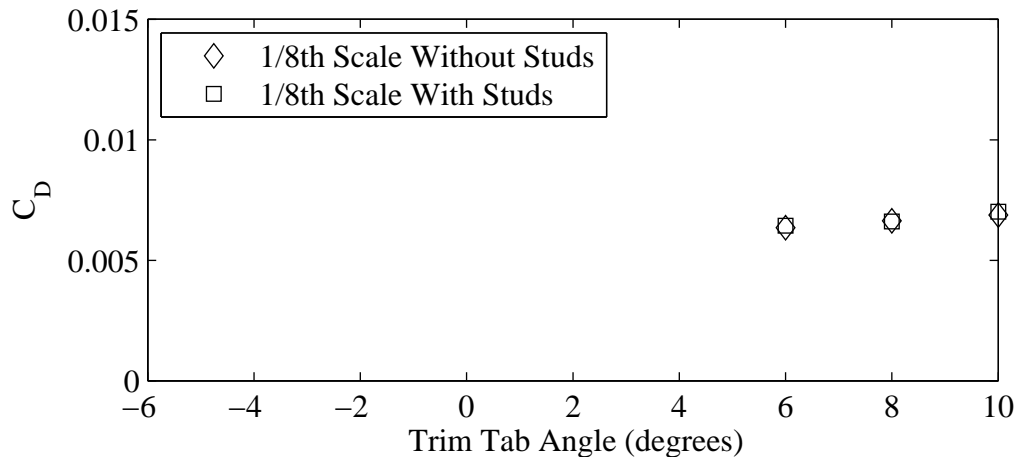


(c) Coefficient of drag plotted against variation in coefficient of lift squared.

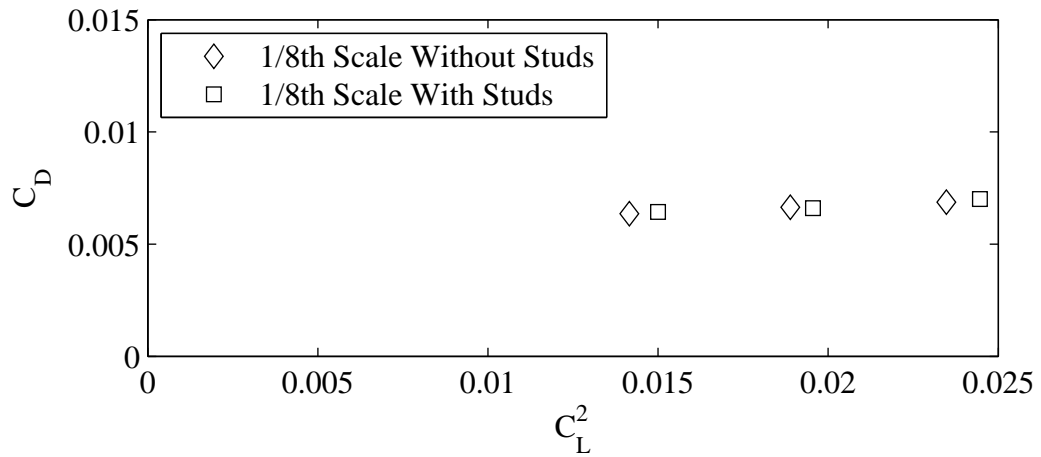
Figure F.31: Froude number 0.34, Yaw 1 degrees, Heel 20 degrees, Rudder 5 degrees.



(a) Coefficient of lift plotted against variation in trim tab angle.

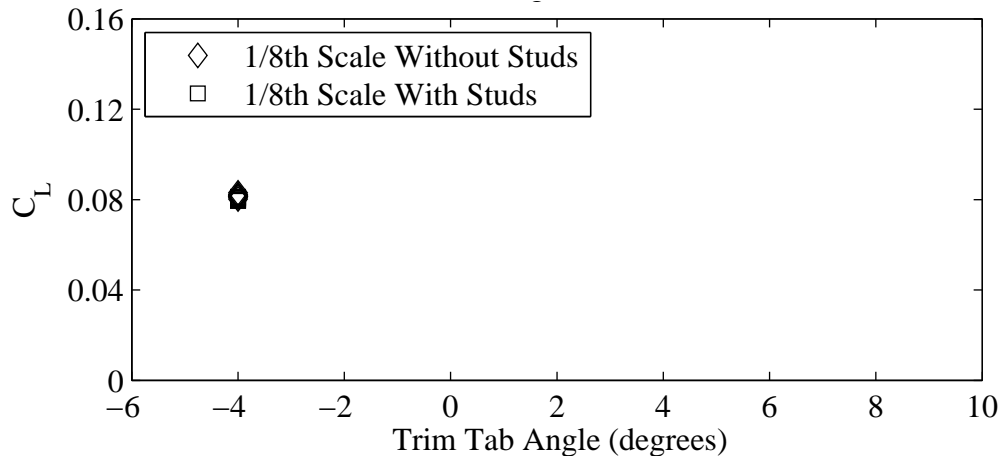


(b) Coefficient of drag plotted against variation in trim tab angle.

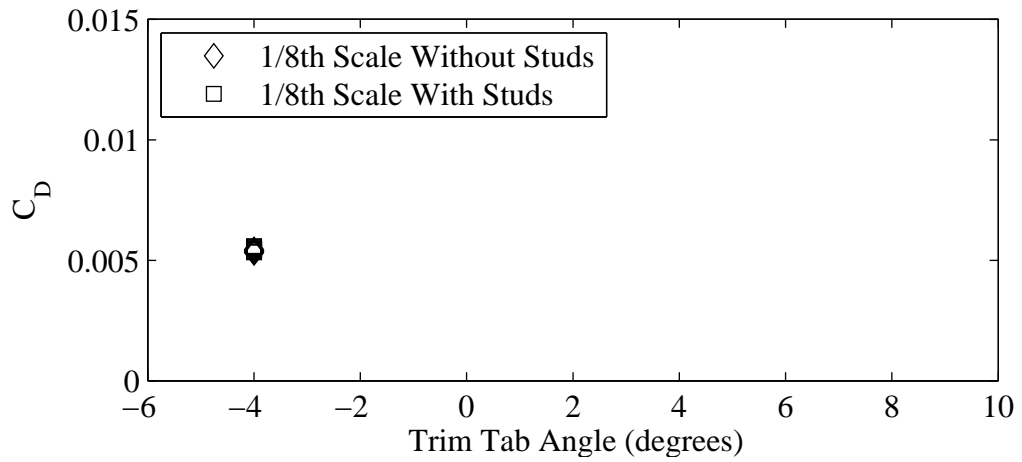


(c) Coefficient of drag plotted against variation in coefficient of lift squared.

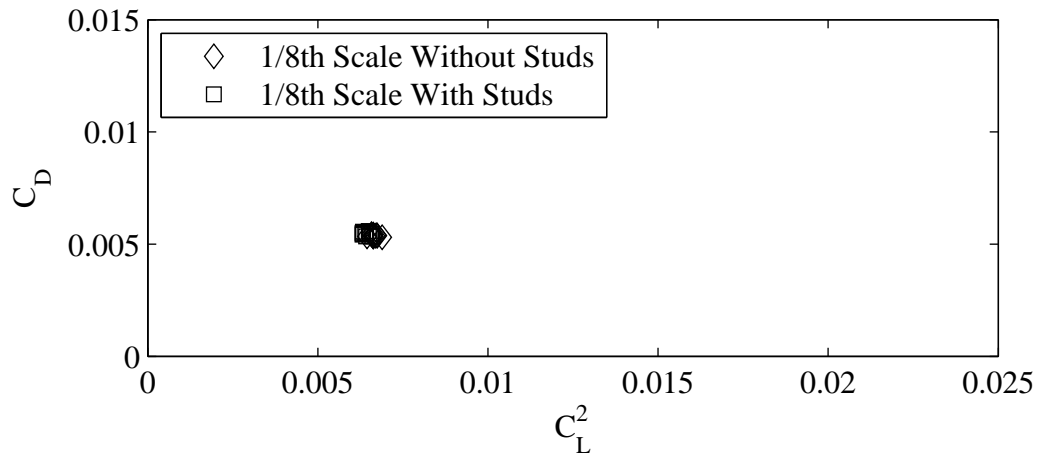
Figure F.32: Froude number 0.34, Yaw 1 degrees, Heel 20 degrees, Rudder 6 degrees.



(a) Coefficient of lift plotted against variation in trim tab angle.

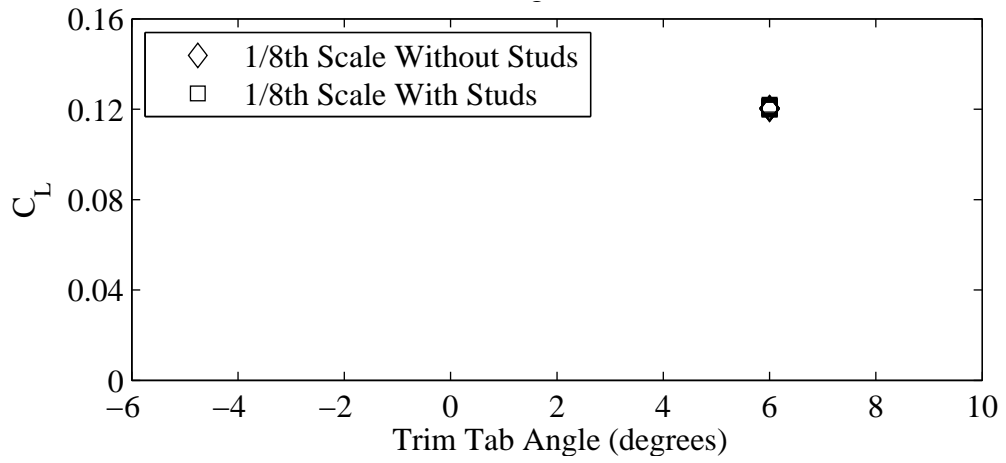


(b) Coefficient of drag plotted against variation in trim tab angle.

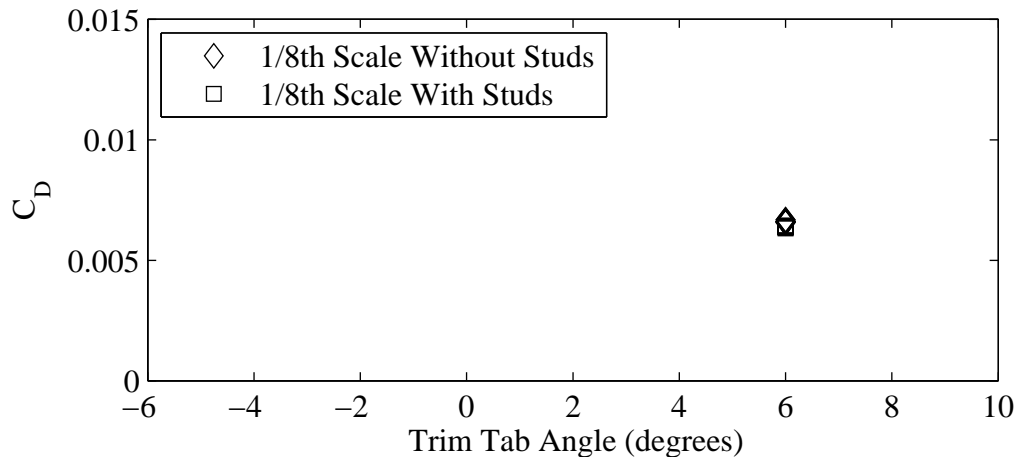


(c) Coefficient of drag plotted against variation in coefficient of lift squared.

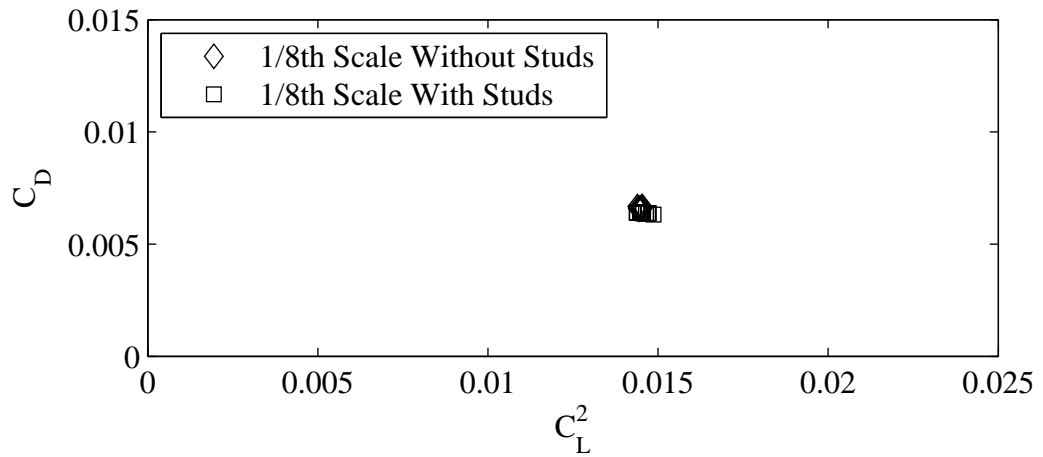
Figure F.33: Froude number 0.27, Yaw -1 degrees, Heel -10 degrees, Tab -4 degrees, Rudder -2 degrees.



(a) Coefficient of lift plotted against variation in trim tab angle.



(b) Coefficient of drag plotted against variation in trim tab angle.



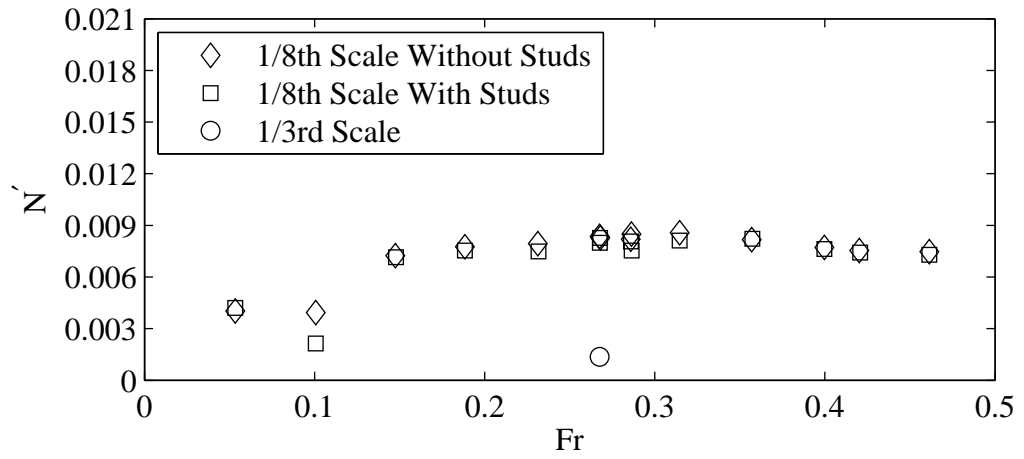
(c) Coefficient of drag plotted against variation in coefficient of lift squared.

Figure F.34: Froude number 0.34, Yaw 1 degrees, Heel 20 degrees, Tab 6 degrees, Rudder 6 degrees.

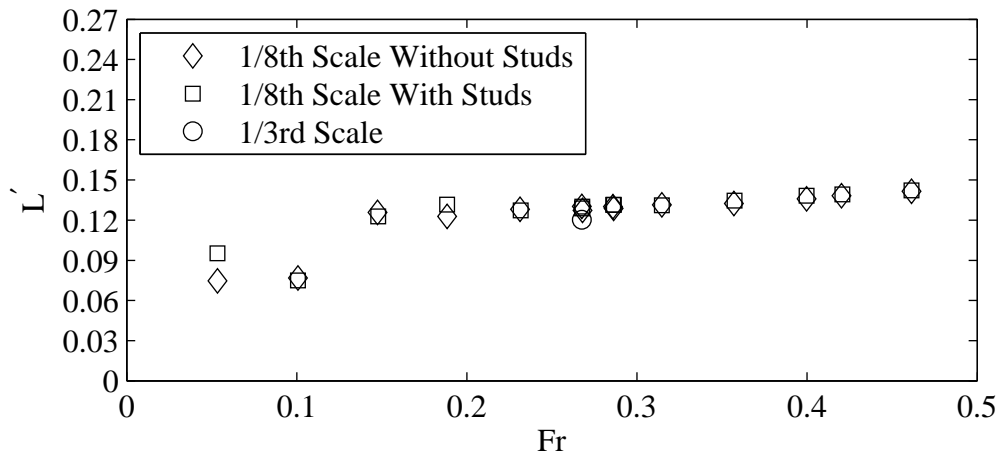
Appendix G

Supplementary Moment Data

This section contains plots of non-dimensional yaw (N') and heel moment (L') with variation in Froude number, rudder angle and trim tab angle. Where available results from the $1/3^{rd}$ model tests are plotted along with those of the $1/8^{th}$ test data.

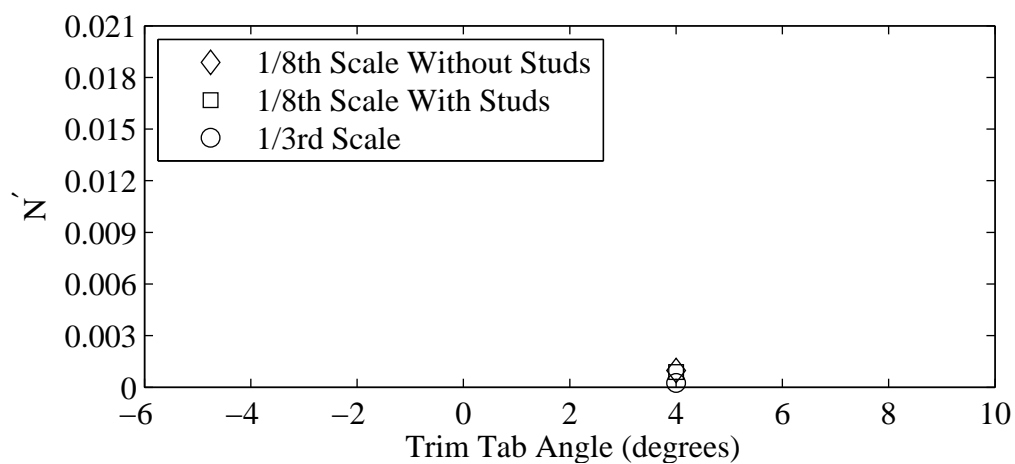


(a) Non-dimensional yaw moment plotted against variation in Froude number.

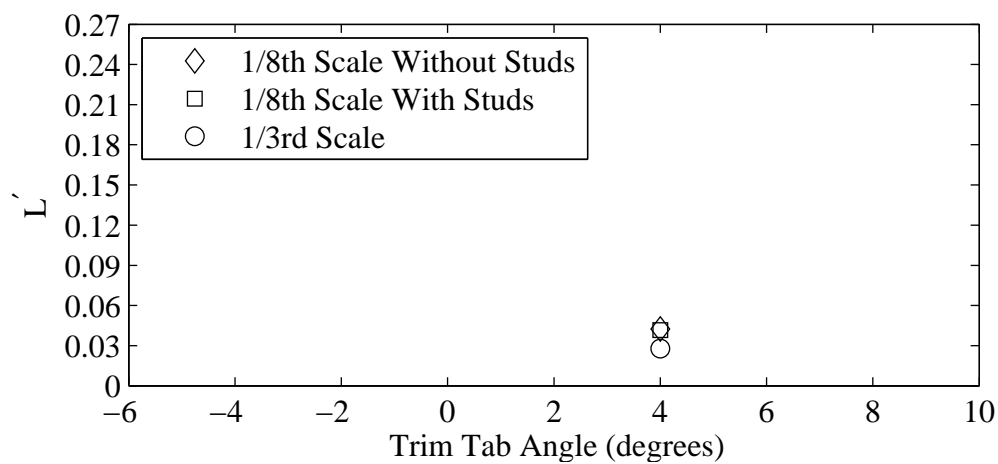


(b) Non-dimensional heel moment plotted against variation in Froude number.

Figure G.1: Yaw 1 degrees, Heel 10 degrees, Tab 4 degrees, Rudder 2 degrees.

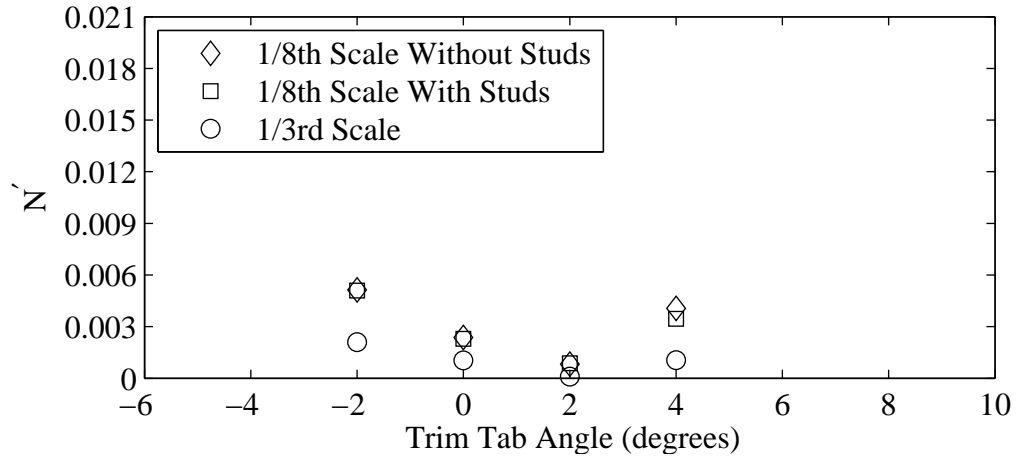


(a) Non-dimensional yaw moment plotted against variation in trim tab angle.

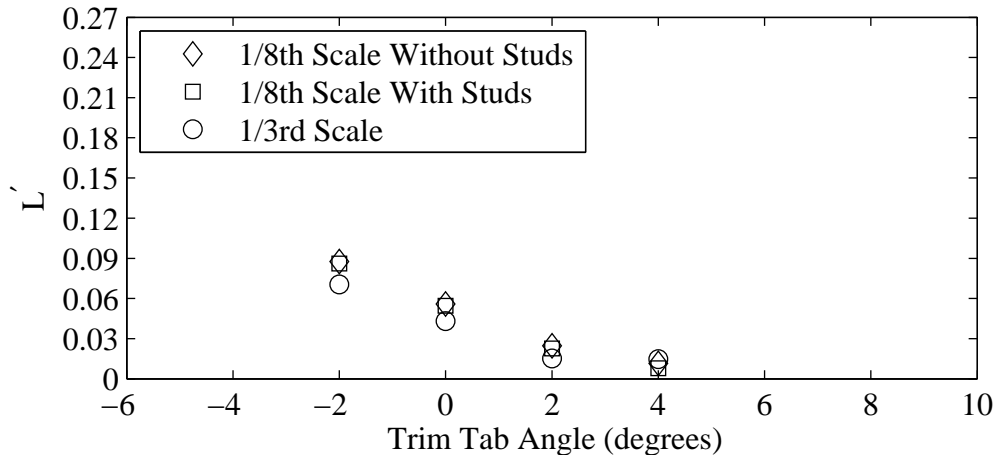


(b) Non-dimensional heel moment plotted against variation in trim tab angle.

Figure G.2: Froude number 0.40, Yaw -2 degrees, Heel 0 degrees, Rudder 0 degrees.

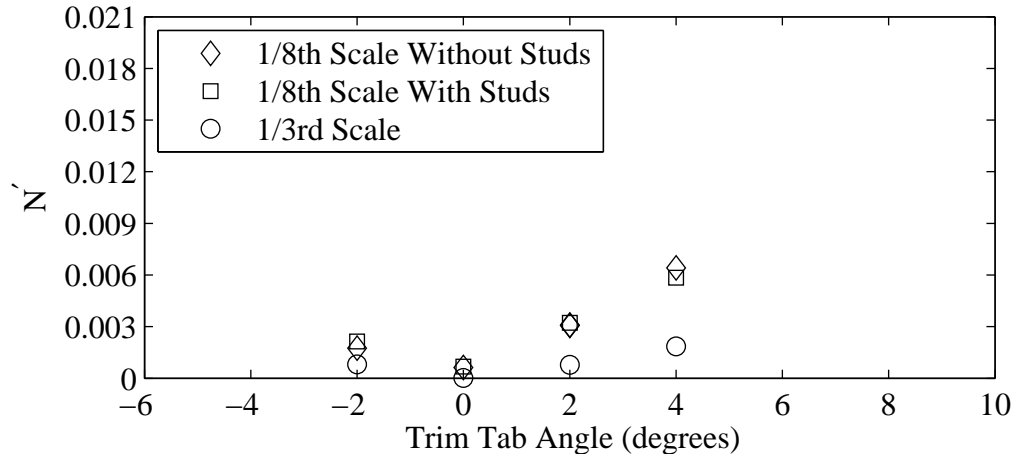


(a) Non-dimensional yaw moment plotted against variation in trim tab angle.

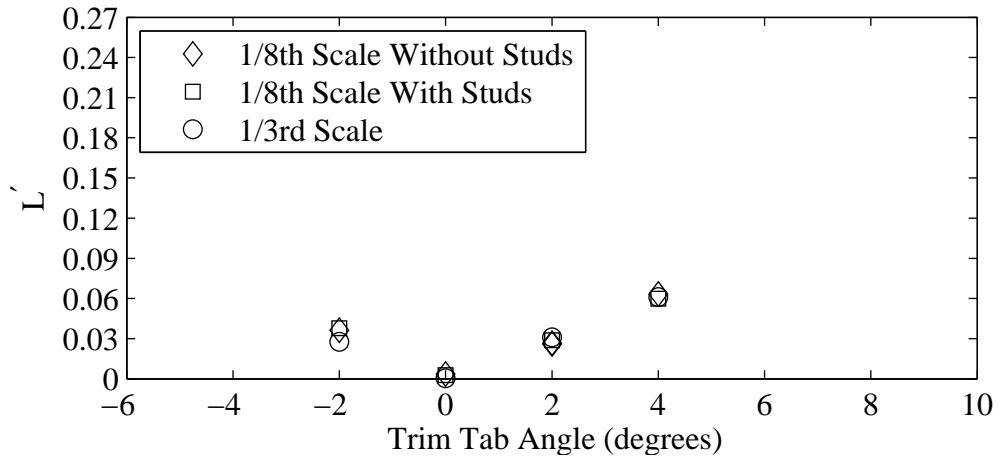


(b) Non-dimensional heel moment plotted against variation in trim tab angle.

Figure G.3: Froude number 0.40, Yaw -1 degrees, Heel 0 degrees, Rudder 0 degrees.

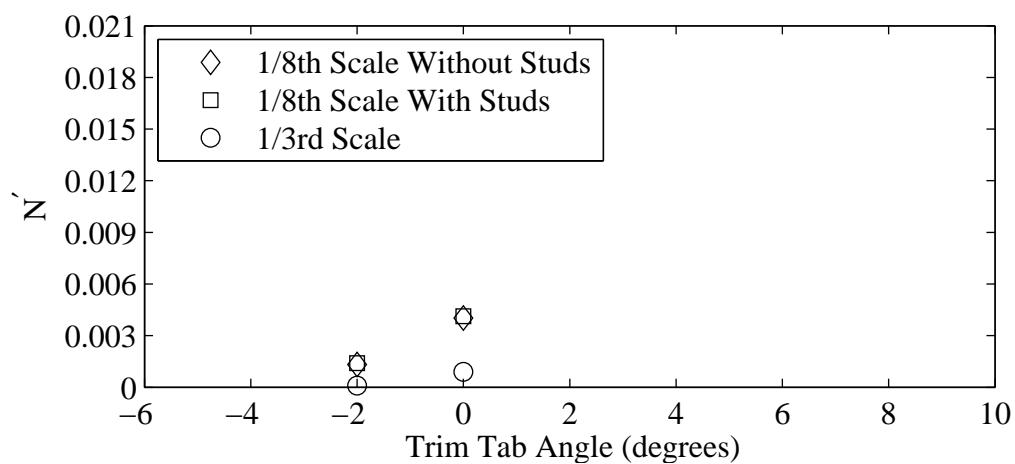


(a) Non-dimensional yaw moment plotted against variation in trim tab angle.

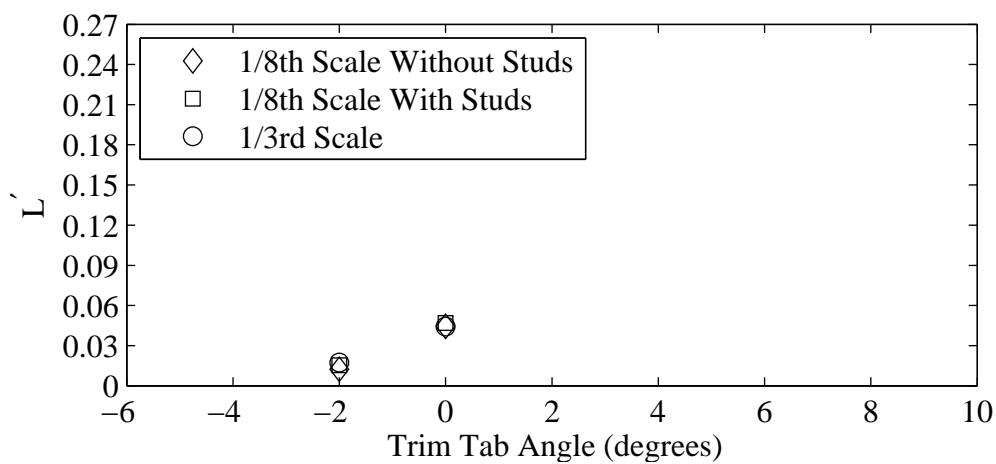


(b) Non-dimensional heel moment plotted against variation in trim tab angle.

Figure G.4: Froude number 0.40, Yaw 0 degrees, Heel 0 degrees, Rudder 0 degrees.

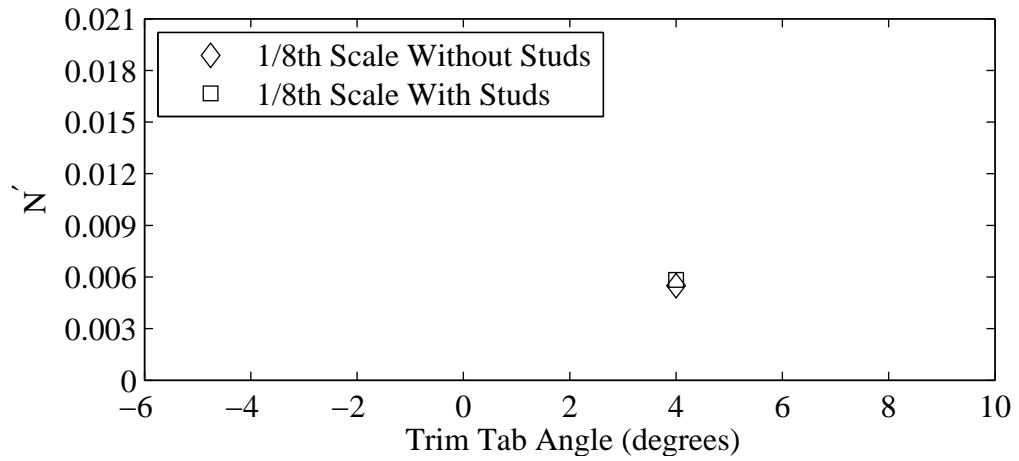


(a) Non-dimensional yaw moment plotted against variation in trim tab angle.

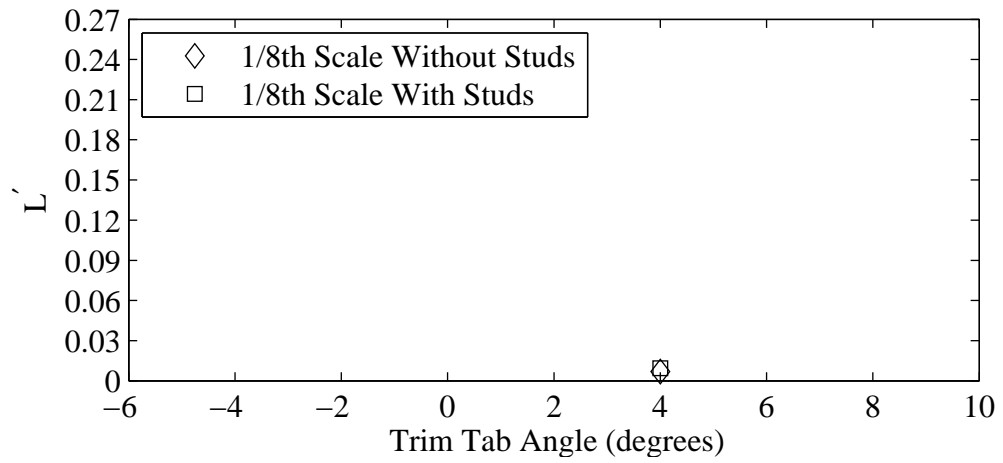


(b) Non-dimensional heel moment plotted against variation in trim tab angle.

Figure G.5: Froude number 0.40, Yaw 1 degrees, Heel 0 degrees, Rudder 0 degrees.

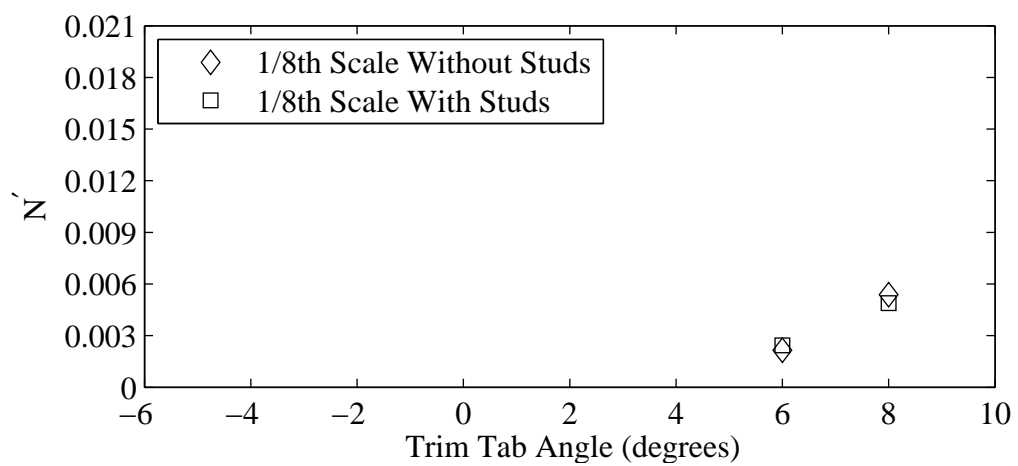


(a) Non-dimensional yaw moment plotted against variation in trim tab angle.

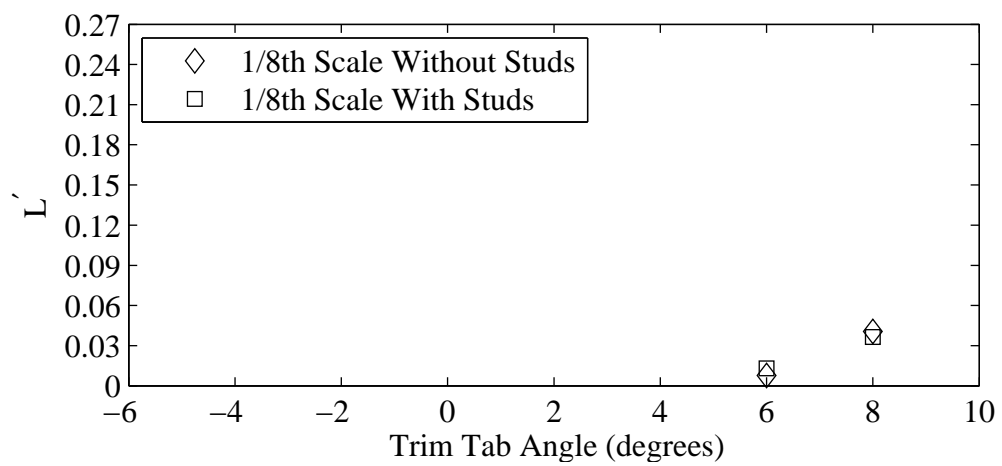


(b) Non-dimensional heel moment plotted against variation in trim tab angle.

Figure G.6: Froude number 0.29, Yaw -2 degrees, Heel 5 degrees, Rudder 4 degrees.

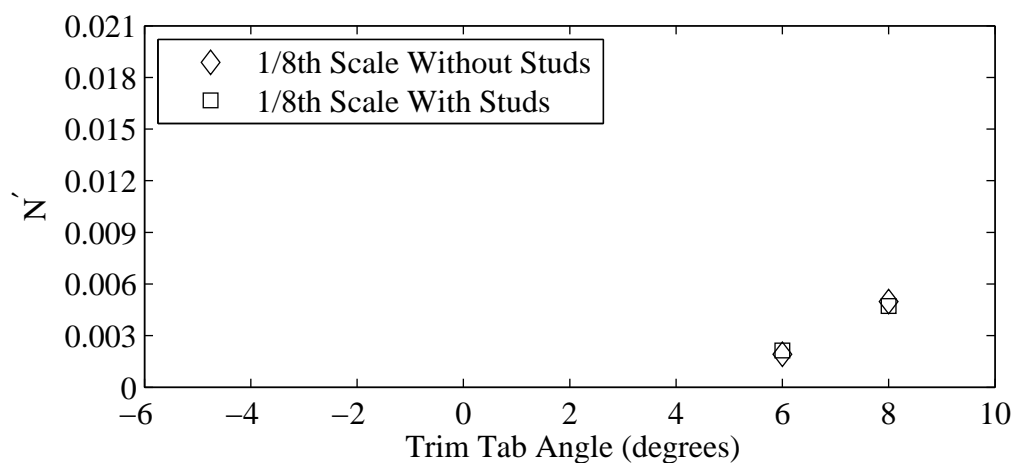


(a) Non-dimensional yaw moment plotted against variation in trim tab angle.

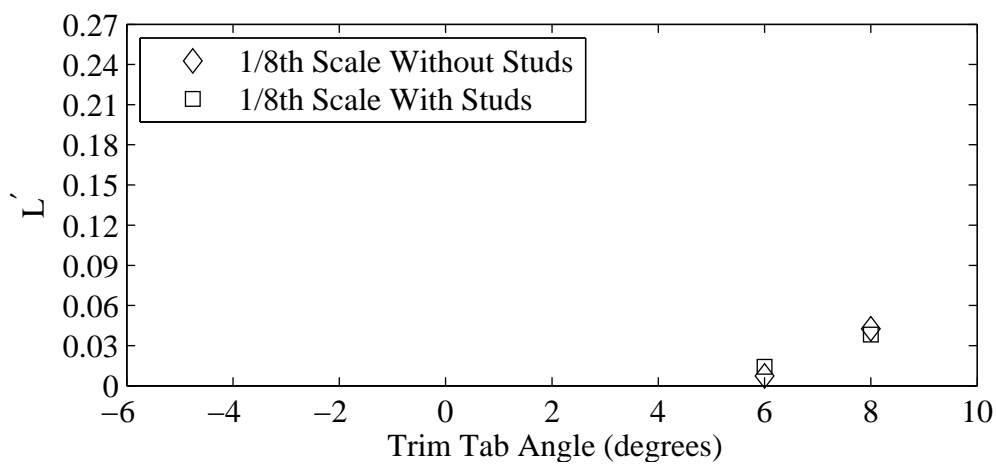


(b) Non-dimensional heel moment plotted against variation in trim tab angle.

Figure G.7: Froude number 0.27, Yaw -2 degrees, Heel 5 degrees, Rudder 2 degrees.

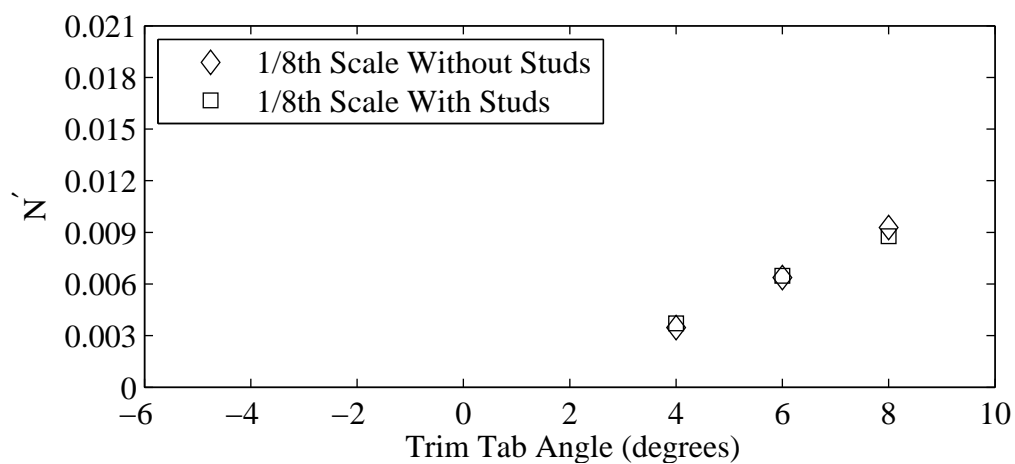


(a) Non-dimensional yaw moment plotted against variation in trim tab angle.

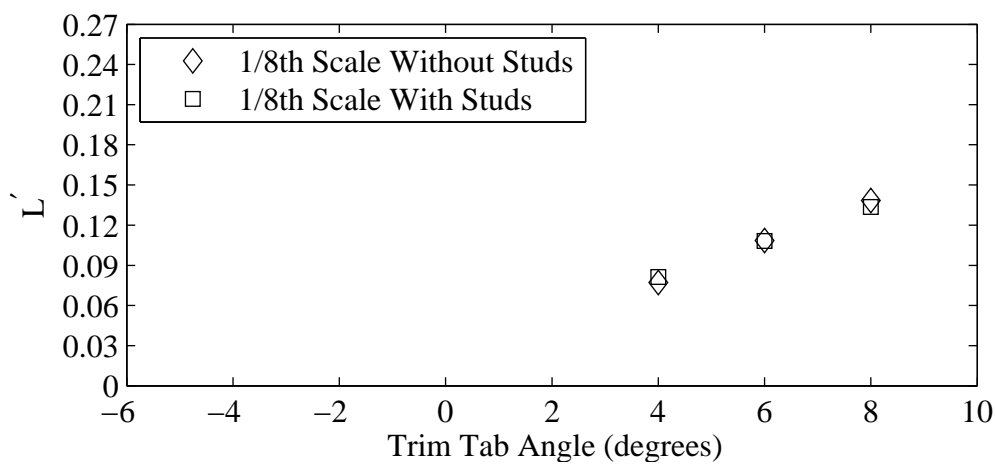


(b) Non-dimensional heel moment plotted against variation in trim tab angle.

Figure G.8: Froude number 0.29, Yaw -2 degrees, Heel 5 degrees, Rudder 2 degrees.

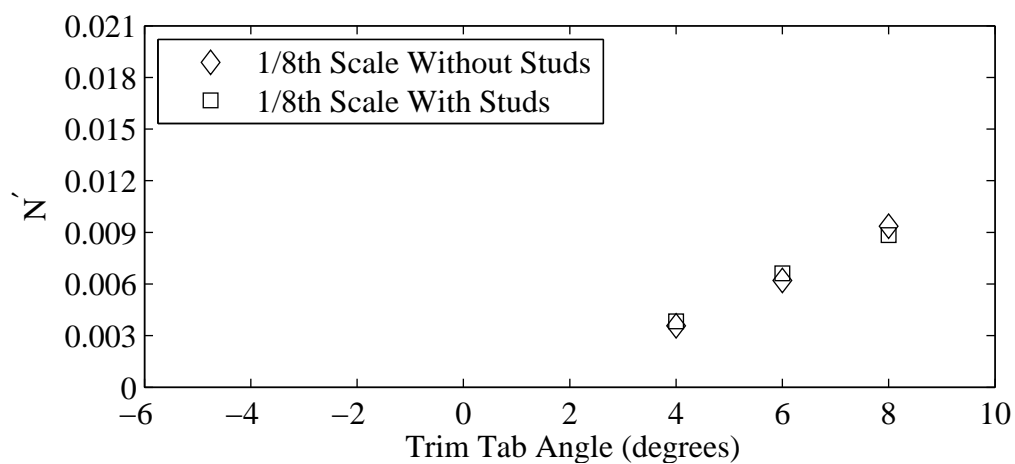


(a) Non-dimensional yaw moment plotted against variation in trim tab angle.

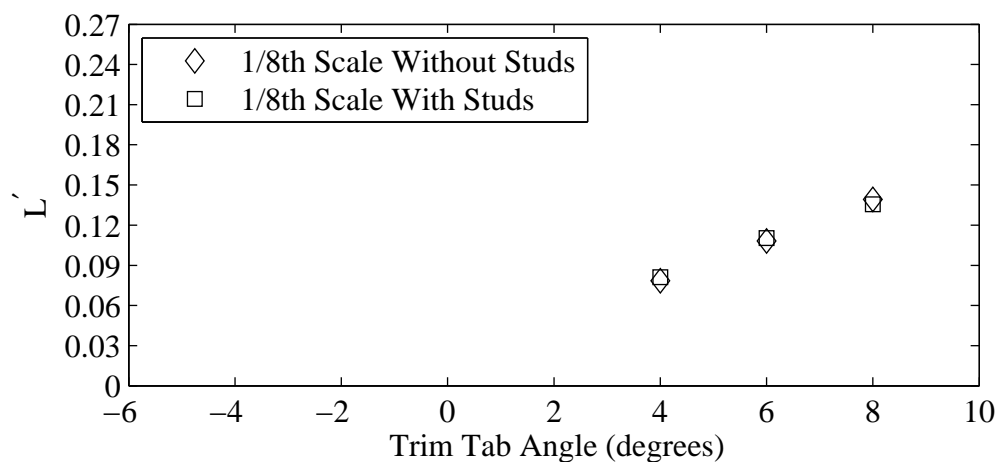


(b) Non-dimensional heel moment plotted against variation in trim tab angle.

Figure G.9: Froude number 0.27, Yaw 0 degrees, Heel 5 degrees, Rudder 2 degrees.

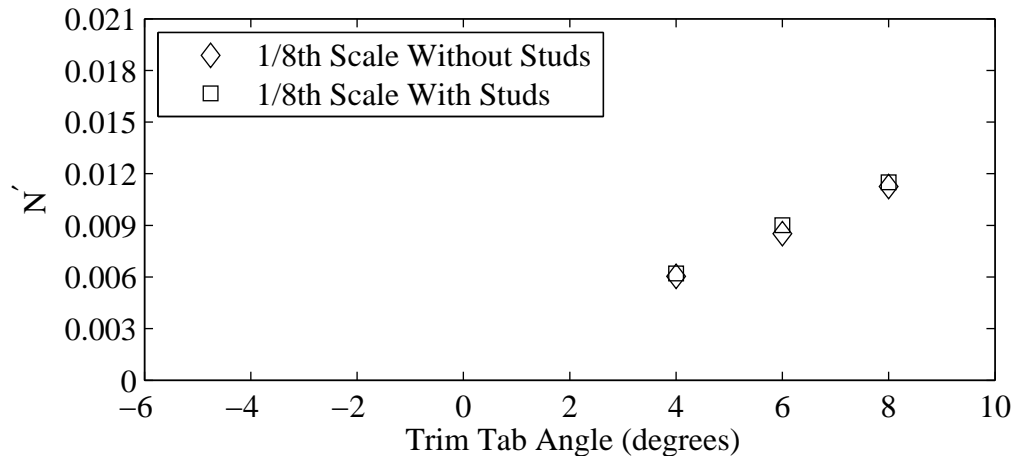


(a) Non-dimensional yaw moment plotted against variation in trim tab angle.

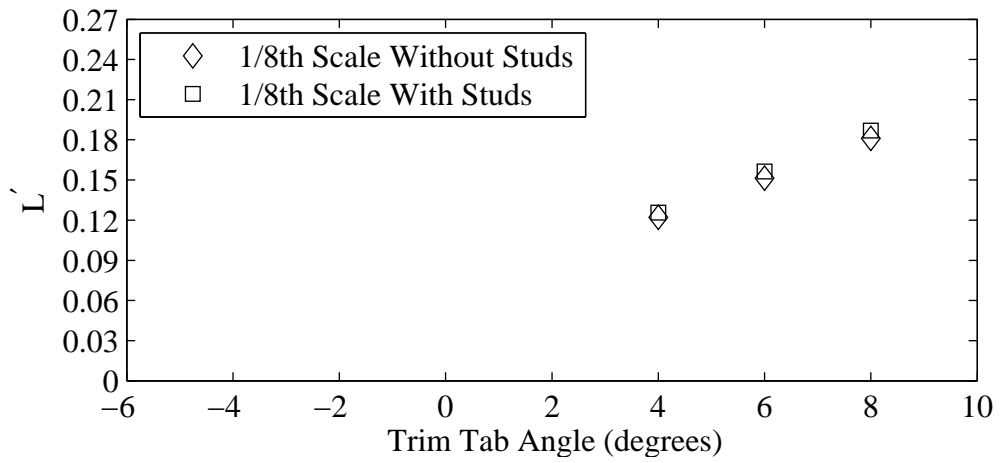


(b) Non-dimensional heel moment plotted against variation in trim tab angle.

Figure G.10: Froude number 0.29, Yaw 0 degrees, Heel 5 degrees, Rudder 2 degrees.

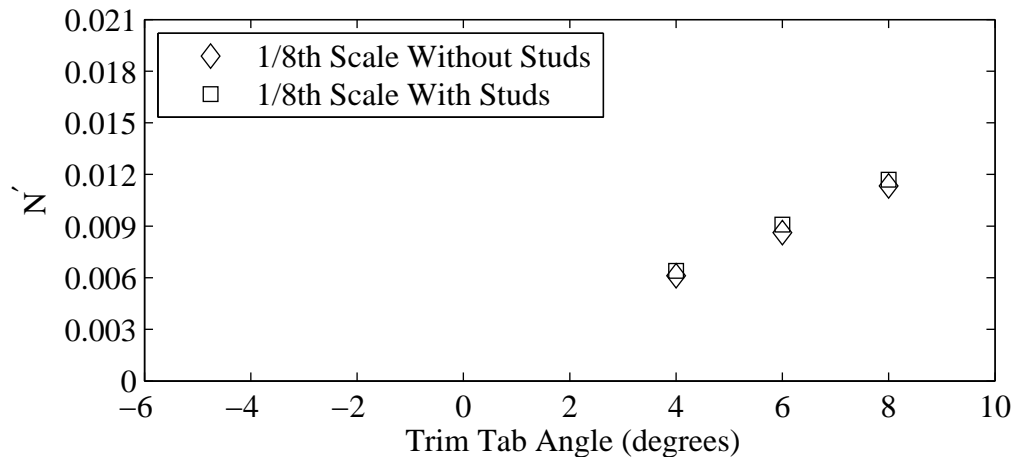


(a) Non-dimensional yaw moment plotted against variation in trim tab angle.

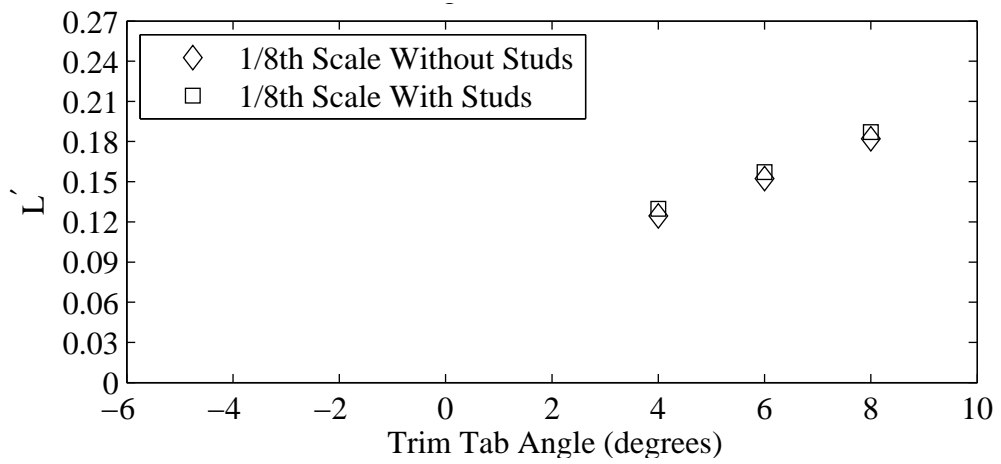


(b) Non-dimensional heel moment plotted against variation in trim tab angle.

Figure G.11: Froude number 0.27, Yaw 1 degrees, Heel 5 degrees, Rudder 2 degrees.

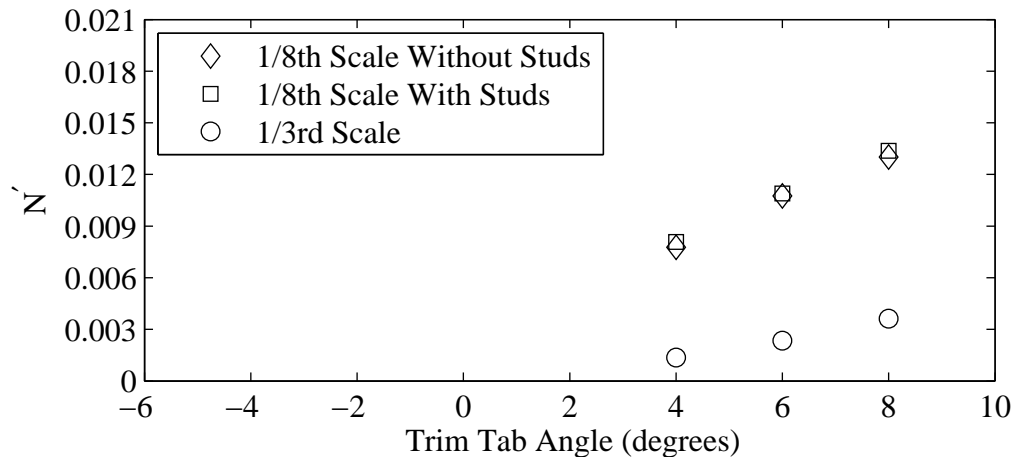


(a) Non-dimensional yaw moment plotted against variation in trim tab angle.

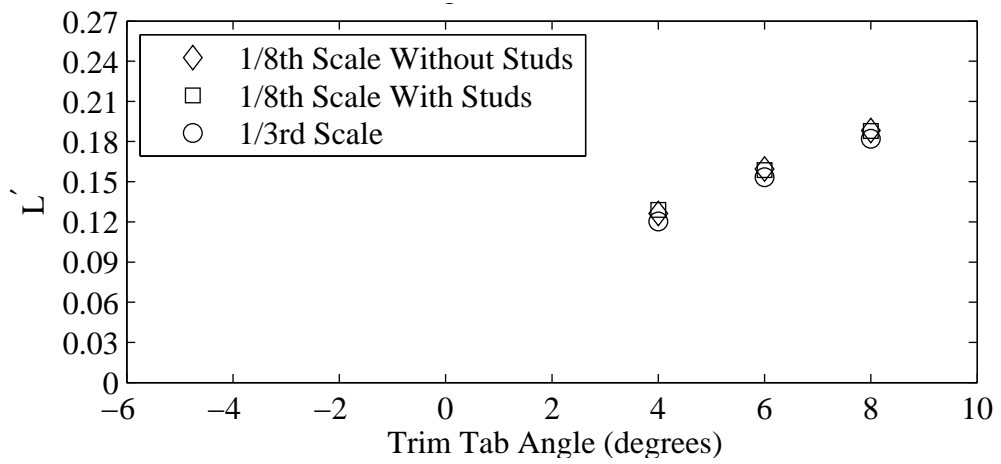


(b) Non-dimensional heel moment plotted against variation in trim tab angle.

Figure G.12: Froude number 0.29, Yaw 1 degrees, Heel 10 degrees, Rudder 2 degrees.

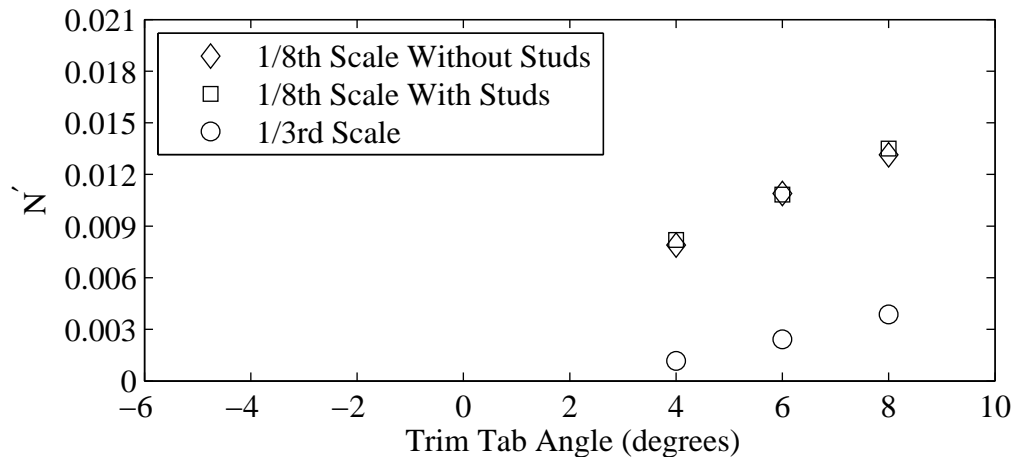


(a) Non-dimensional yaw moment plotted against variation in trim tab angle.

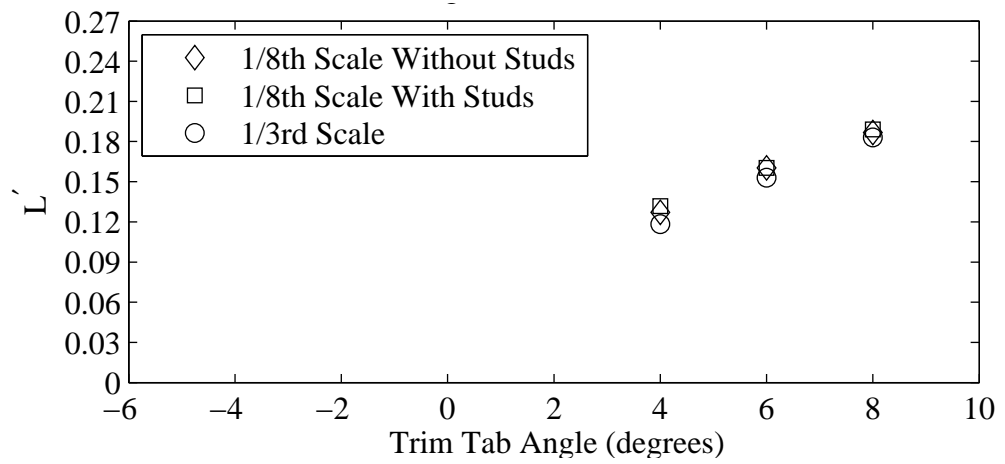


(b) Non-dimensional heel moment plotted against variation in trim tab angle.

Figure G.13: Froude number 0.27, Yaw 1 degrees, Heel 10 degrees, Rudder 2 degrees.

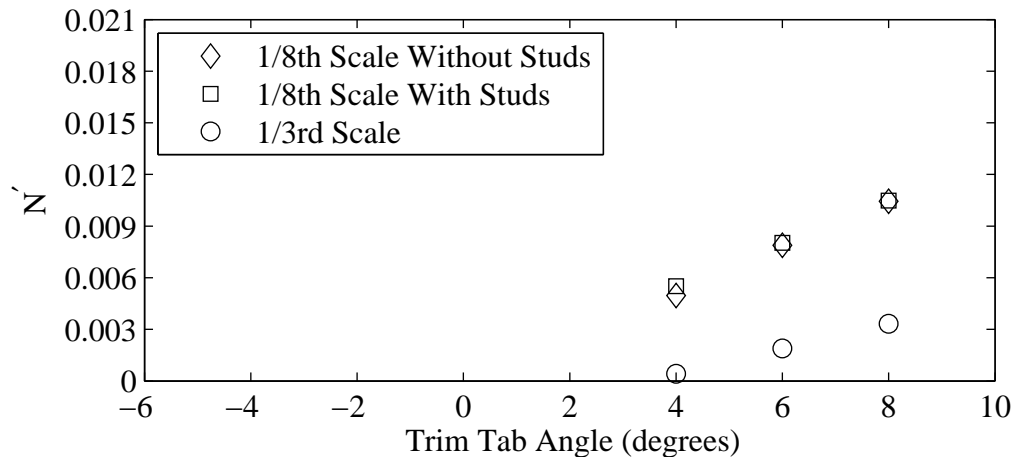


(a) Non-dimensional yaw moment plotted against variation in trim tab angle.

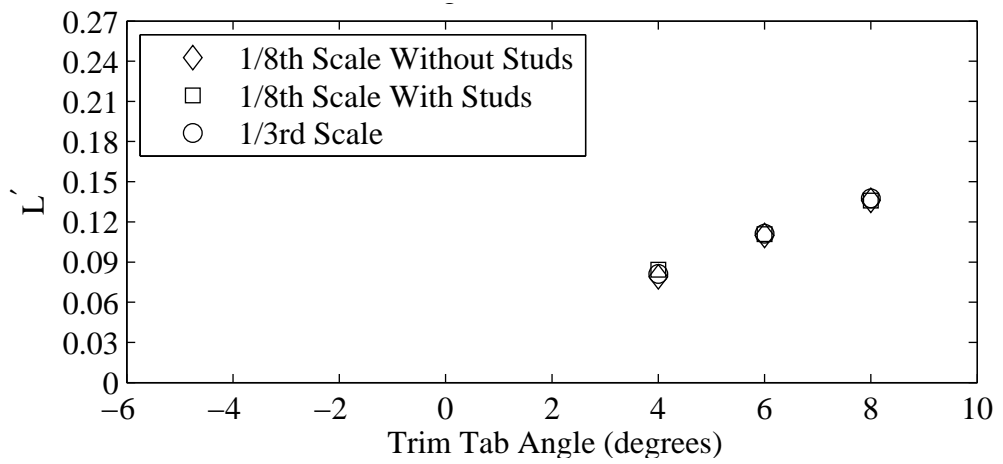


(b) Non-dimensional heel moment plotted against variation in trim tab angle.

Figure G.14: Froude number 0.29, Yaw 1 degrees, Heel 10 degrees, Rudder 2 degrees.

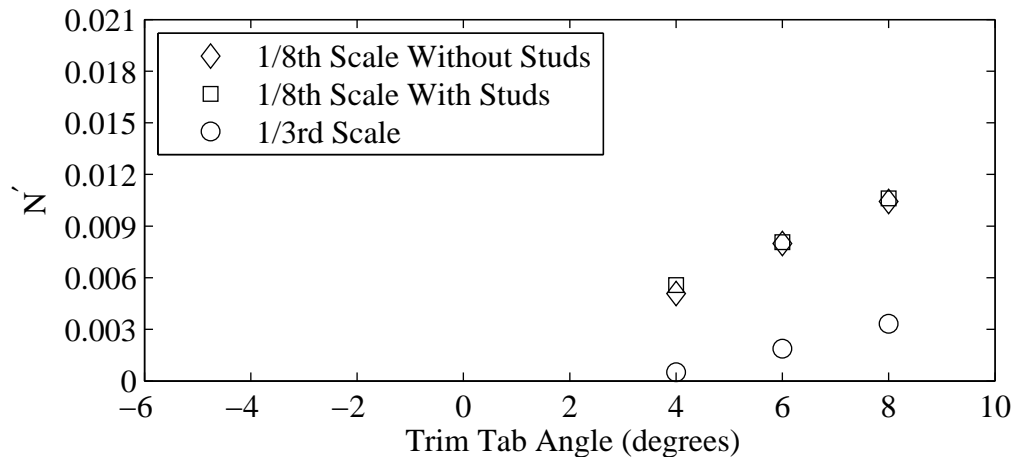


(a) Non-dimensional yaw moment plotted against variation in trim tab angle.

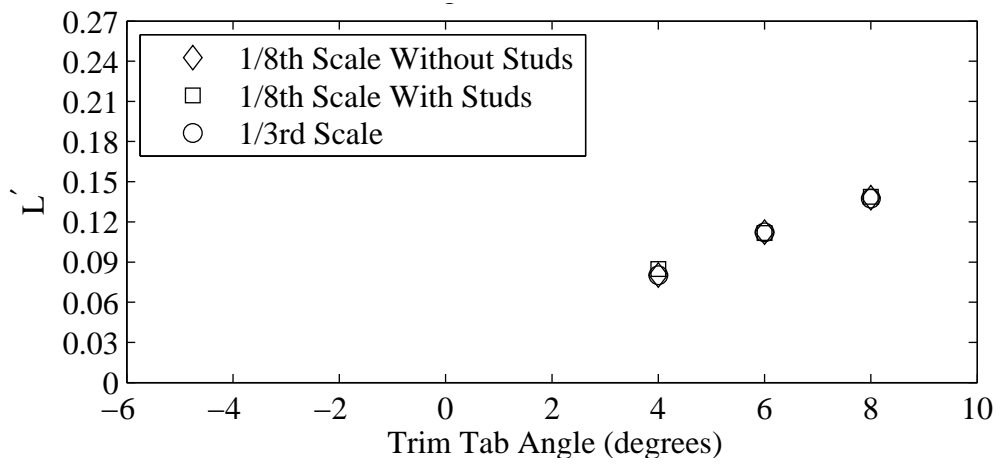


(b) Non-dimensional heel moment plotted against variation in trim tab angle.

Figure G.15: Froude number 0.27, Yaw 0 degrees, Heel 10 degrees, Rudder 2 degrees.

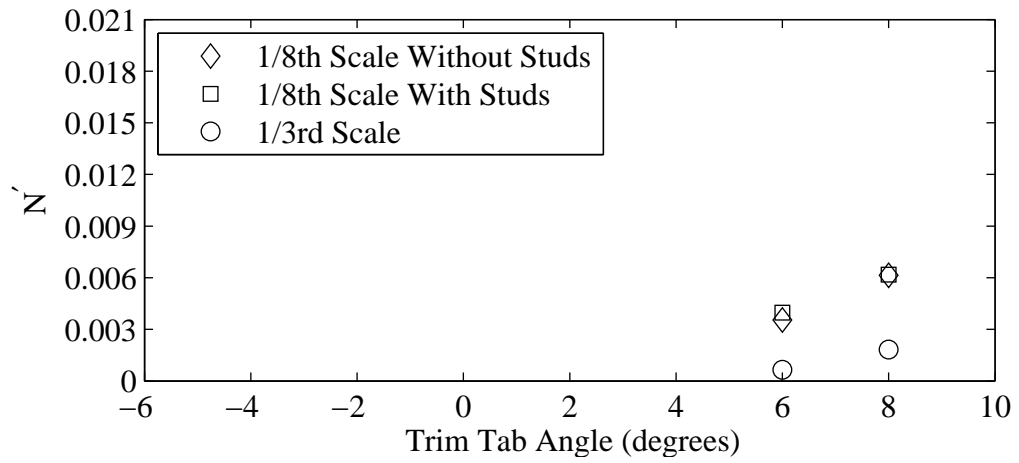


(a) Non-dimensional yaw moment plotted against variation in trim tab angle.

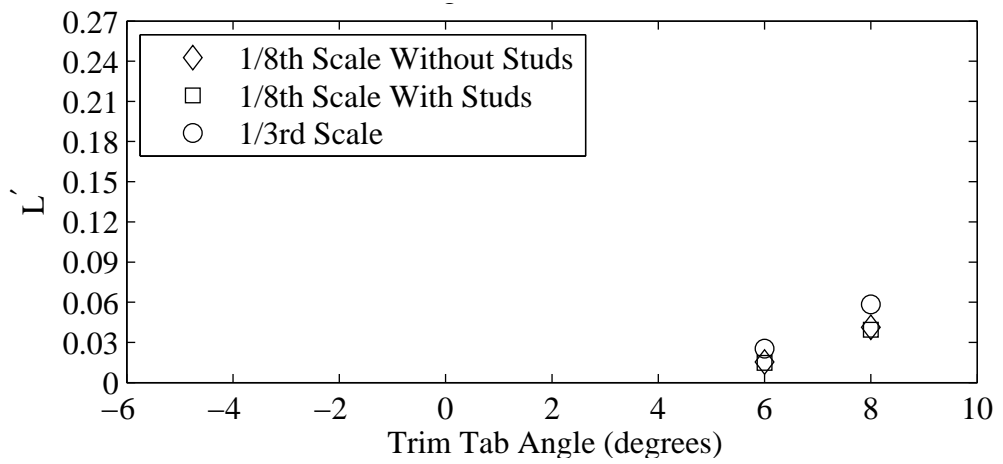


(b) Non-dimensional heel moment plotted against variation in trim tab angle.

Figure G.16: Froude number 0.29, Yaw 0 degrees, Heel 10 degrees, Rudder 2 degrees.

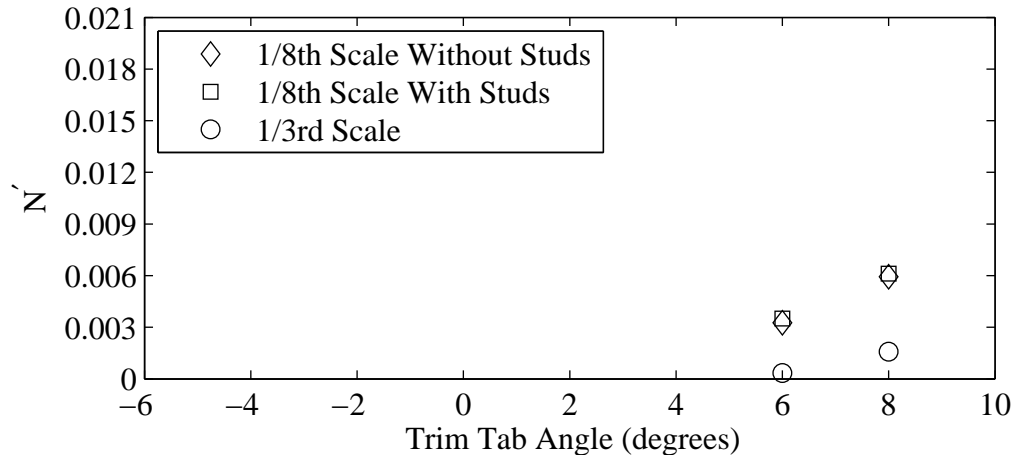


(a) Non-dimensional yaw moment plotted against variation in trim tab angle.

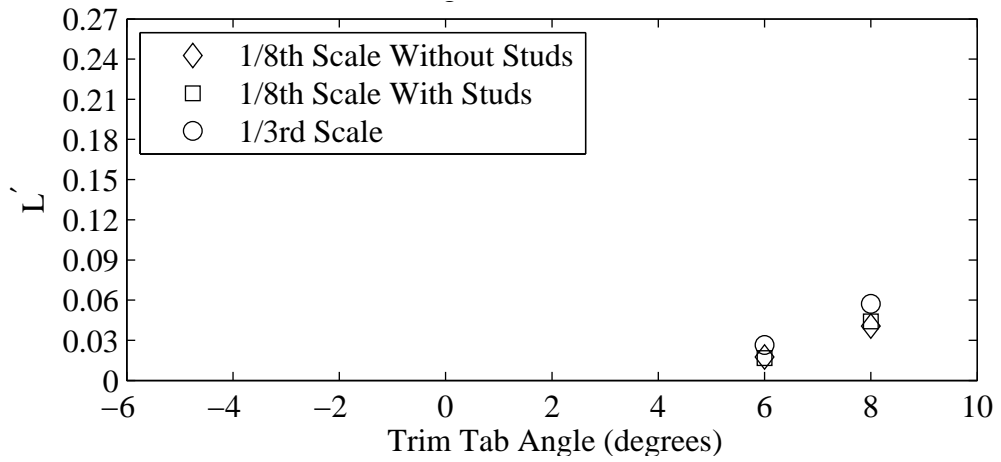


(b) Non-dimensional heel moment plotted against variation in trim tab angle.

Figure G.17: Froude number 0.27, Yaw -2 degrees, Heel 10 degrees, Rudder 2 degrees.

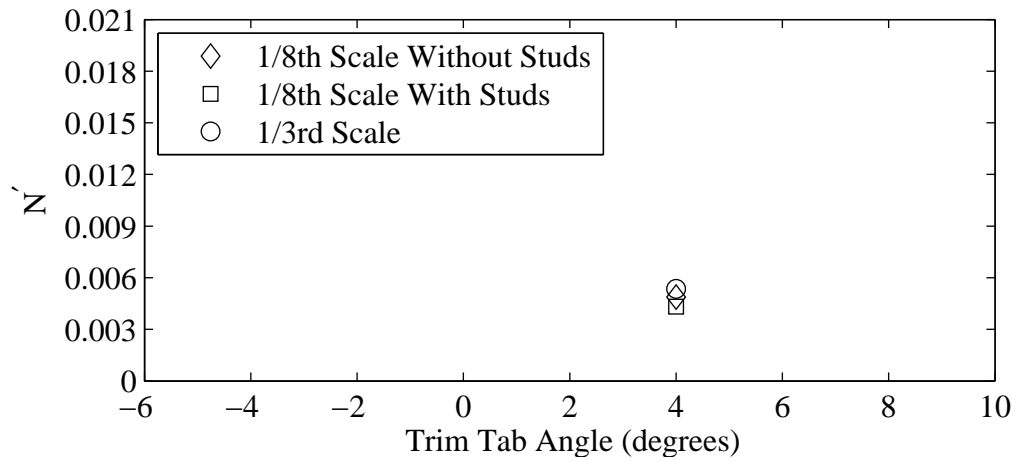


(a) Non-dimensional yaw moment plotted against variation in trim tab angle.

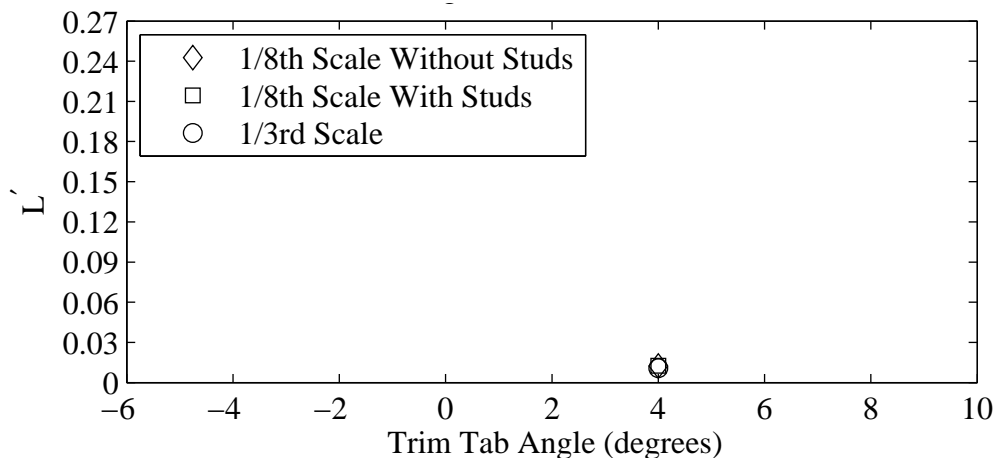


(b) Non-dimensional heel moment plotted against variation in trim tab angle.

Figure G.18: Froude number 0.29, Yaw -2 degrees, Heel 10 degrees, Rudder 2 degrees.

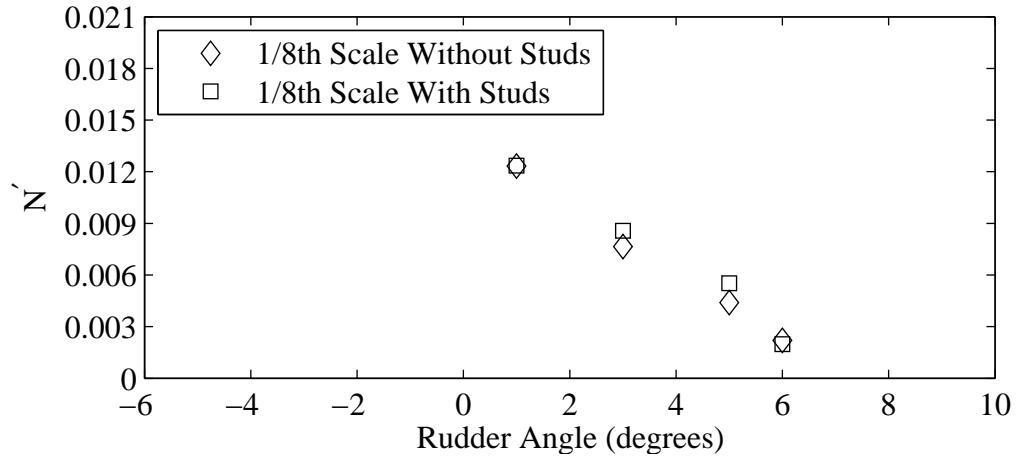


(a) Non-dimensional yaw moment plotted against variation in trim tab angle.

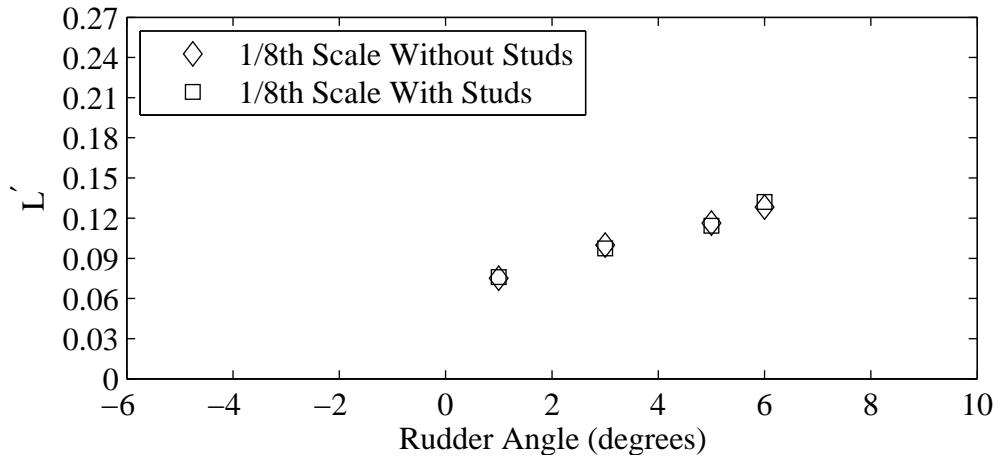


(b) Non-dimensional heel moment plotted against variation in trim tab angle.

Figure G.19: Froude number 0.29, Yaw -2 degrees, Heel 10 degrees, Rudder 4 degrees.

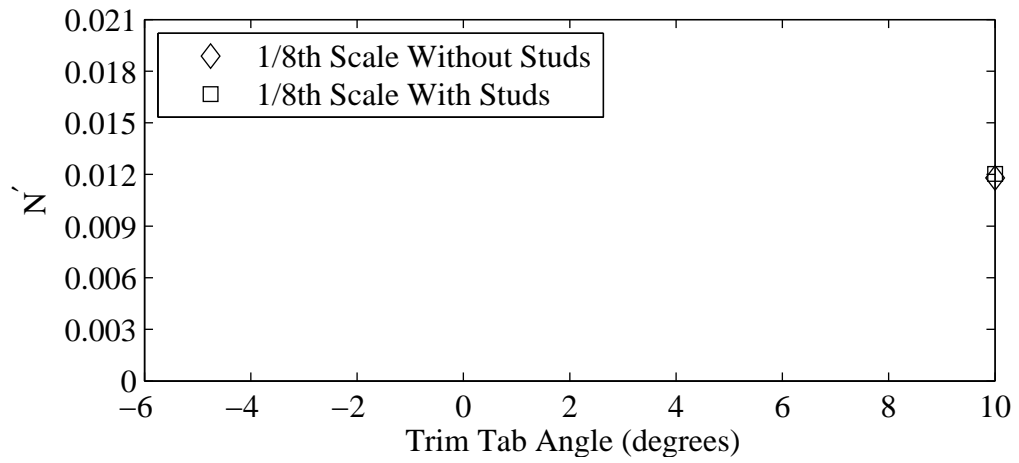


(a) Non-dimensional yaw moment plotted against variation in rudder angle.

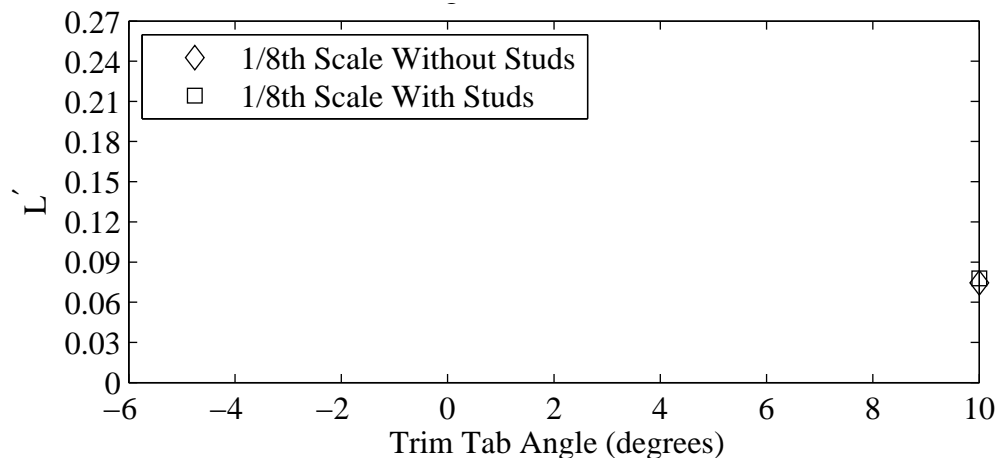


(b) Non-dimensional heel moment plotted against variation in rudder angle.

Figure G.20: Froude number 0.32, Yaw -2 degrees, Heel 20 degrees, Tab 10 degrees.

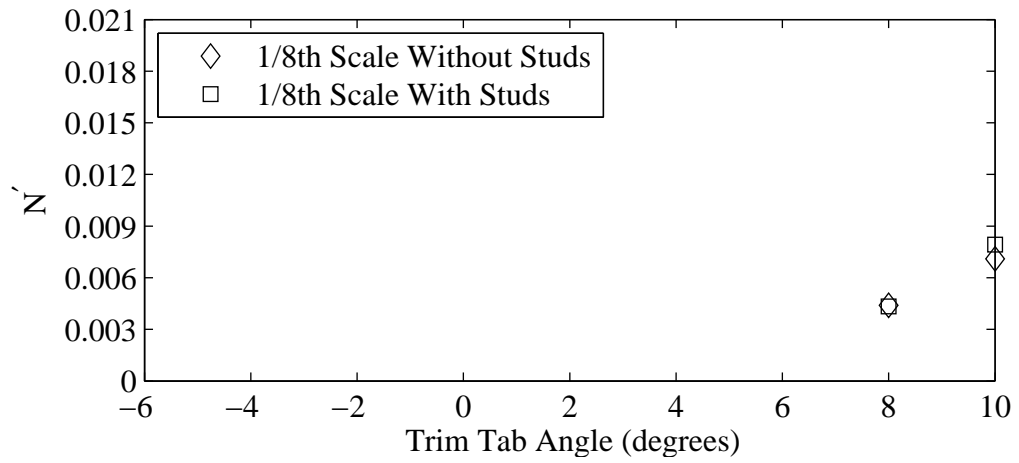


(a) Non-dimensional yaw moment plotted against variation in trim tab angle.

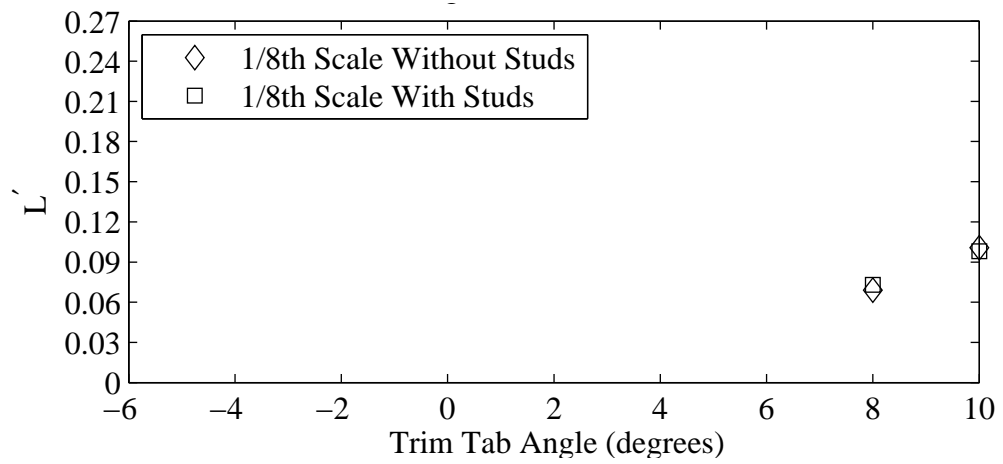


(b) Non-dimensional heel moment plotted against variation in trim tab angle.

Figure G.21: Froude number 0.34, Yaw -2 degrees, Heel 20 degrees, Rudder 1 degrees.

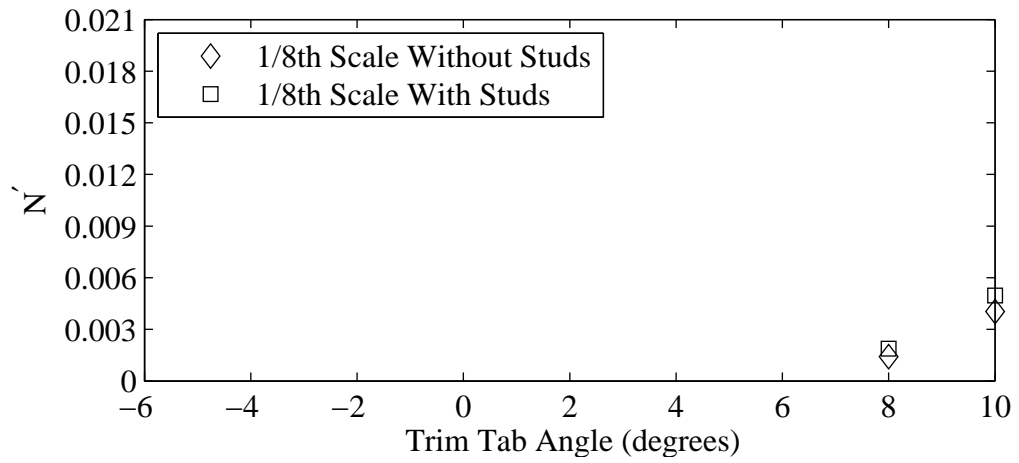


(a) Non-dimensional yaw moment plotted against variation in trim tab angle.

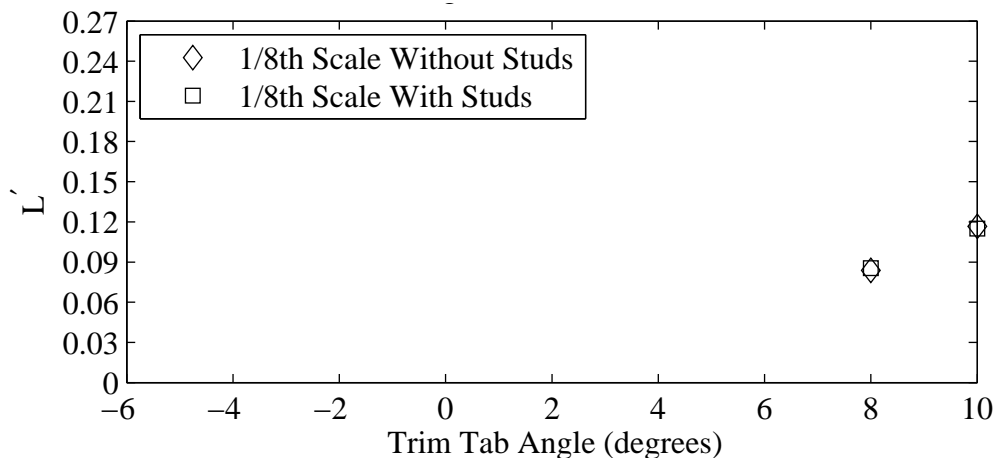


(b) Non-dimensional heel moment plotted against variation in trim tab angle.

Figure G.22: Froude number 0.34, Yaw -2 degrees, Heel 20 degrees, Rudder 3 degrees.

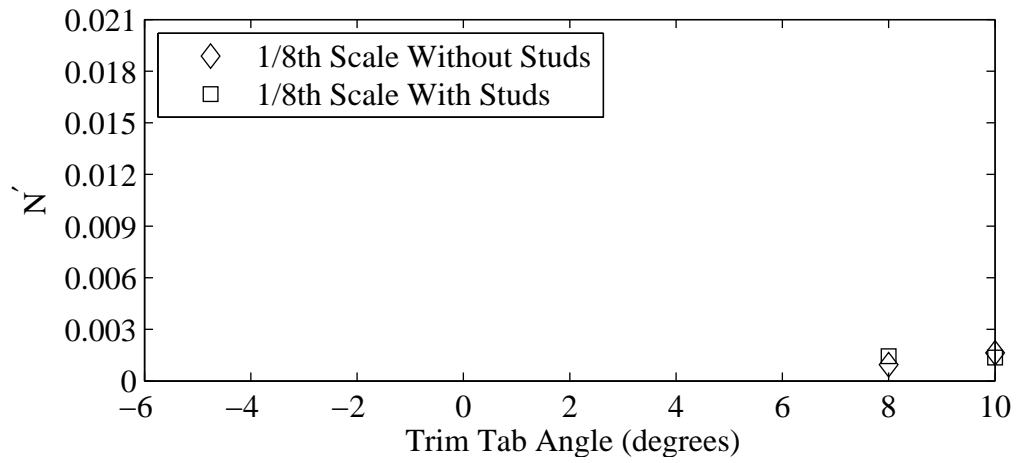


(a) Non-dimensional yaw moment plotted against variation in trim tab angle.

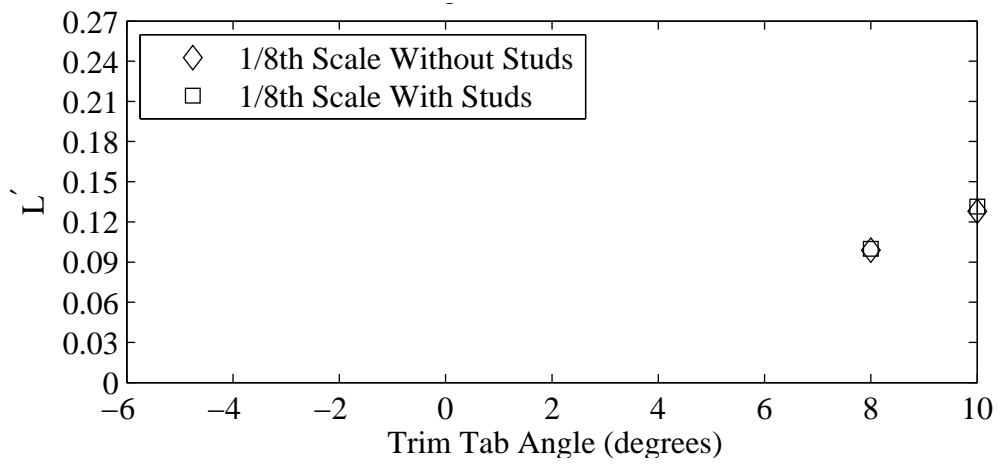


(b) Non-dimensional heel moment plotted against variation in trim tab angle.

Figure G.23: Froude number 0.34, Yaw -2 degrees, Heel 20 degrees, Rudder 5 degrees.

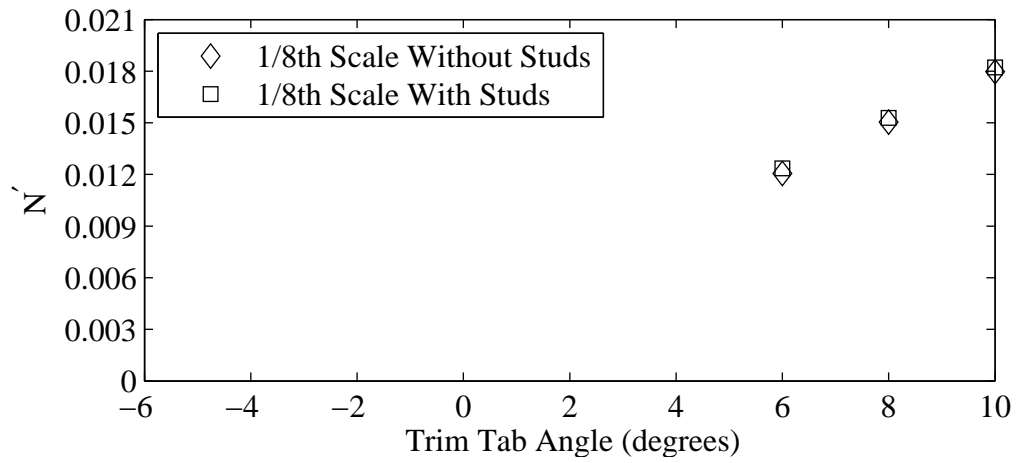


(a) Non-dimensional yaw moment plotted against variation in trim tab angle.

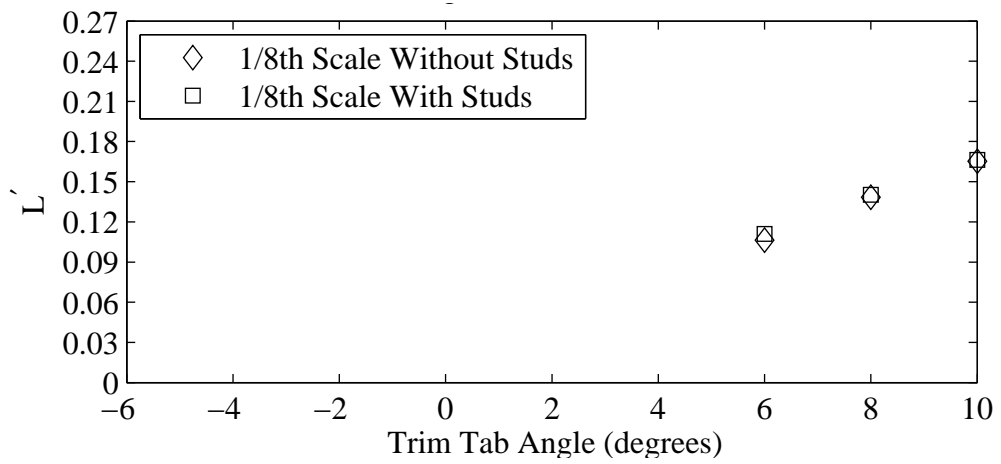


(b) Non-dimensional heel moment plotted against variation in trim tab angle.

Figure G.24: Froude number 0.34, Yaw -2 degrees, Heel 20 degrees, Rudder 6 degrees.

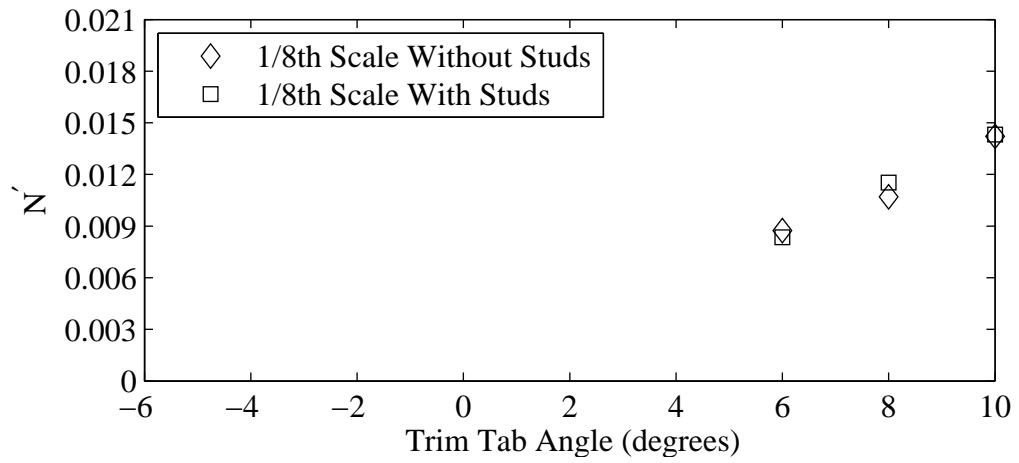


(a) Non-dimensional yaw moment plotted against variation in trim tab angle.

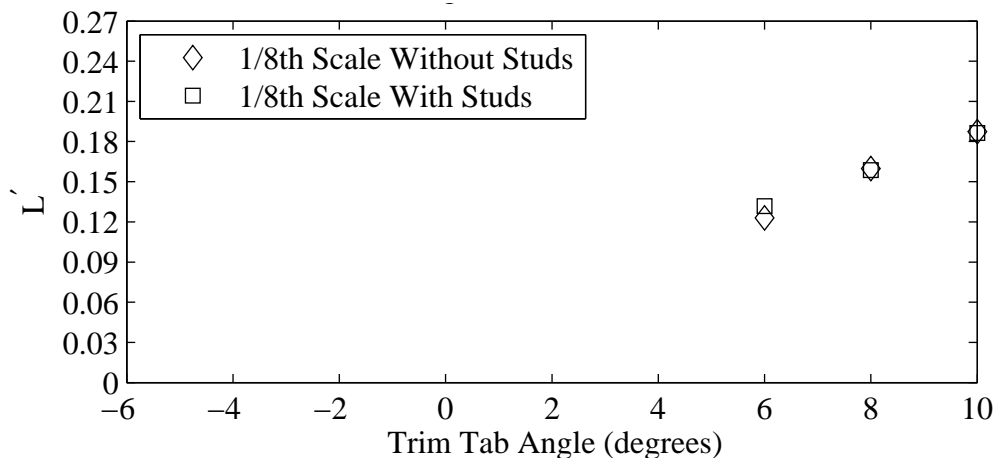


(b) Non-dimensional heel moment plotted against variation in trim tab angle.

Figure G.25: Froude number 0.34, Yaw 0 degrees, Heel 20 degrees, Rudder 1 degrees.

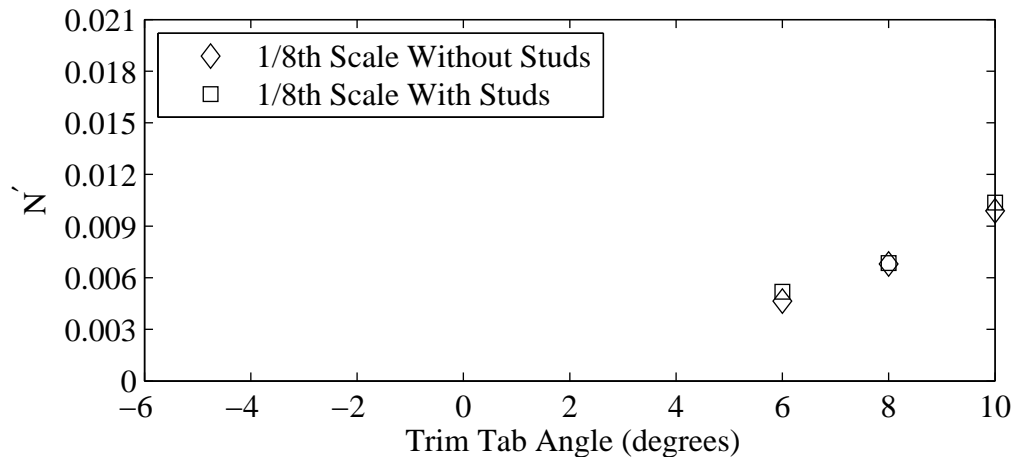


(a) Non-dimensional yaw moment plotted against variation in trim tab angle.

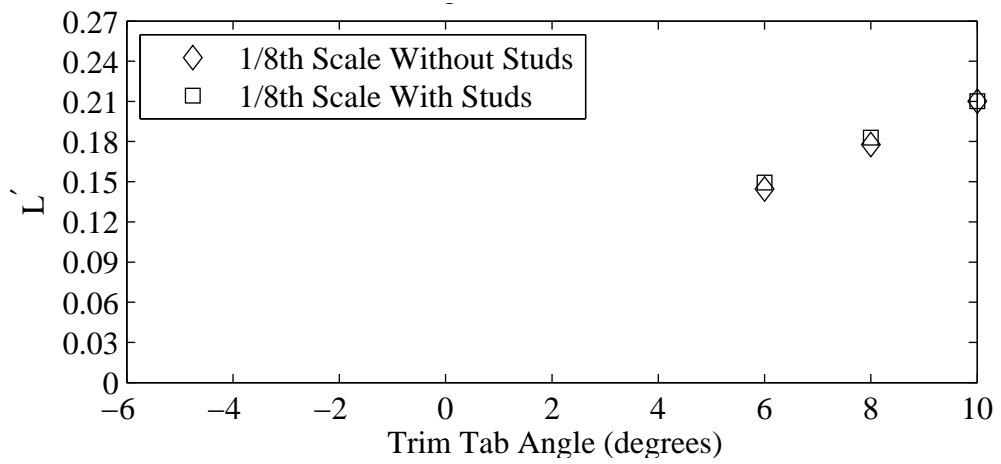


(b) Non-dimensional heel moment plotted against variation in trim tab angle.

Figure G.26: Froude number 0.34, Yaw 0 degrees, Heel 20 degrees, Rudder 3 degrees.

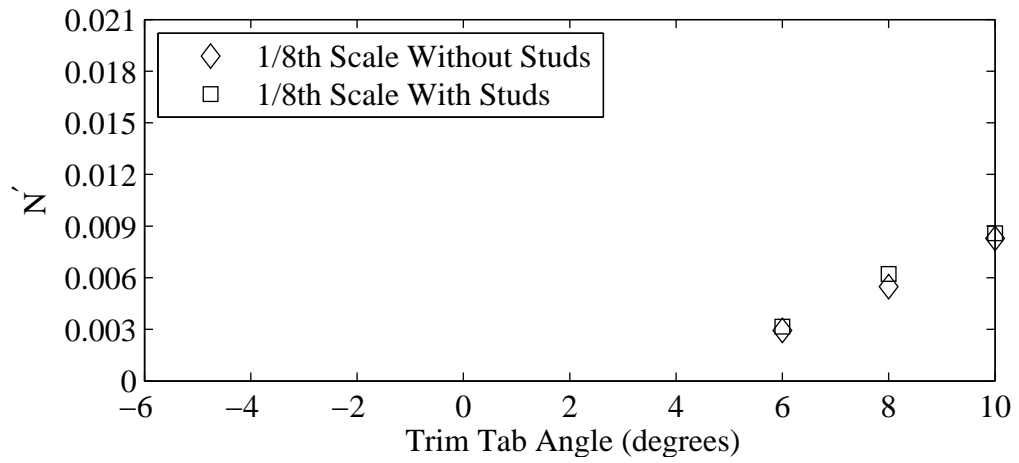


(a) Non-dimensional yaw moment plotted against variation in trim tab angle.

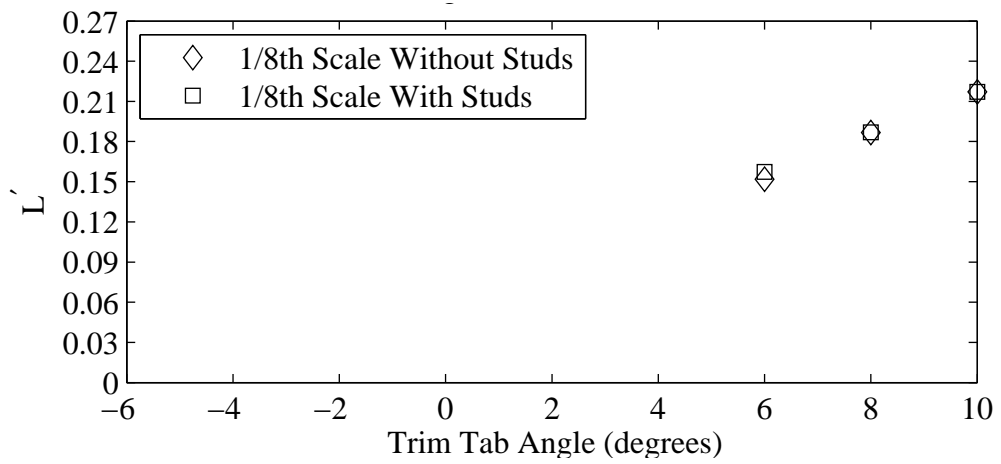


(b) Non-dimensional heel moment plotted against variation in trim tab angle.

Figure G.27: Froude number 0.34, Yaw 0 degrees, Heel 20 degrees, Rudder 5 degrees.

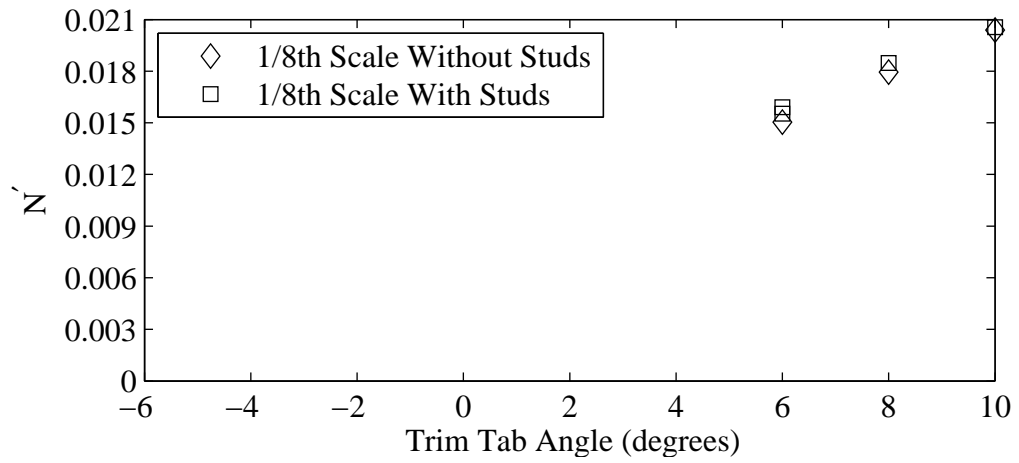


(a) Non-dimensional yaw moment plotted against variation in trim tab angle.

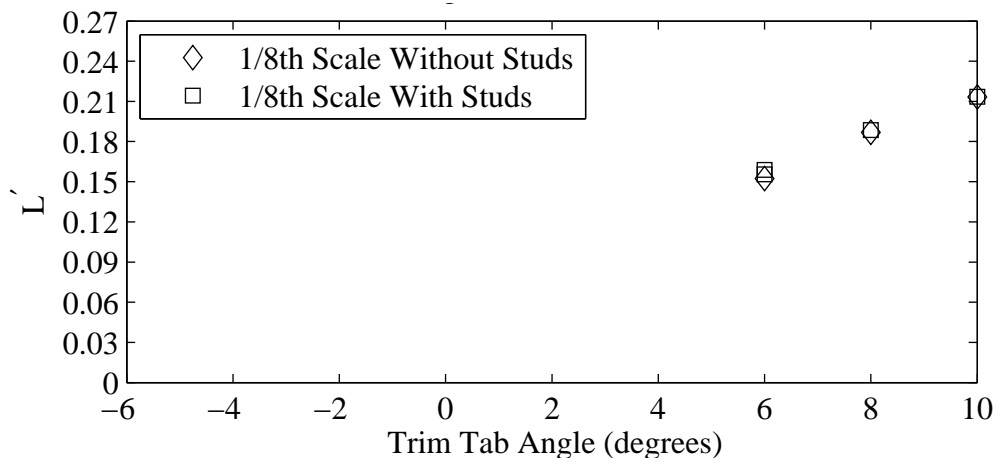


(b) Non-dimensional heel moment plotted against variation in trim tab angle.

Figure G.28: Froude number 0.34, Yaw 0 degrees, Heel 20 degrees, Rudder 6 degrees.

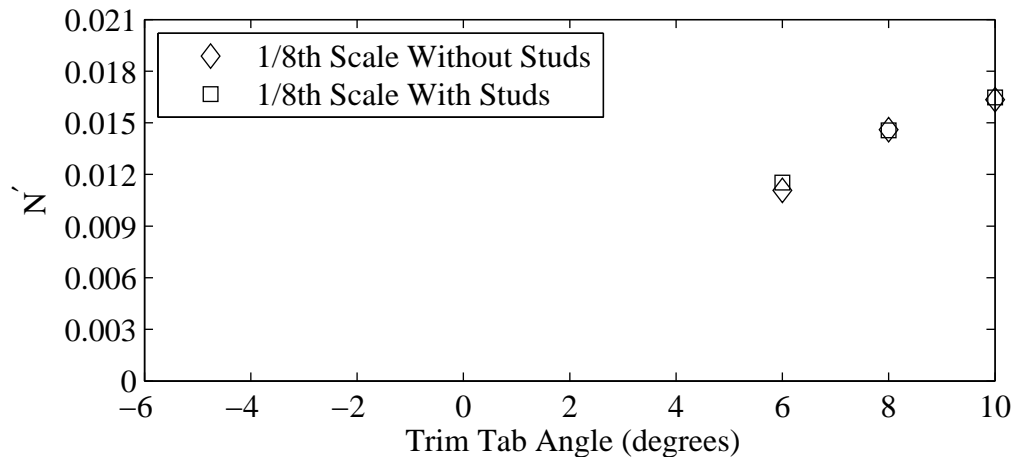


(a) Non-dimensional yaw moment plotted against variation in trim tab angle.

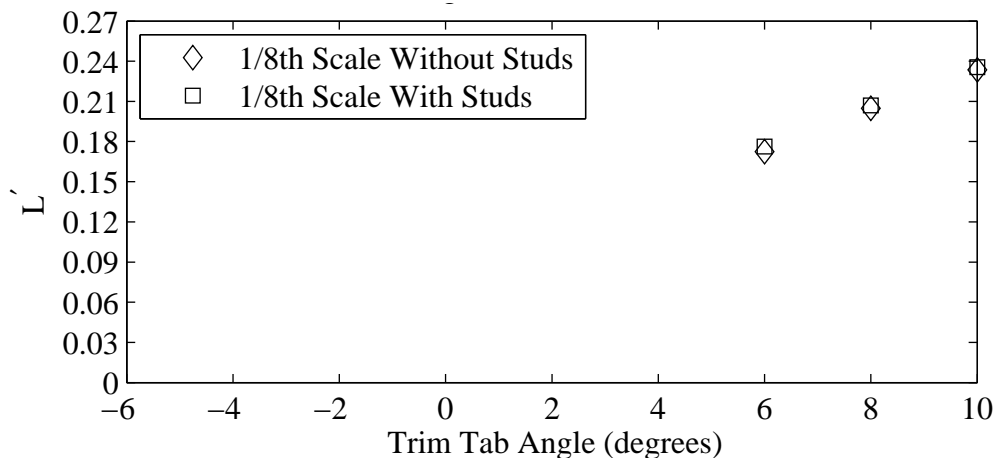


(b) Non-dimensional heel moment plotted against variation in trim tab angle.

Figure G.29: Froude number 0.34, Yaw 1 degrees, Heel 20 degrees, Rudder 1 degrees.

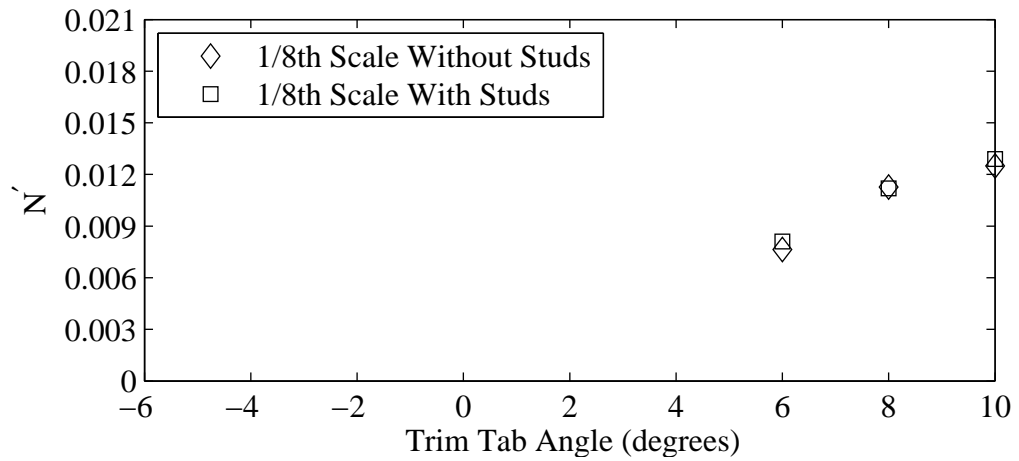


(a) Non-dimensional yaw moment plotted against variation in trim tab angle.

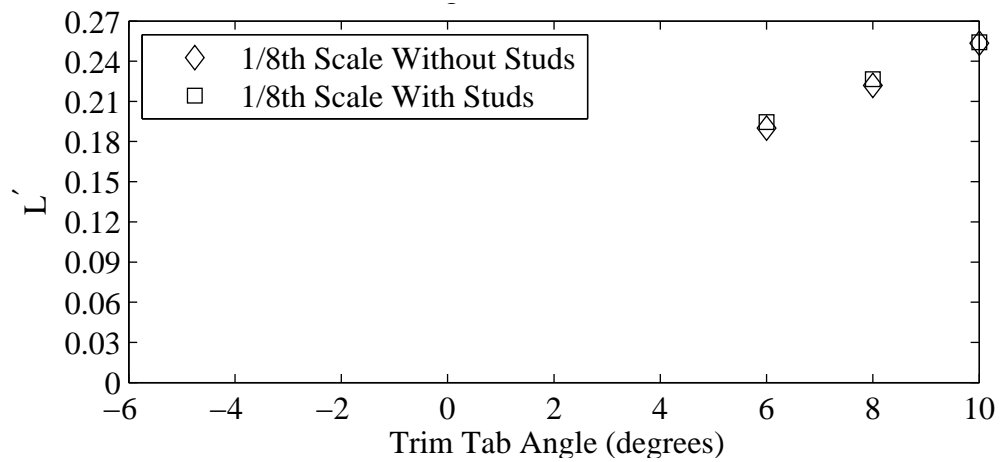


(b) Non-dimensional heel moment plotted against variation in trim tab angle.

Figure G.30: Froude number 0.34, Yaw 1 degrees, Heel 20 degrees, Rudder 3 degrees.

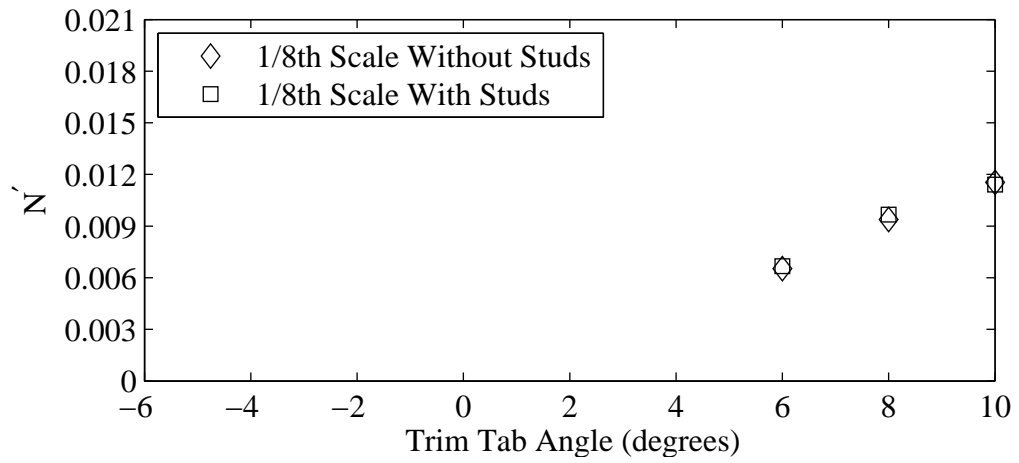


(a) Non-dimensional yaw moment plotted against variation in trim tab angle.

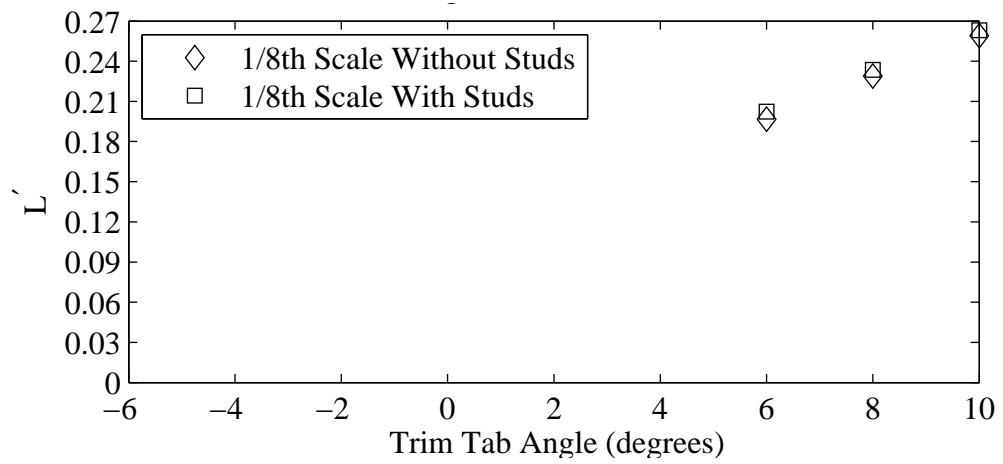


(b) Non-dimensional heel moment plotted against variation in trim tab angle.

Figure G.31: Froude number 0.34, Yaw 1 degrees, Heel 20 degrees, Rudder 5 degrees.

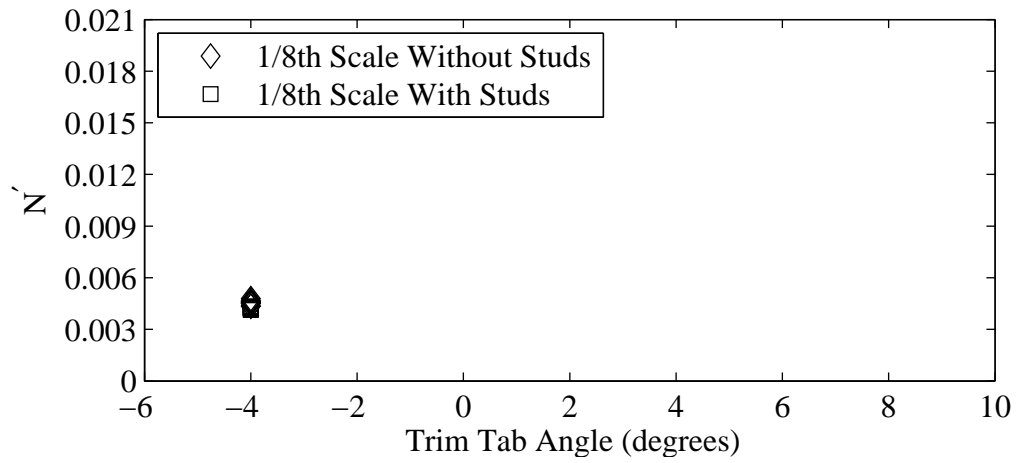


(a) Non-dimensional yaw moment plotted against variation in trim tab angle.

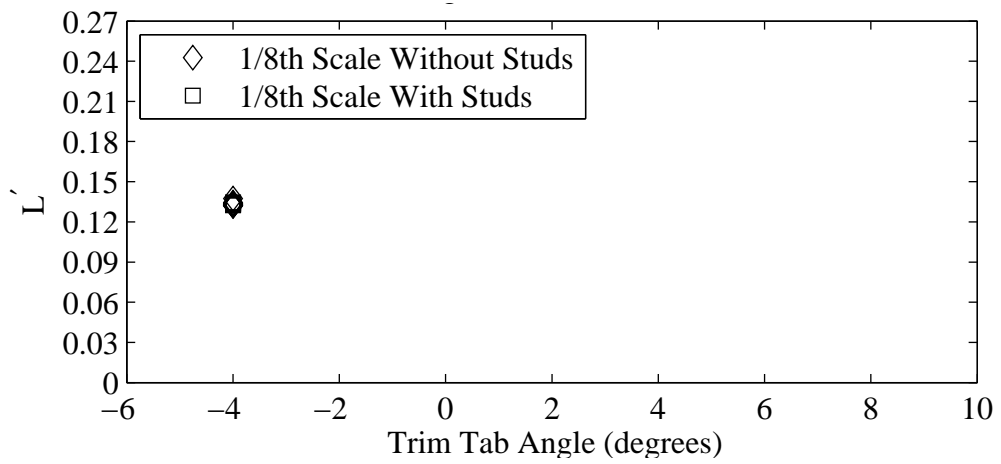


(b) Non-dimensional heel moment plotted against variation in trim tab angle.

Figure G.32: Froude number 0.34, Yaw 1 degrees, Heel 20 degrees, Rudder 6 degrees.

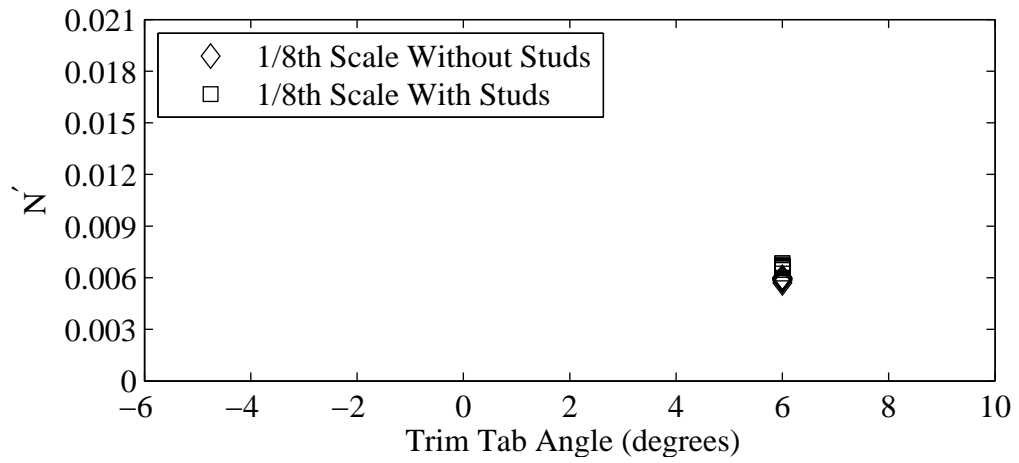


(a) Non-dimensional yaw moment plotted against variation in trim tab angle.

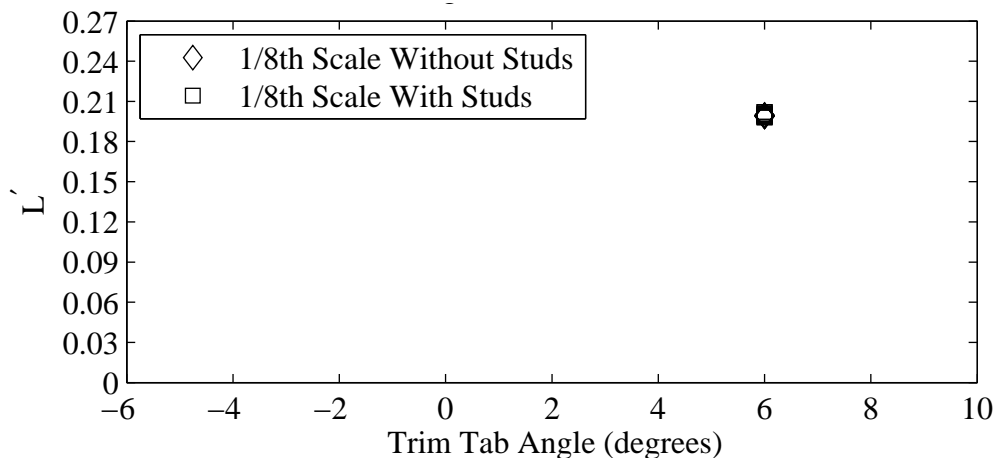


(b) Non-dimensional heel moment plotted against variation in trim tab angle.

Figure G.33: Froude number 0.27, Yaw -1 degrees, Heel -10 degrees, Tab -4 degrees, Rudder -2 degrees.



(a) Non-dimensional yaw moment plotted against variation in trim tab angle.



(b) Non-dimensional heel moment plotted against variation in trim tab angle.

Figure G.34: Froude number 0.34, Yaw 1 degrees, Heel 20 degrees, Tab 6 degrees, Rudder 6 degrees.

Appendix H

Supplementary Hot-Film Data for 4 Hz High-Pass Filter

This section contains plots of the hot-film data analysed using a 4 Hz high-pass filter.

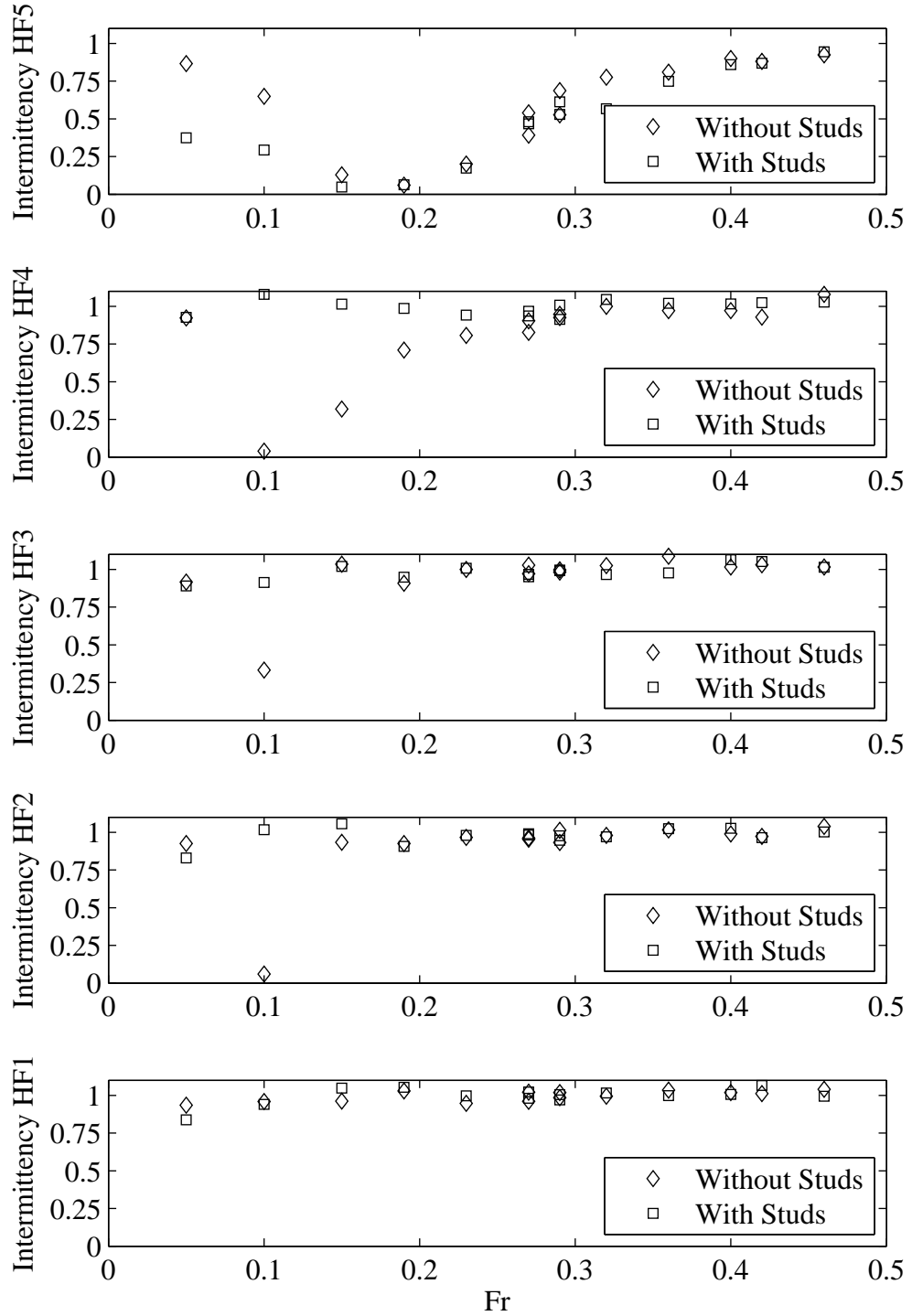


Figure H.1: Intermittency plotted with respect to variation in Froude number. Yaw 1 degrees, Heel 10 degrees, Tab 4 degrees, Rudder 2 degrees.

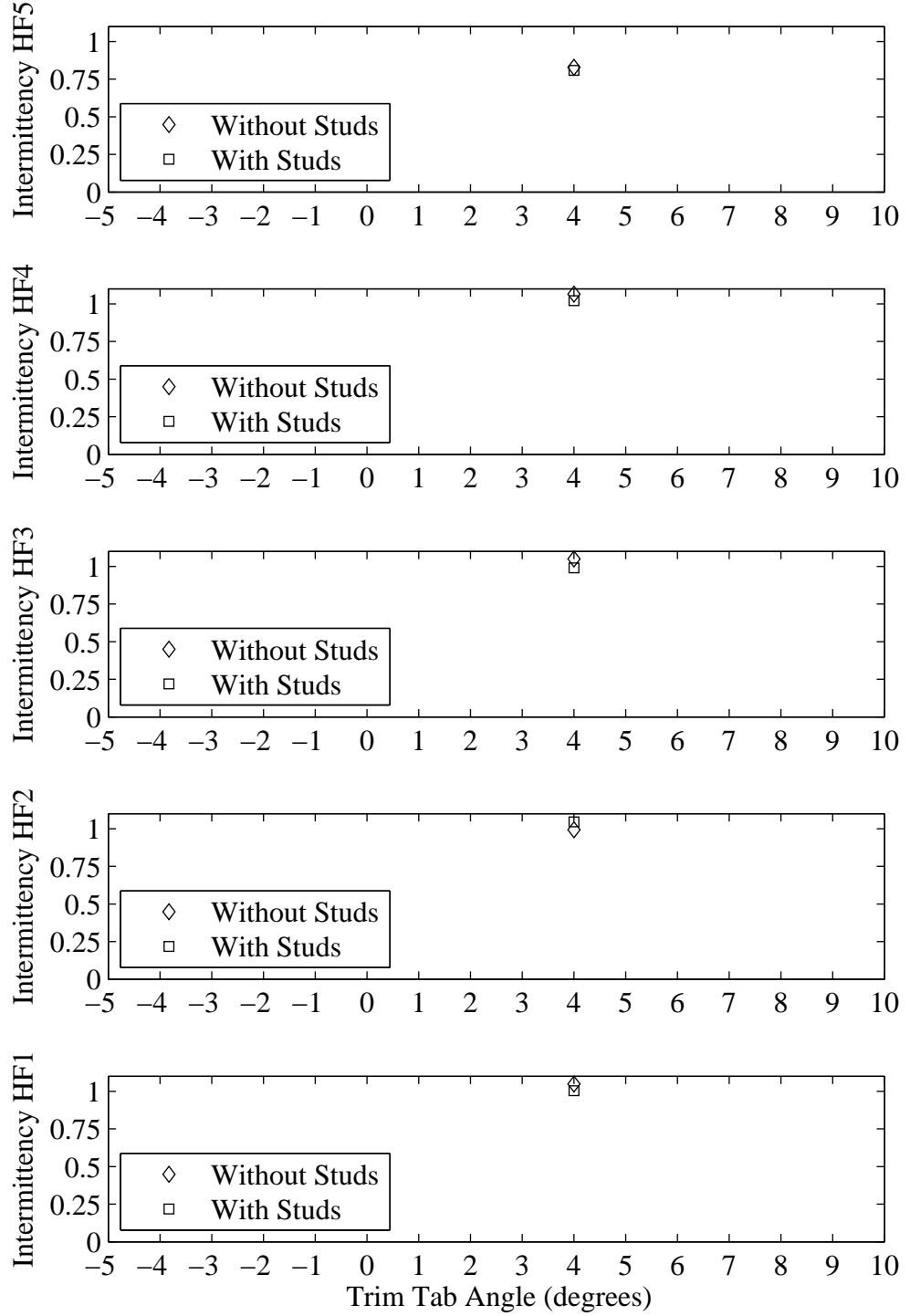


Figure H.2: Intermittency plotted with respect to variation in trim tab angle. Froude number 0.40, Yaw -2 degrees, Heel 0 degrees, Rudder 0 degrees.

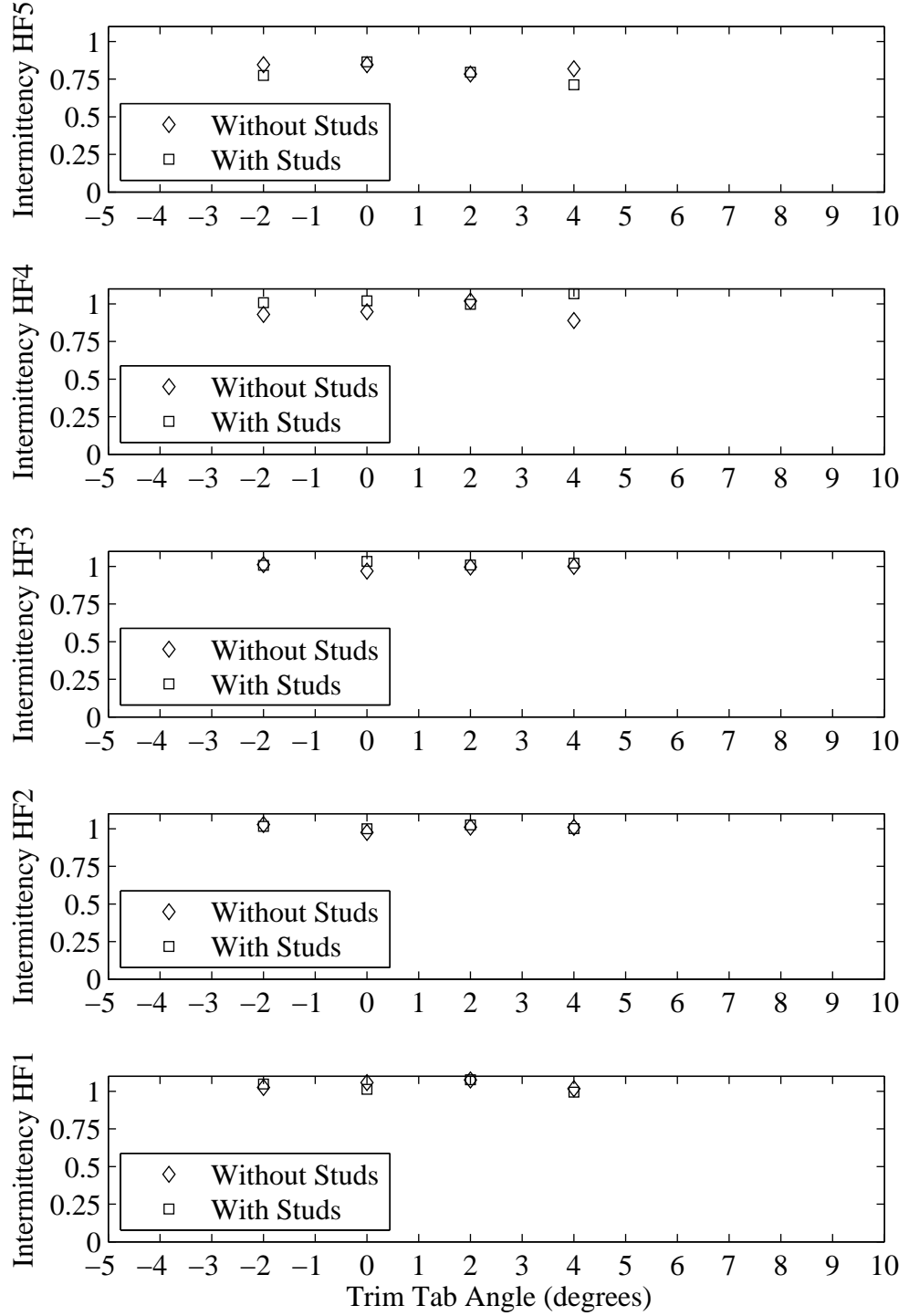


Figure H.3: Intermittency plotted with respect to variation in trim tab angle. Froude number 0.40, Yaw -1 degrees, Heel 0 degrees, Rudder 0 degrees.

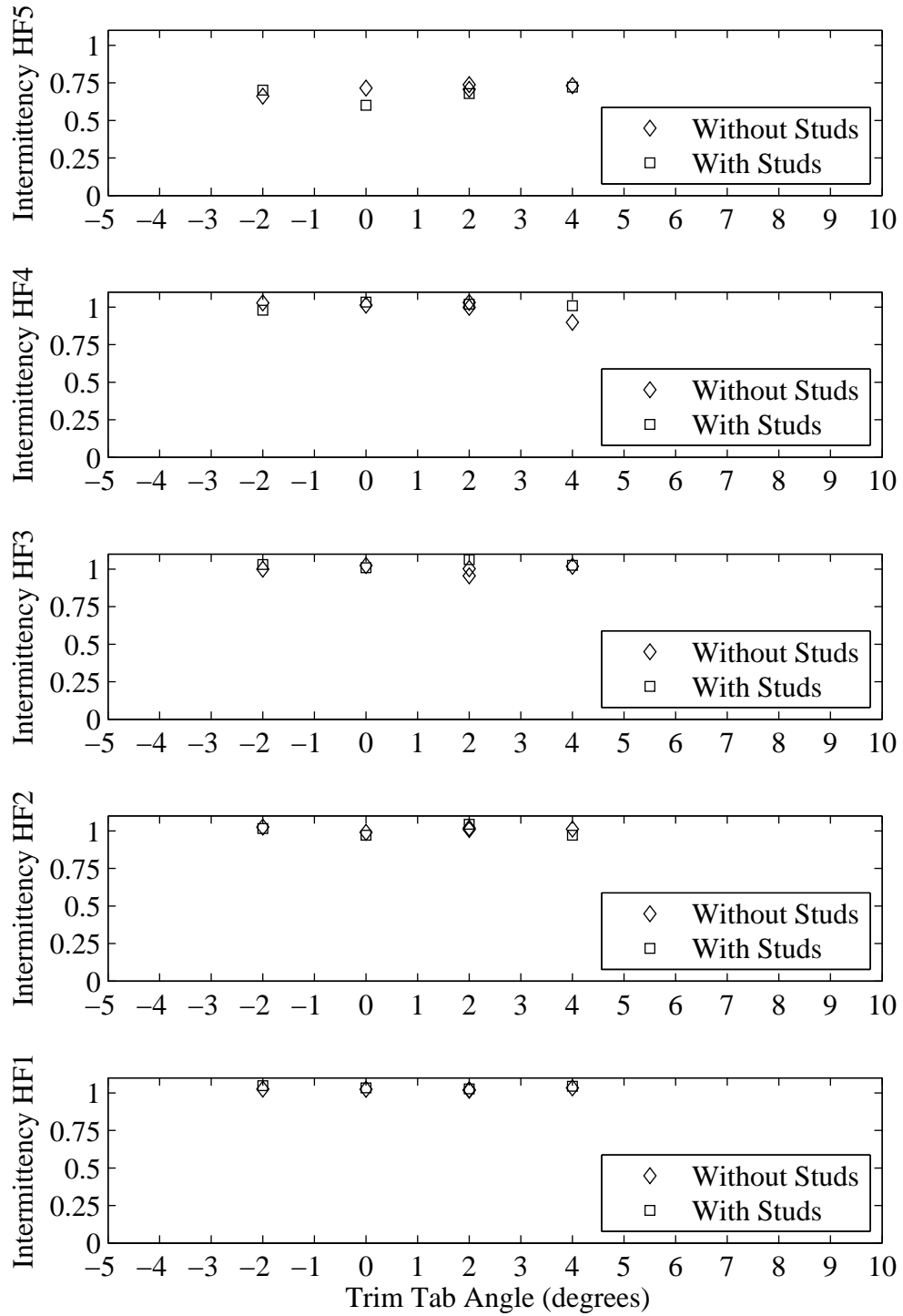


Figure H.4: Froude number 0.40, Yaw 0 degrees, Heel 0 degrees, Rudder 0 degrees.

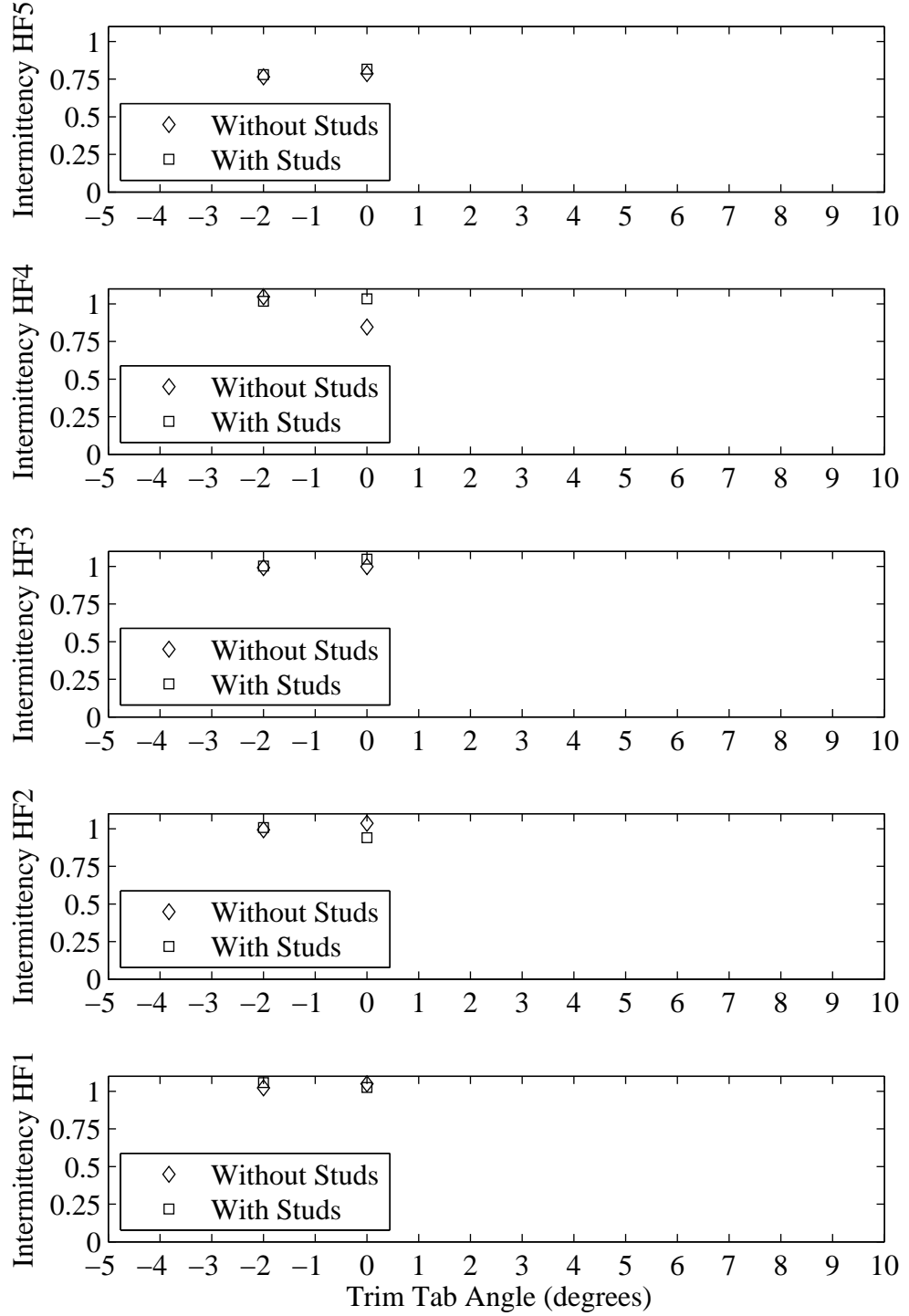


Figure H.5: Intermittency plotted with respect to variation in trim tab angle. Froude number 0.40, Yaw 1 degrees, Heel 0 degrees, Rudder 0 degrees.

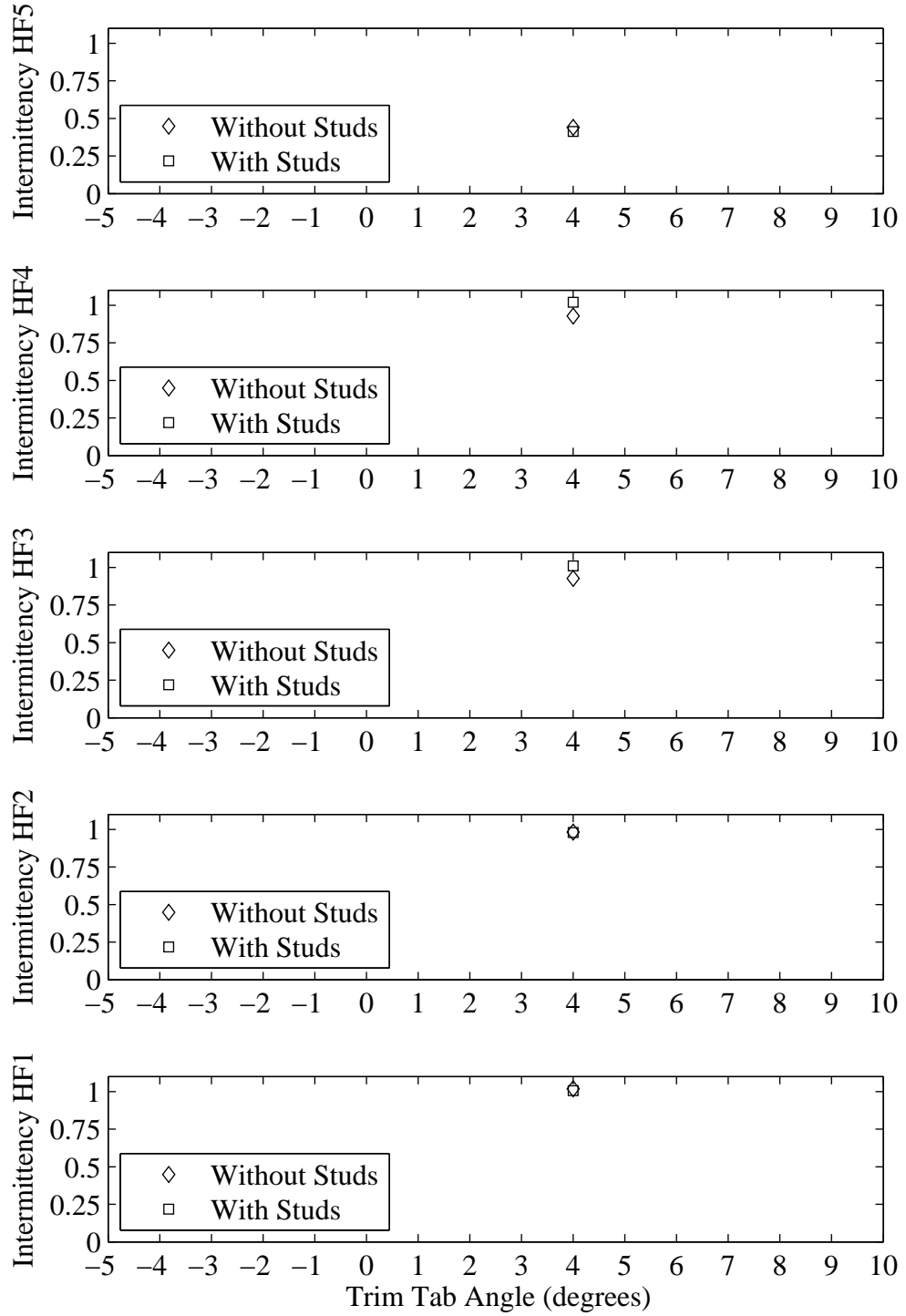


Figure H.6: Intermittency plotted with respect to variation in trim tab angle. Froude number 0.29, Yaw -2 degrees, Heel 5 degrees, Rudder 4 degrees.

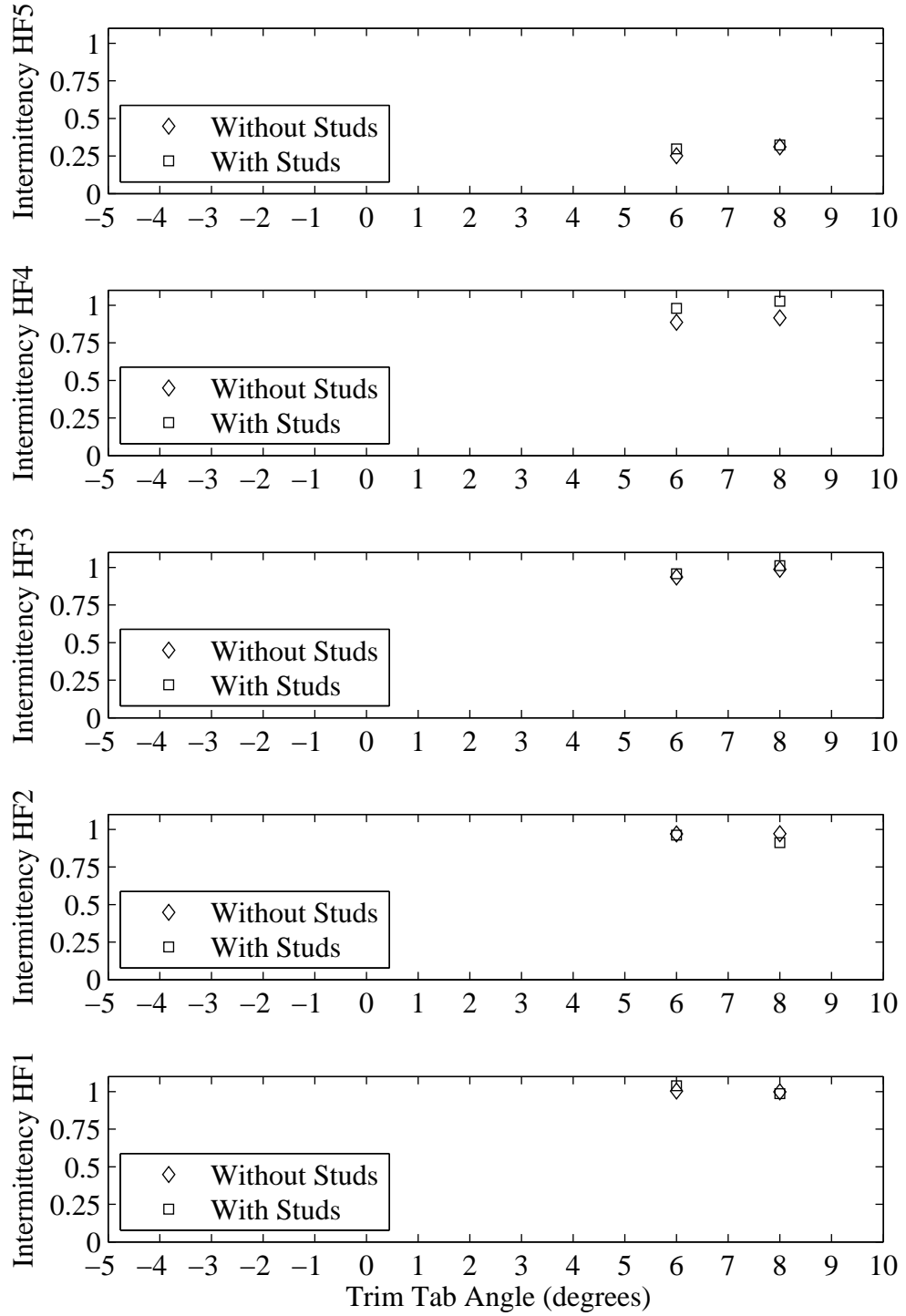


Figure H.7: Intermittency plotted with respect to variation in trim tab angle. Velocity 1.28 m/s, Yaw -2 degrees, Heel 5 degrees, Rudder 2 degrees.

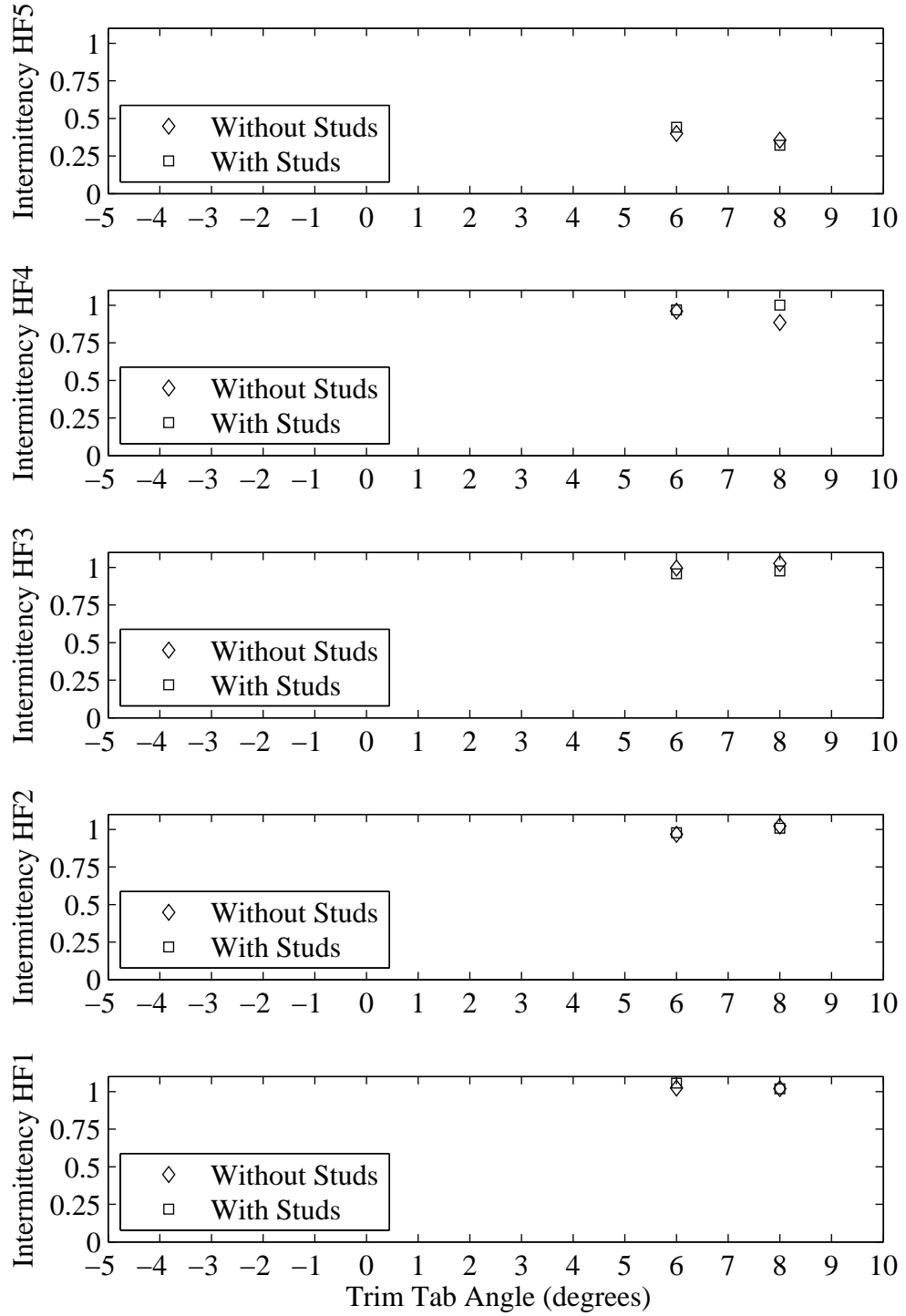


Figure H.8: Intermittency plotted with respect to variation in trim tab angle. Froude number 0.29, Yaw -2 degrees, Heel 5 degrees, Rudder 2 degrees.

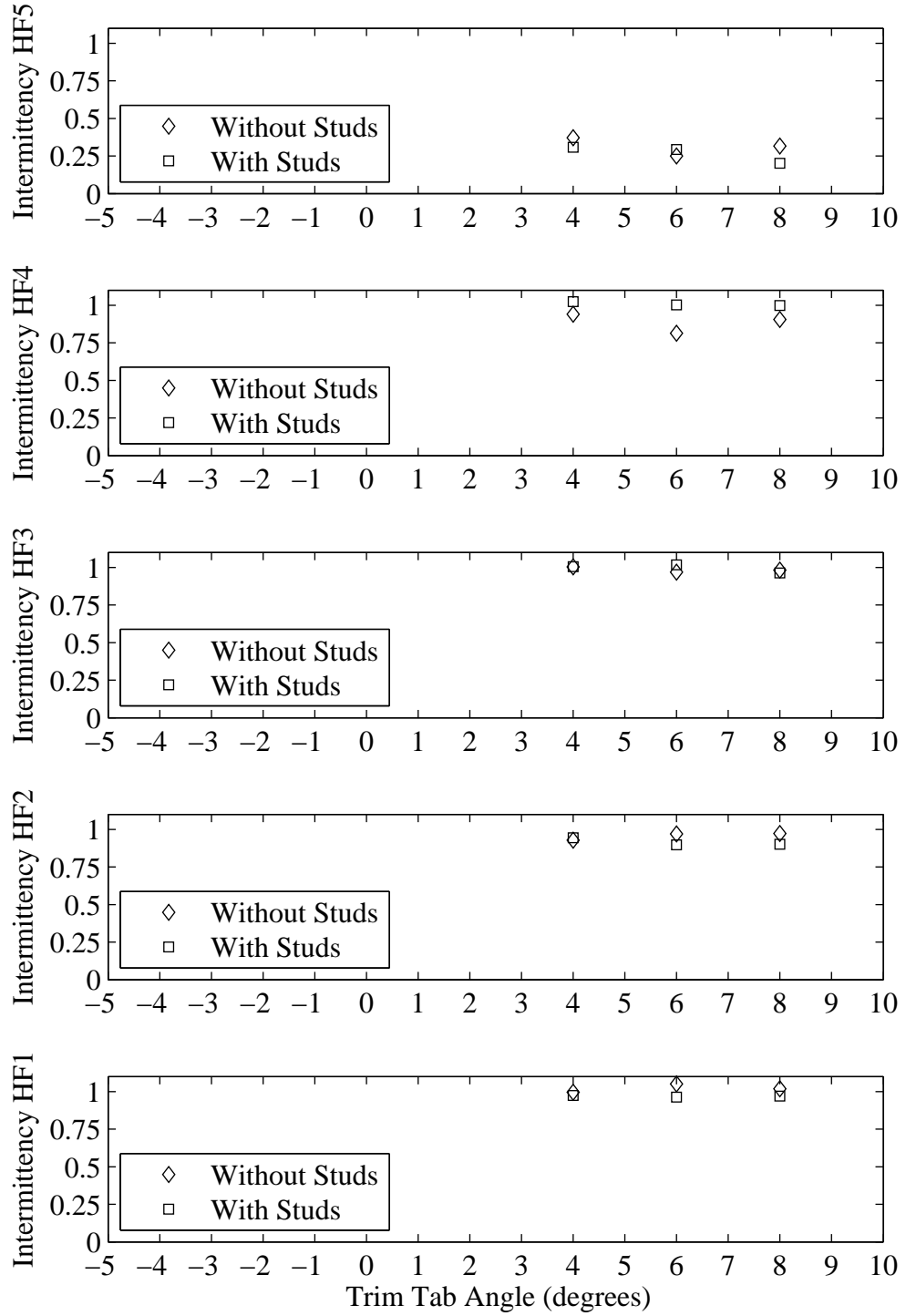


Figure H.9: Intermittency plotted with respect to variation in trim tab angle. Velocity 1.28 m/s, Yaw 0 degrees, Heel 5 degrees, Rudder 2 degrees.

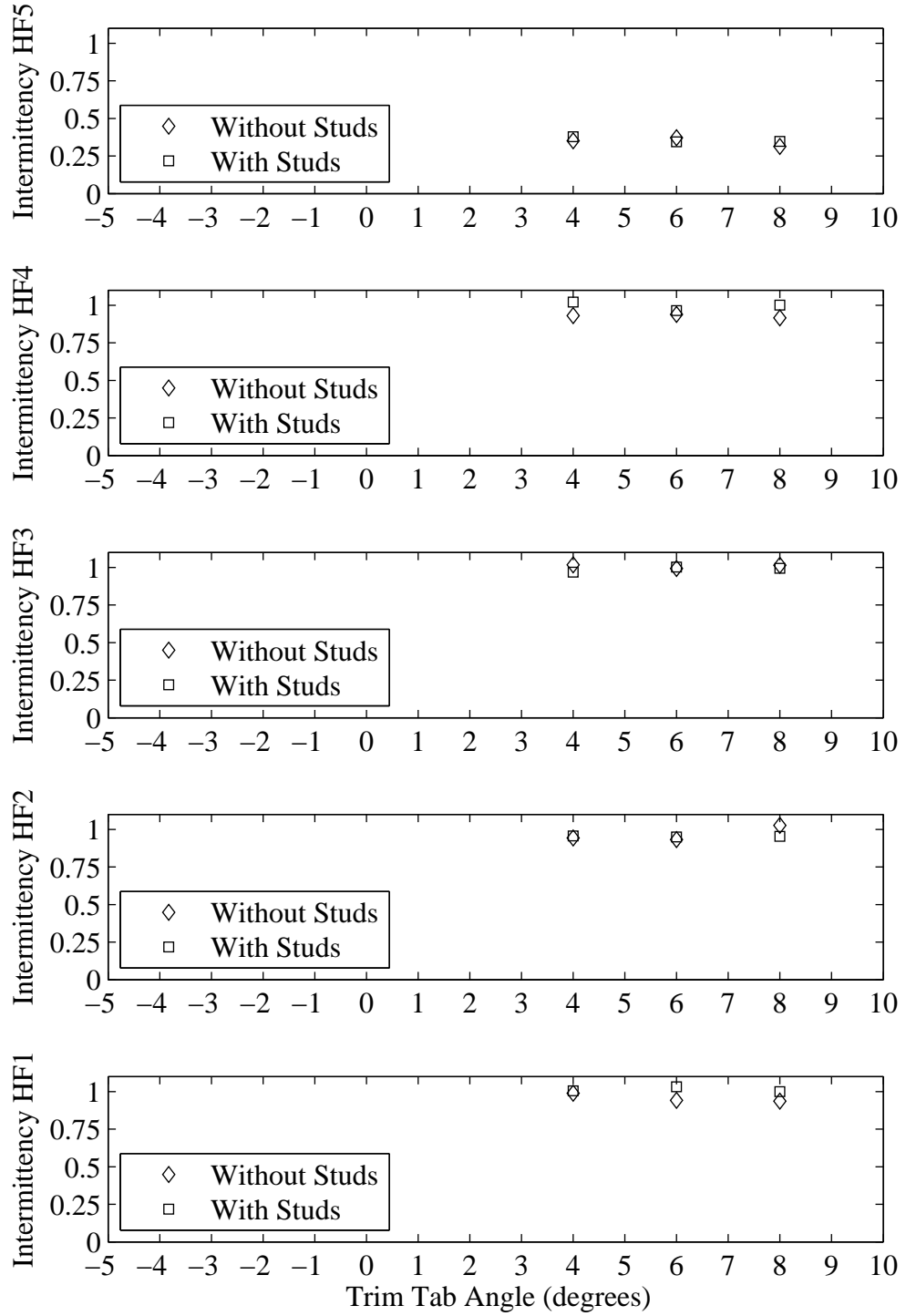


Figure H.10: Intermittency plotted with respect to variation in trim tab angle. Froude number 0.29, Yaw 0 degrees, Heel 5 degrees, Rudder 2 degrees.

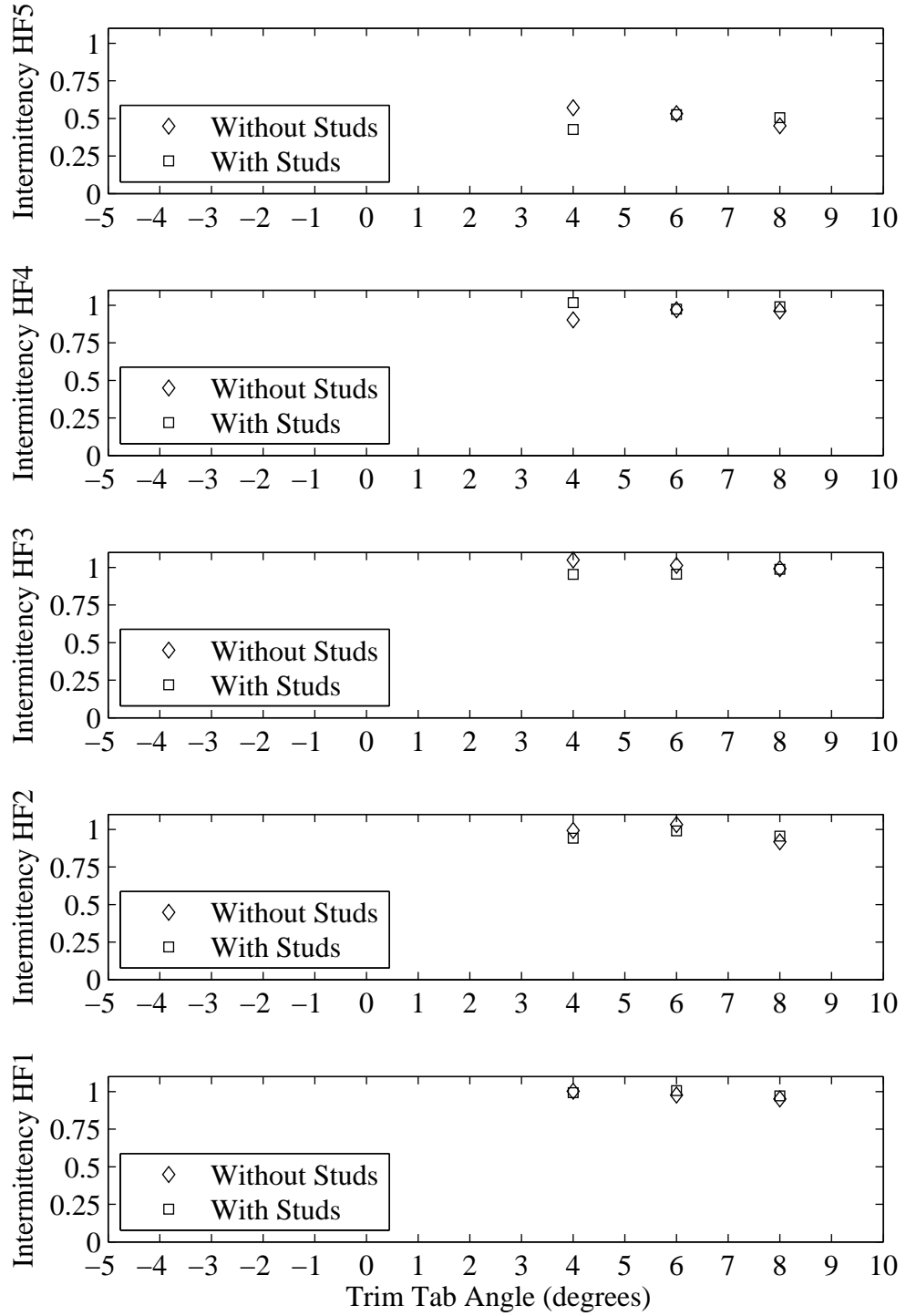


Figure H.11: Intermittency plotted with respect to variation in trim tab angle. Velocity 1.28 m/s, Yaw 1 degrees, Heel 5 degrees, Rudder 2 degrees.

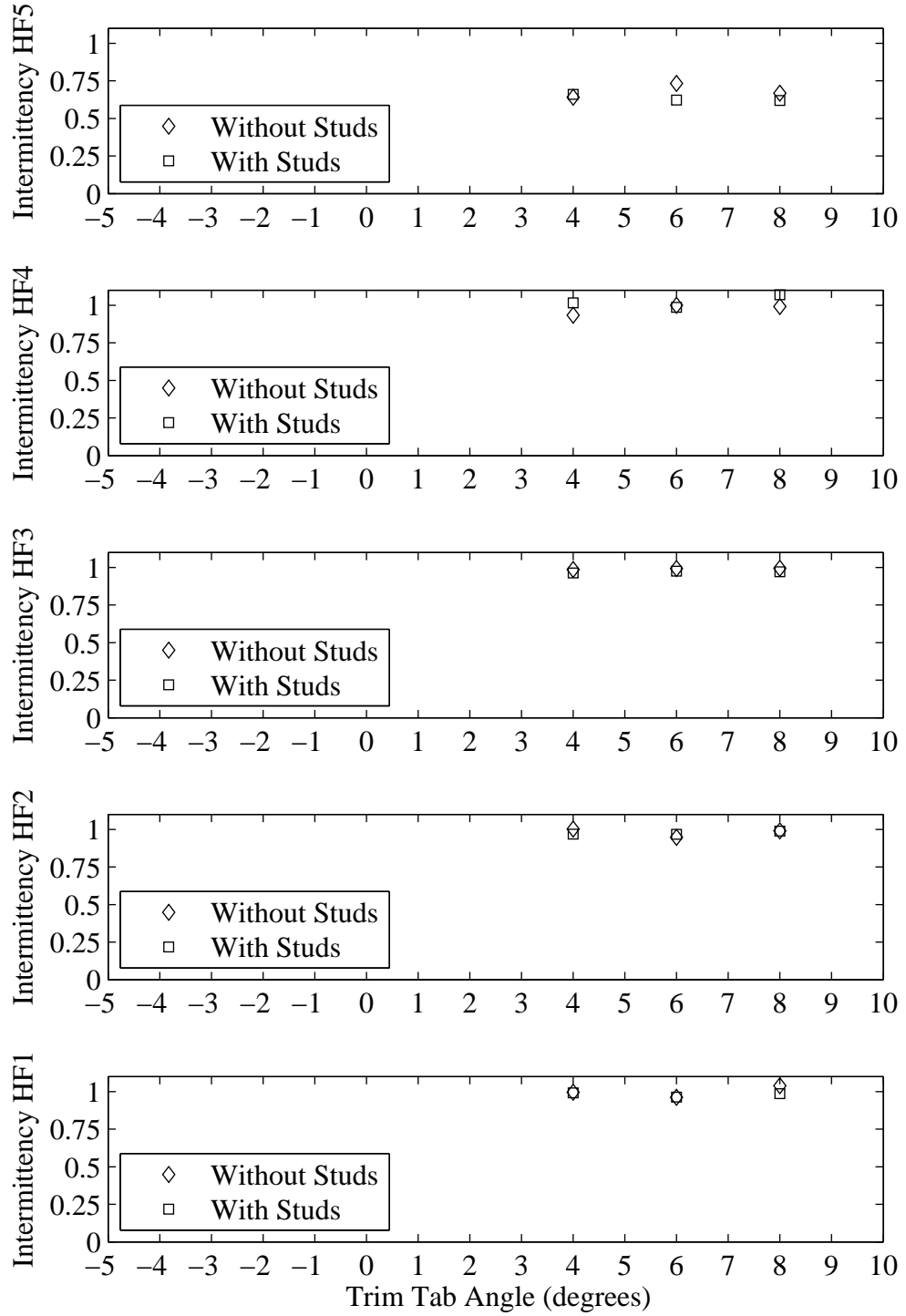


Figure H.12: Intermittency plotted with respect to variation in trim tab angle. Froude number 0.29, Yaw 1 degrees, Heel 10 degrees, Rudder 2 degrees.

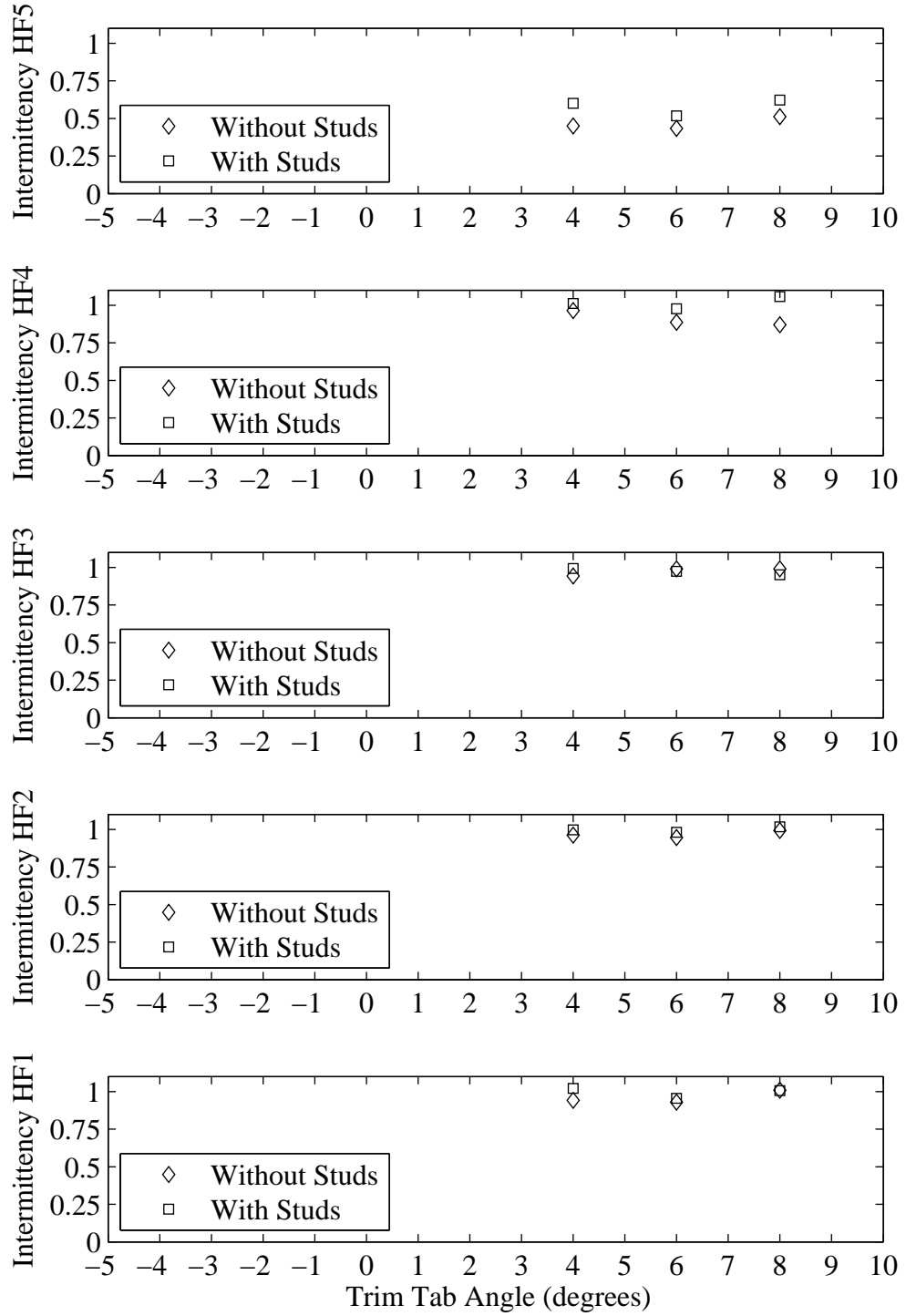


Figure H.13: Intermittency plotted with respect to variation in trim tab angle. Velocity 1.28 m/s, Yaw 1 degrees, Heel 10 degrees, Rudder 2 degrees.

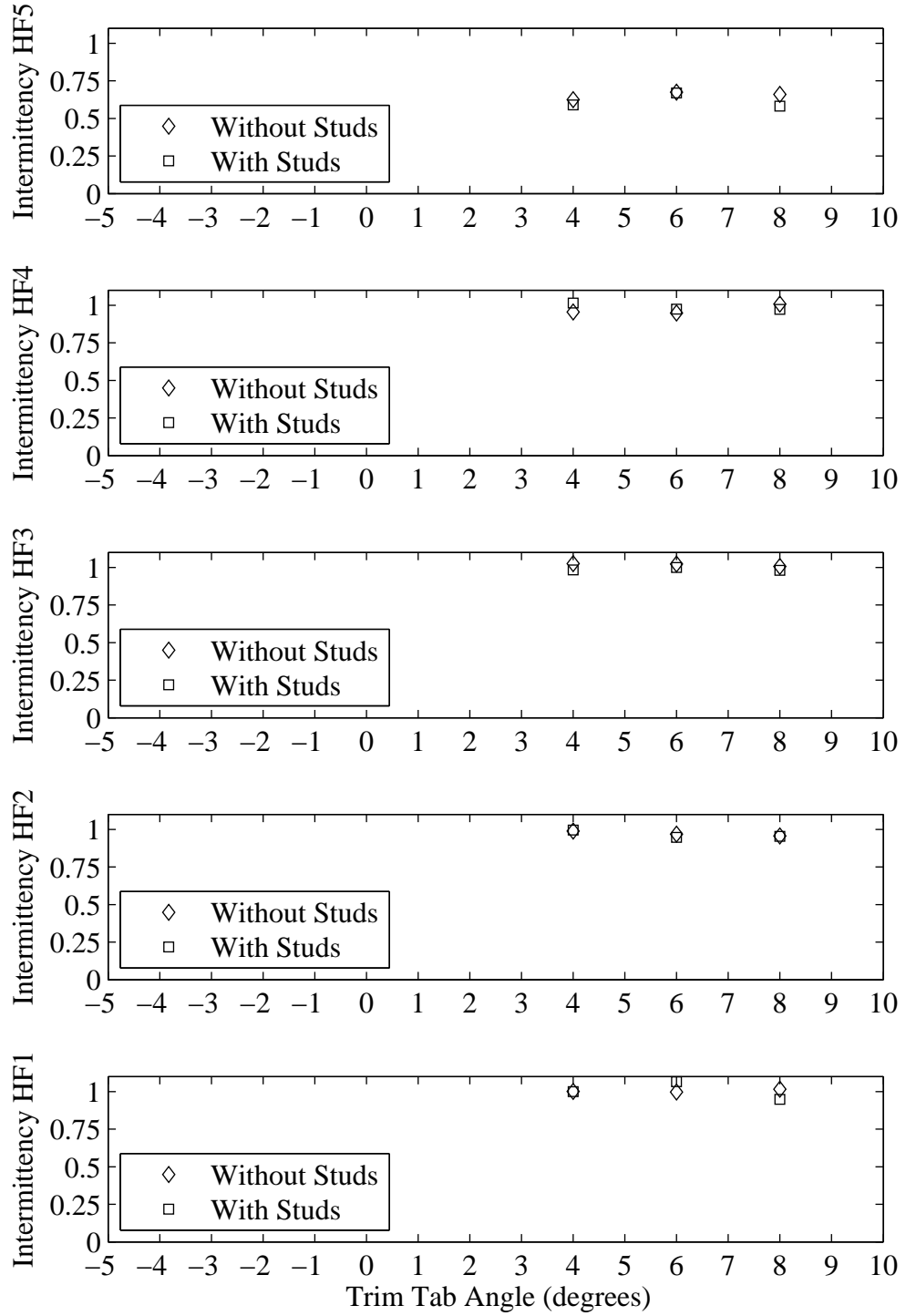


Figure H.14: Intermittency plotted with respect to variation in trim tab angle. Froude number 0.29, Yaw 1 degrees, Heel 10 degrees, Rudder 2 degrees.

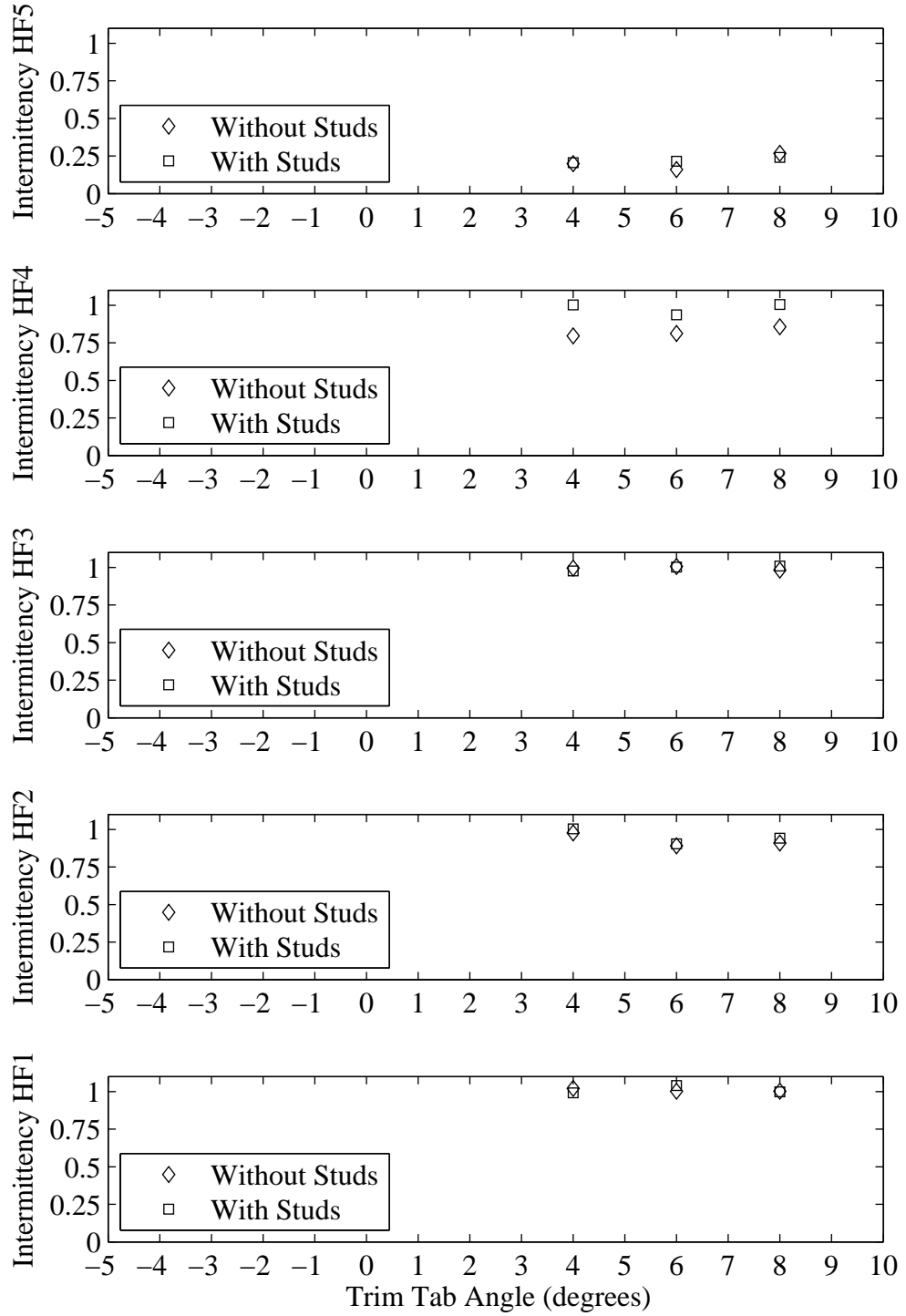


Figure H.15: Intermittency plotted with respect to variation in trim tab angle. Froude number 0.27, Yaw 0 degrees, Heel 10 degrees, Rudder 2 degrees.

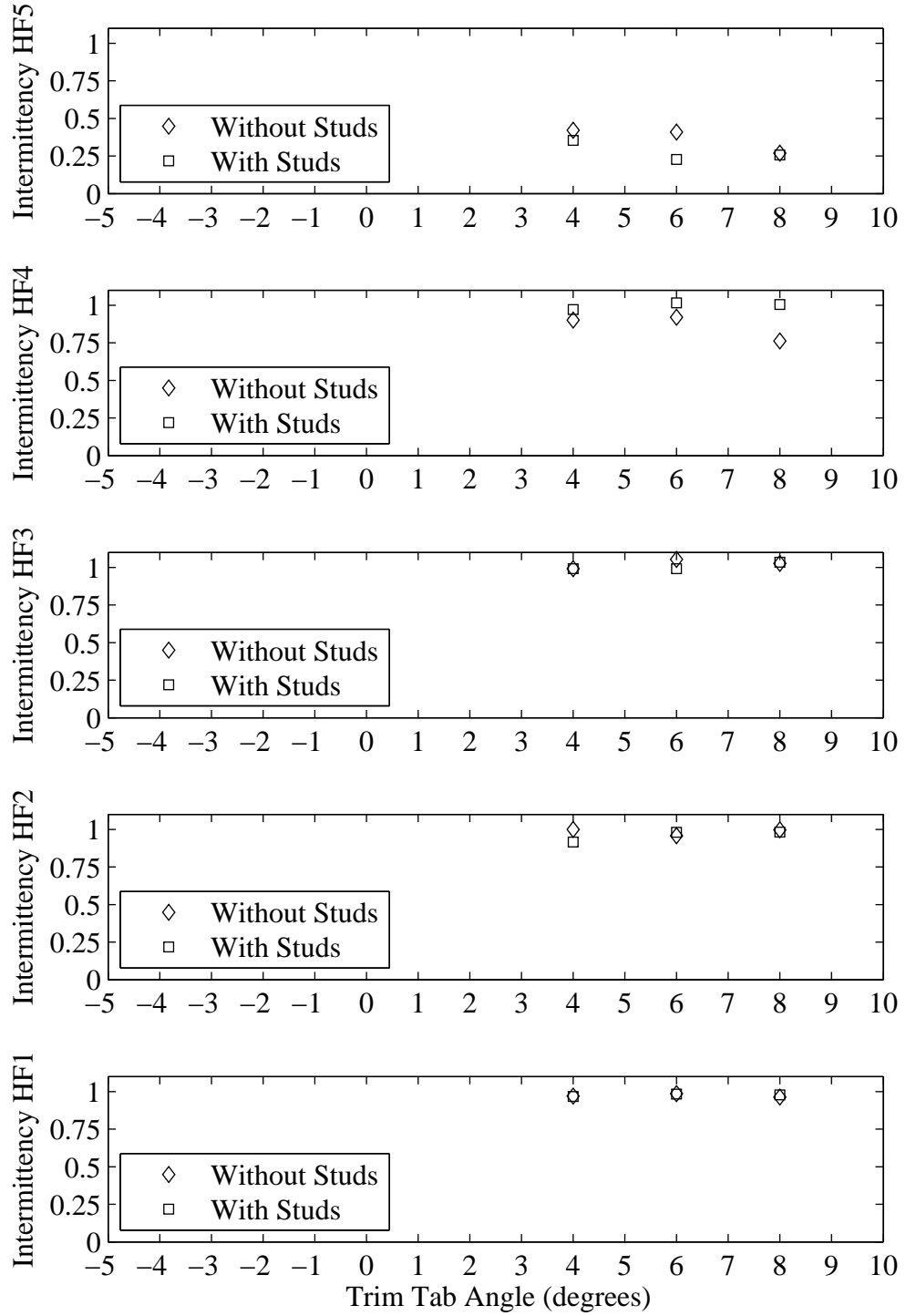


Figure H.16: Intermittency plotted with respect to variation in trim tab angle. Froude number 0.29, Yaw 0 degrees, Heel 10 degrees, Rudder 2 degrees.

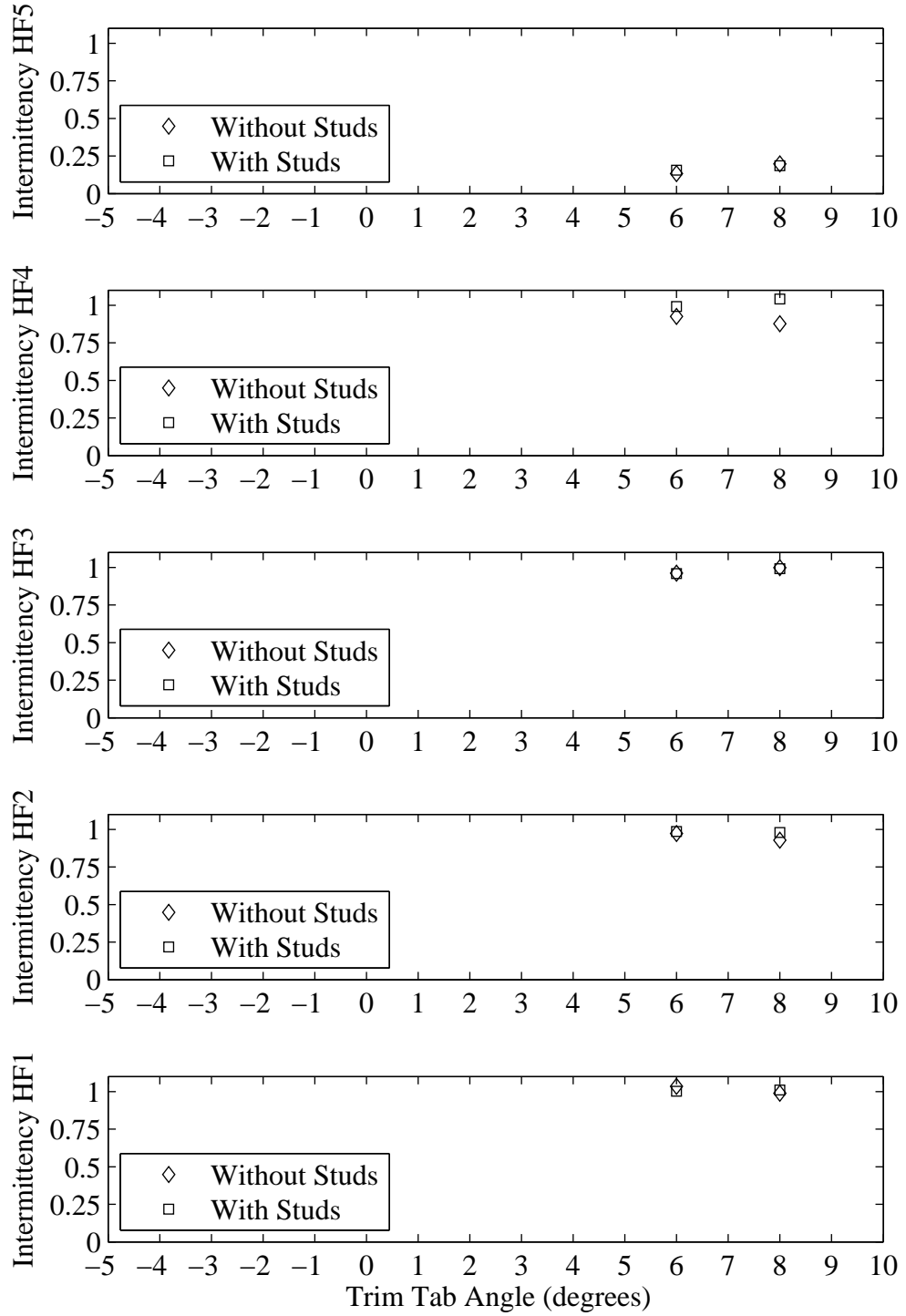


Figure H.17: Intermittency plotted with respect to variation in trim tab angle. Froude number 0.27, Yaw -2 degrees, Heel 10 degrees, Rudder 2 degrees.

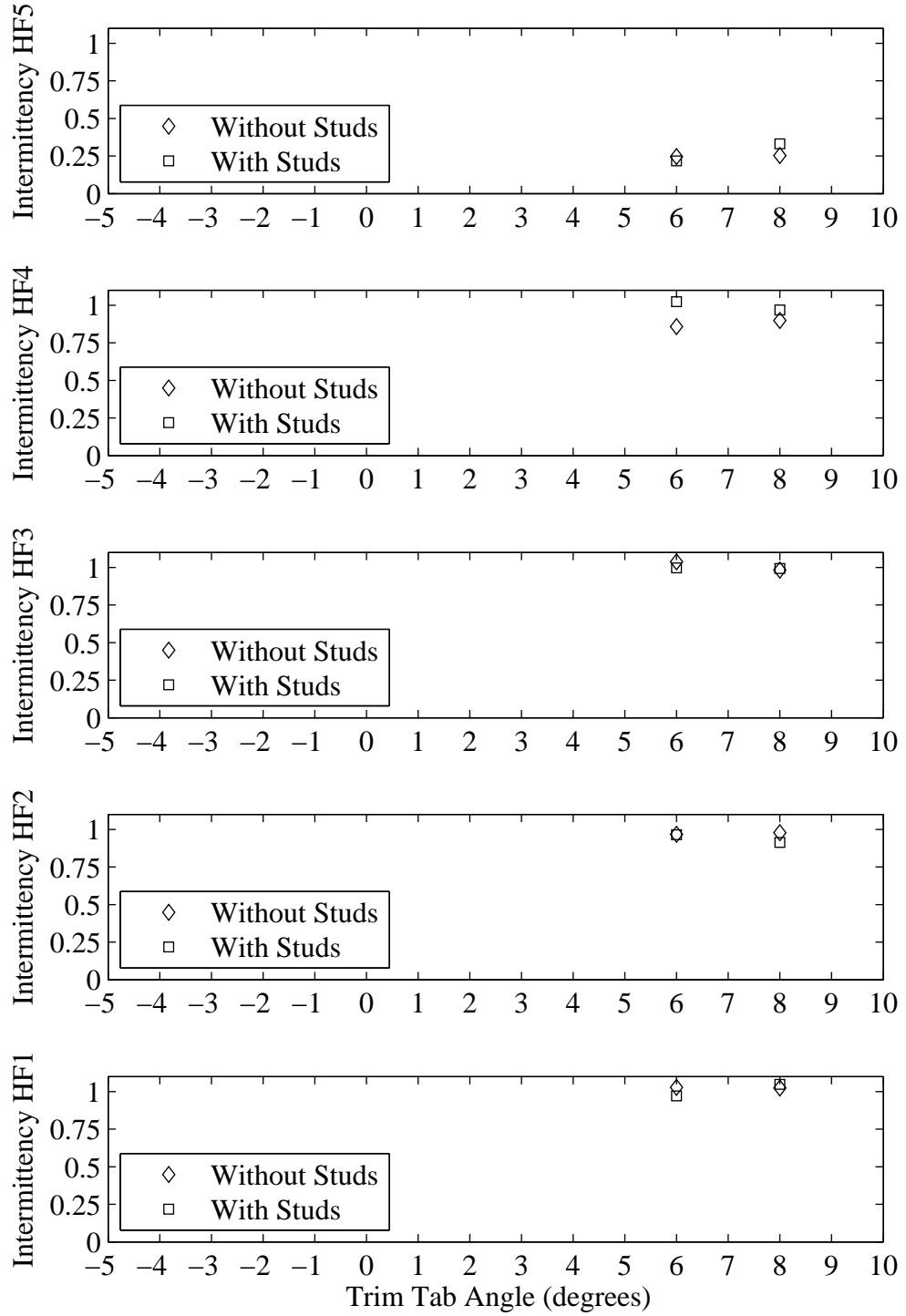


Figure H.18: Intermittency plotted with respect to variation in trim tab angle. Froude number 0.29, Yaw -2 degrees, Heel 10 degrees, Rudder 2 degrees.

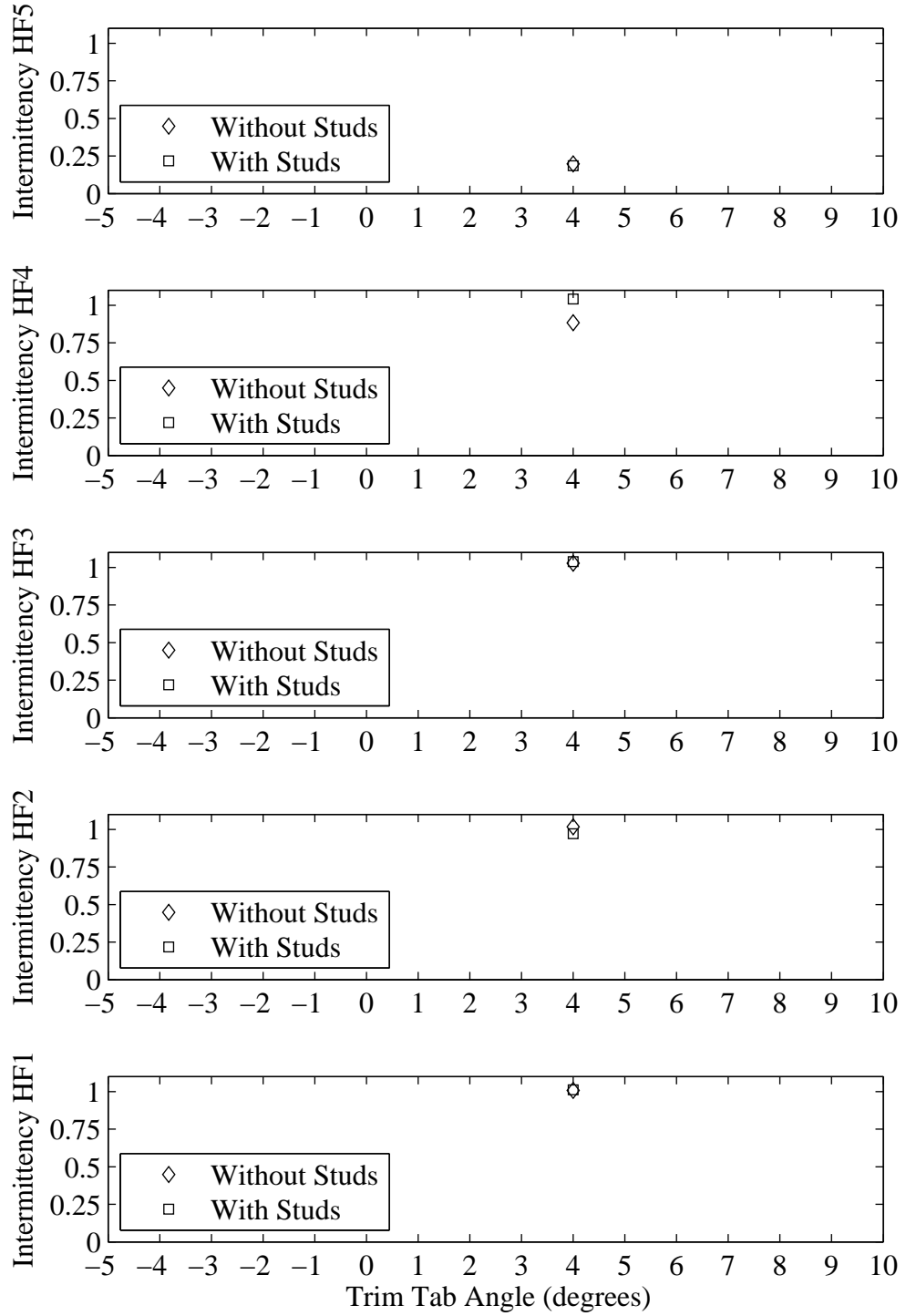


Figure H.19: Intermittency plotted with respect to variation in trim tab angle. Froude number 0.29, Yaw -2 degrees, Heel 10 degrees, Rudder 4 degrees.

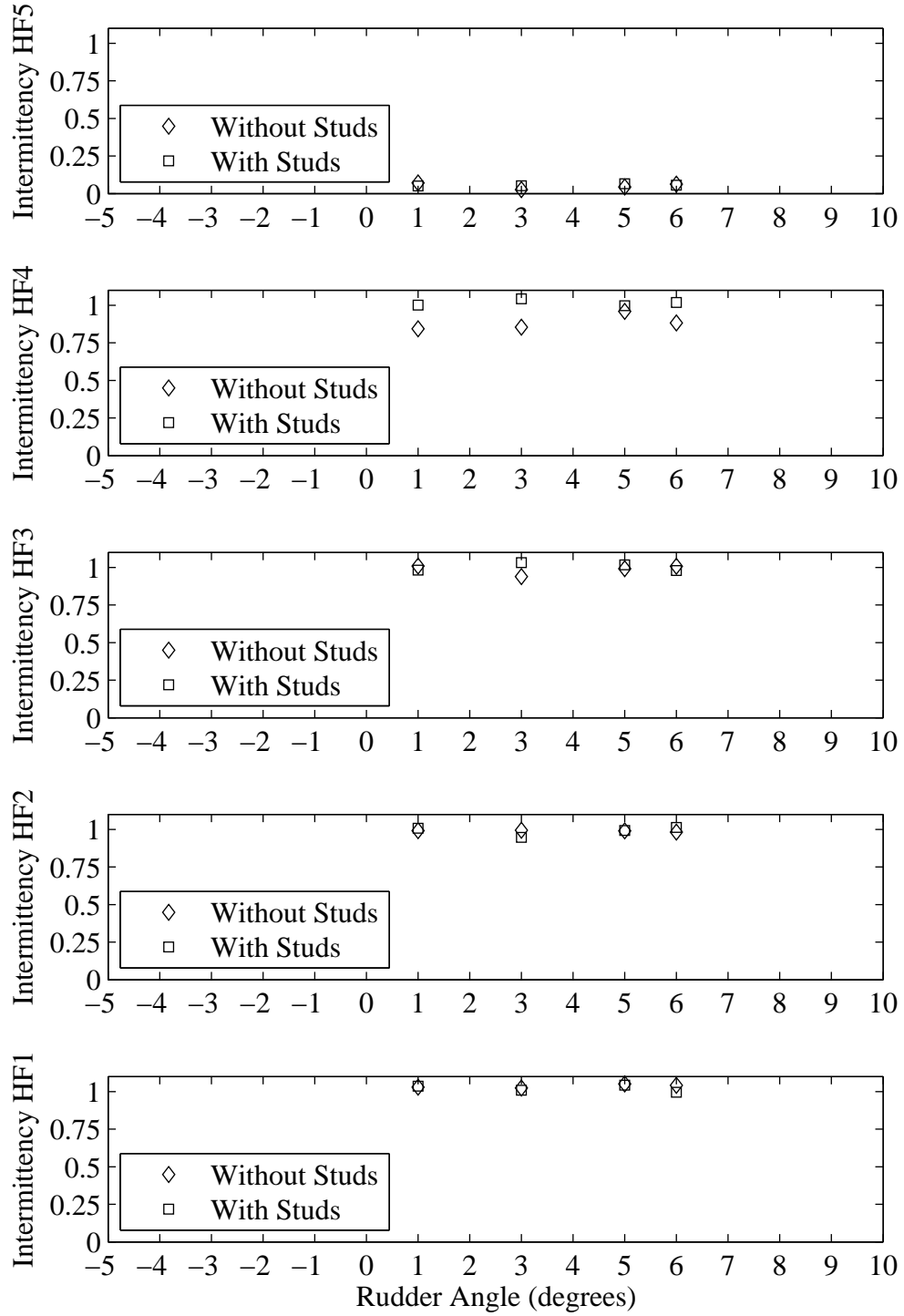


Figure H.20: Intermittency plotted with respect to variation in rudder angle. Froude number 0.32, Yaw -2 degrees, Heel 20 degrees, Tab 10 degrees.

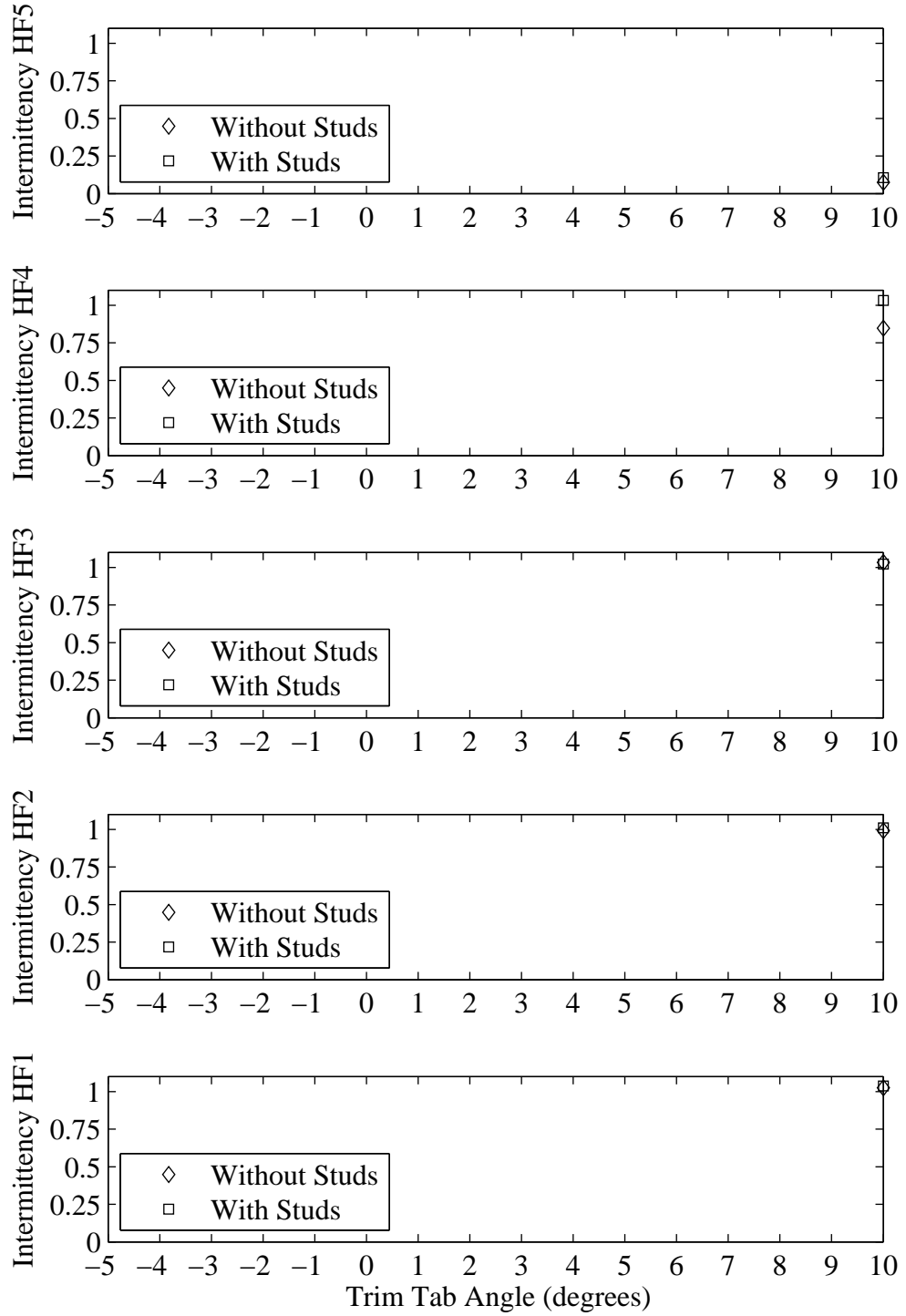


Figure H.21: Intermittency plotted with respect to variation in trim tab angle. Froude number 0.34, Yaw -2 degrees, Heel 20 degrees, Rudder 1 degrees.

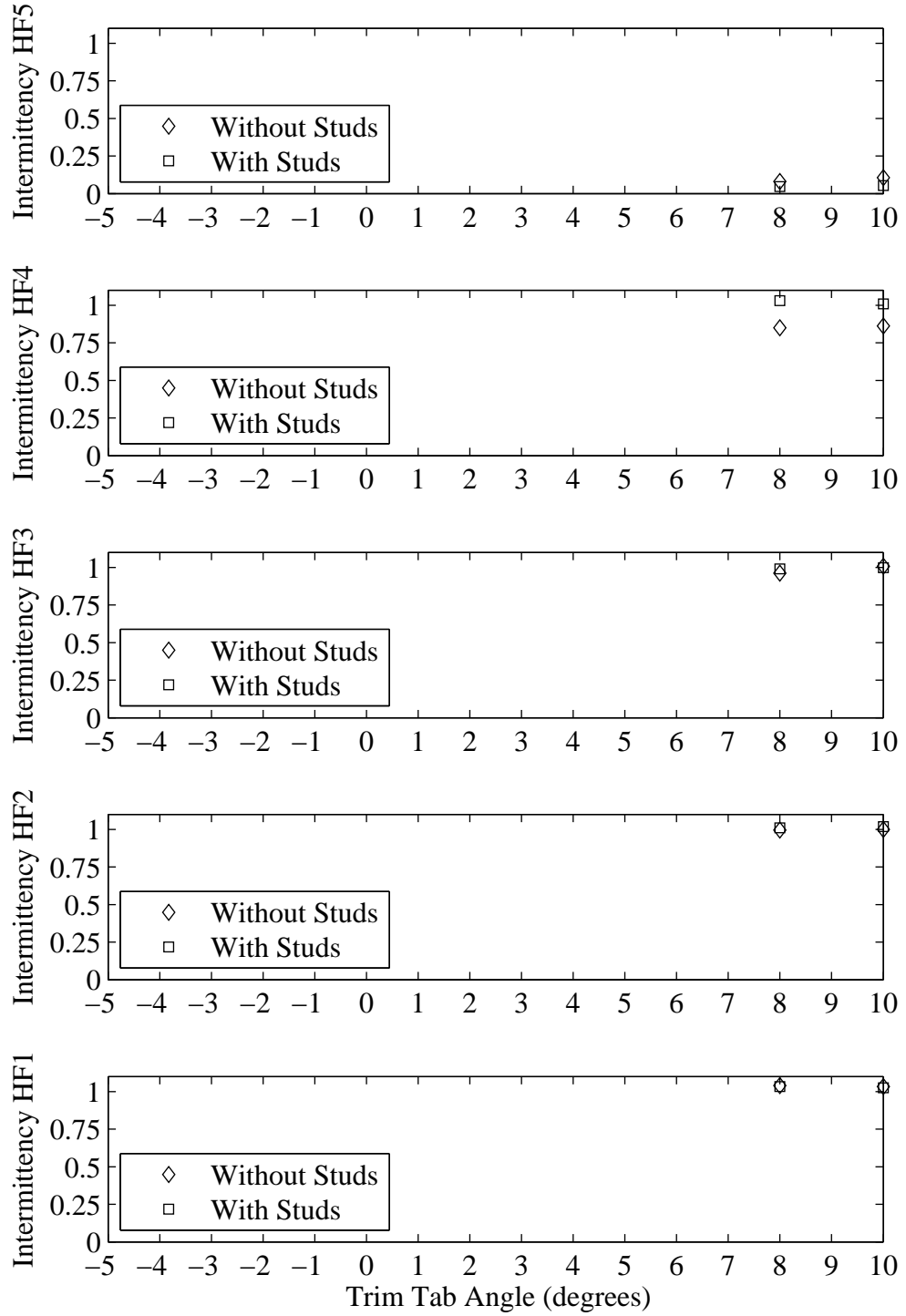


Figure H.22: Intermittency plotted with respect to variation in trim tab angle. Froude number 0.34, Yaw -2 degrees, Heel 20 degrees, Rudder 3 degrees.

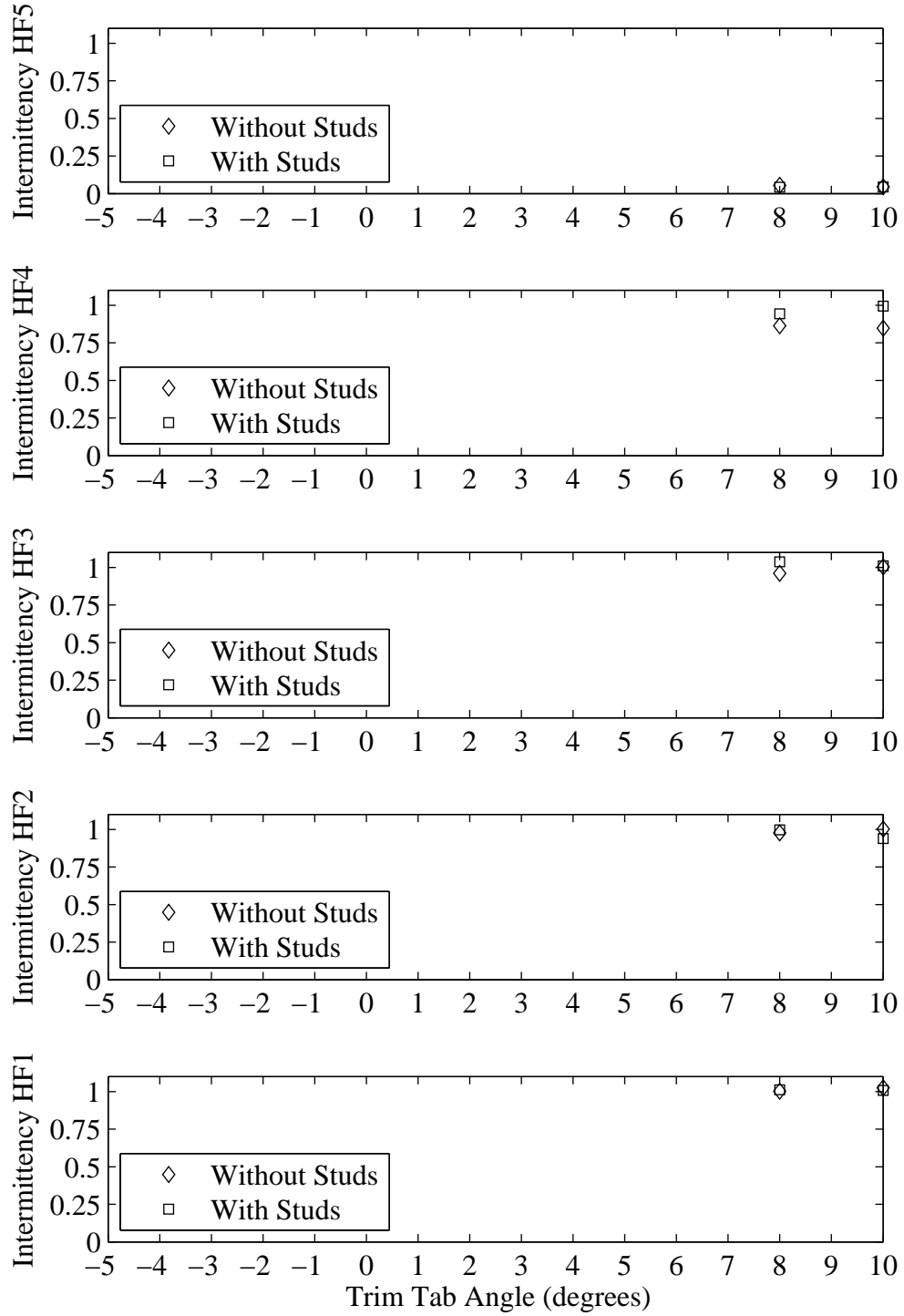


Figure H.23: Intermittency plotted with respect to variation in trim tab angle. Froude number 0.34, Yaw -2 degrees, Heel 20 degrees, Rudder 5 degrees.

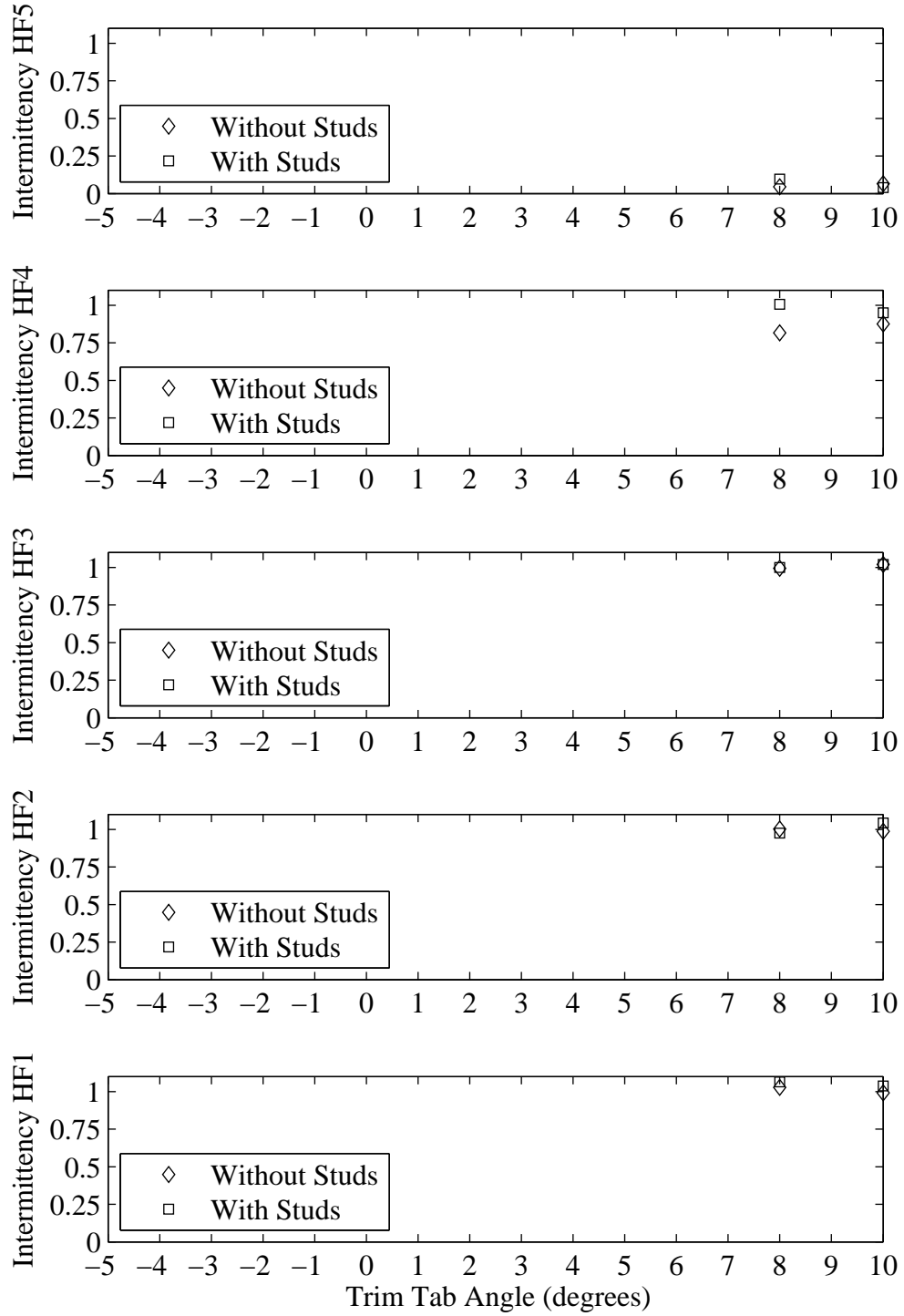


Figure H.24: Intermittency plotted with respect to variation in trim tab angle. Froude number 0.34, Yaw -2 degrees, Heel 20 degrees, Rudder 6 degrees.

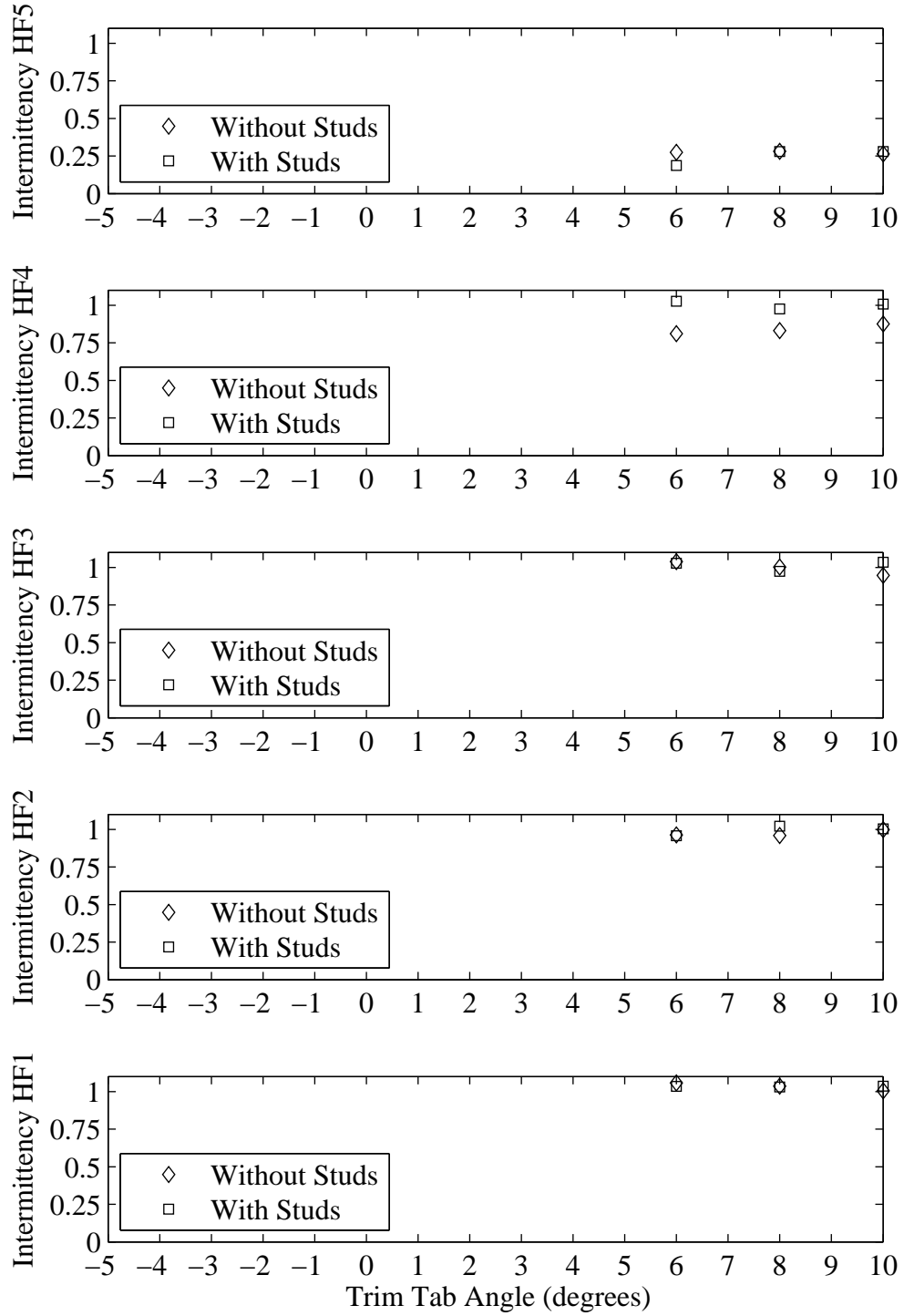


Figure H.25: Intermittency plotted with respect to variation in trim tab angle. Froude number 0.34, Yaw 0 degrees, Heel 20 degrees, Rudder 1 degrees.

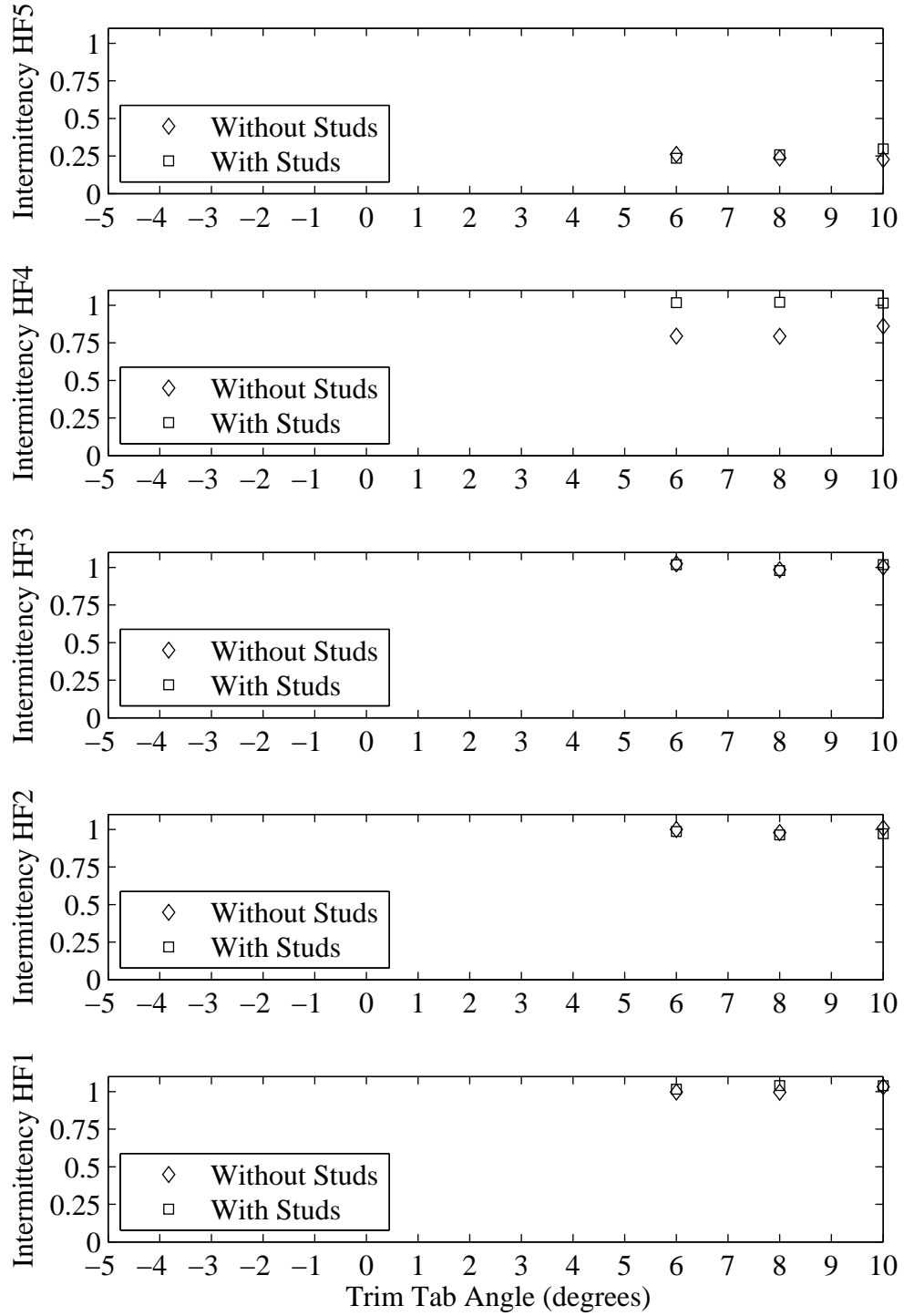


Figure H.26: Intermittency plotted with respect to variation in trim tab angle. Froude number 0.34, Yaw 0 degrees, Heel 20 degrees, Rudder 3 degrees.

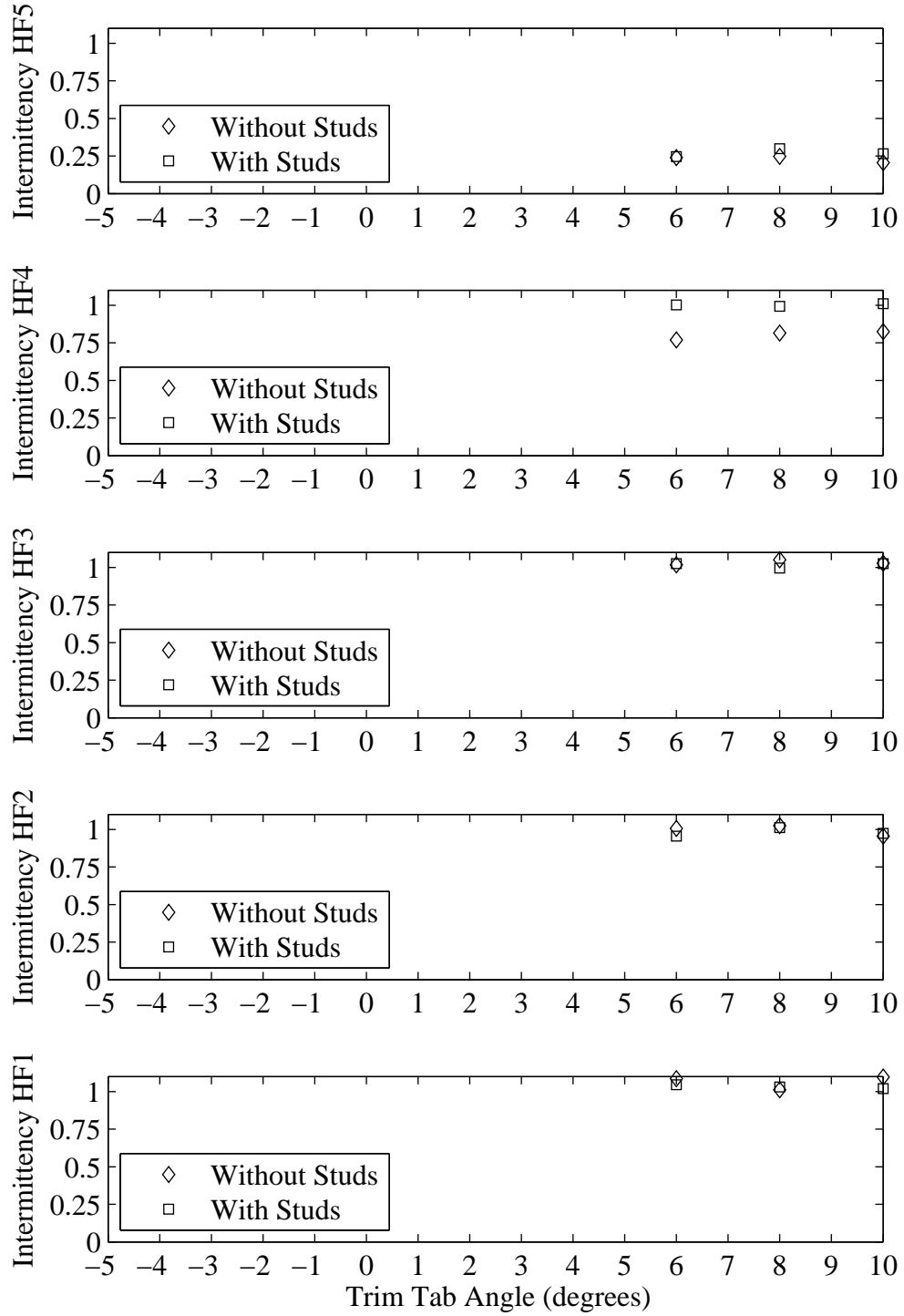


Figure H.27: Intermittency plotted with respect to variation in trim tab angle. Froude number 0.34, Yaw 0 degrees, Heel 20 degrees, Rudder 5 degrees.

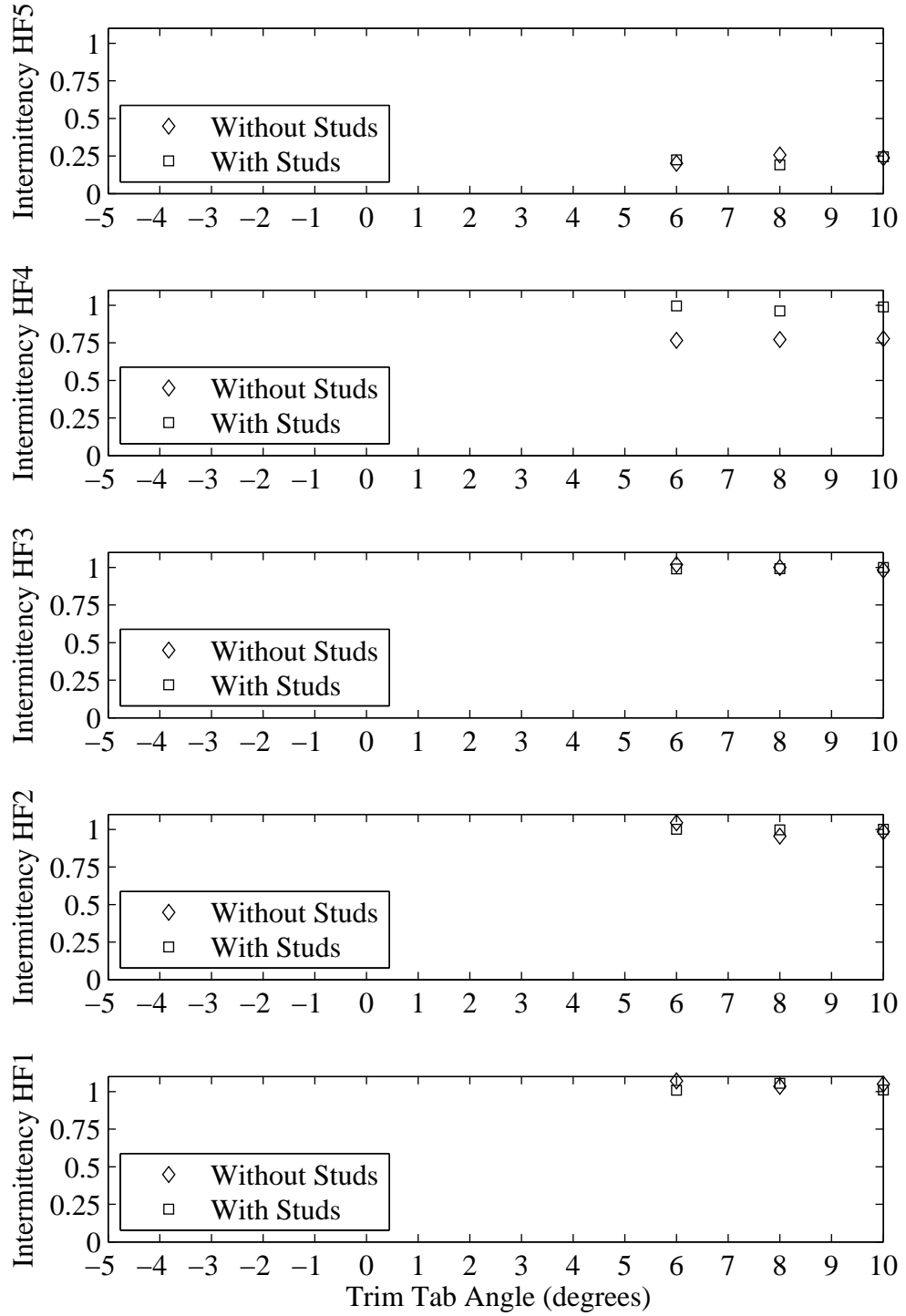


Figure H.28: Intermittency plotted with respect to variation in trim tab angle. Froude number 0.34, Yaw 0 degrees, Heel 20 degrees, Rudder 6 degrees.

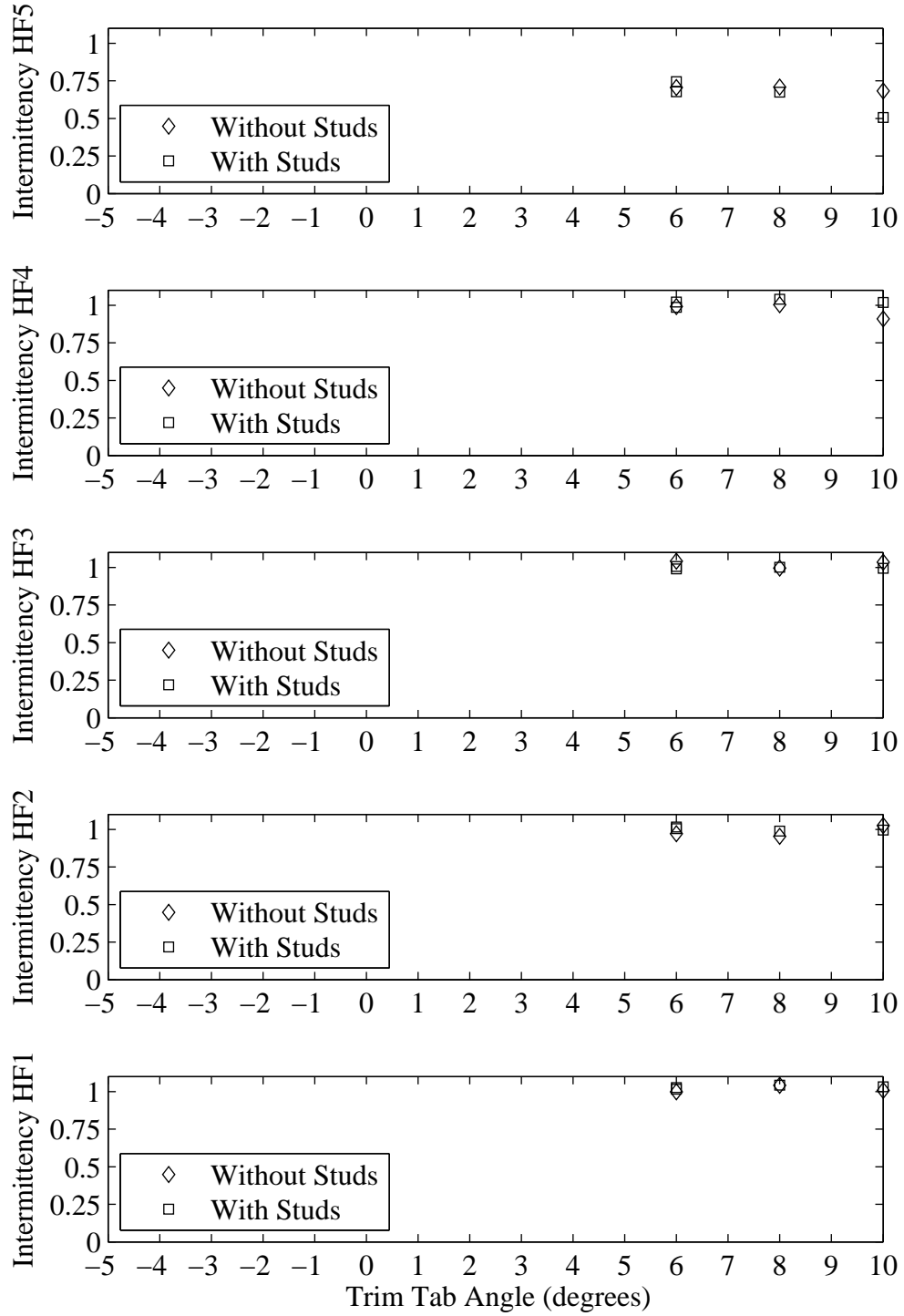


Figure H.29: Intermittency plotted with respect to variation in trim tab angle. Froude number 0.34, Yaw 1 degrees, Heel 20 degrees, Rudder 1 degrees.

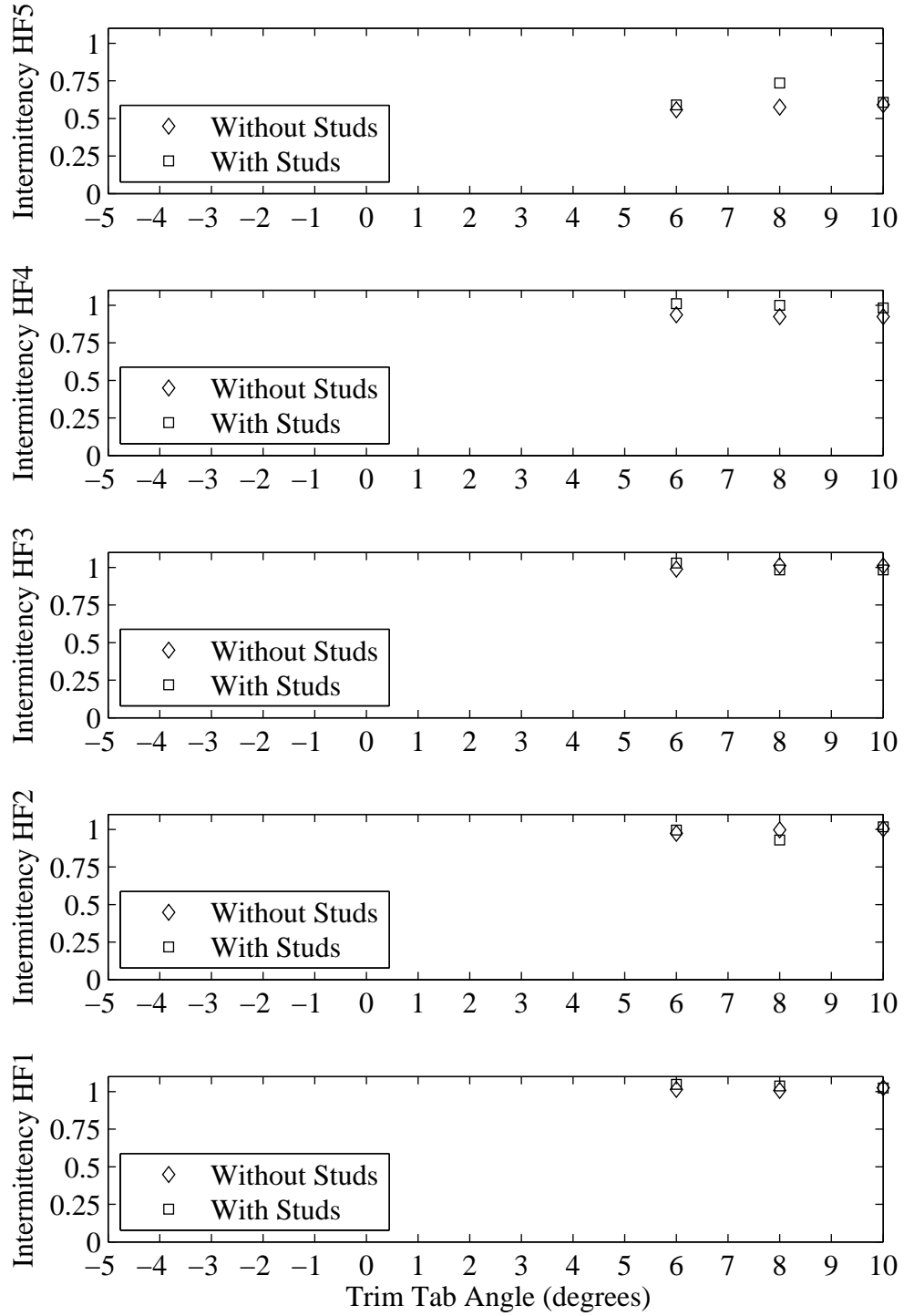


Figure H.30: Intermittency plotted with respect to variation in trim tab angle. Froude number 0.34, Yaw 1 degrees, Heel 20 degrees, Rudder 3 degrees.

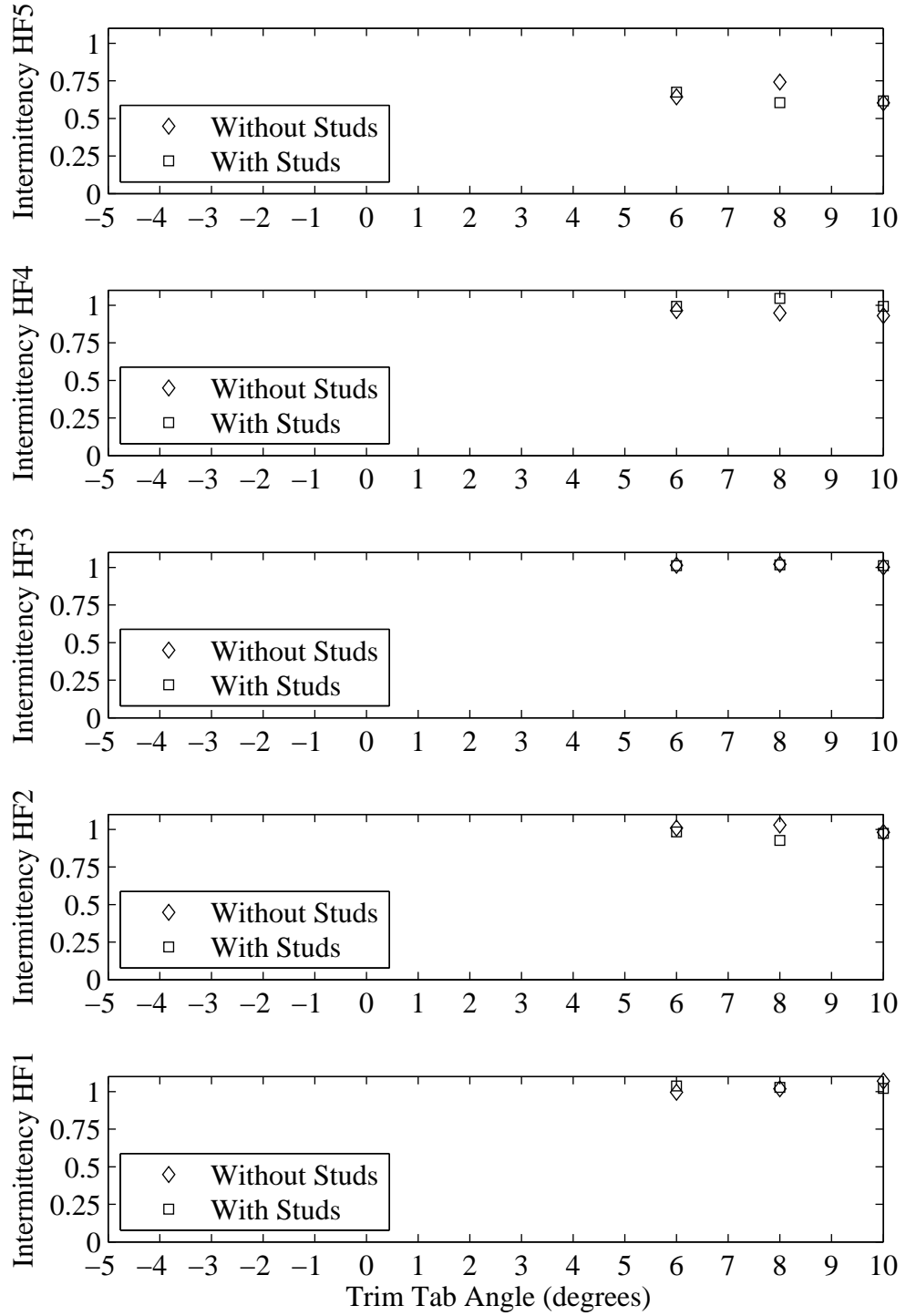


Figure H.31: Intermittency plotted with respect to variation in trim tab angle. Froude number 0.34, Yaw 1 degrees, Heel 20 degrees, Rudder 5 degrees.

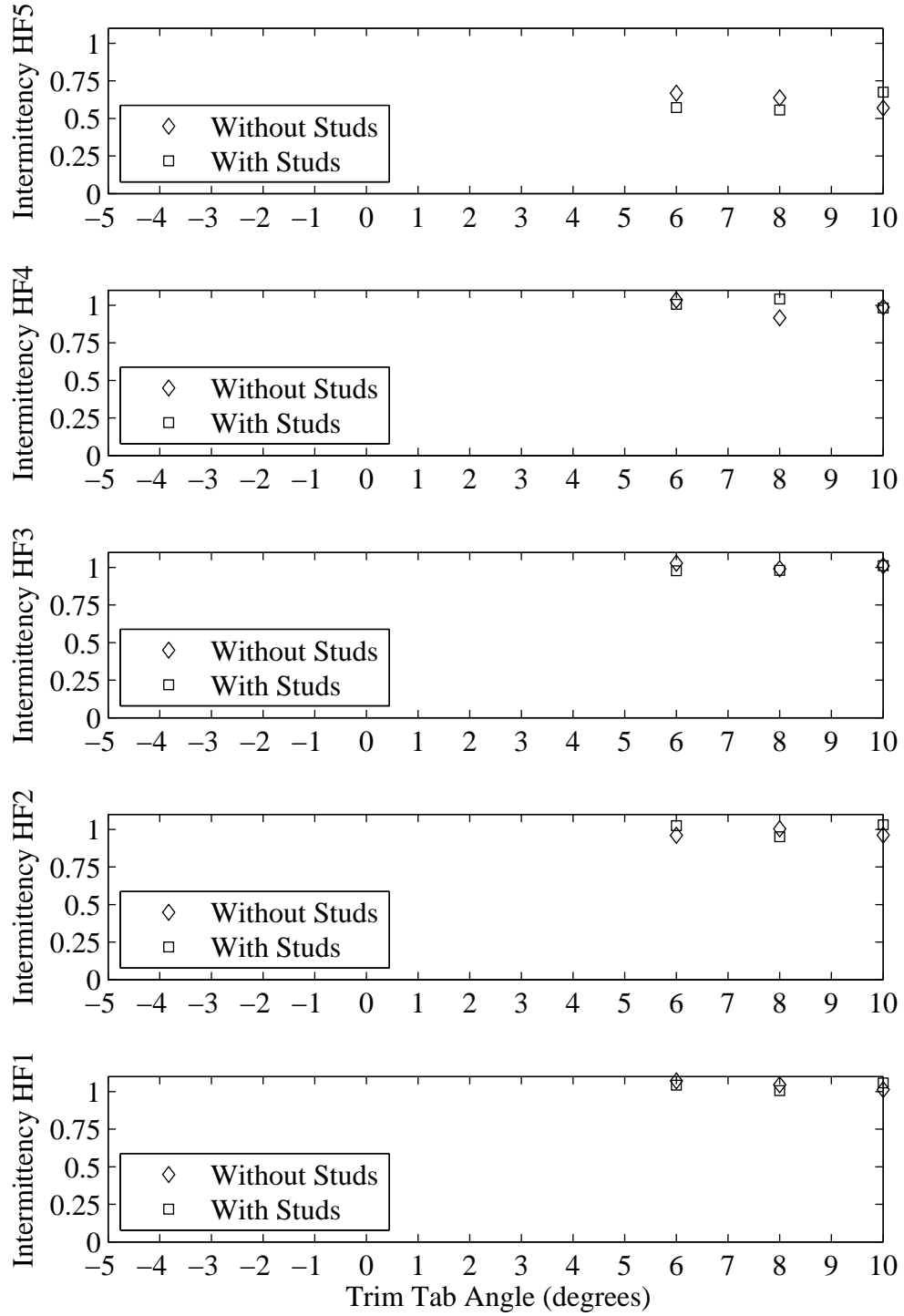


Figure H.32: Intermittency plotted with respect to variation in trim tab angle. Froude number 0.34, Yaw 1 degrees, Heel 20 degrees, Rudder 6 degrees.

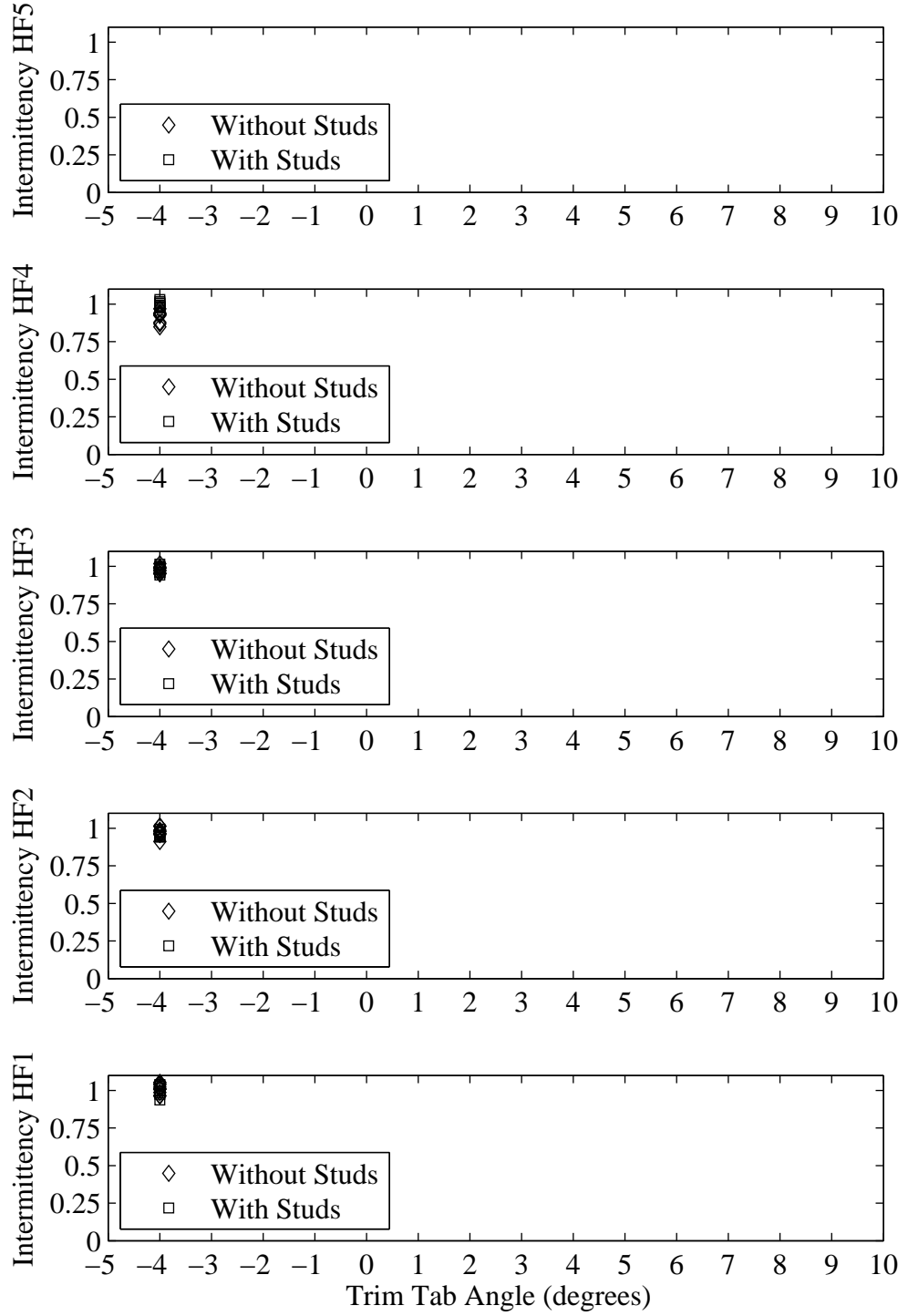


Figure H.33: Intermittency plotted with respect to variation in trim tab angle. Froude number 0.27, Yaw -1 degrees, Heel -10 degrees, Tab -4 degrees, Rudder -2 degrees.

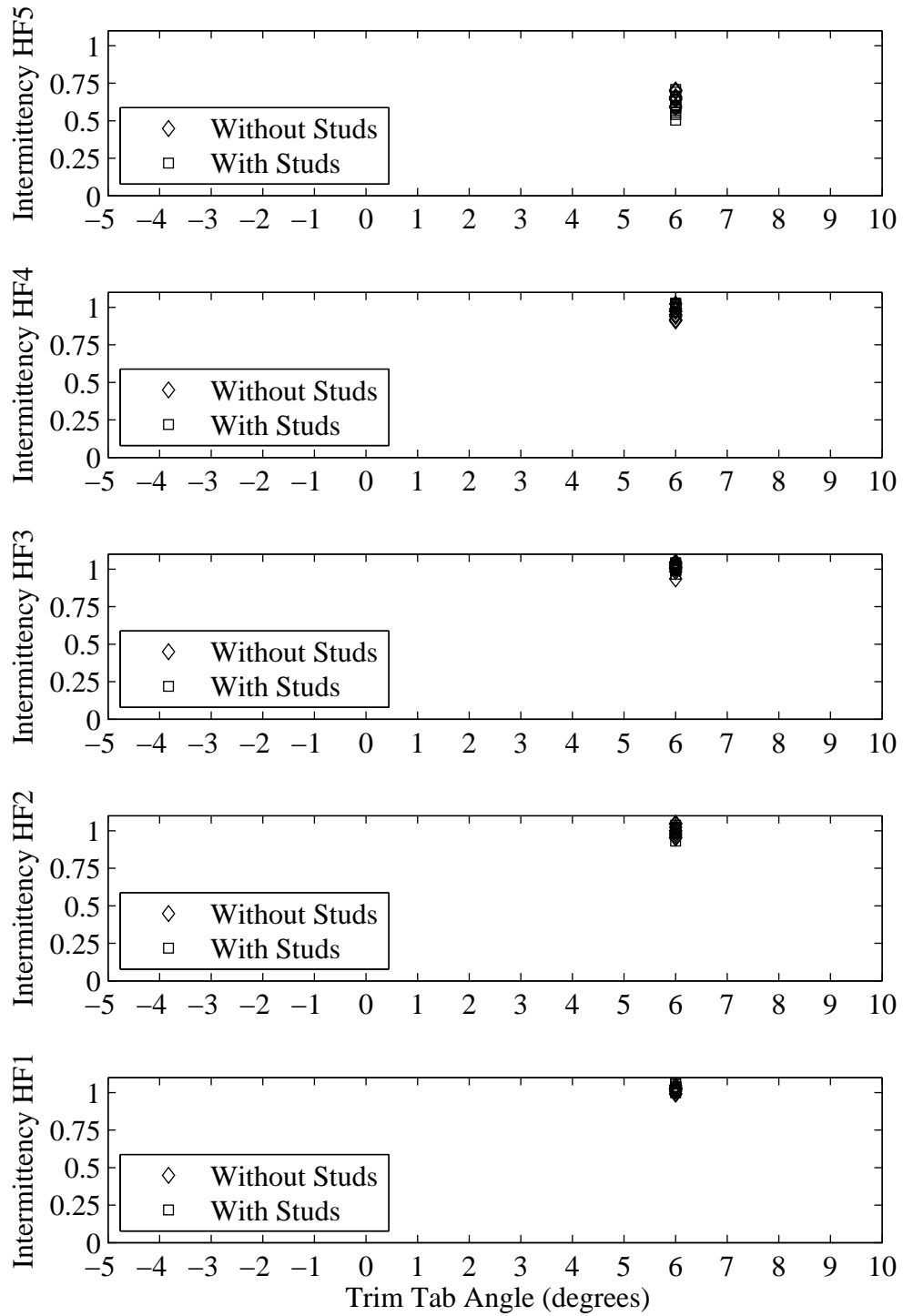


Figure H.34: Intermittency plotted with respect to variation in trim tab angle. Froude number 0.34, Yaw 1 degrees, Heel 20 degrees, Tab 6 degrees, Rudder 6 degrees.

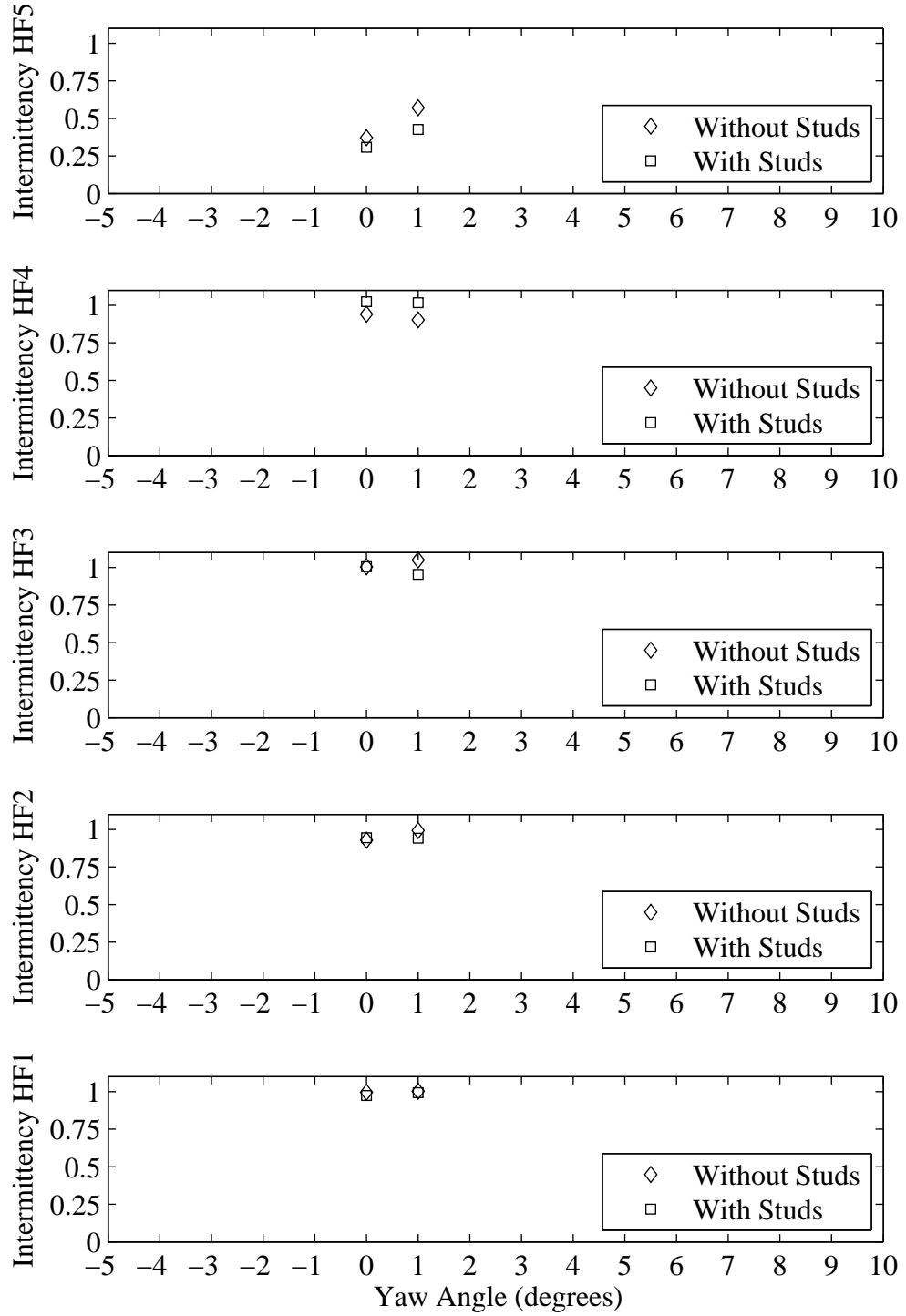


Figure H.35: Intermittency plotted with respect to variation in yaw angle. Froude number 0.27, Heel 5 degrees, Tab 4 degrees, Rudder 2 degrees.

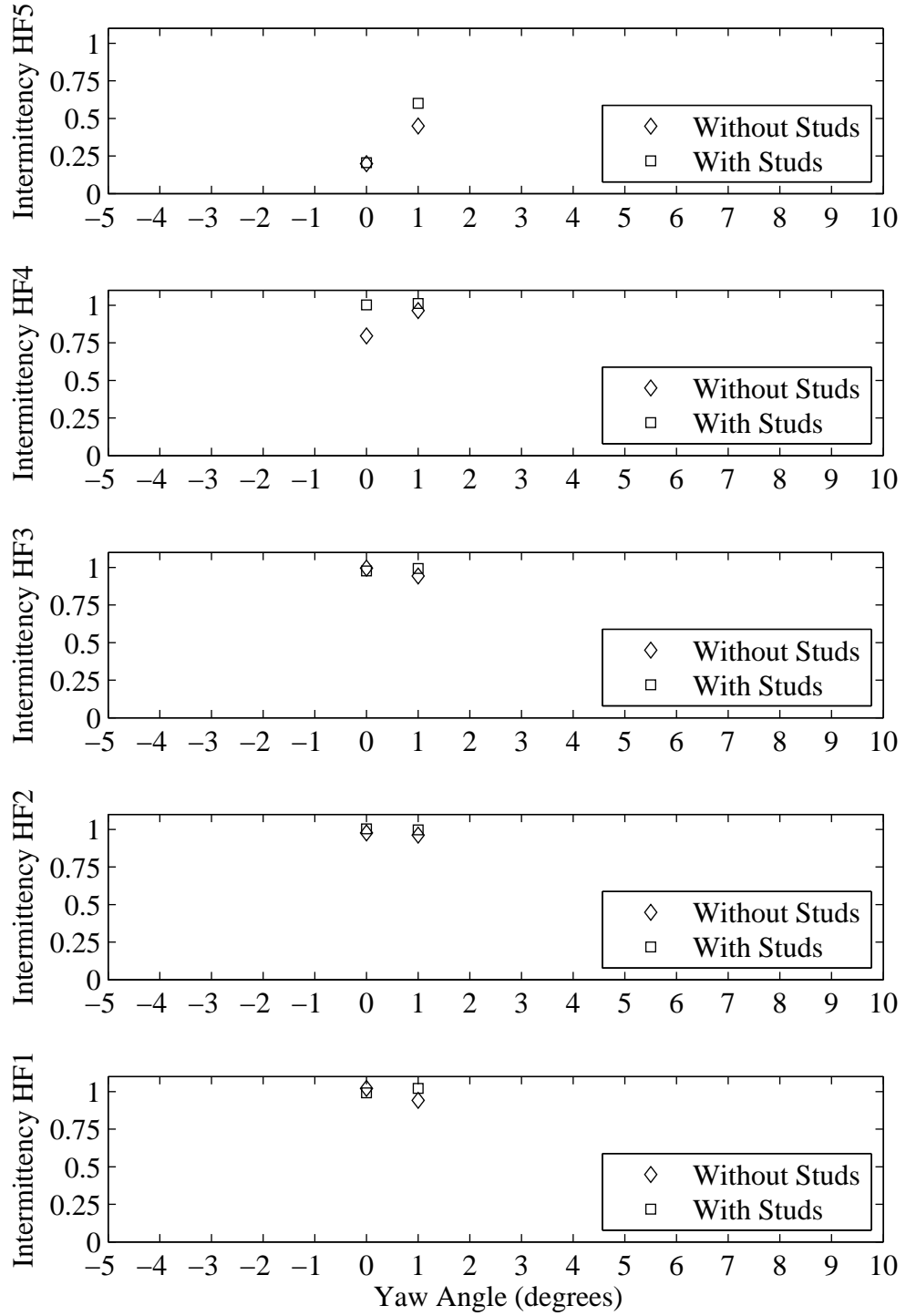


Figure H.36: Intermittency plotted with respect to variation in yaw angle. Froude number 0.27, Heel 10 degrees, Tab 4 degrees, Rudder 2 degrees.

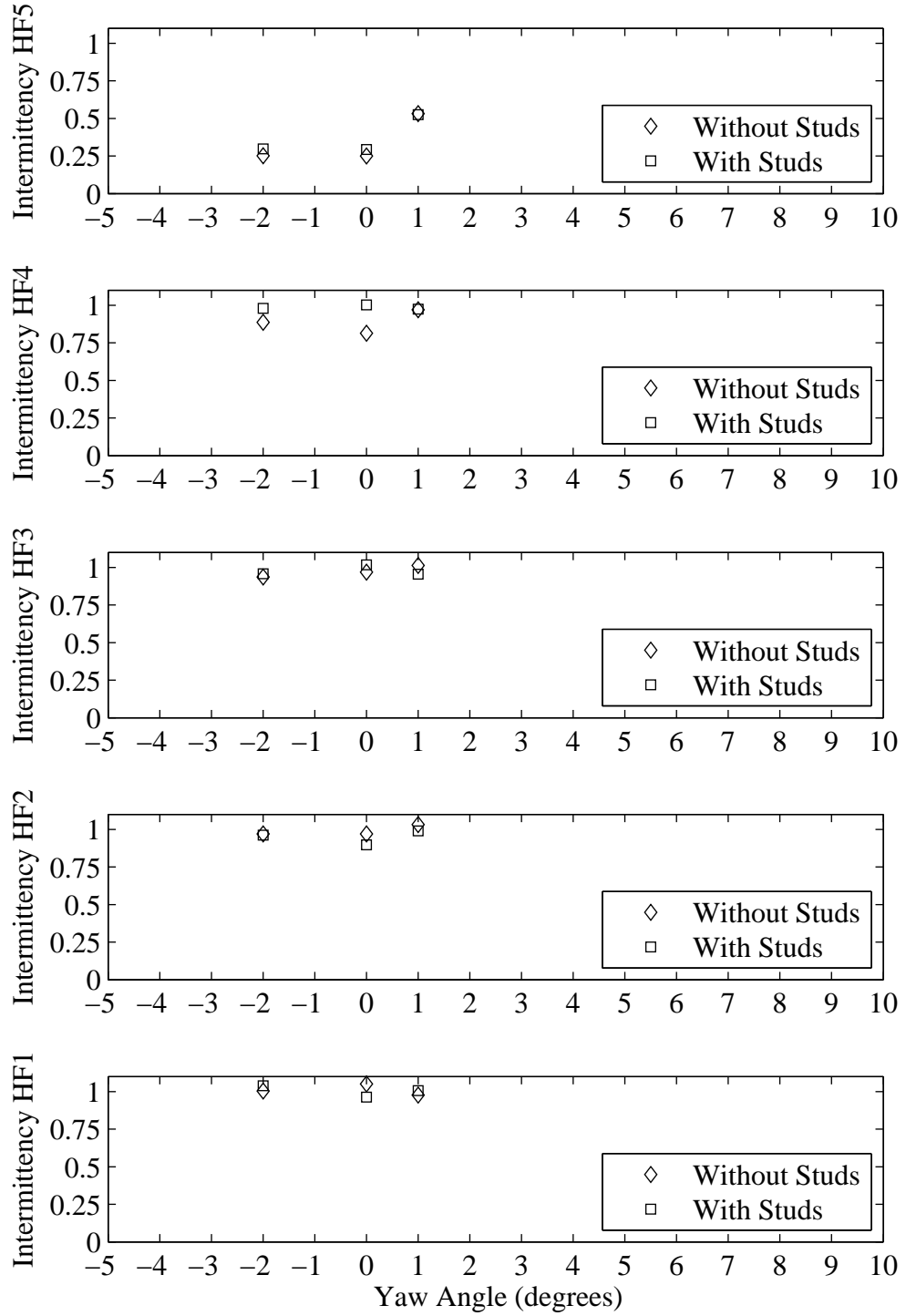


Figure H.37: Intermittency plotted with respect to variation in yaw angle. Froude number 0.27, Heel 5 degrees, Tab 6 degrees, Rudder 2 degrees.

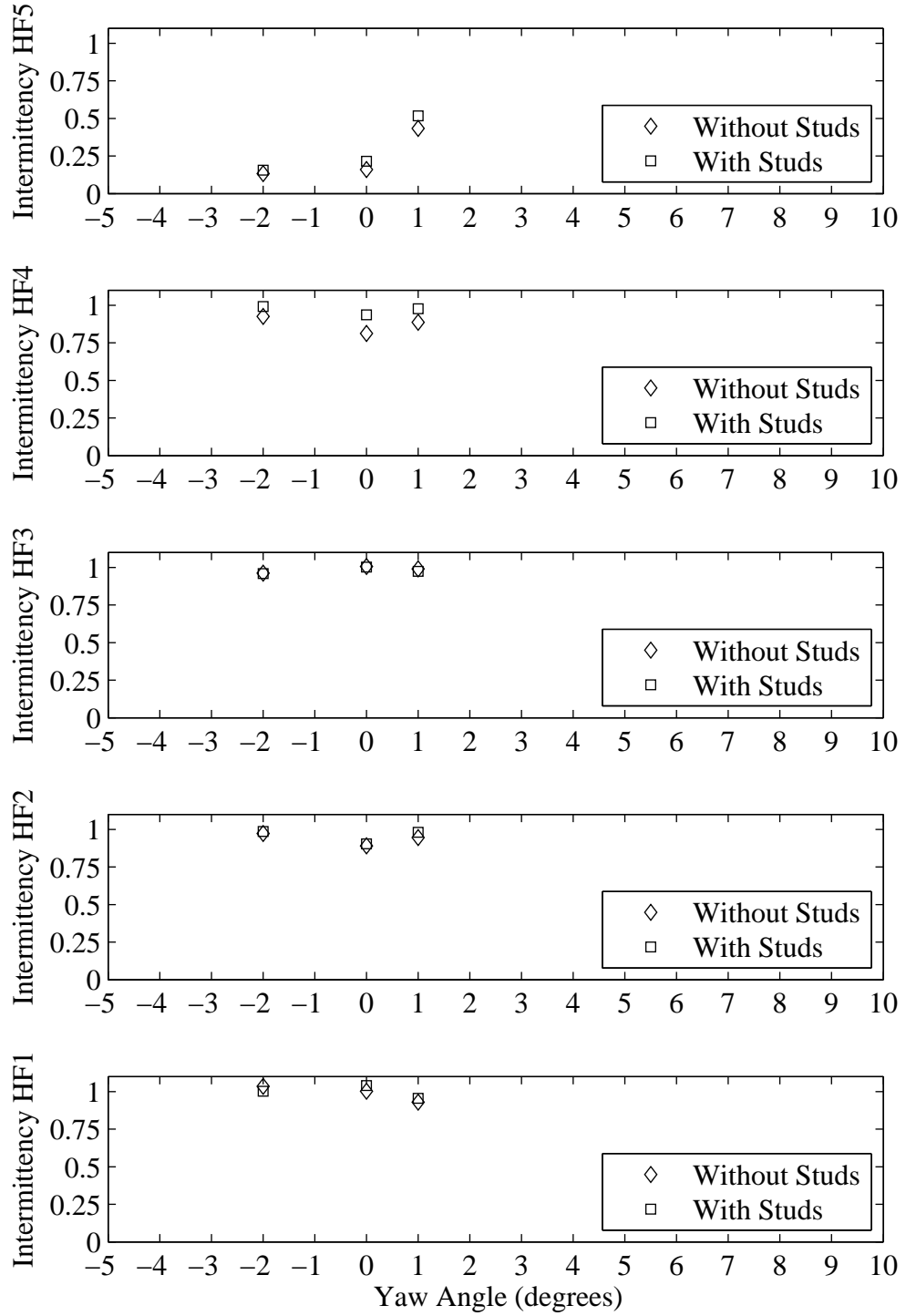


Figure H.38: Intermittency plotted with respect to variation in yaw angle. Froude number 0.27, Heel 10 degrees, Tab 6 degrees, Rudder 2 degrees.

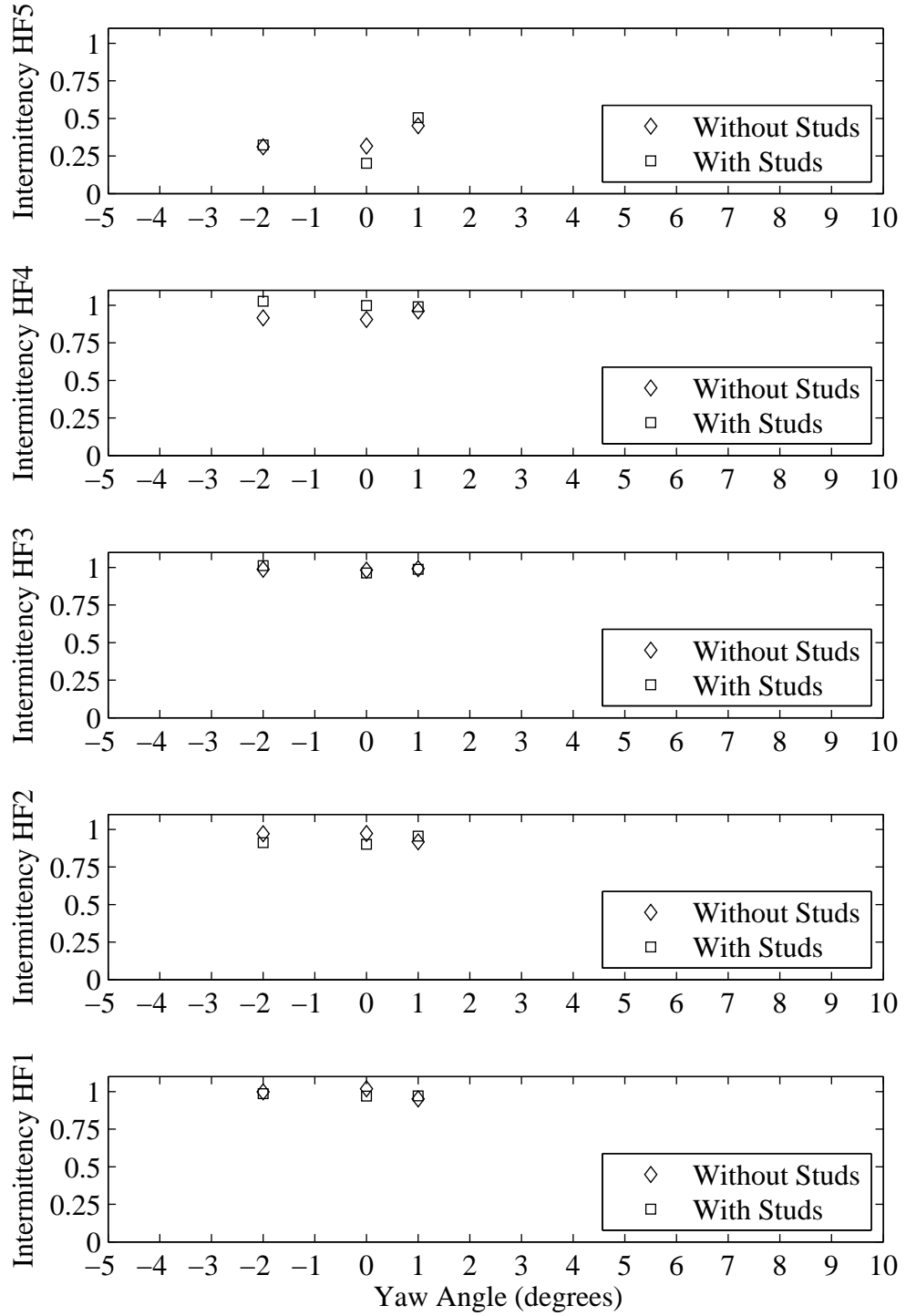


Figure H.39: Intermittency plotted with respect to variation in yaw angle. Froude number 0.27, Heel 5 degrees, Tab 8 degrees, Rudder 2 degrees.

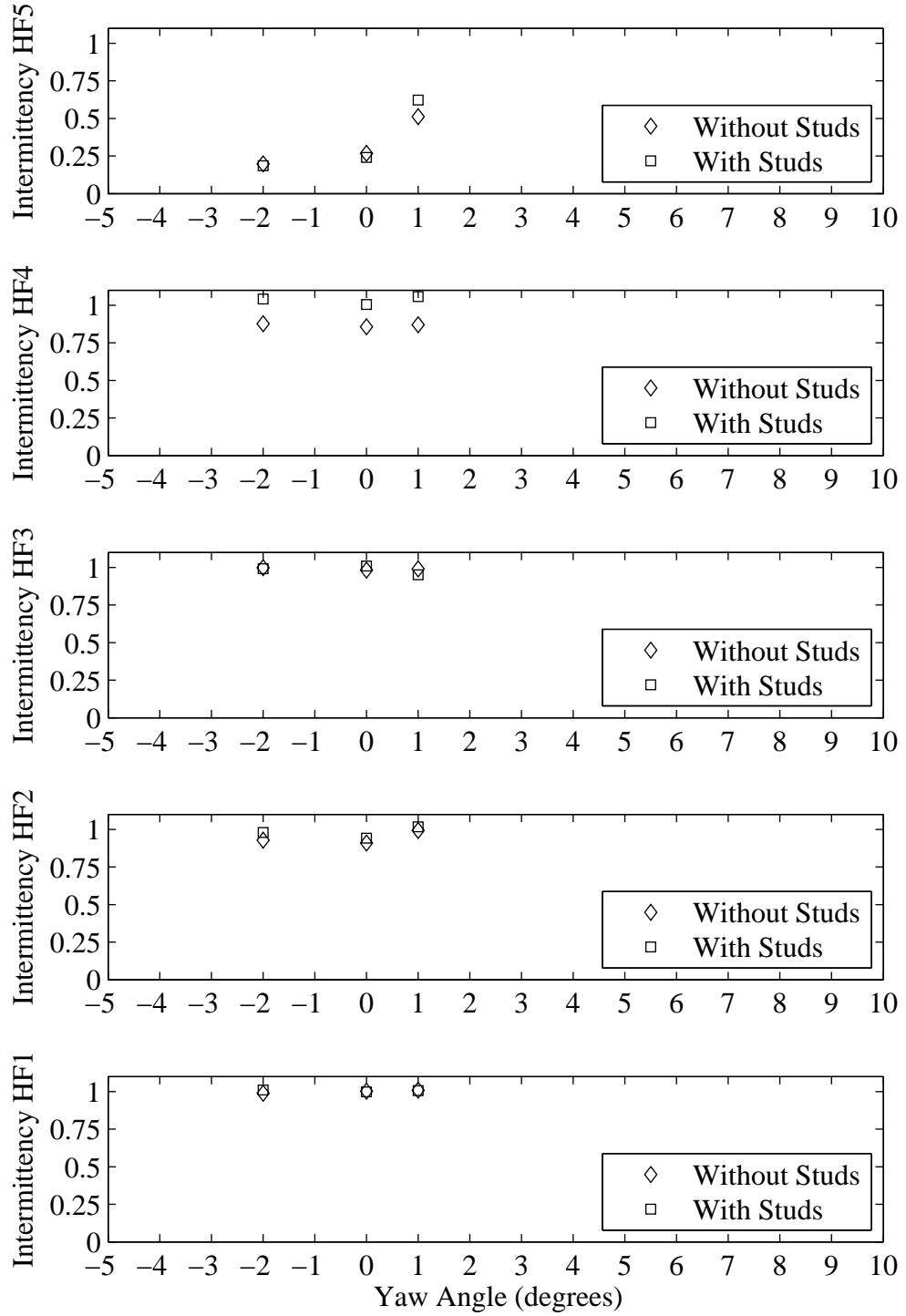


Figure H.40: Intermittency plotted with respect to variation in yaw angle. Froude number 0.27, Heel 10 degrees, Tab 8 degrees, Rudder 2 degrees.

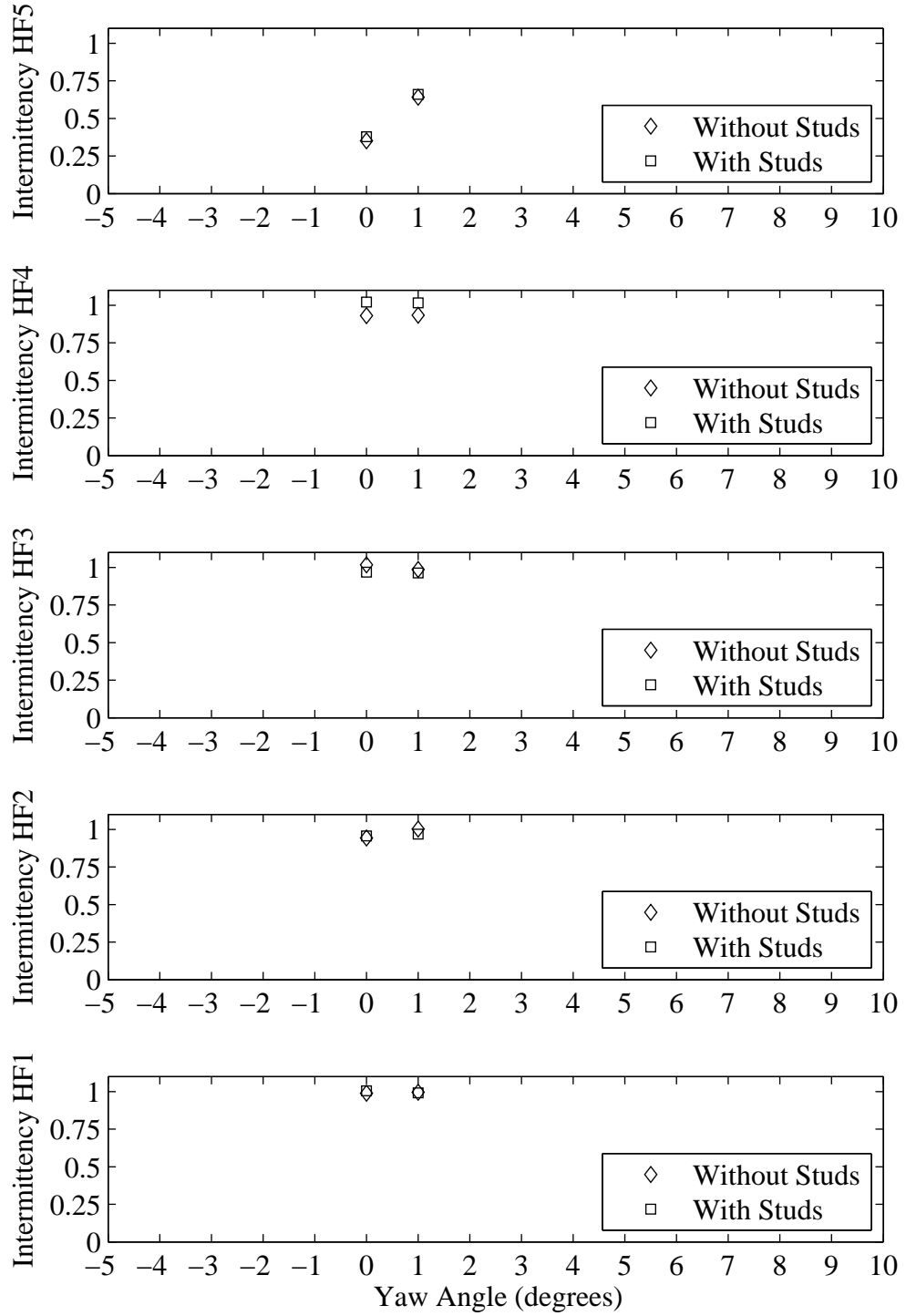


Figure H.41: Intermittency plotted with respect to variation in yaw angle. Froude number 0.29, Heel 5 degrees, Tab 4 degrees, Rudder 2 degrees.

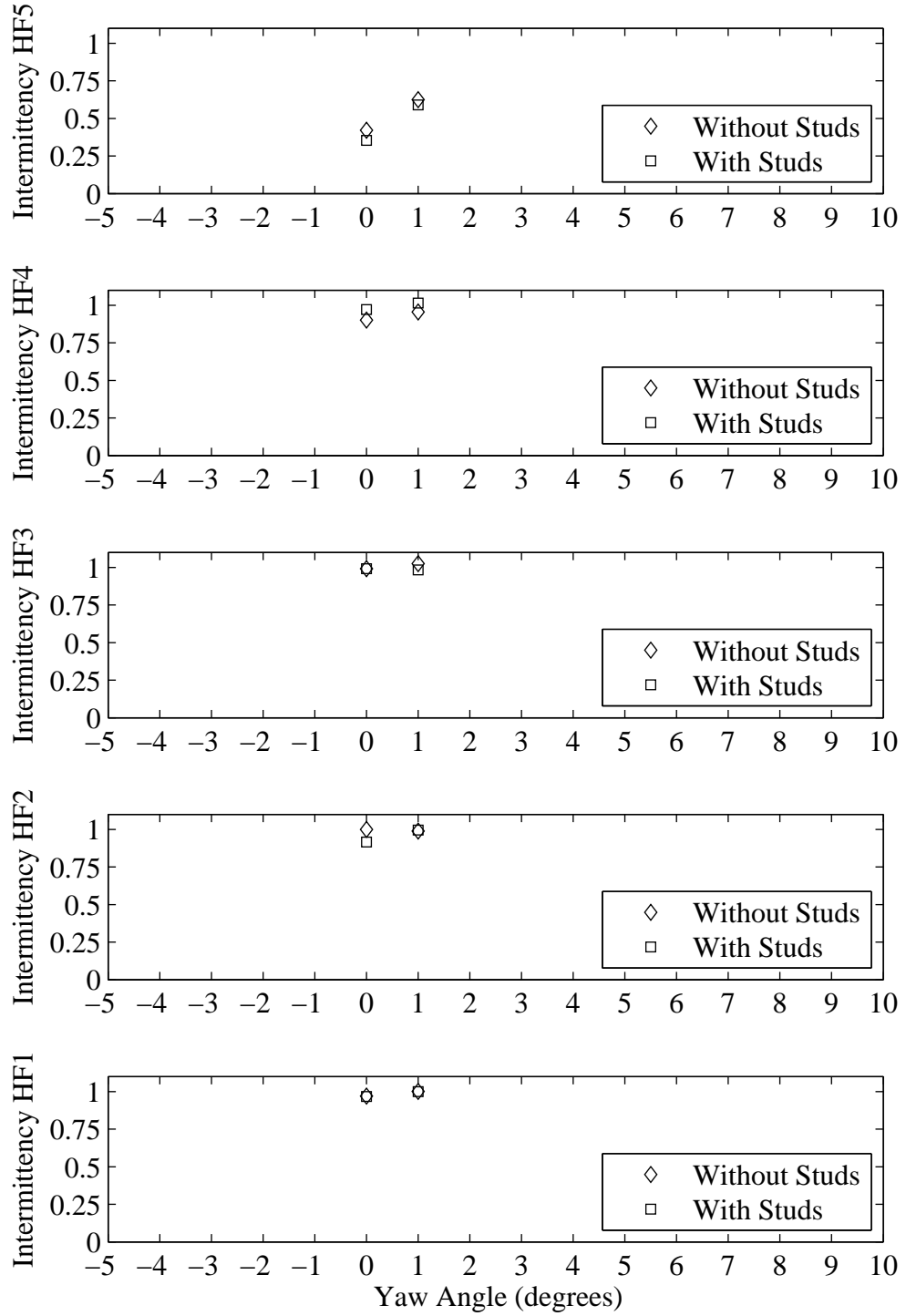


Figure H.42: Intermittency plotted with respect to variation in yaw angle. Froude number 0.29, Heel 10 degrees, Tab 4 degrees, Rudder 2 degrees.

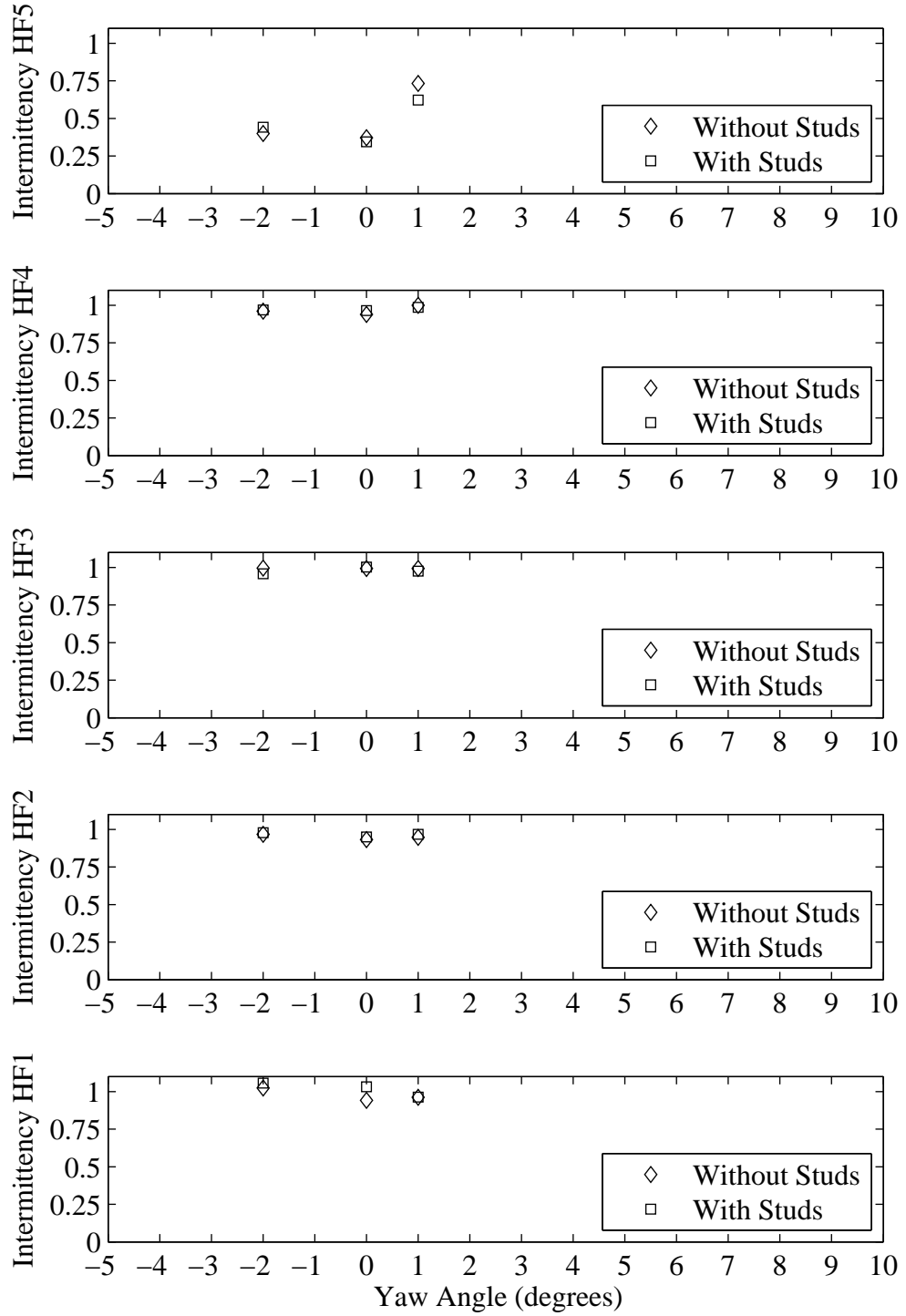


Figure H.43: Intermittency plotted with respect to variation in yaw angle. Froude number 0.29, Heel 5 degrees, Tab 6 degrees, Rudder 2 degrees.

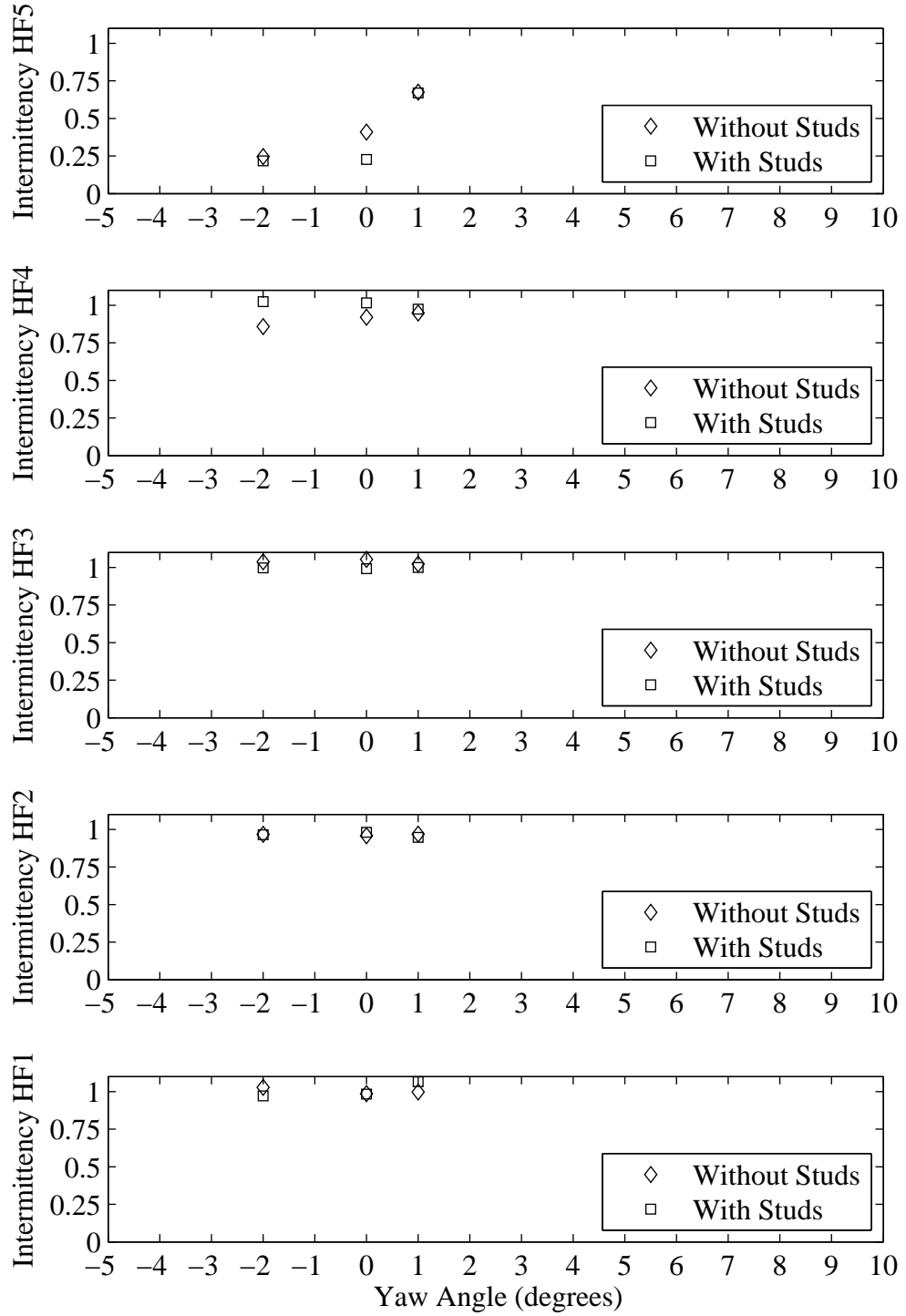


Figure H.44: Intermittency plotted with respect to variation in yaw angle. Froude number 0.29, Heel 10 degrees, Tab 6 degrees, Rudder 2 degrees.

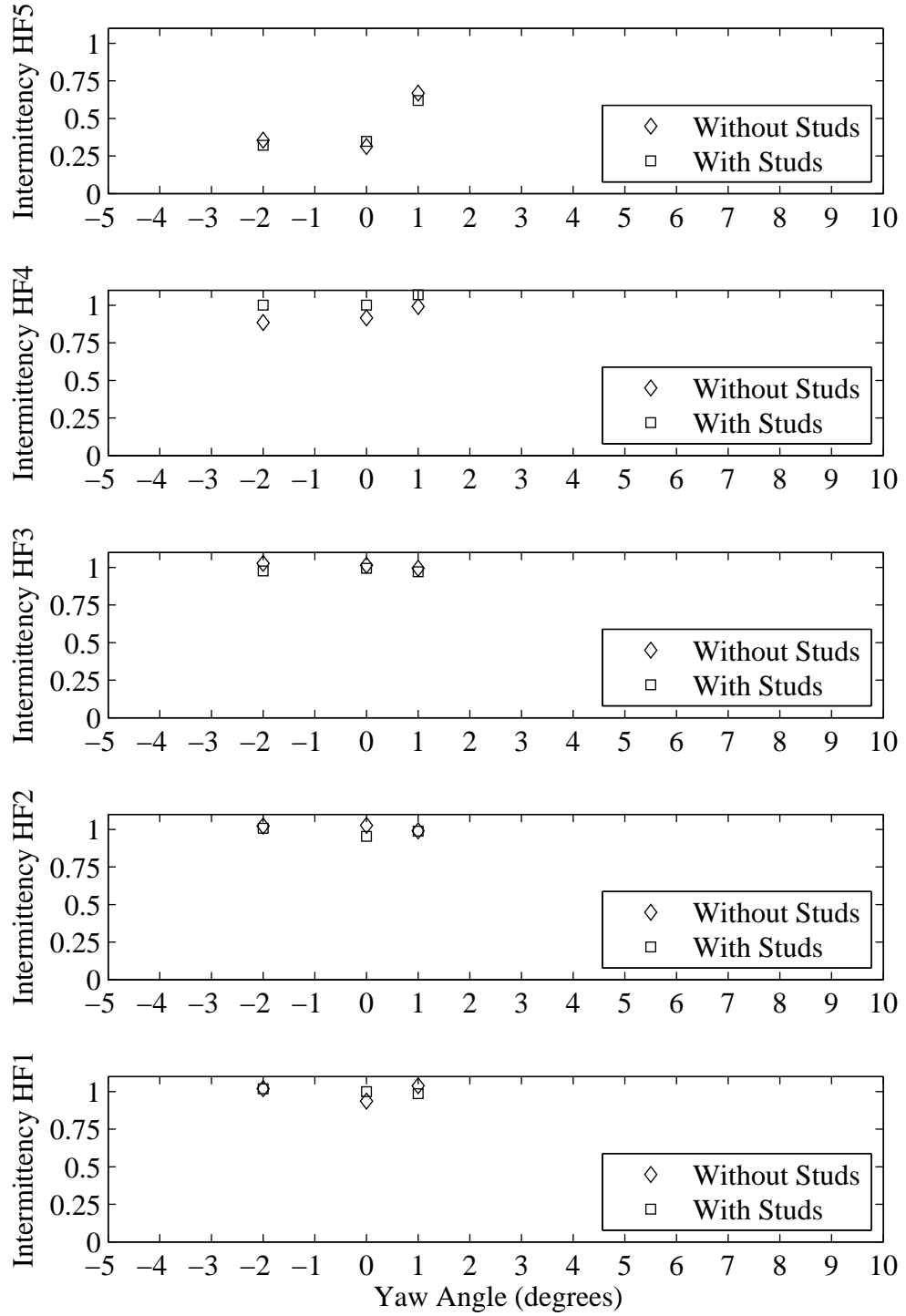


Figure H.45: Intermittency plotted with respect to variation in yaw angle. Froude number 0.29, Heel 5 degrees, Tab 8 degrees, Rudder 2 degrees.

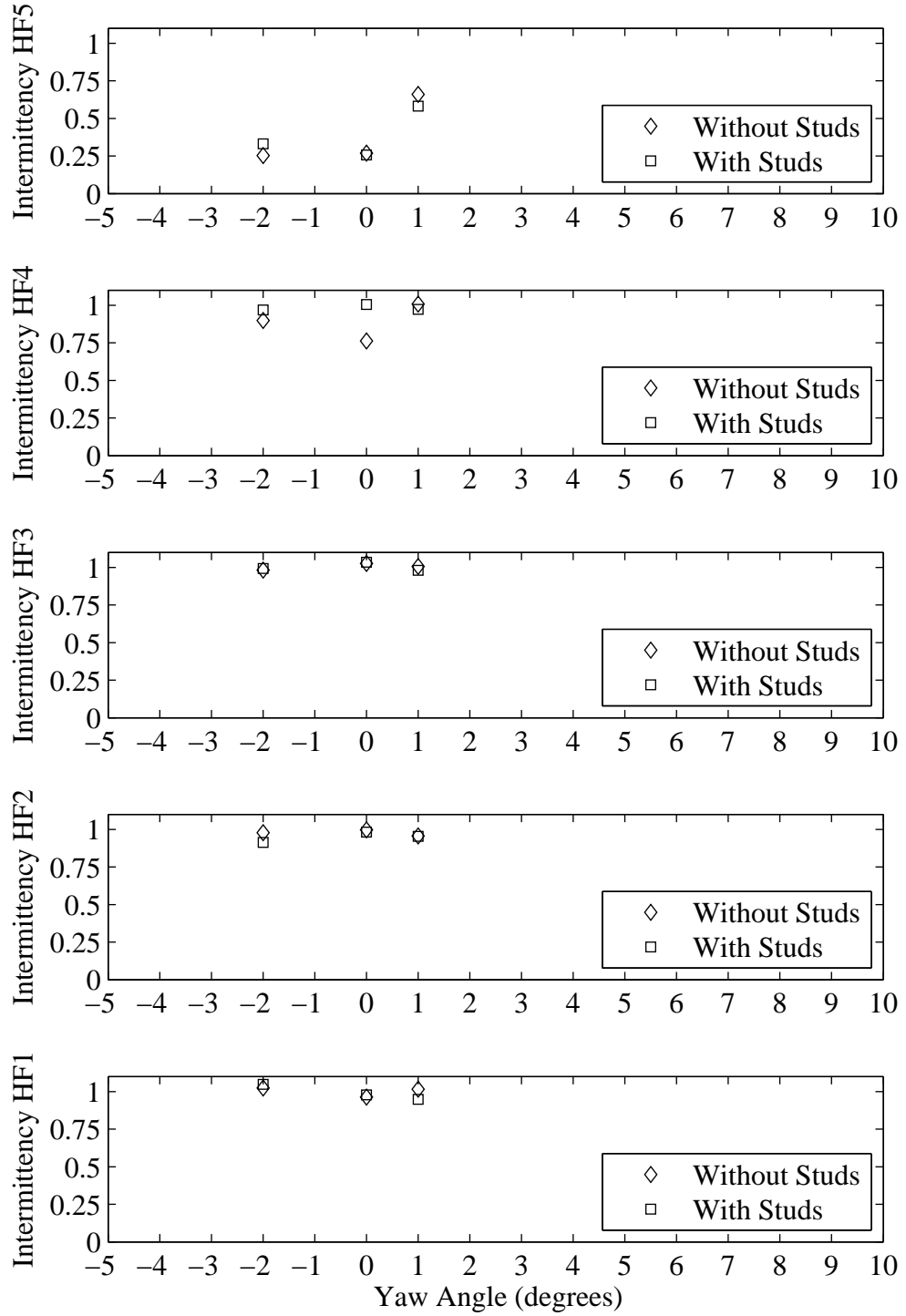


Figure H.46: Intermittency plotted with respect to variation in yaw angle. Froude number 0.29, Heel 10 degrees, Tab 8 degrees, Rudder 2 degrees.

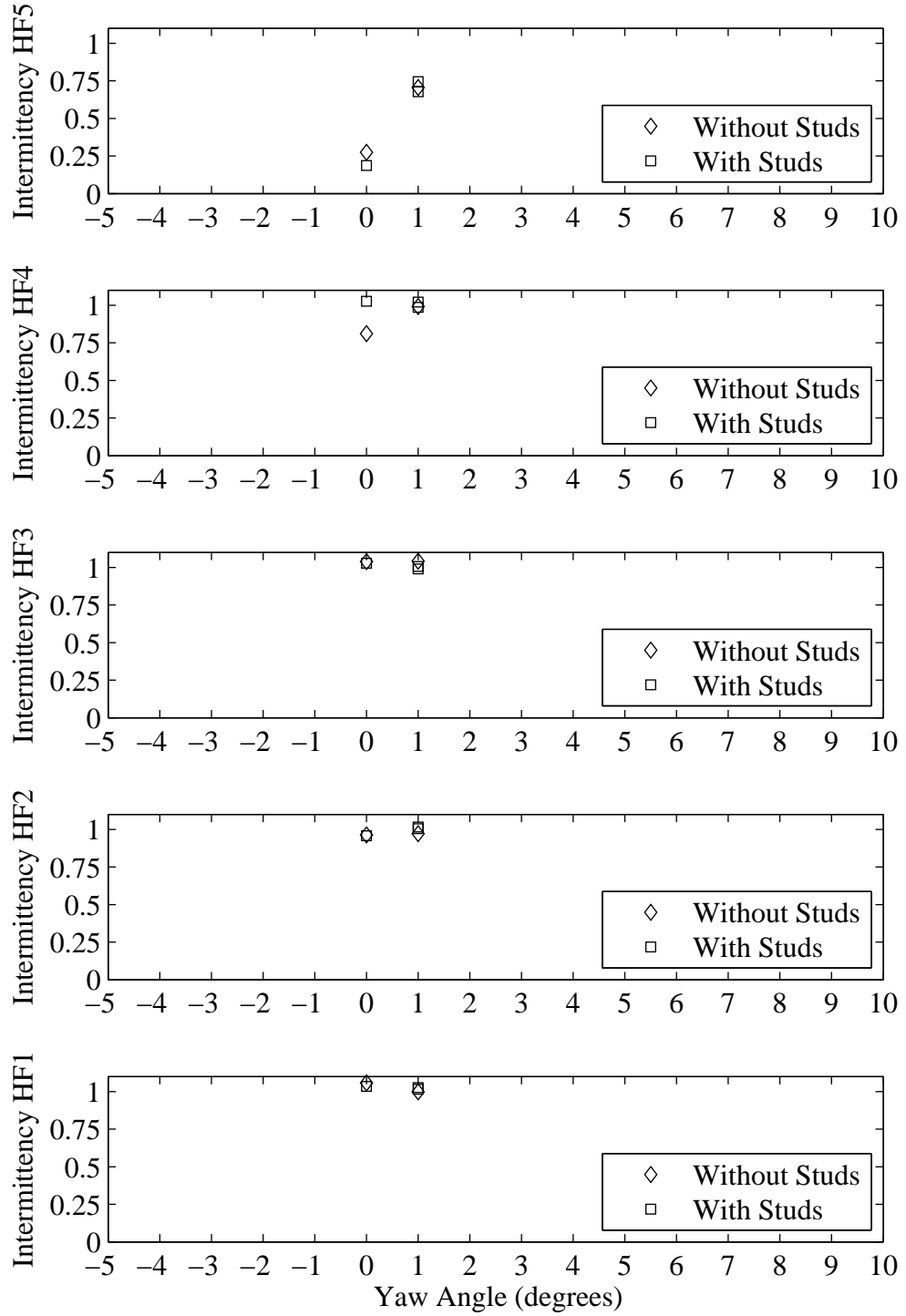


Figure H.47: Intermittency plotted with respect to variation in yaw angle. Froude number 0.34, Heel 20 degrees, Tab 6 degrees, Rudder 1 degrees.

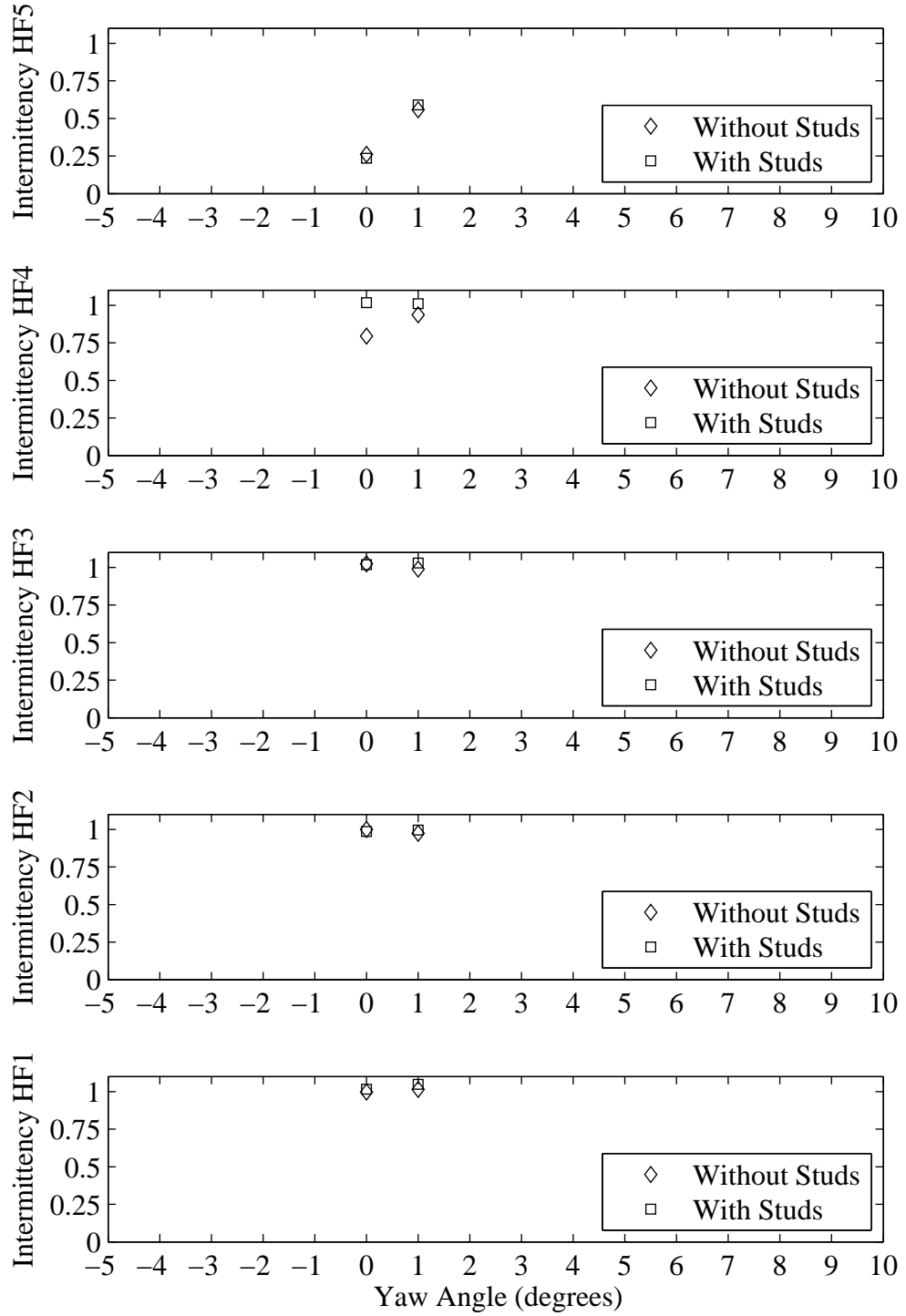


Figure H.48: Intermittency plotted with respect to variation in yaw angle. Froude number 0.34, Heel 20 degrees, Tab 6 degrees, Rudder 3 degrees.

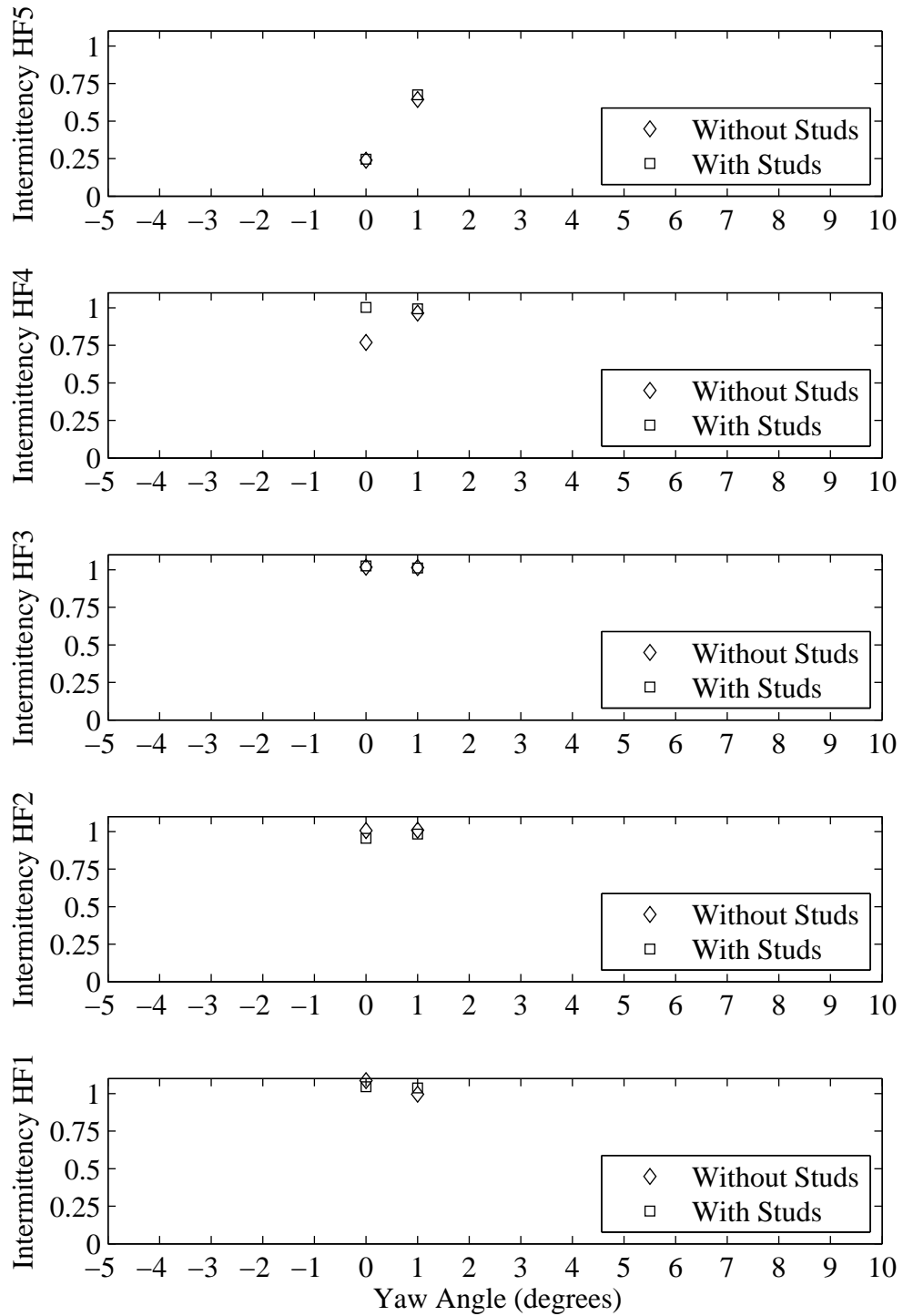


Figure H.49: Intermittency plotted with respect to variation in yaw angle. Froude number 0.34, Heel 20 degrees, Tab 6 degrees, Rudder 5 degrees.

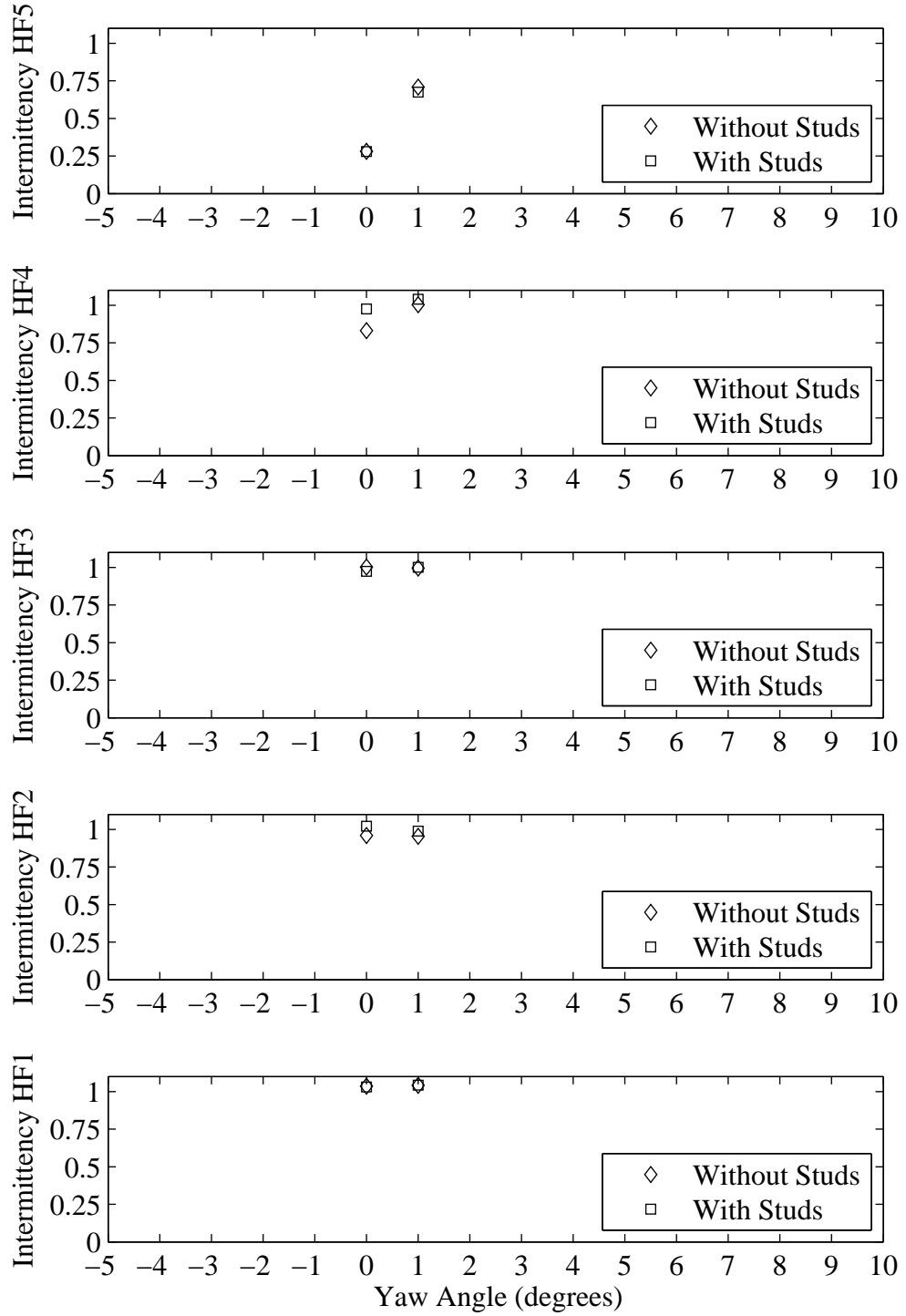


Figure H.50: Intermittency plotted with respect to variation in yaw angle. Froude number 0.34, Heel 20 degrees, Tab 8 degrees, Rudder 1 degrees.

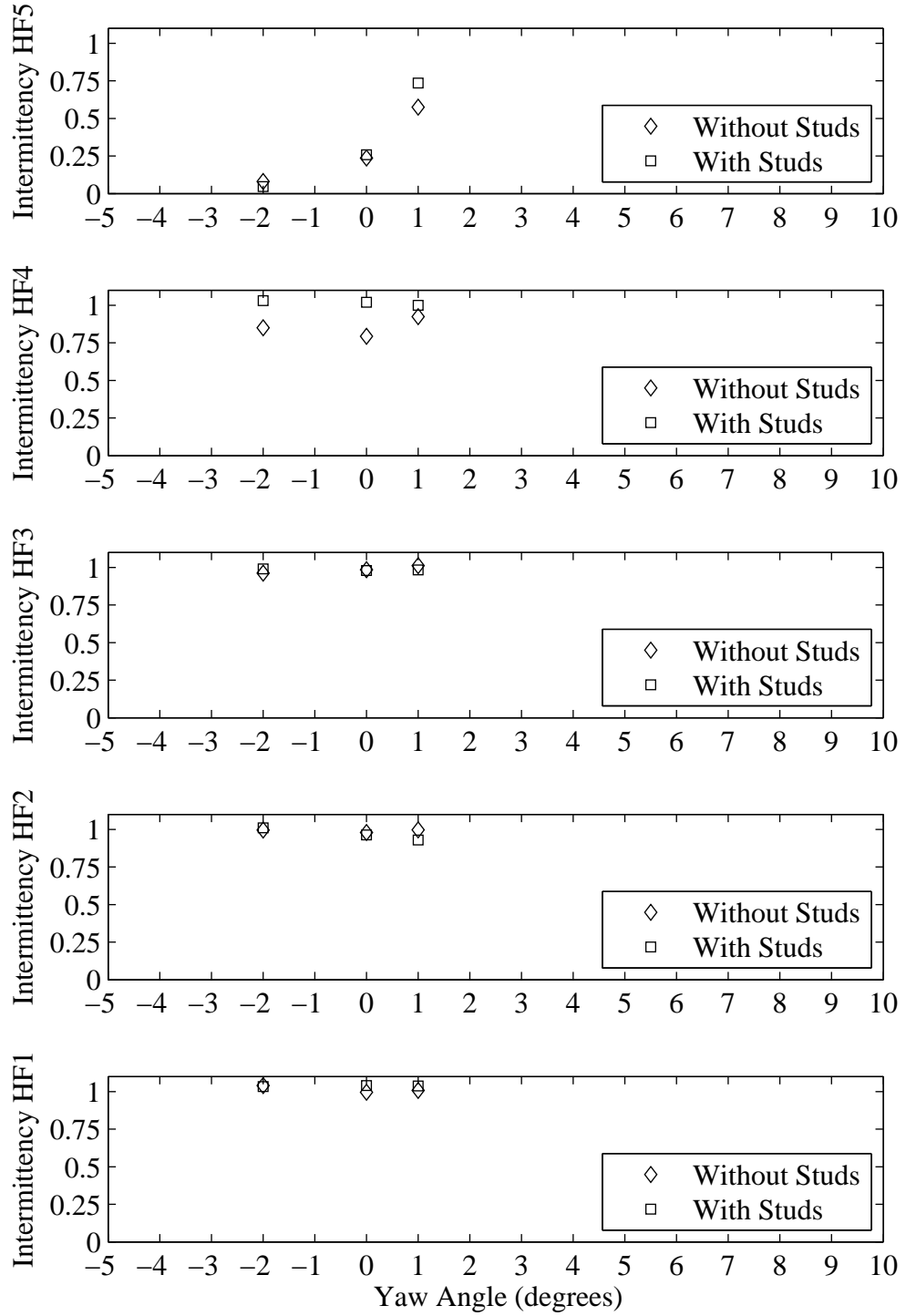


Figure H.51: Intermittency plotted with respect to variation in yaw angle. Froude number 0.34, Heel 20 degrees, Tab 8 degrees, Rudder 3 degrees.

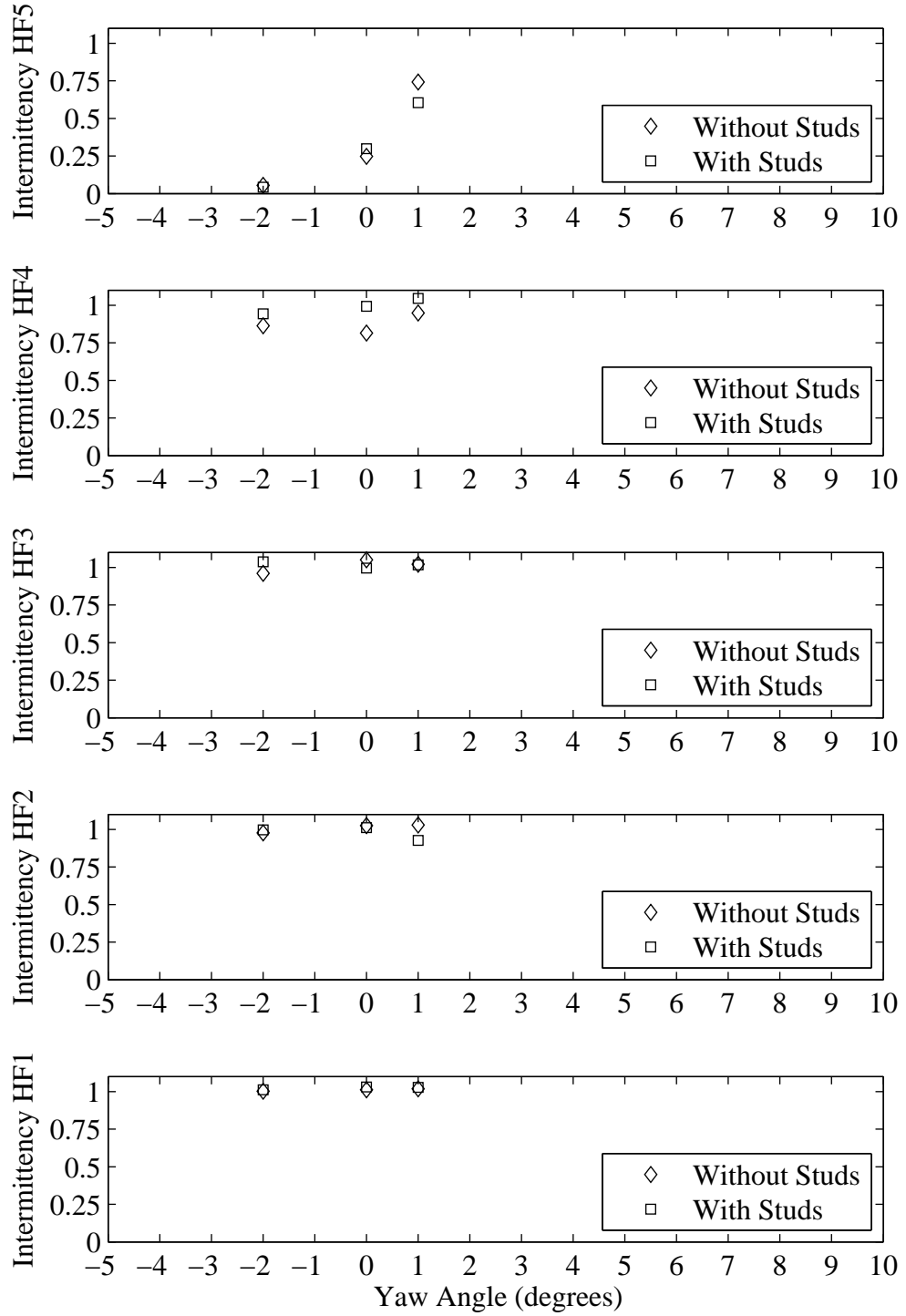


Figure H.52: Intermittency plotted with respect to variation in yaw angle. Froude number 0.34, Heel 20 degrees, Tab 8 degrees, Rudder 5 degrees.

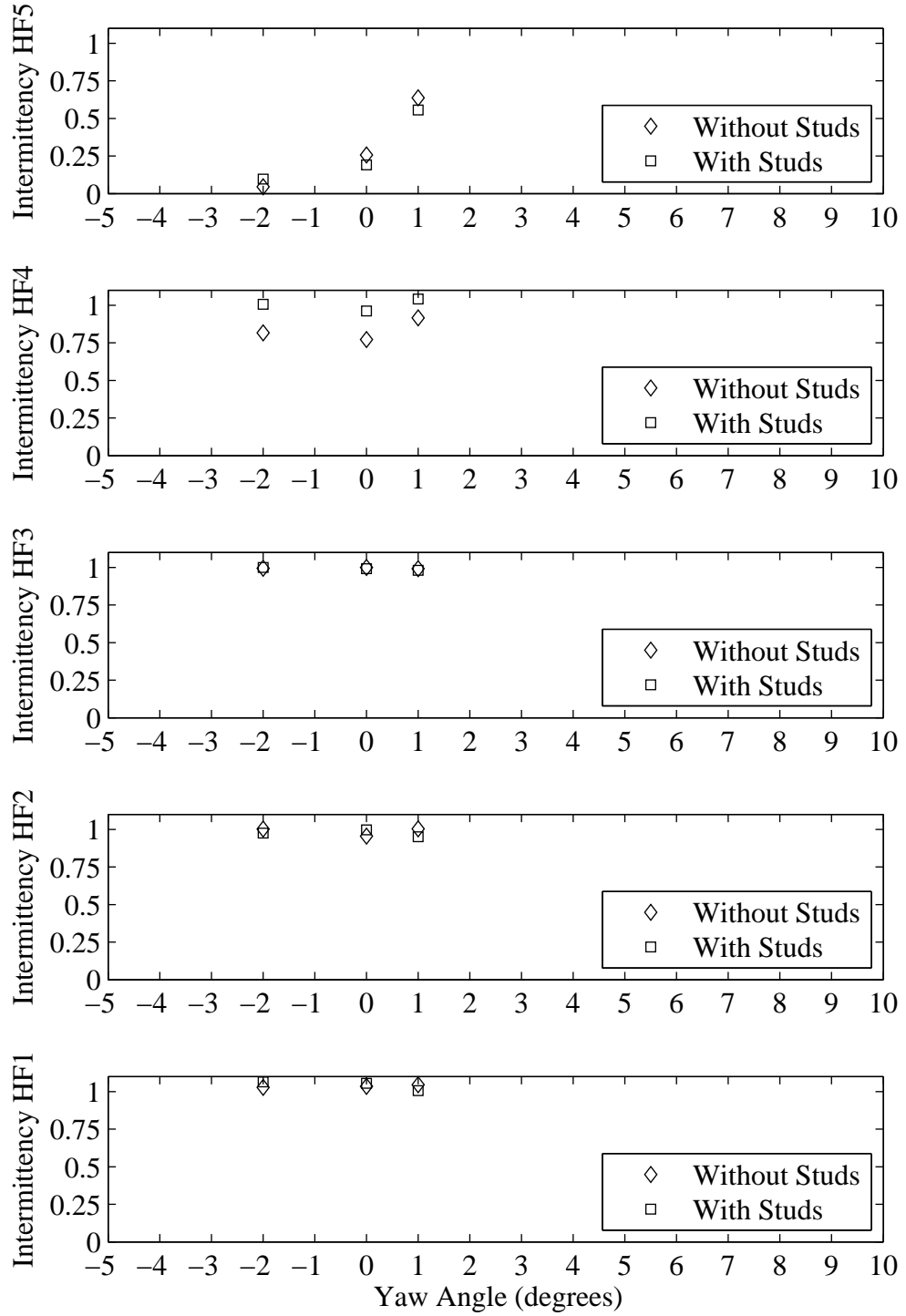


Figure H.53: Intermittency plotted with respect to variation in yaw angle. Froude number 0.34, Heel 20 degrees, Tab 8 degrees, Rudder 6 degrees.

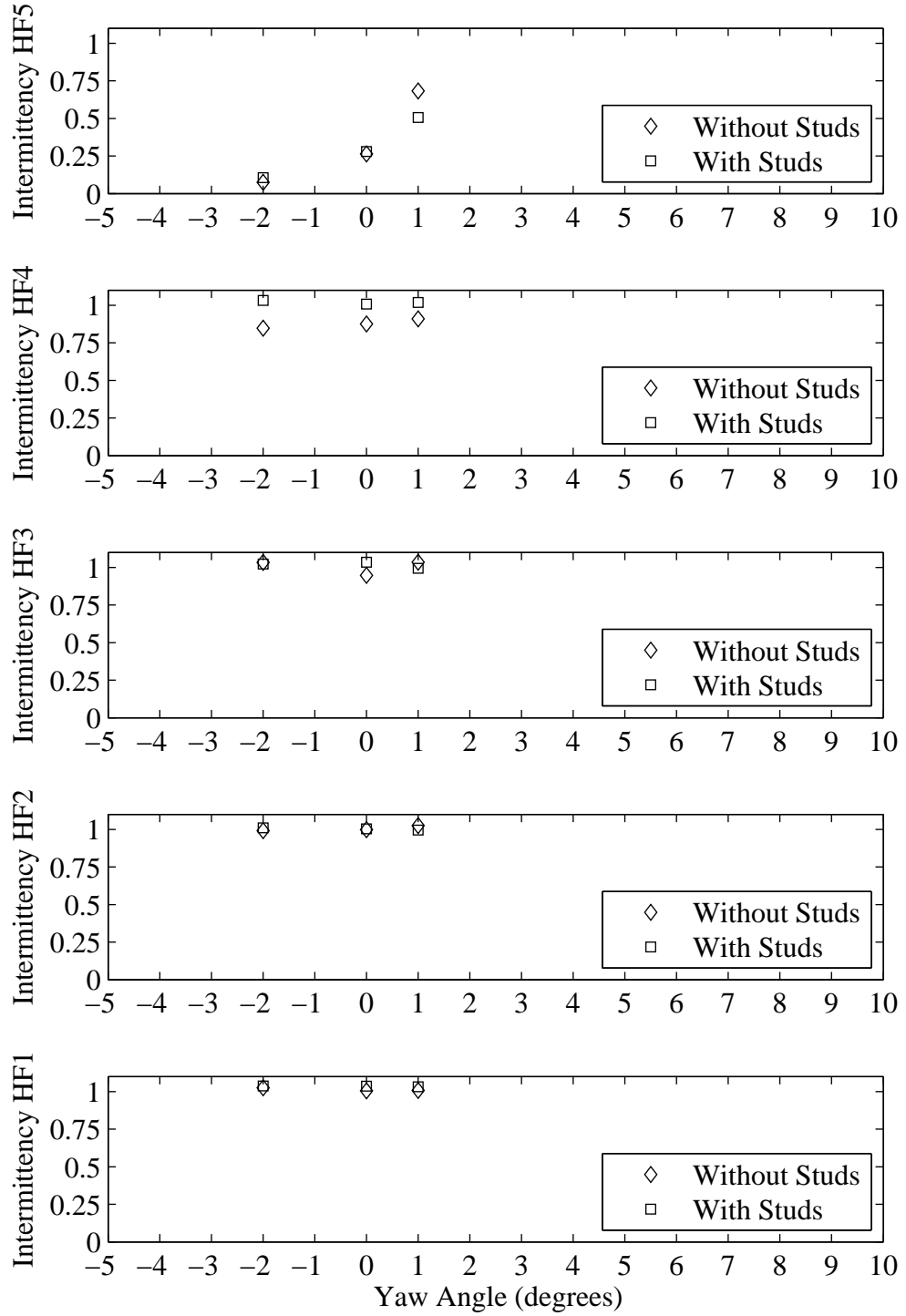


Figure H.54: Intermittency plotted with respect to variation in yaw angle. Froude number 0.34, Heel 20 degrees, Tab 10 degrees, Rudder 1 degrees.

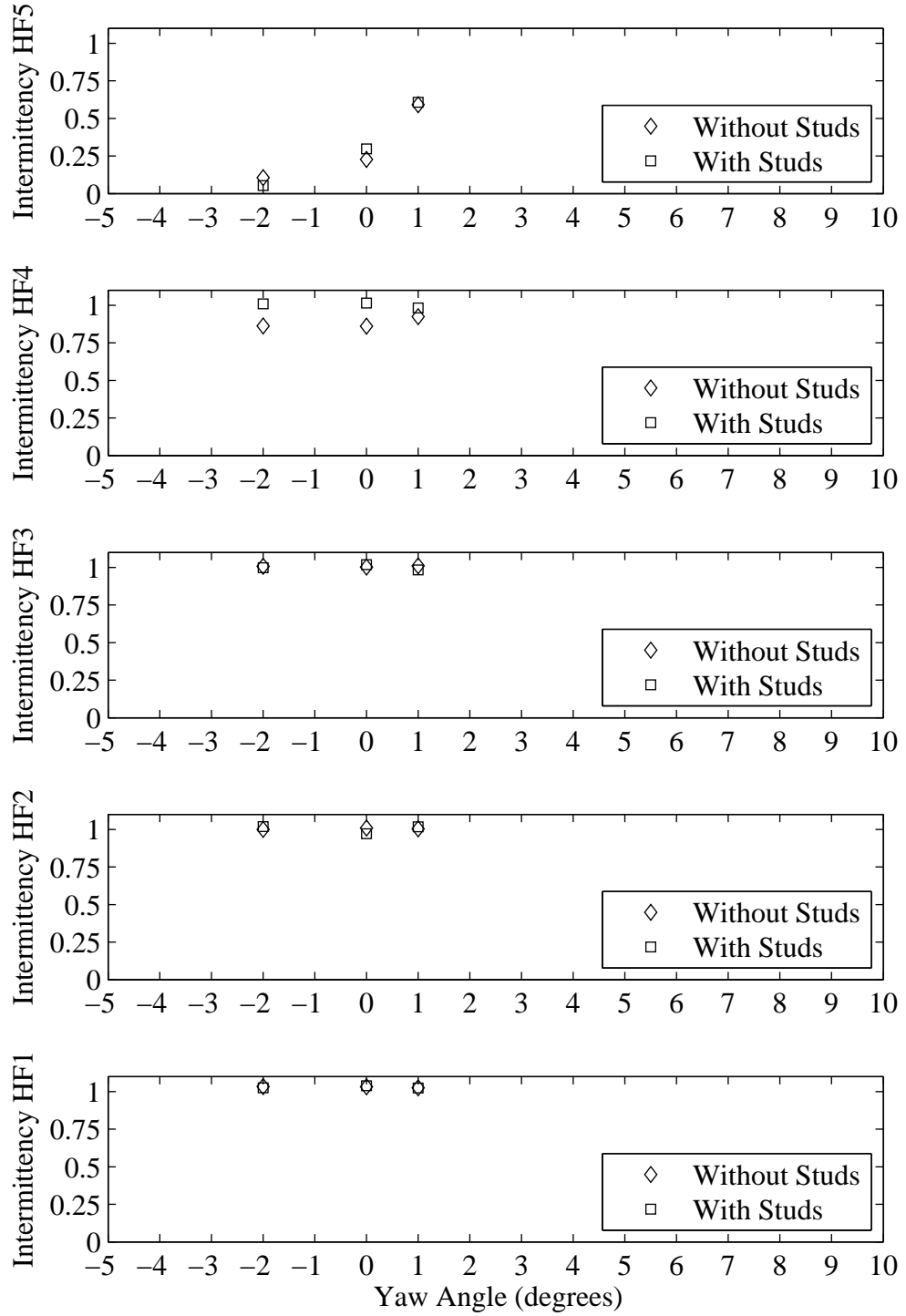


Figure H.55: Intermittency plotted with respect to variation in yaw angle. Froude number 0.34, Heel 20 degrees, Tab 10 degrees, Rudder 3 degrees.

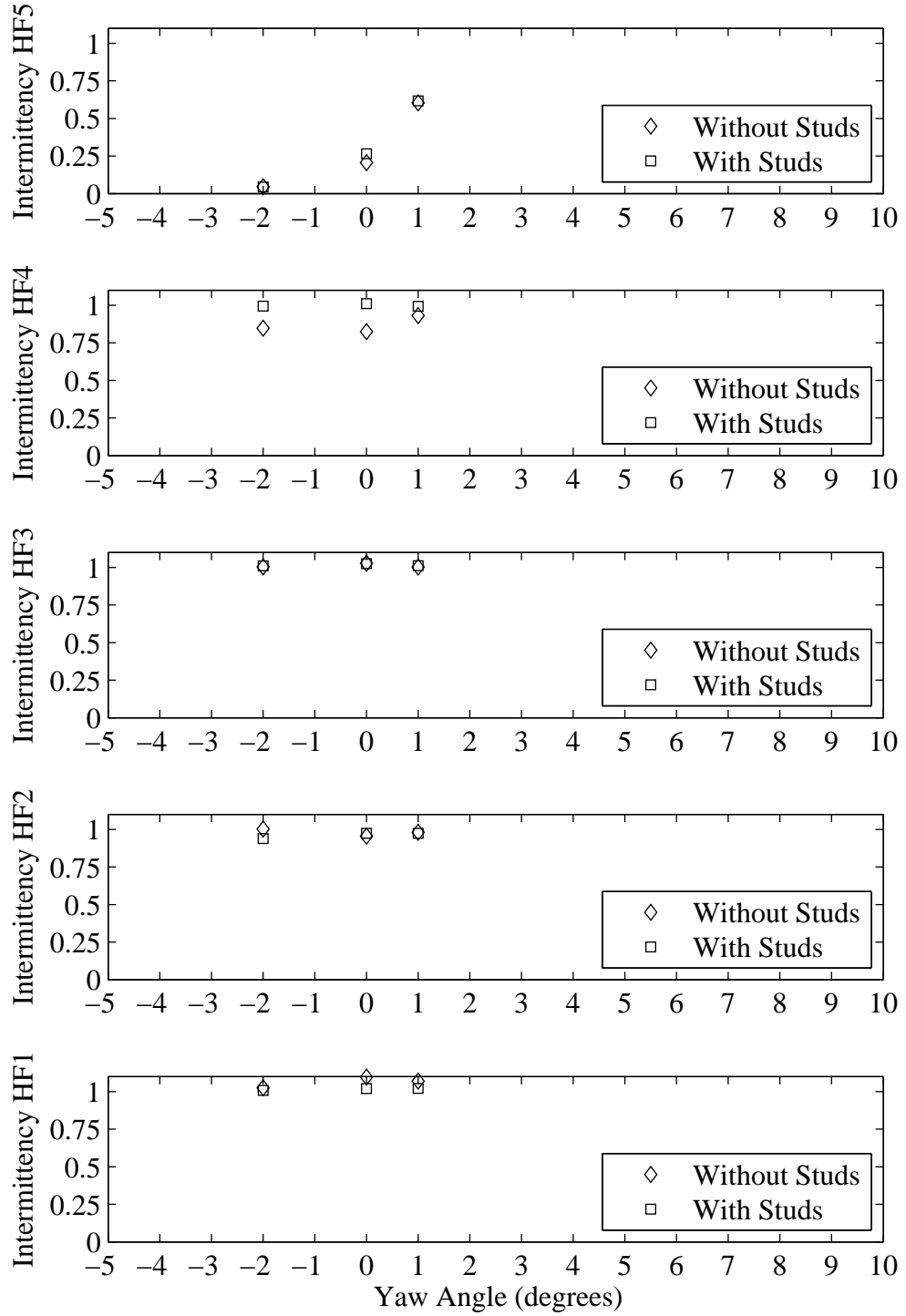


Figure H.56: Intermittency plotted with respect to variation in yaw angle. Froude number 0.34, Heel 20 degrees, Tab 10 degrees, Rudder 5 degrees.

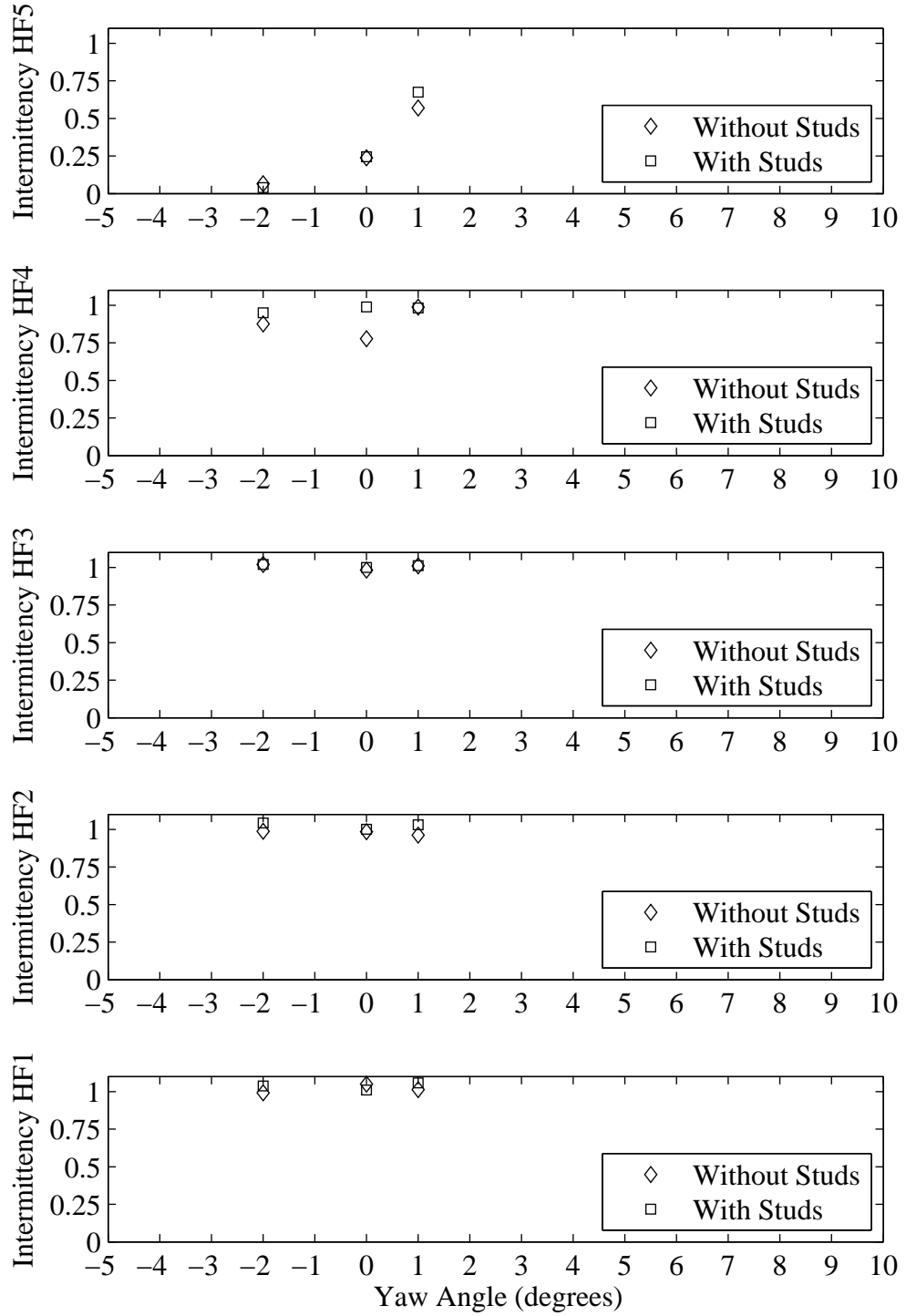


Figure H.57: Intermittency plotted with respect to variation in yaw angle. Froude number 0.34, Heel 20 degrees, Tab 10 degrees, Rudder 6 degrees.

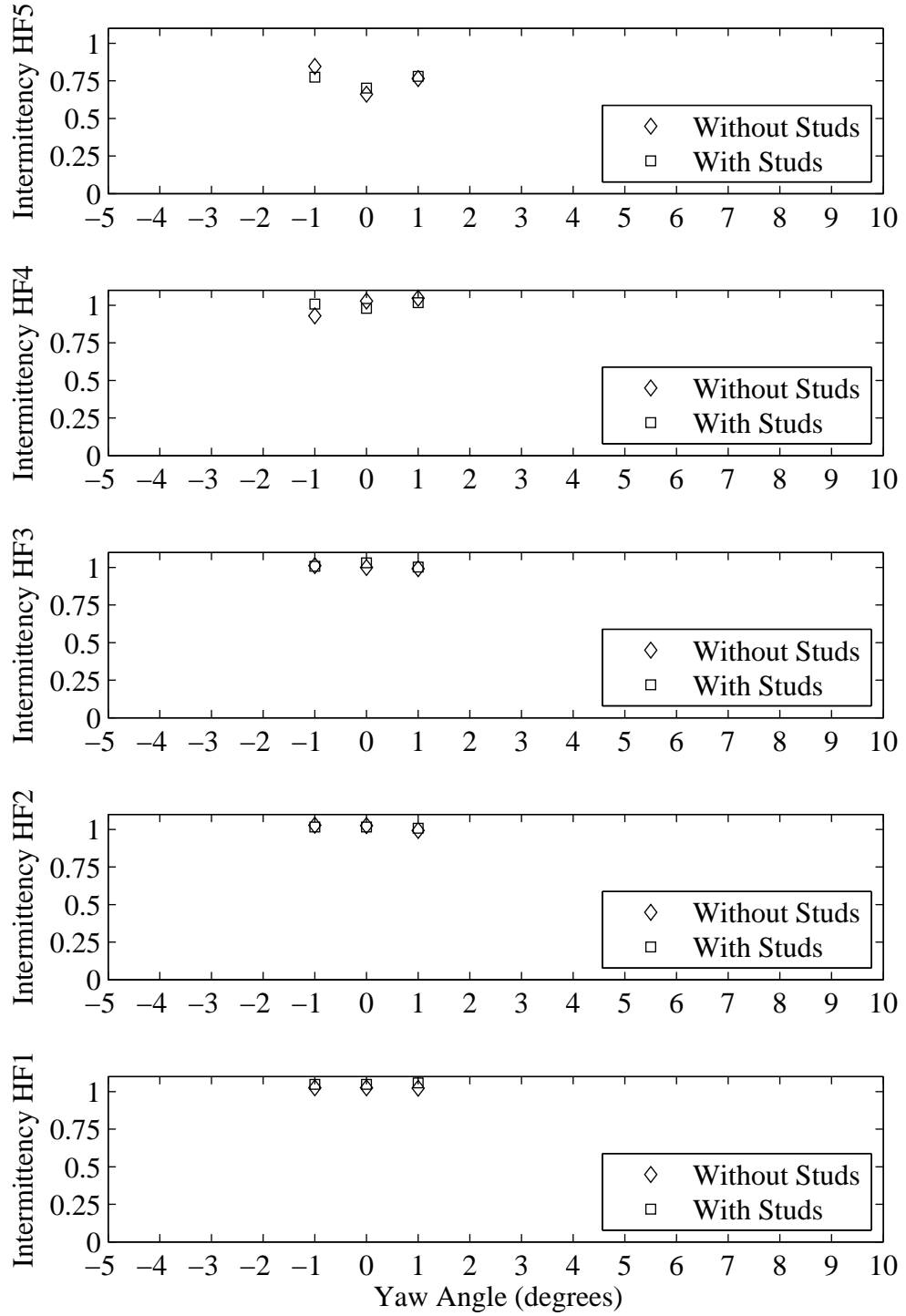


Figure H.58: Intermittency plotted with respect to variation in yaw angle. Froude number 0.40, Heel 0 degrees, Tab -2 degrees, Rudder 0 degrees.

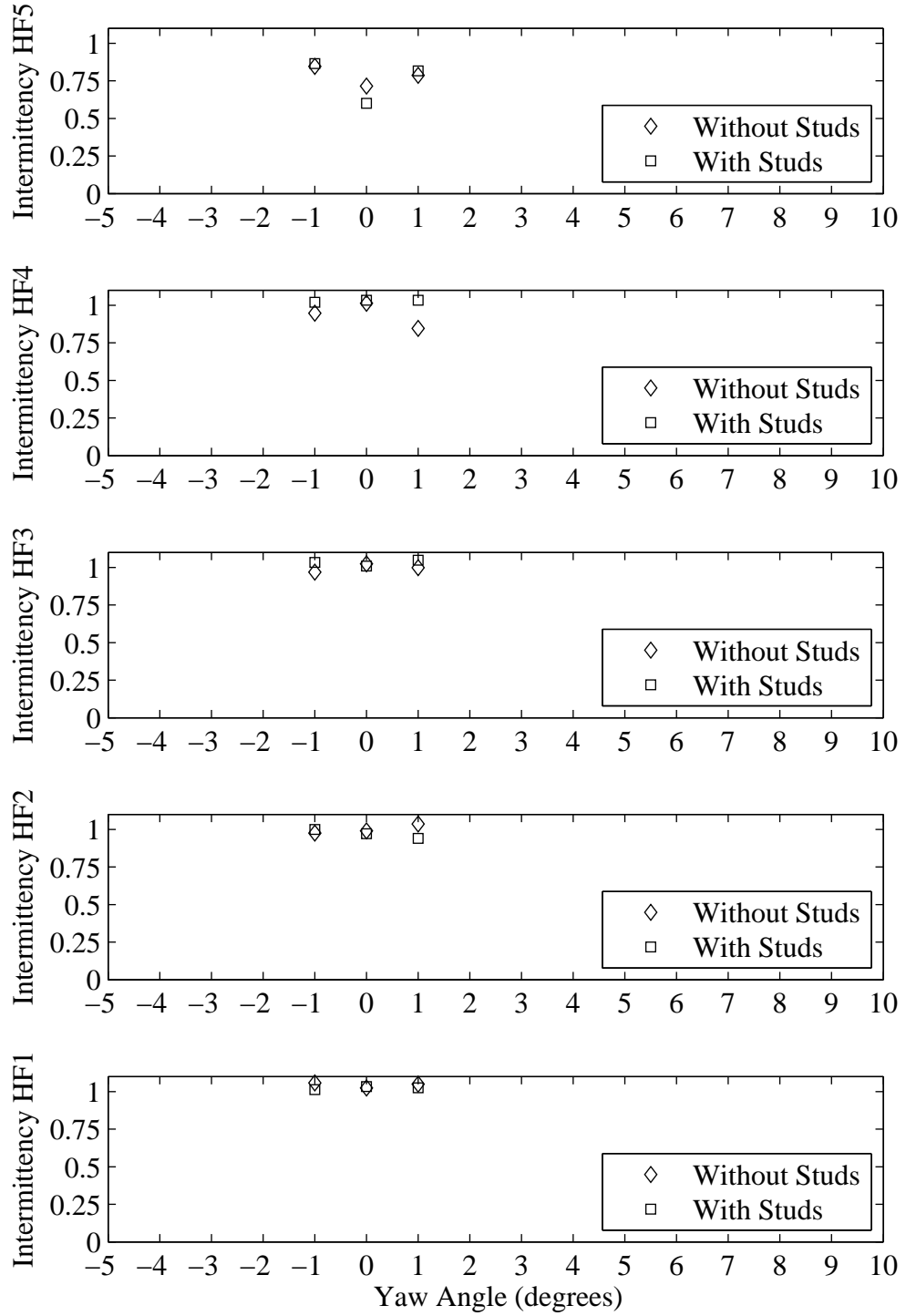


Figure H.59: Intermittency plotted with respect to variation in yaw angle. Froude number 0.40, Heel 0 degrees, Tab 0 degrees, Rudder 0 degrees.

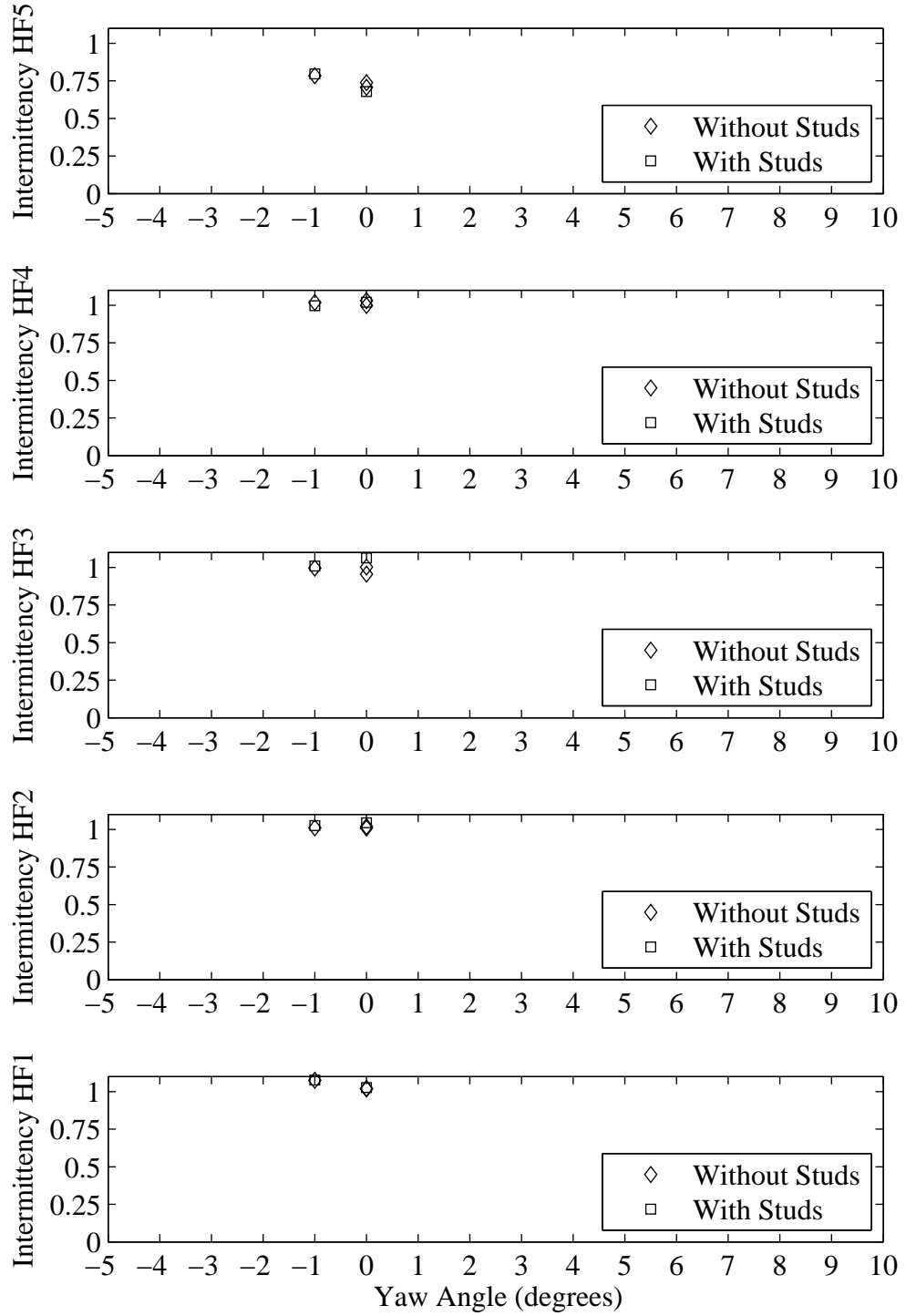


Figure H.60: Intermittency plotted with respect to variation in yaw angle. Froude number 0.40, Heel 0 degrees, Tab 2 degrees, Rudder 0 degrees.

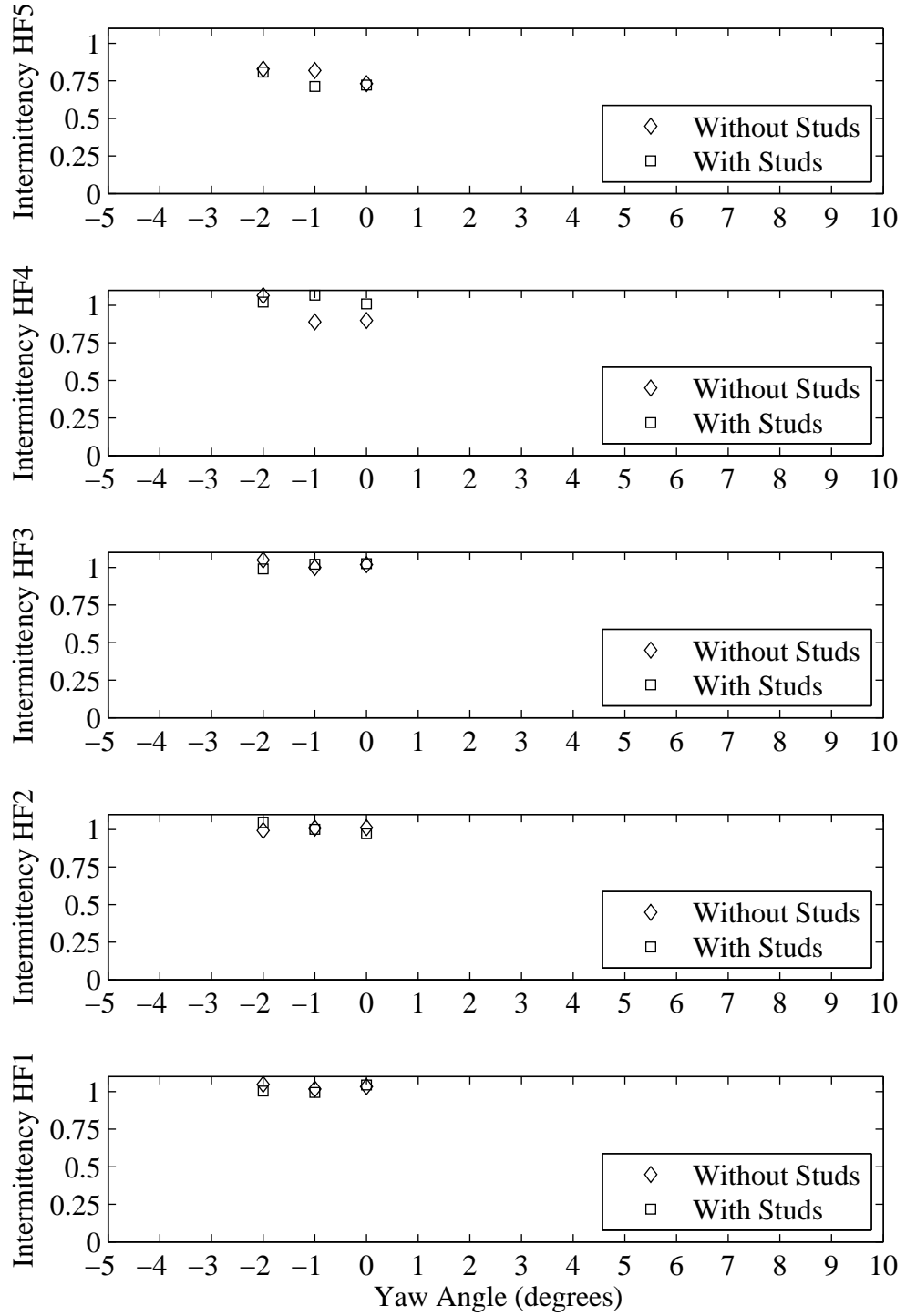


Figure H.61: Intermittency plotted with respect to variation in yaw angle. Froude number 0.40, Heel 0 degrees, Tab 4 degrees, Rudder 0 degrees.

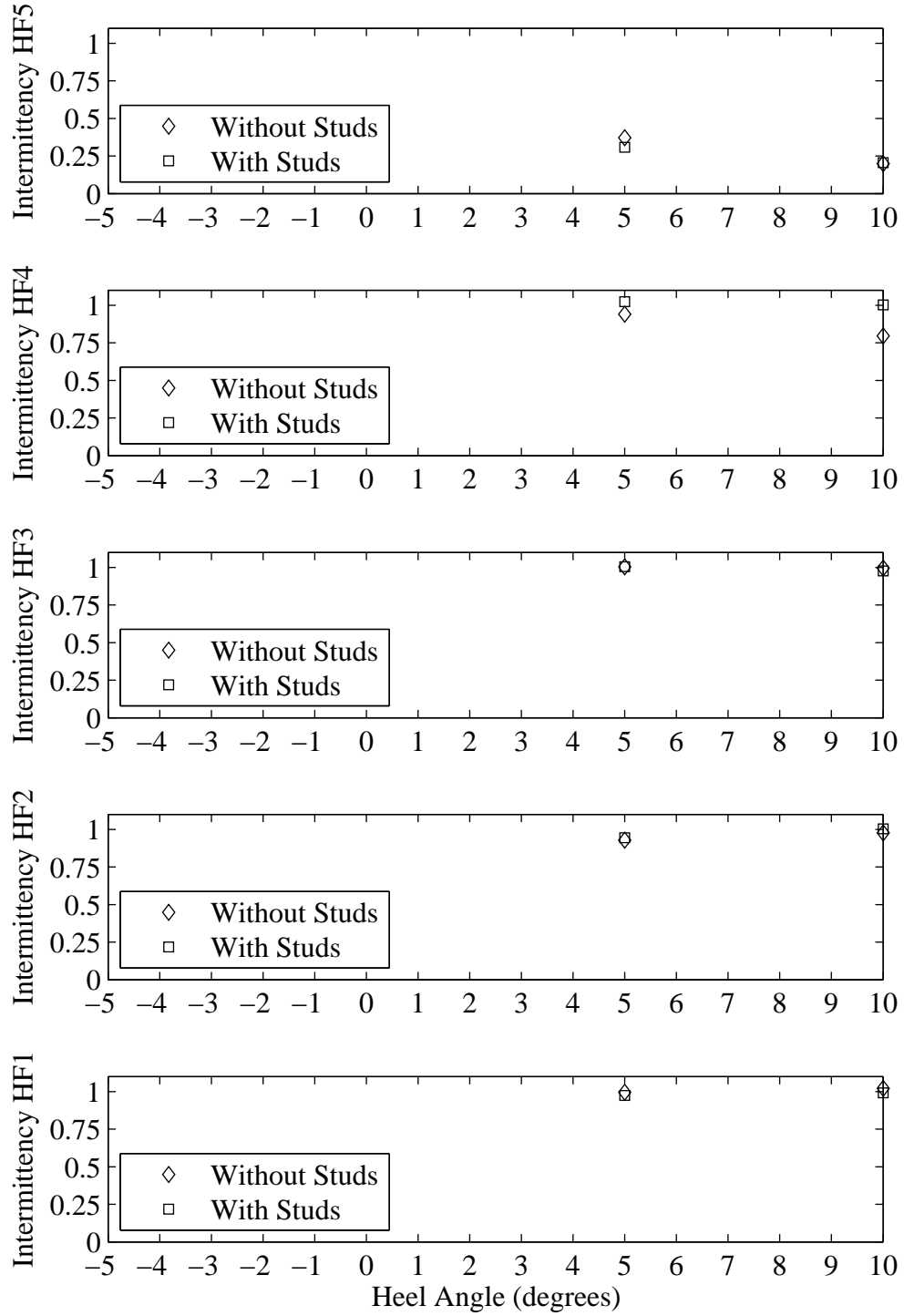


Figure H.62: Intermittency plotted with respect to variation in heel angle. Froude number 0.27, Yaw 0 degrees, Tab 4 degrees, Rudder 2 degrees.

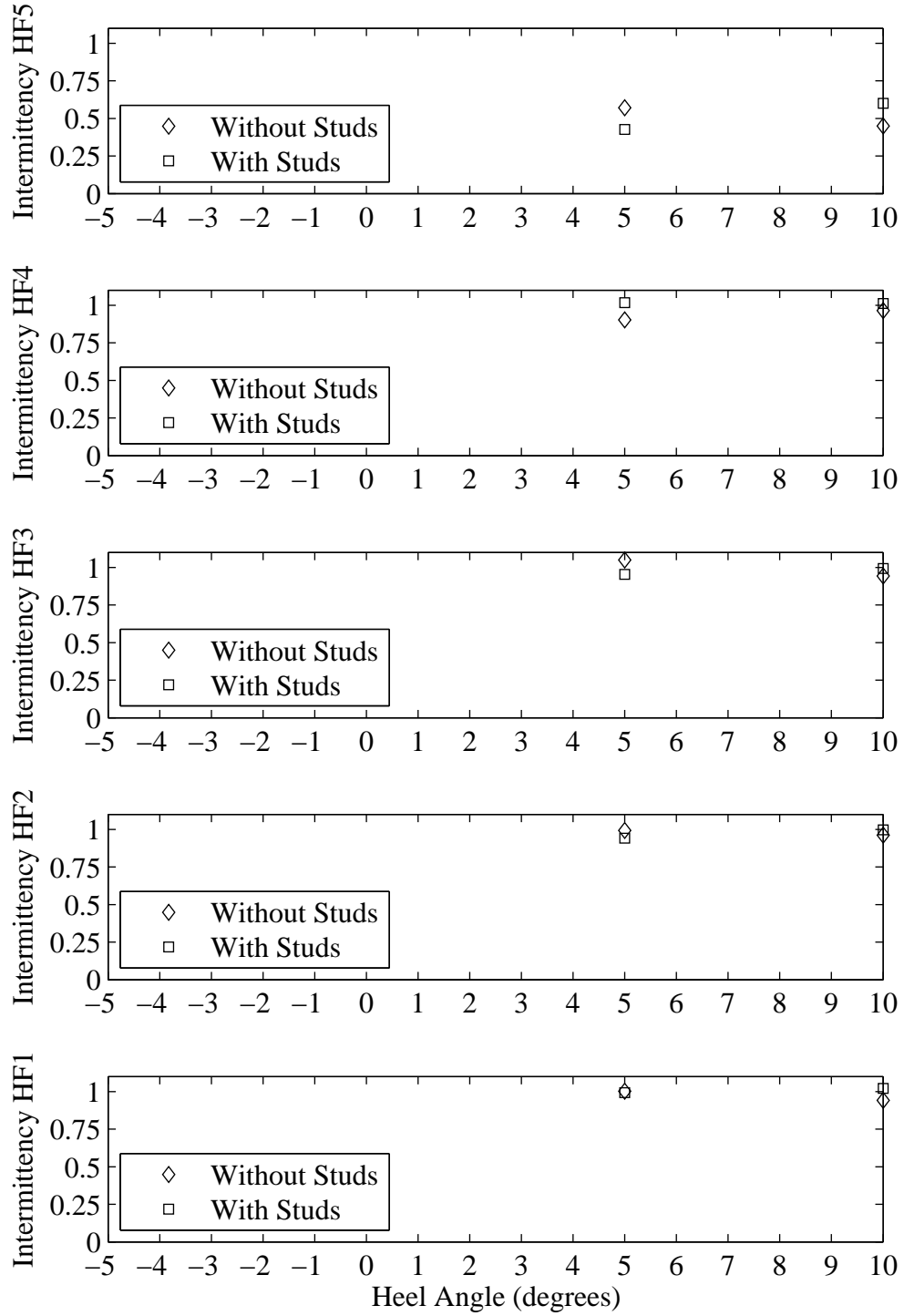


Figure H.63: Intermittency plotted with respect to variation in heel angle. Froude number 0.27, Yaw 1 degrees, Tab 4 degrees, Rudder 2 degrees.

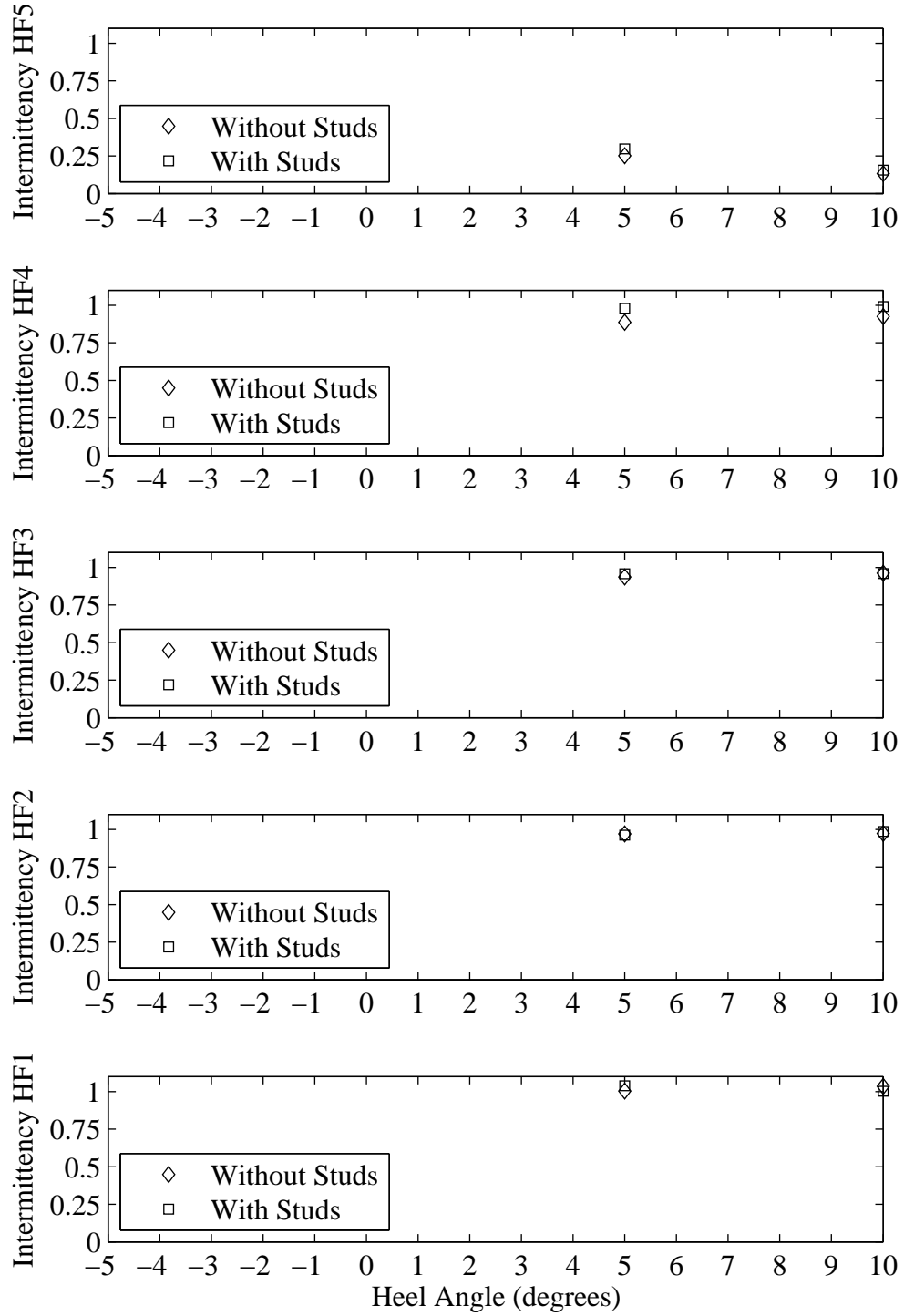


Figure H.64: Intermittency plotted with respect to variation in heel angle. Froude number 0.27, Yaw -2 degrees, Tab 6 degrees, Rudder 2 degrees.

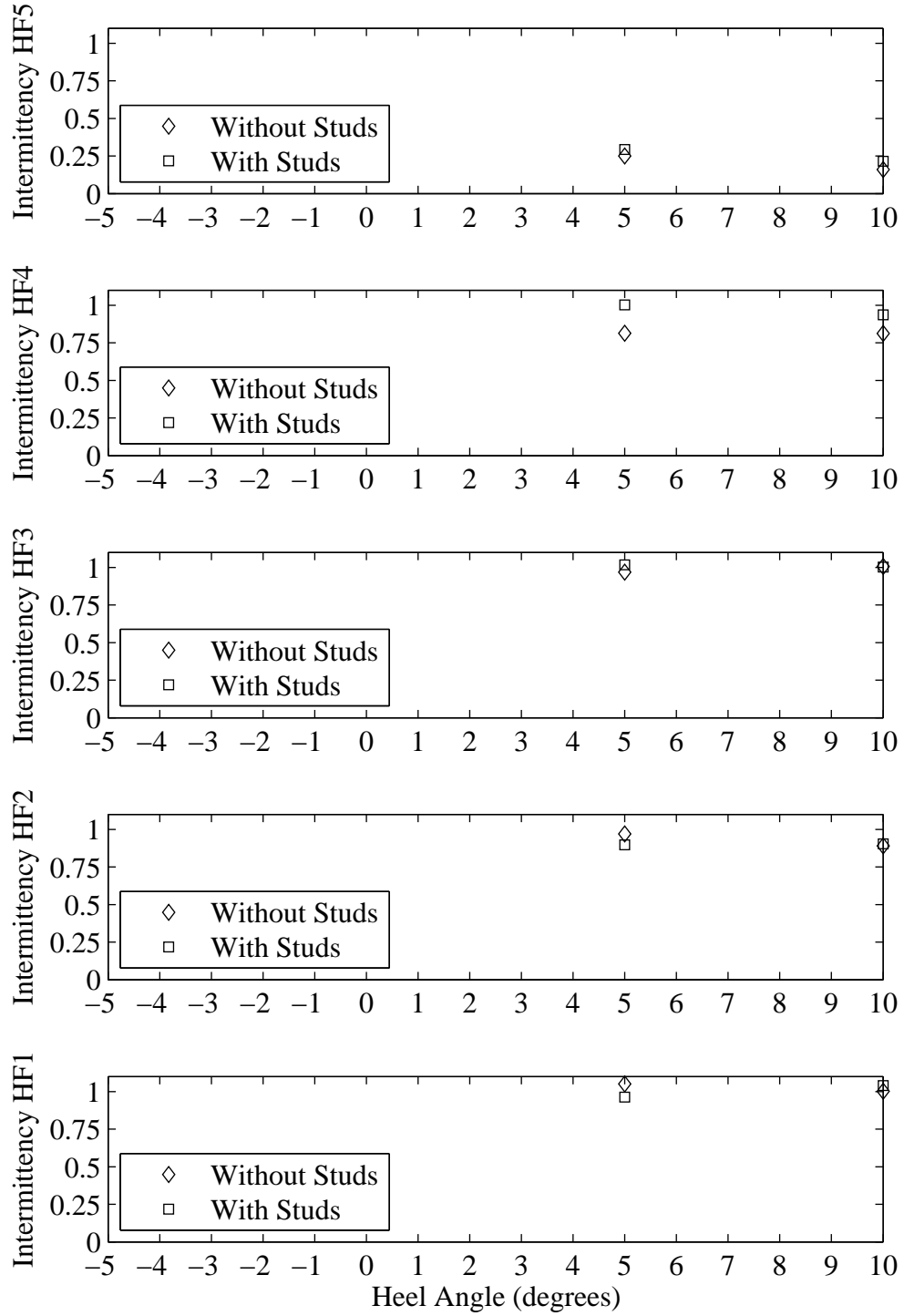


Figure H.65: Intermittency plotted with respect to variation in heel angle. Froude number 0.27, Yaw 0 degrees, Tab 6 degrees, Rudder 2 degrees.

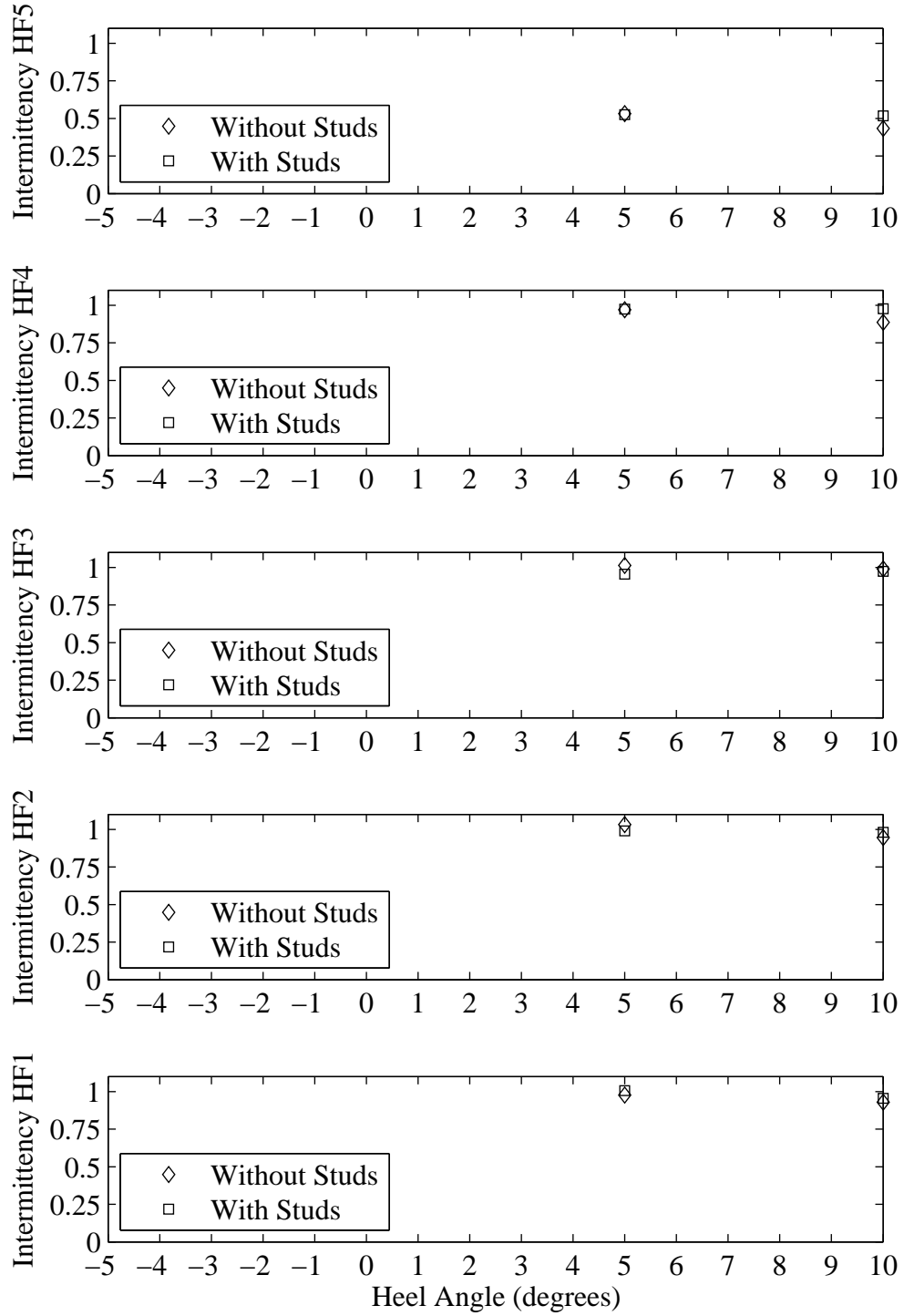


Figure H.66: Intermittency plotted with respect to variation in heel angle. Froude number 0.27, Yaw 1 degrees, Tab 6 degrees, Rudder 2 degrees.

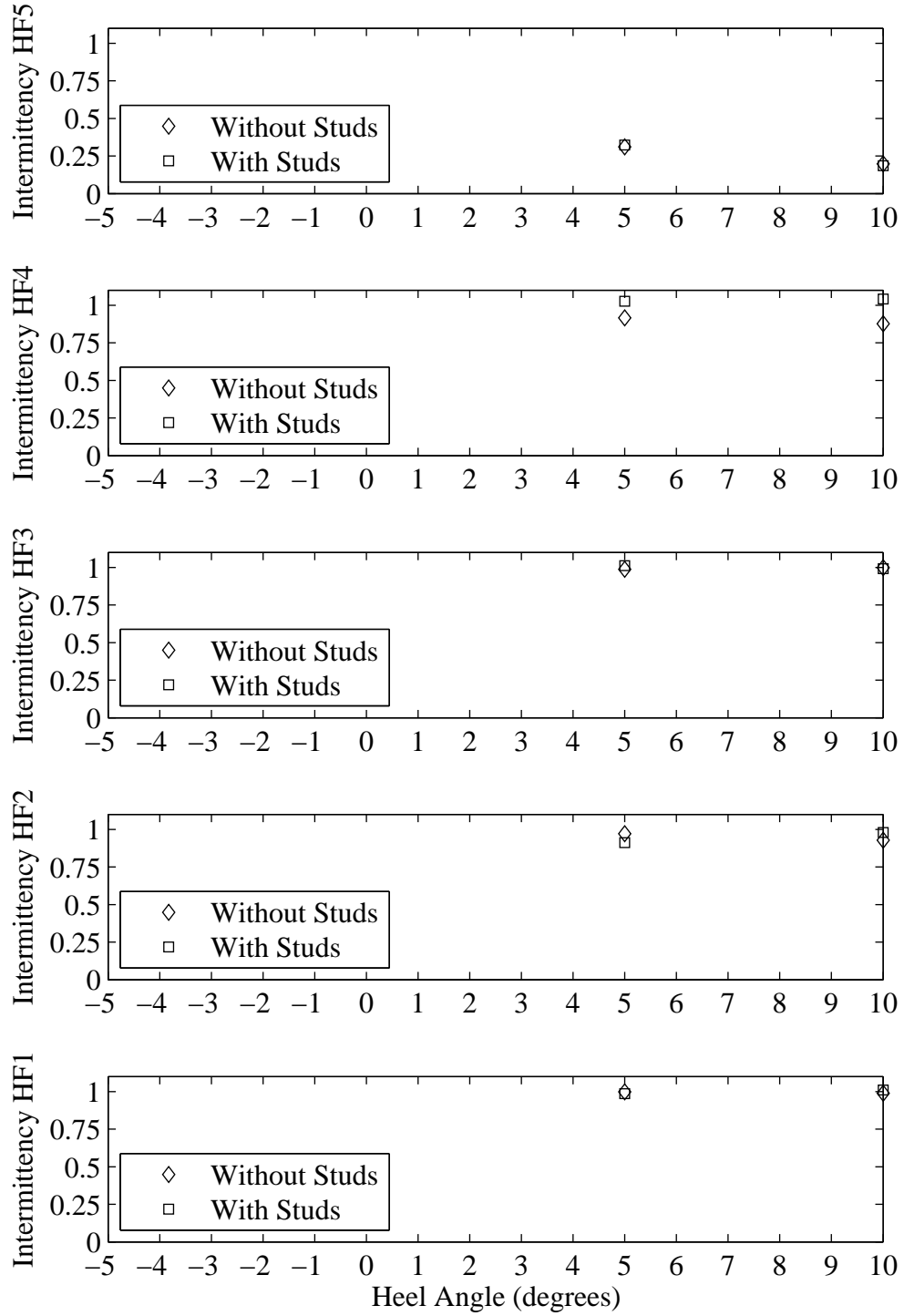


Figure H.67: Intermittency plotted with respect to variation in heel angle. Froude number 0.27, Yaw -2 degrees, Tab 8 degrees, Rudder 2 degrees.

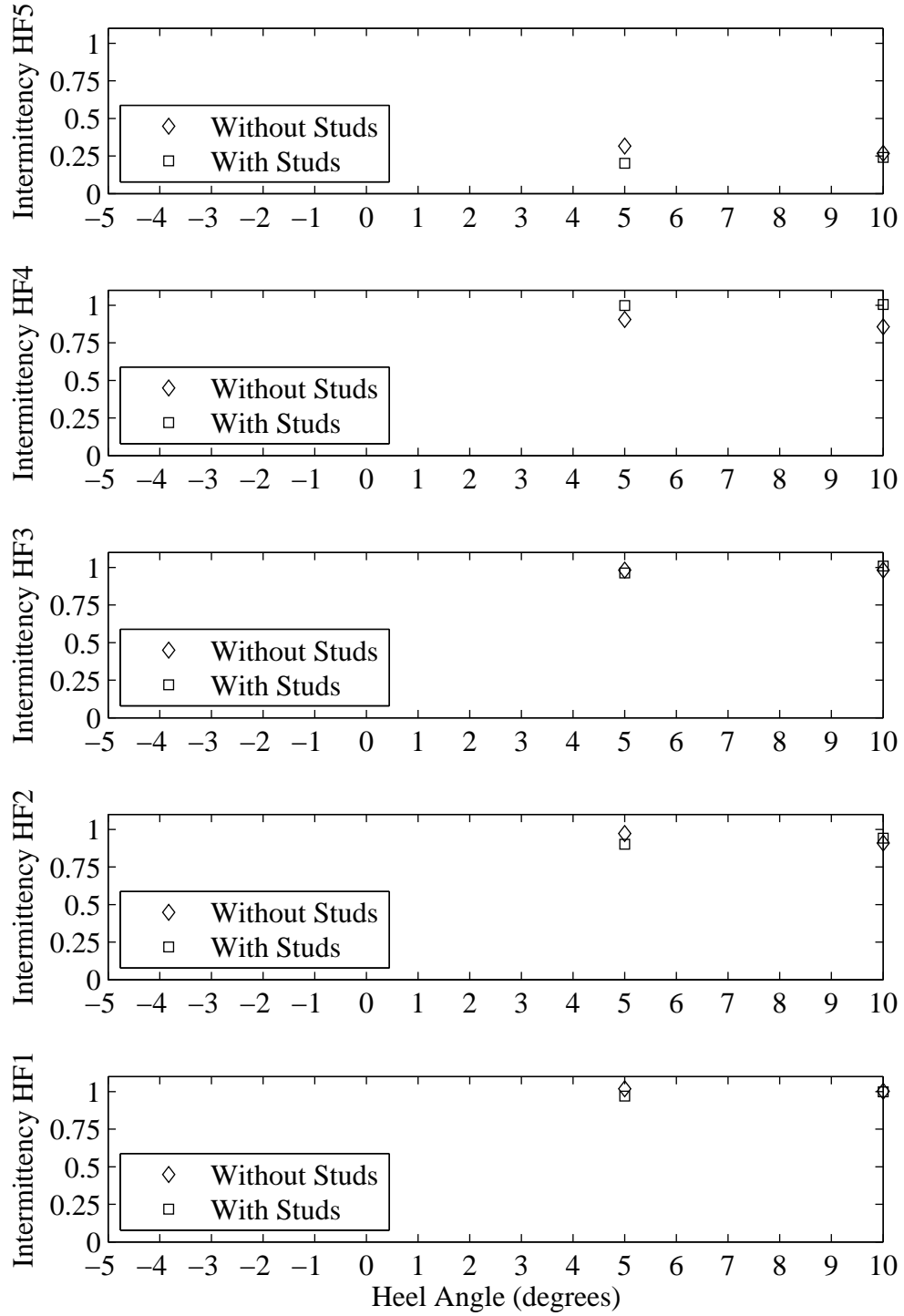


Figure H.68: Intermittency plotted with respect to variation in heel angle. Froude number 0.27, Yaw 0 degrees, Tab 8 degrees, Rudder 2 degrees.

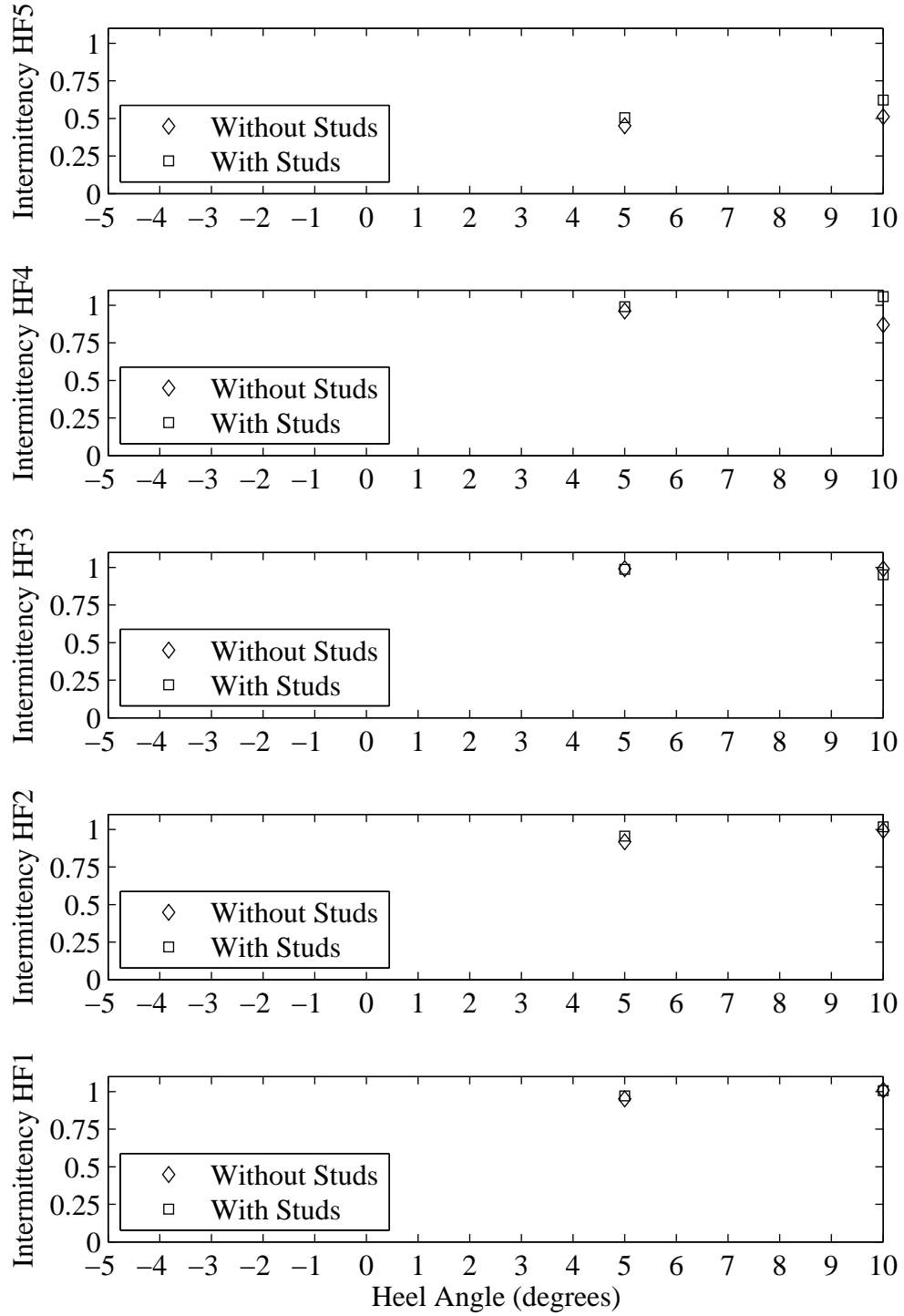


Figure H.69: Intermittency plotted with respect to variation in heel angle. Froude number 0.27, Yaw 1 degrees, Tab 8 degrees, Rudder 2 degrees.

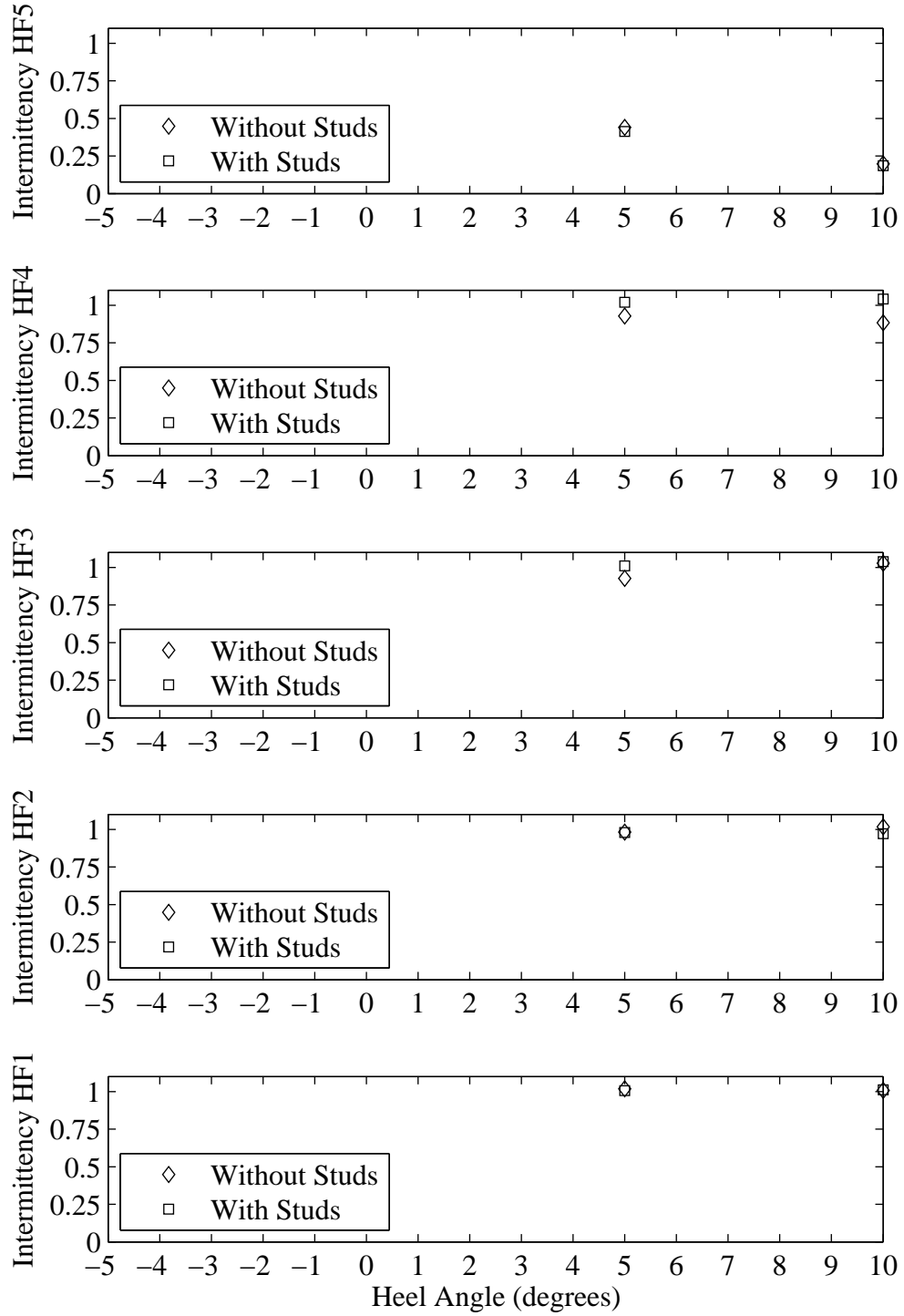


Figure H.70: Intermittency plotted with respect to variation in heel angle. Froude number 0.29, Yaw -2 degrees, Tab 4 degrees, Rudder 4 degrees.

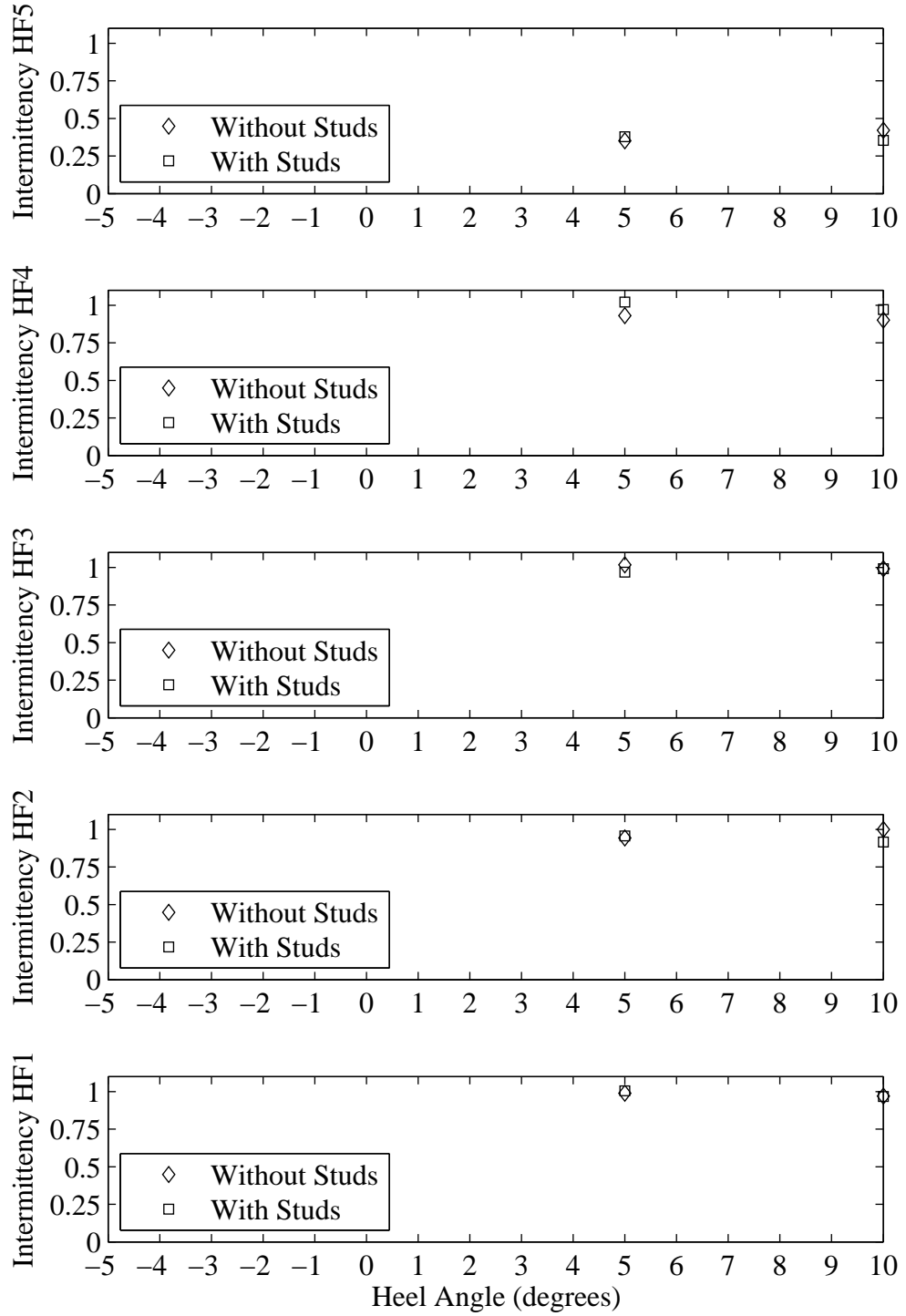


Figure H.71: Intermittency plotted with respect to variation in heel angle. Froude number 0.29, Yaw 0 degrees, Tab 4 degrees, Rudder 2 degrees.

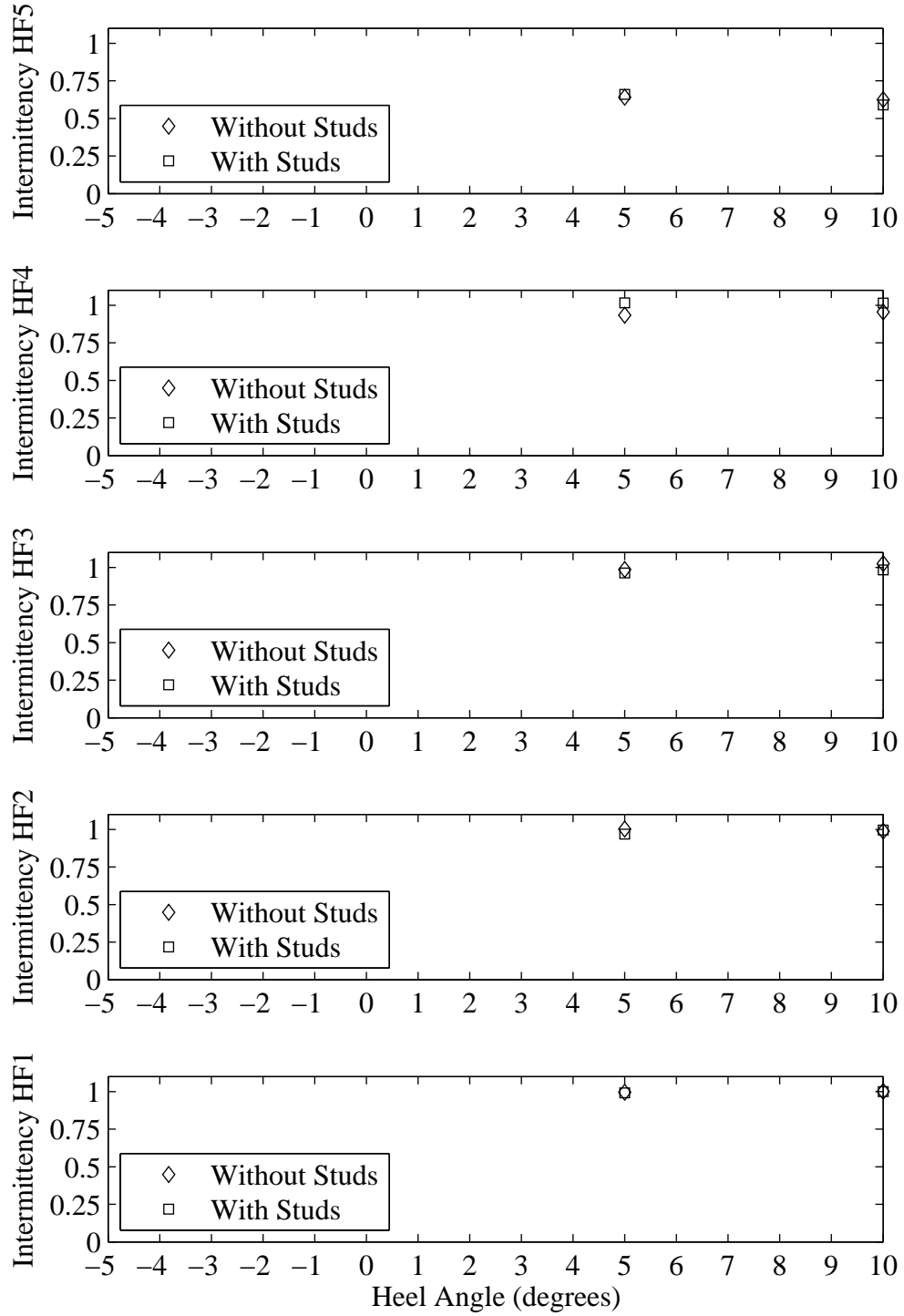


Figure H.72: Intermittency plotted with respect to variation in heel angle. Froude number 0.29, Yaw 1 degrees, Tab 4 degrees, Rudder 2 degrees.

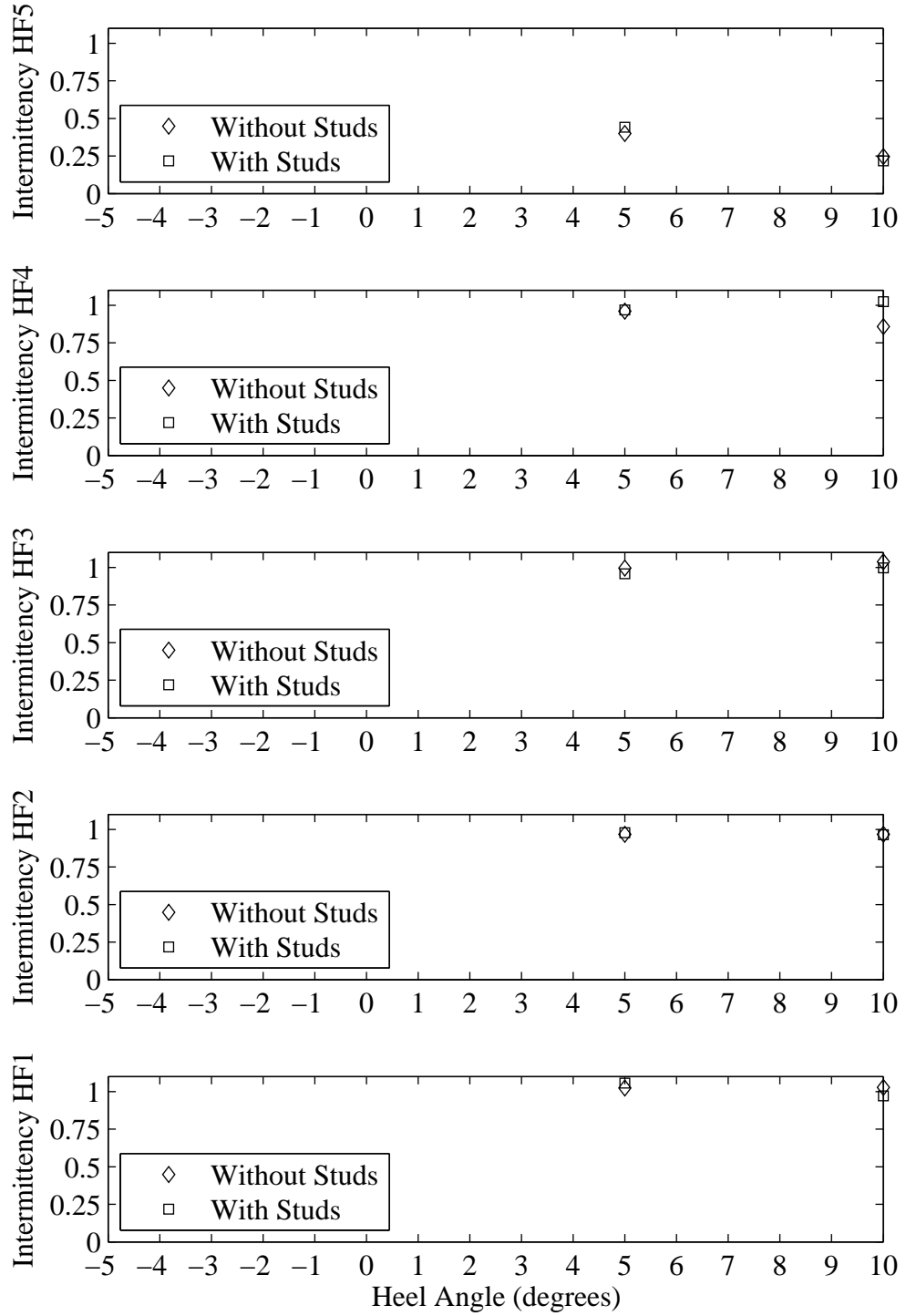


Figure H.73: Intermittency plotted with respect to variation in heel angle. Froude number 0.29, Yaw -2 degrees, Tab 6 degrees, Rudder 2 degrees.

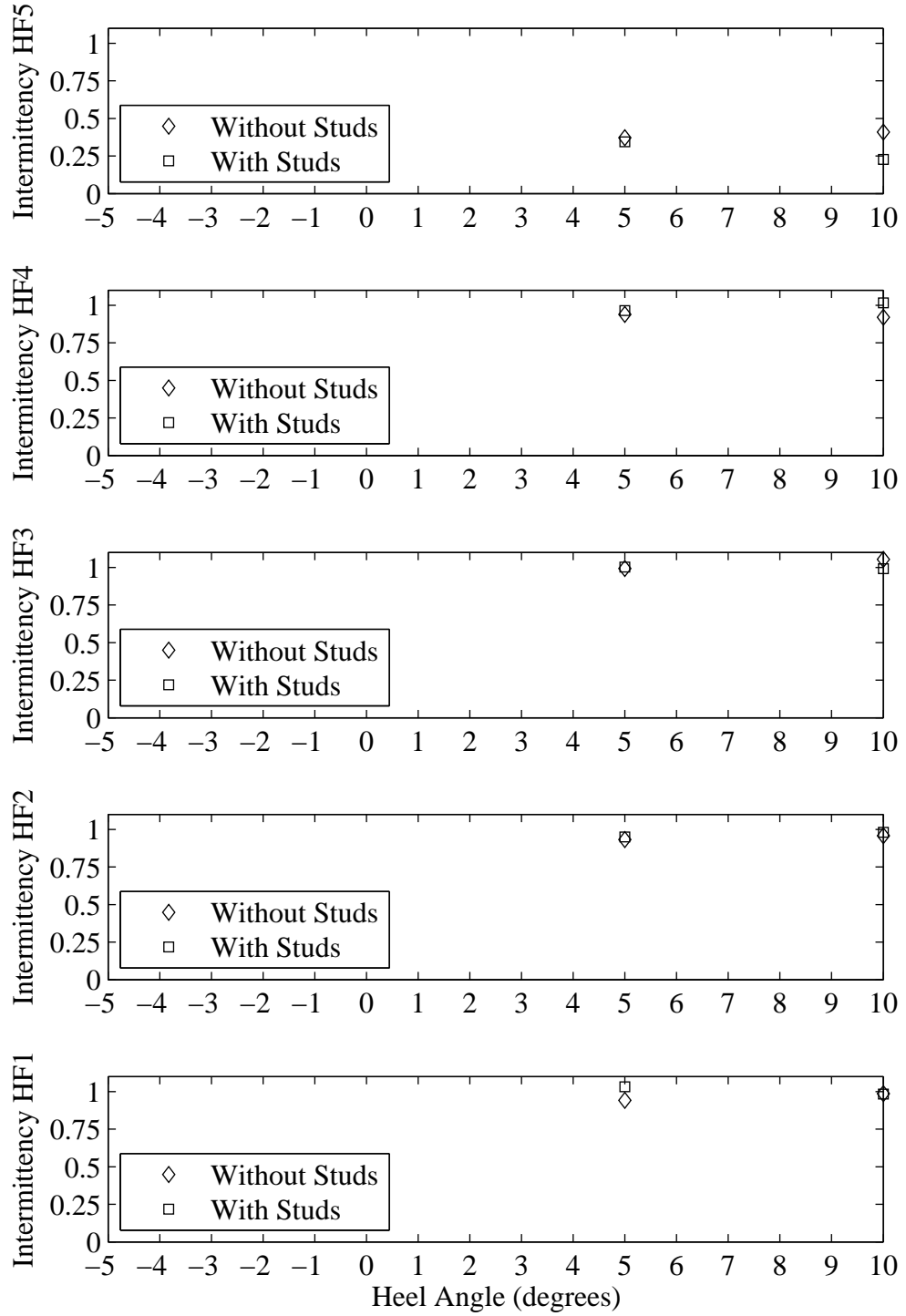


Figure H.74: Intermittency plotted with respect to variation in heel angle. Froude number 0.29, Yaw 0 degrees, Tab 6 degrees, Rudder 2 degrees.

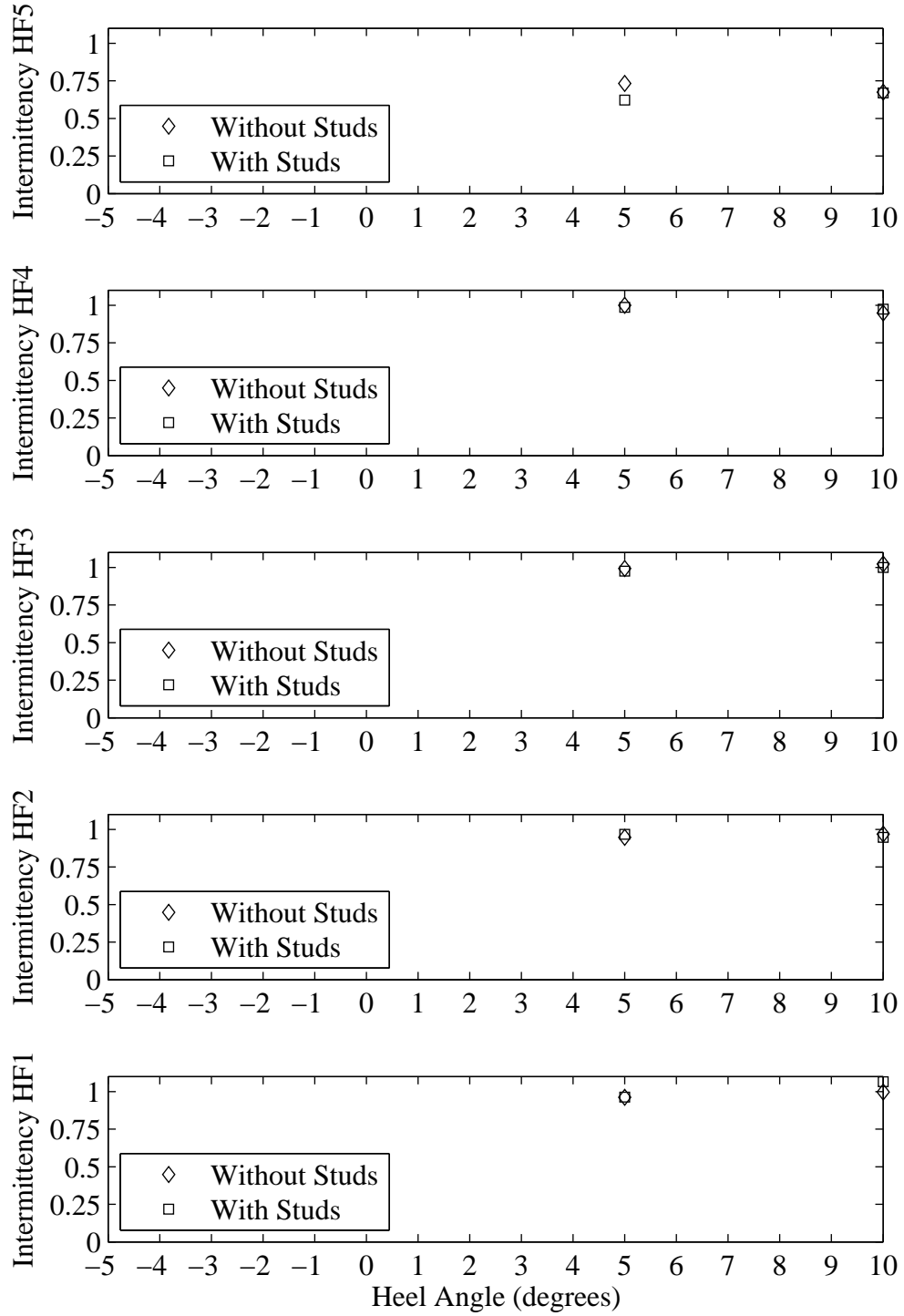


Figure H.75: Intermittency plotted with respect to variation in heel angle. Froude number 0.29, Yaw 1 degrees, Tab 6 degrees, Rudder 2 degrees.

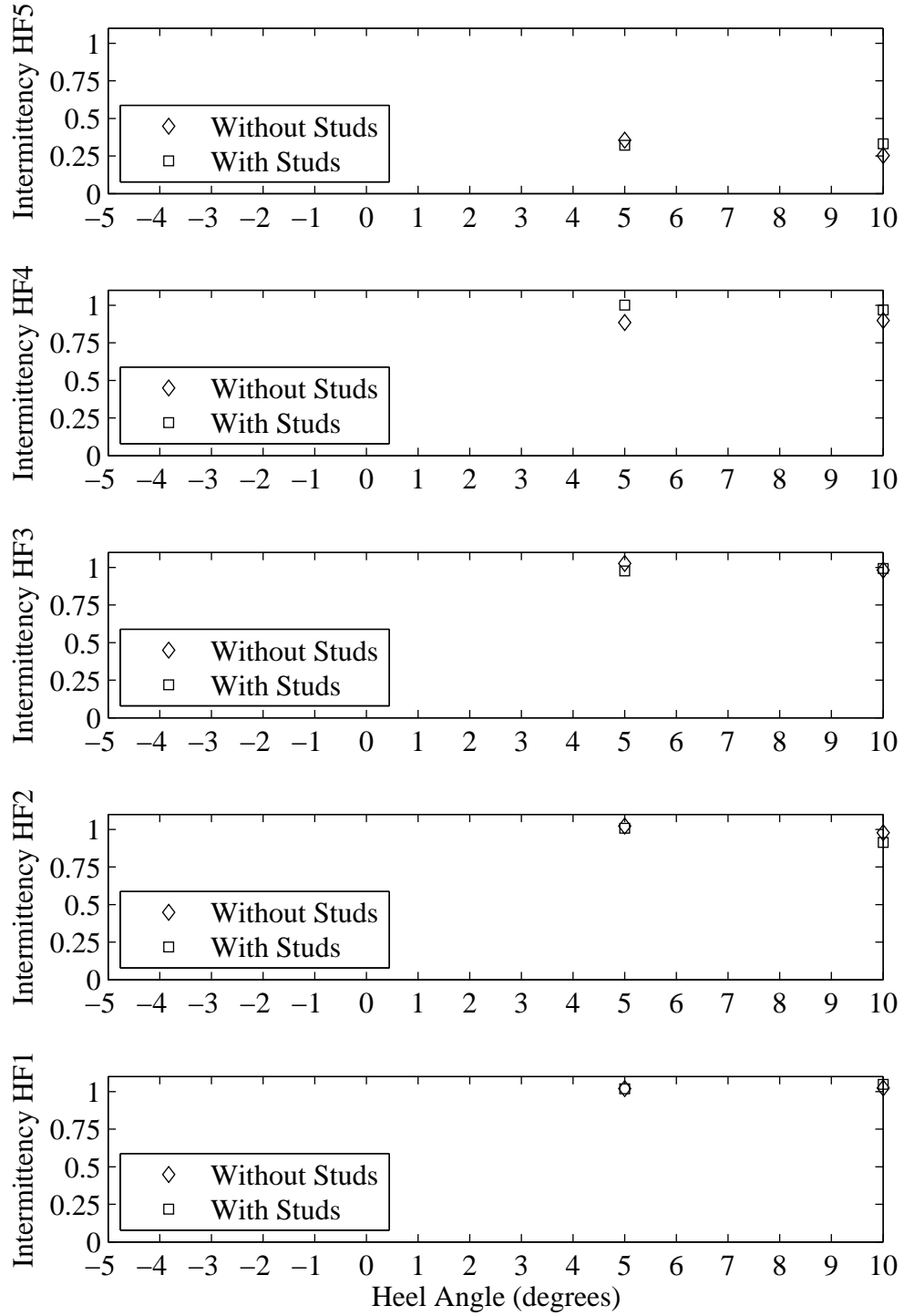


Figure H.76: Intermittency plotted with respect to variation in heel angle. Froude number 0.29, Yaw -2 degrees, Tab 8 degrees, Rudder 2 degrees.

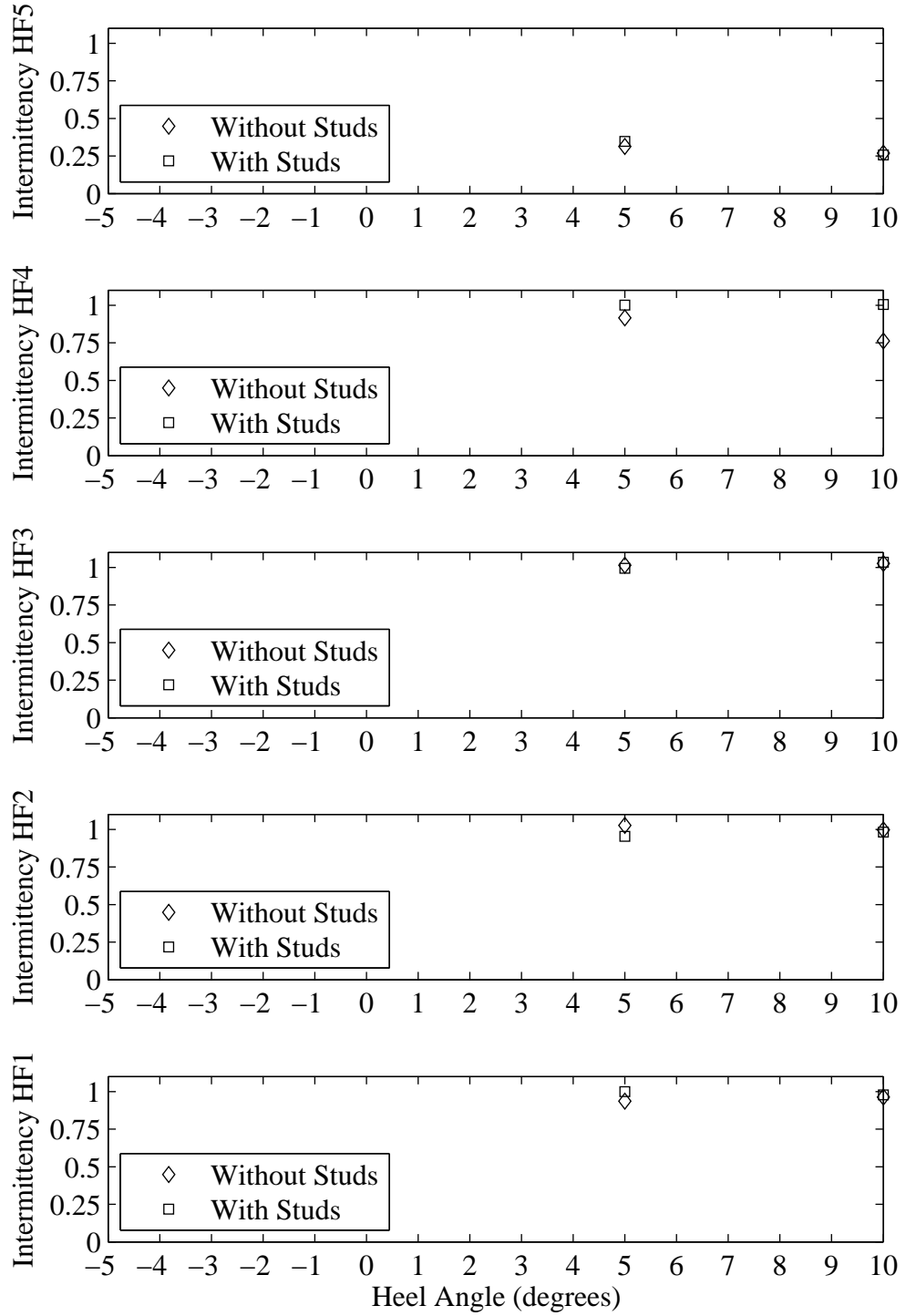


Figure H.77: Intermittency plotted with respect to variation in heel angle. Froude number 0.29, Yaw 0 degrees, Tab 8 degrees, Rudder 2 degrees.

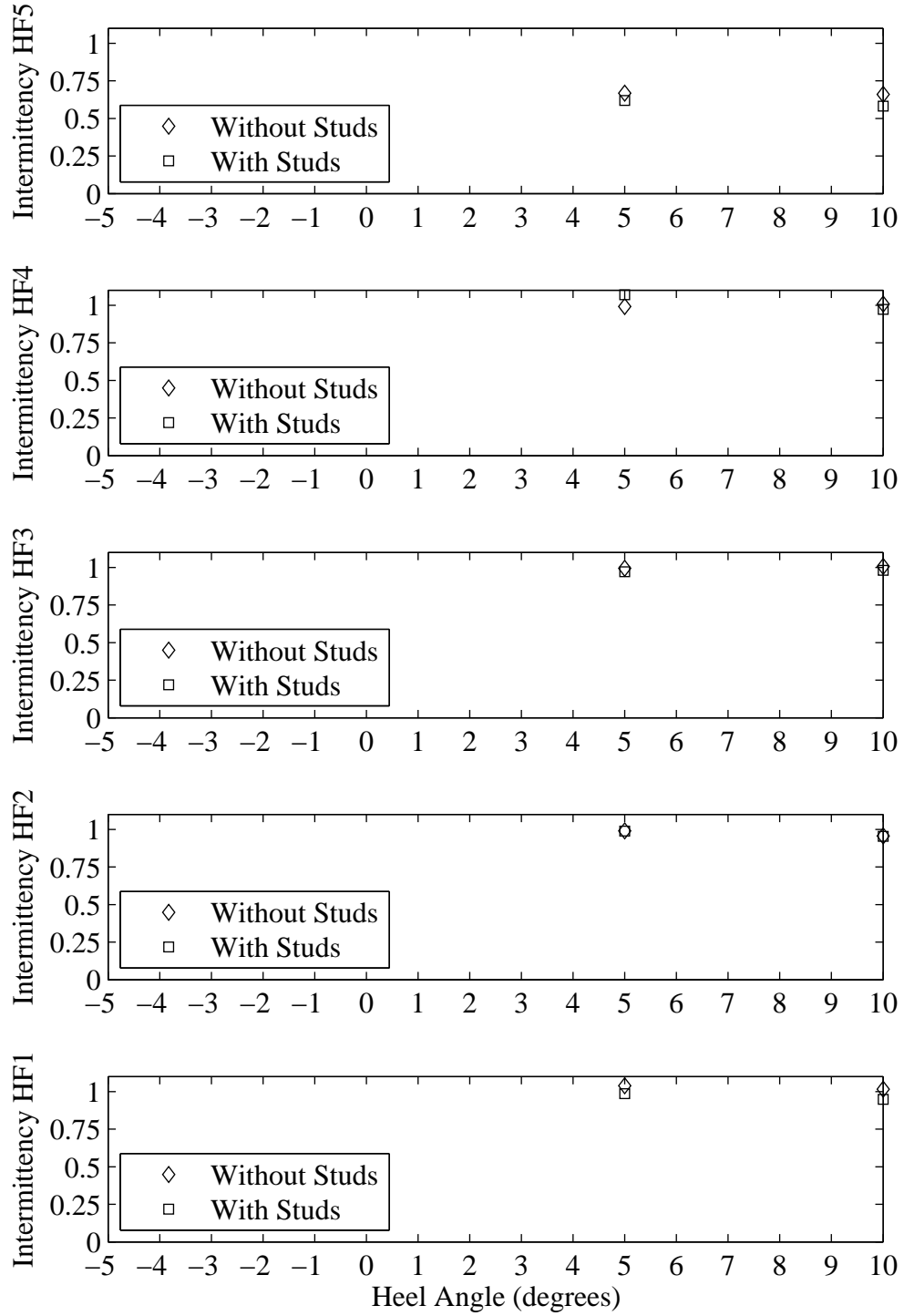


Figure H.78: Intermittency plotted with respect to variation in heel angle. Froude number 0.29, Yaw 1 degrees, Tab 8 degrees, Rudder 2 degrees.